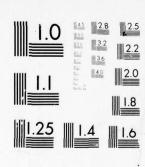


AD A051272



MICROCOPY RESOLUTION TEST CHART NATIONAL BUREAU OF STANDARDS-1963-8

AGARD-LS-88

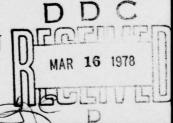
ADVISORY GROUP FOR AEROSPACE RESEARCH & DEVELOPMENT

7 RUE ANCELLE 92200 NEUILLY SUR SEINE FRANCE

AGARD LECTURE SERIES No. 88

Applications of Remote Sensing to Ocean Surveillance

FINAL VERSION



NORTH ATLANTIC TREATY ORGANIZATION



DISTRIBUTION AND AVAILABILITY
ON BACK COVER

15 NOTION

NORTH ATLANTIC TREATY ORGANIZATION

ADVISORY GROUP FOR AEROSPACE RESEARCH AND DEVELOPMENT

(ORGANISATION DU TRAÎTE DE L'ATLANTIQUE NORD)

	AGARD Lecture Series No.88 CATIONS OF REMOTE SENSING TO
	GEAN SURVEILLANCE
AGRESSION for RTIR Unito Section BOG Gert Section UNARROUNCED JUSTIFICATION	(11) Sep 77] (12) 269 P.
ESTPROTION/AVAILABILITY CORS Olat. AVAIL ond/er SPECIAL	DDC DECOMMAR 16 1978 MAR 16 1978

The material in this publication was assembled to support a Lecture Series under the sponsorship of the Electromagnetic Wave Propagation Panel and the Consultant and Exchange Programme of AGARD, presented on 3-4 October 1977 in Oslo, Norway, 6-7 October 1977 in Den Helder, Netherlands and 11-12 October 1977 in Rome, Italy.

DISTRIBUTION STATEMENT A

Approved for public release; Distribution Unlimited

JOB

THE MISSION OF AGARD

The mission of AGARD is to bring together the leading personalities of the NATO nations in the fields of science and technology relating to aerospace for the following purposes:

- Exchanging of scientific and technical information;
- Continuously stimulating advances in the aerospace sciences relevant to strengthening the common defence posture;
- Improving the co-operation among member nations in aerospace research and development;
- Providing scientific and technical advice and assistance to the North Atlantic Military Committee in the field of aerospace research and development;
- Rendering scientific and technical assistance, as requested, to other NATO bodies and to member nations
 in connection with research and development problems in the aerospace field;
- Providing assistance to member nations for the purpose of increasing their scientific and technical potential;
- Recommending effective ways for the member nations to use their research and development capabilities for the common benefit of the NATO community.

The highest authority within AGARD is the National Delegates Board consisting of officially appointed senior representatives from each member nation. The mission of AGARD is carried out through the Panels which are composed of experts appointed by the National Delegates, the Consultant and Exchange Program and the Aerospace Applications Studies Program. The results of AGARD work are reported to the member nations and the NATO Authorities through the AGARD series of publications of which this is one.

Participation in AGARD activities is by invitation only and is normally limited to citizens of the NATO nations.

A large part of the content of this publication has been reproduced directly from material supplied by AGARD or the authors; the remainder has been set by Technical Editing and Reproduction Ltd.

Published September 1977

Copyright © AGARD 1977 All Rights Reserved

ISBN 92-835-0202-7



Printed by Technical Editing and Reproduction Ltd Harford House, 7–9 Charlotte St., London, W1P 1HD

THEME

The sea covers more than three quarters of the earth and the concealment it provides to military forces will make it the area of major activities in the next decade. The defence of land and sea is vital to the NATO alliance. Land surveillance has been covered in several AGARD meetings while the oceans thus far have received little attention. Techniques for ocean surveillance from satellites and aircraft reached a high degree of sophistication as the result of the combined efforts in space and military programs. The limitations of these techniques come not so much from technology itself but rather from the propagation medium, air and sea. These techniques and the interpretation of results are totally different for land and sea.

This lecture series therefore presents the mathematical tools and their applications to the problems of resolving, recognizing and identifying targets and sources of activities in the ocean. This series should be of interest to physicists and engineers who want to learn the mathematical methods applicable to ocean surveillance, to military users who want to interpret results and infer tactical and strategic implications and to industries interested in developing future generation hardware.

The lecture topics cover two broad categories of surveillance:

- Ocean targets, for instance ships (Imaging).
- Ocean phenomena indicative of military activities, for instance changes in biology or surface temperatures.

LIST OF SPEAKERS

Lecture Series Director:

Dr R.N.Keeler

Director of Navy Technology Naval Material Command Department of the Navy Washington DC

USA

Lecture Series

Deputy Director:

Mr F.P.Diemer

Research/Program Coordinator

Ocean Science Program Office of Naval Research Arlington, Virginia

USA

Dr W.L.Barnes

Goddard Space Flight Center

Greenbelt Maryland USA

Dr H.Hodara Vice President Tetra Tech Inc

630 N Rosemeade Boulevard

Pasadena, California

USA

Mr R.Buntzen

Head, Non-Acoustic ASW Group Naval Ocean Systems Center

San Diego, California

USA

Dr J.P.Hollinger

Naval Research Laboratory 4555 Overlook Avenue, S.W.

Washington DC 20375

USA

RADM R.K.Geiger, USN Chief of Naval Research

Office of Naval Research 800 N Quincy Street

Arlington, Virginia USA

Professor E.Raschke Institute of Geophysics and Meteorology

University of Cologne

Cologne Germany

Mr J.Genuist

Societe Thomson - CSF Division Avionics/Space 178 Boulevard Gabriel Peri

92200 Malakoff

France

Dr G. Tacconi

Electrical Engineering Dept

University of Genoa

Viale Causa; 13 Genoa

Italy

Mr E.P.L.Windsor

British Aircraft Corporation Limited

Space Systems Group, Filton House

Bristol

UK

CONTENTS

	Page
ТНЕМЕ	ш
LIST OF SPEAKERS	iv
	Reference
KEYNOTE ADDRESS – REMOTE SENSING IN OCEAN SURVEILLANCE – PROMISES, PROBLEMS AND PERSPECTIVES by R.K.Geiger	1
OPERATIONAL REQUIREMENTS AND PROBLEMS by R.N.Keeler	2
RADIATION AND ENVIRONMENTAL PHYSICS REFRESHER by E.Raschke	3
MICROWAVE SCANNING RADIOMETRY by J.P.Hollinger	4
MICROWAVE SCANNING RADIOMETRY (APPLICATIONS) by E.P.L.Windsor and H.McD.Mooney	5
INFRARED RADIOMETRY AND VISIBLE SPECTROMETRY by H.Hodara and W.H.Wells	6
VISIBLE AND INFRARED IMAGING RADIOMETERS FOR OCEAN OBSERVATIONS by W.L.Barnes	7
RADAR A FAISCEAU LATERAL UTILISANT UNE ANTENNE SYNTHETIQUE — In French and English. (SIDEWAYS-LOOKING RADAR (SLR) USING A SYNTHETIC AERIAL)	
par J.Genuist	8
FUNDAMENTALS OF ELF COMMUNICATION AND DETECTION by G.Tacconi	9
ELECTRIC AND MAGNETIC SENSING SYSTEMS: APPLICATIONS by F.Chilton, L.Wood and R.Buntzen	10
BIBLIOGRAPHY	В

REMOTE SENSING IN OCEAN SURVEILLANCE--PROMISES, PROBLEMS AND PERSPECTIVES By

Rear Admiral Robert K. Geiger, USN

Summary

Chief of Naval Research Admiral Robert K. Geiger discusses the U.S. Navy's mission and need for global real time information of the environmental factors that affect naval operations. The potential of remote sensing technology for ocean surveillance needs to be developed through a program of research and engineering and a coordinated exchange of information among the disciplinary scientists, industry, and the military commanders who must interpret remotely sensed data for tactical and strategic decisions.

I am honored to address this session of the AGARD Lecture Series 88, "Application of Remote Sensing to Ocean Surveillance." It is a field of great interest to me as Chief of Naval Research.

I am aware that the distinguished lecturers who will follow me in this series are eminently qualified to discuss the state-of-the-art of remote sensing of the environment and its potential as a tool for surveillance of the oceans.

Remote sensing is a technological and scientific field that has undergone drastic changes in the last three decades. From the first efforts consisting of subjective analysis of occasional aerial photography it has advanced to automated processing of information about the environment gathered several times a day by manned and unmanned satellites.

The advances in remote sensing are due to several factors. Principal among these factors are: growth of aerospace technology; the concurrent rapid development of data processing capability; communication technology; and the requirements of the military departments for early warning reconnaisance and surveillance. It was in great part these requirements which provided the impetus behind the research and engineering for application of remote sensing for surveillance of the ocean.

The birth and growth of modern remote sensing received a major thrust from the Office of Naval Research. The very term "Remote Sensing" originated within the Geography Branch of the Office of Naval Research in 1961 when a project entitled, "Interpretation of Aerial Photography" was renamed "Remote Sensing of the Environment." The new term was coined to take into account the development of sensors able to make observations in the regions of electromagnetic spectrum beyond the range of human vision and photographic sensitivity, and to encompass the observation process from remote platforms.

Two aspects of ocean surveillance are of vital importance to the Navy. First is the detection, location and classification of targets or false alarms; the second encompasses the ability to measure and predict the environmental parameters to support command decisions for improved mission effectiveness.

The Navy must be able to carry out its responsibility for national defense and in support of our commitments to our allies. These commitments span the globe. The Navy must operate in every part of the world and it has great need for knowledge, on a global scale, of the factors that can influence the operation of ships and aircraft, weapons, and sensor systems. The success or failure of a mission can be determined by the availability, or lack of, timely information of environmental factors such as water temperature, sea state, winds, or sea ice. Cost effective utilization of resources is also influenced by accurate information about existing and forecasted environmental conditions.

The information must be timely and accurate, considering the multiplicity of requirements for tactical and strategic plannings. These requirements range from a 0-6 hours forecast for tactical operations, to a 30-day forecast for ship routing and strategic planning. The space scale requirement ranges from "battlefield" size area of 50 km, to global.

Timely requirements are all the more critical in view of the dynamic nature of the environment in which the Navy must operate. The classic picture of the deep ocean has been one consisting of large sluggish gyres and slowly changing structures, except for the Gulf Stream. Recent basic research has revealed that the ocean is quite complex, and in many respects it is analogous to the atmosphere: it contains the oceanic counterpart of atmospheric weather. This oceanic "weather" consists of highs, lows, fronts, jets, which, relative to general ocean climatology, travel quite rapidly.

The sharp temperature gradients associated with this weather are known to cause rapid changes in sonar conditions and provide acoustic shadows that obscure an object from detection. These conditions may be exploited by the fleet, if we can provide, in real time, a mechanistic explanation on how they form and develop the tools to monitor their formations and movement on a global scale.

Even more dynamic than the deep ocean are the shallow waters of the coastal areas. Here, wind, waves, currents, turbidity and tides and bathimetry have a major influence on the various types of operations, particularly amphibious or mine warfare operations. The success of a mission is greatly dependent upon timely and accurate information concerning existing and forecast environmental conditions; the usefulness, precision and validity of environmental assessments forecast models are directly proportional to the precision, resolution, density and the geographical area covered by the measurements of the environmental parameters.

Current and projected conventional oceanographic measurements—point source observation from ship and aircraft—are by necessity limited. The ratio of observed to unobserved is 1 to 1000 at least. This is inadequate to permit timely and accurate assessments and forecasts of ocean environment on a global scale. Further, conventional measurements are costly; delays in the transmission and receipt of the data diminishes its usefulness; the presence of the ships and their activities in a certain location may potentially compromise the military position and intentions. These measurements may be nonexistent and impractical to obtain over hostile waters; many areas of the world's oceans, polar regions and mid-latitudes as well, are remote from normal operating and shipping lanes and measurements by conventional means. Indeed, about 50 percent of the world's oceans and coastal areas are routinely unobserved and provide no data on which to base accurate assessment or accurately forecast the ability of the Navy to provide improved environmental support.

Can remote sensing technology provide the tools needed to solve these problems?

Before attempting to answer the question, let us review the achievements by some of the past and current systems as well as those that are planned for the near future.

A complete chronology of these systems would be too long.

Table 1 shows some of the milestones since the launch of the first environmental satellite.

Table 2 shows what we may call current systems. The DMSP Block 5 incorporates an advanced atmospheric sampler of temperature and humidity profile and total ozone. LANDSAT-C inaugurated the use of a multispectral scanner providing 240-m spacial resolution infrared imagery in 10.4--12.6 mincron interval scale.

Table 3 represents the systems available in the near future.

TIROS-N will start a new series of NOAA polar orbiting satellites.

SEASAT-A represents the first dedicated oceanographic satellite.

It has five sensors: Radar altimeter; Wind field Scatterometer; Synthetic Aperture Radar; Visual and Infrared Imaging Radiometer; and Scanning Multichannel Microwave Radiometer.

NIMBUS G, STORMSAT-A, DMSP, and SEOS each represent a step forward in sensing capabilities.

Let's look at illustrations of the capabilities of the present systems (mainly in the visible and infrared sections of the spectrum.)

This is an actual surface photo of a Japanese fishing fleet, at night. (Fig. 1)

Seen from the DMSP satellite, the fleet looks like this. (Fig. 2)

The eastern half of the U.S. at night shows the lights of the main urban centers. (Fig. 3)

The next illustration shows an event that occured in 1975--a fire in the Los Angeles area. (Fig.4)

Smoke produced by the fire is clearly visible in this image. (Fig. 5)

Also clearly visible are such phenomena as Mistral wind over the Gulf of Lyons (Fig. 6)

And a sandstorm over the Arabian Sea. (Fig. 7)

The next few illustrations are images of sea surface temperature such as:

A mesoscale eddy of cold water pinched off by the Gulf Stream. (Fig. 8)

And an eddy of warm water in the Mediterranean Sea south of Sicily. (Fig.9)

This shows warm eddies in Baja, California. (Fig 10)

This IR enhanced image depicts Sea Surface Temperature in the Sea of Japan and Korea. (Fig. 11)

Winds influence the reflectivity of the sea surface; the black area indicates rough sea near the Strait of Gilbraltar. (Fig. 12)

Fig. 13 on the other hand, depicts the barrier effects off the West coast of the United States.

Among other parameters that can be detected are coastal silt (Fig 14), typhoons (Fig 15), or sea ice (Fig 16).

Clearly, the systems that are available now indicate that the potential exists for remote sensing from satellites for ocean surveillance as well as for oceanographic research. But in order to develop this potential fully for operational applications, a strong program of research and exploratory development must be undertaken to remove some of the limitations in present sensors and to develop new capabilities.

Some of the limitations in present systems are unacceptable signal-to-noise ratio, distortion of the data transmitted and data processing constraints. Technology must improve platforms, sensors and data links. We need greater spacial resolution, increased image repetition rates, adjustable sensor gain, narrower spectral bands for observation as well as all-weather, day/night capabilities.

In planning the direction of future remote sensing we must no lose sight of the fact that the needs of the military are in many cases different and more stringent than those of the civilian agencies. Within the military itself, the requirements differ. For the Army, battlefield visibility, rainfall, and trafficablity may be the principal parameters; for the Air Force, the conditions at air bases and possibly near space. For the Navy, however, these important parameters include the myriad everchanging phenomena that constitute the dynamics of the ocean.

It is critical that the systems be able to match the time and spacial variability that is required to detect the real changes in the environment—to match the right resolution with the right frequency.

In view of the investment that we are to make, it is imperative that the contributions of the disciplinary scientists be closely integrated with the technological development community. We must communicate and exchange ideas to bring together the synergistic efforts of the different groups involved in the different phases of development and utilization of this technology. There is a need for continuous dialogue among: the scientists and engineers who need to know the state of the art of sensor technology and the mathematical tools that can be applied to ocean surveillance problems; the defense agencies and the contracting industrial concern which has the ability to contribute to the direction of sensor system development; and finally, the ultimate user— the military commander who must interpret the data and use it tactical and strategic situations.

The capabilities of remote sensing, are of questionable use to the commander unless he can interpret accurately the phenomena, and eliminate every possibility of being misled--"aliasing."

Allow me to close with an illustration apropos of this point. (Fig. 17) How many of us recognize the phenomenon illustrated here?

Do we see what we want to see? And once we know what the phenomenon is, can we see anything else? (The subject is a cow).

I am pleased to be part of this lecture series and its intent to bring together different groups for a better understanding fo the requirements, problems, and promises fo remote sensing.

TABLE I

LAUNCH DATE	ACHIEVEMENTS	SATELLITE
April 1, 1960	Daytime cloud cover photography from space	TIROS I
Aug. 28, 1964	Nightime cloud cover imagery	NIMBUS I
July 1, 1965	First operational satellite	TIROS X
Feb. 28, 1966	World's first operational satellite system	ESSA 1 and 2
Jan. 17, 1970	Operational satellite with scanning radiometer(day & night)	ITOS 1
Oct. 15, 1972	Very high resolution and vertical temperature profile radiometers.	NOAA 2
May 17, 1974	First geosynchronous satellite with visual and infrared spin-scan radiometer	SMS-1
Mar. 10, 1975	Two-satellite system for near- continuous viewing of United States and adjacent waters	SMS-2

TABLE 2

LAUNCH DATE	SATELLITE	
April 1976	Block 5-D	
September 1977	LANDSAT-C	

TABLE 3

LAUNCH DATE	SATELLITE	
Early 1978	TIROS-N	
May 1978	SEASAT-A	
Late 1978	NIMBUS G	
1981	STORMSAT-A	
1981	DMSP	
1985	SEOS A	



Figure 1



Figure 2



Figure 3

Jose Mercury

Raging Fire Routs Thousands In L.A.



15,000 Acres Up In Flames



Figure 5



Figure 6



Figure 7



Figure 8

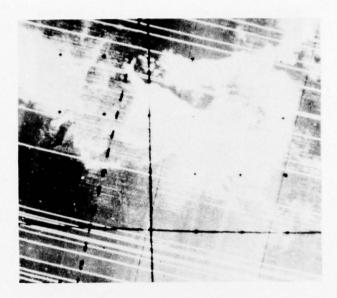


Figure 9



Figure 10



Figure 11



Figure 12



Figure 13



Figure 14



Figure 15



Figure 16



Figure 17



OPERATIONAL REQUIREMENTS AND PROBLEMS

by
Dr R.N.Keeler
Director of Navy Technology
Department of the Navy
Washington, D.C., USA

In the event of hostilities, NATO naval forces are tasked with establishing sea control and projecting power. Sea control involves establishing an acceptable level of risk for all naval forces operating within the area "controlled". Having established this sea superiority, our commanders can then turn to the sea control task of maintaining open sea lines of communication for our shipping and the power projection tasks of tactical air projection and amphibious assault.

To quickly establish an acceptable level of risk, we must have the earliest possible indicators of an enemy buildup. Because of the nature of Soviet naval assets, they must initiate hostilities with a highly coordinated attack. This coordination itself will be a strong indicator that attack may be imminent.

The nature of our surveillance assets, number, type and surveillance platform employed all depend upon the level of threat deployed against our forces.

During the past ten years, Warsaw Pact naval capability has increased substantially. An examination of out of area cruises of Soviet and Warsaw Pact naval forces indicates that the number of hours spent out of normal operating areas has increased almost ten-fold. This increase is shown in Figures 1–5. Whereas 10 to 15 years ago the major threat to NATO forces were Soviet coastal craft, surface units and diesel submarines, there is now a three dimensional threat which exists in all the maritime areas contiguous to NATO: The Northern Sea, Norwegian Sea, the Mediterranean, the Baltic Sea, and the Atlantic Ocean.

The current three dimensional threat consists of a Soviet Ocean Surveillance System (SOSS) utilizing HF-DF, Elint and Radar satellites, and tattletale aircraft and ships, all operating under centralized control and direction from Moscow; naval aircraft such as the Bear, Badger and new Backfire, which can cover the entire Mediterranean, Baltic and Norwegian Sea area at speeds up to Mach 2.5 and altitudes in excess of 50,000 feet; a balanced surface fleet with carrier based aircraft available for the first time to support amphibious operations and a host of high speed missile firing fast attack craft for use in littoral or inland waters; and a submarine force employing exceptionally quiet diesel units and units capable of firing missiles submerged at ranges up to 30 miles, and surfaced at ranges up to 250 miles.

Clearly this three dimensional threat which has evolved so rapidly over the past ten years places maximum strain upon our capability in ocean surveillance.

In general, surveillance functions for naval forces, with or without air support are: (1) area surveillance for early warning; (2) over-the-horizon detection, classification and targeting for launch of offensive weapons; and (3) threat detection. Each of these functions levies distinct requirements for upgrading the current surveillance system, but all requirements can be grouped under three general headings. The first is improved sensors. These would be active and passive, and organic or remote. The second general heading is location or identification technique, and the third is data transfer analysis or dissemination or that aspect of command, control and communications.

Having set out the surveillance functions and requirement, let us consider problem areas related to some of the more critical elements of the threat spectrum.

Broad area surveillance for early warning is a major deficiency in submarine detection. Various techniques have been explored, however, these technologies all seem to be useful in very limited situations. The rapid increase in numbers and types of Soviet ships requires that we now not only detect and localize targets but also identify them. In the initial stages of combat, particularly when neutrality must be observed, IFFN (identification – friend, foe or neutral) would be an important aspect of the NATO targeting problem. We do not currently have the capability of making such discrimination in the Baltic or Mediterranean Sea which is cluttered with various merchant ships of many different nations as well as Soviet commercial units which can be easily disguised as naval units. It is important that the Soviet targeting and strike aircraft be identified at long range. The requirement here is that the Bear-Delta aircraft should be at a range in excess of radar line-of-sight to Soviet undersea or fleet units – some 300 miles or more. Therefore these aircraft should be detected and identified at ranges in excess of this. The Backfire and Badger bombers should also be detectable and identifiable in excess of their anti-ship missiles. The targeting problem is a serious one for NATO forces and

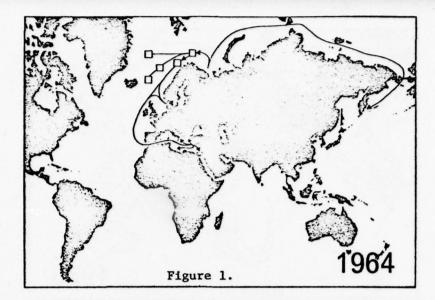
it relates to our surveillance capability as well. There does not, at present, exist the over-the-horizon detection classification and targeting for launch of offensive weapons that would enable us to utilize missiles of very long range, such as the submarine-launched cruise missile or air launched cruise missile (Tomahawk). It will be necessary to develop a much more sophisticated and useful over-the-horizon surveillance targeting capability than we currently possess. It is my feeling that until a two-dimensional sensor capability, which utilizes the dimensional characteristics of the ships involved, is developed that our sensors will always be countermeasure-vulnerable.

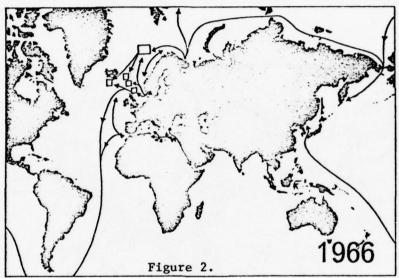
In undersea surveillance we still do not have an adequate solution to the shallow water problem. Perhaps coherent active expendable acoustic sources can be developed, but this development will require considerable ingenuity.

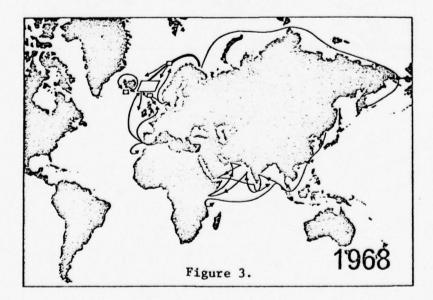
The use of over-the-horizon radar should be explored further. High intensity radar also presents possibilities, particularly with low radar cross-section targets. More sophisticated passive sensors would be helpful, such as the pyroelectric vidicon and the microwave radiometer which will be discussed in the following lectures. The techniques for locating and identifying targets are also in fairly good shape but data transfer, analysis and dissemination still fall short.

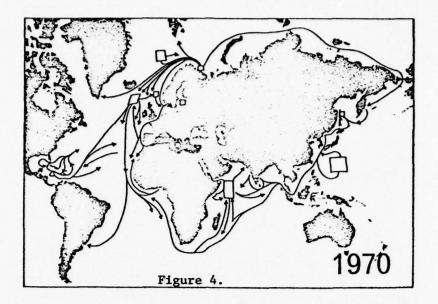
Because of the various platforms, and the various countries involved, the communication problems of NATO are more acute than those of any single country. There is also serious fractionation in the approach to surveillance; various platform sponsors have had individual approaches, and the general surveillance community has operated in isolation from the weapons control, target acquisition and tracking community.

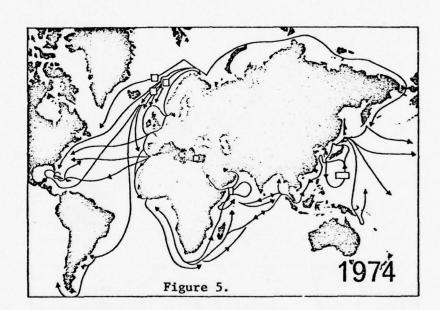
In conclusion, based on these new requirements, only a very well coordinated approach can meet the overall Navy NATO requirements for ocean surveillance. No single platform or sensor system can do the job. It remains therefore, for us to emphasize those problem areas which I have stated previously and which will be discussed in the following lectures, always keeping in mind the requirement of data transfer, analysis and dissemination which gets the information obtained by sensors into the hands of those who can use it to counter the threat.











REFRESHER

Ehrhard Raschke, Köln Fed. Rep. of Germany

1 Summary

In this lecture are briefly outlined basic facts of radiative transfer theory and of physical and radiative transfer properties of the atmosphere and oceans. In the oral presentation this text will be accompanied by a large variety of figures.

2 Introduction

Remote measurements of atmospheric and surface state parameters became an important tool in the past years for a variety of purposes. They are in principle based on measurements of radiation reflected or emitted from the target of interest to the observer.

There are now many active and passive methods known. In active methods an artificial radiation source - radars, lidars or even searchlights - is used to illuminate an area of interest and measure the characteristics of radiation reflected and scattered back to the receiver. Passive methods make use of the sun's radiation emitted from the targets. There have been studied during recent years a large variety of such observing methods and instruments developed for use on ground, in aircraft or even in satellites. The spectral region of interest ranges from the ultraviolet (0.2 - 0.3 μm) to the microwave (10 μm) portions of the spectrum. A thorough study of such measurements requires some knowledge on the basic interactions between radiation fields and the materials of interest. This also includes some contaminating effects, such as scattering and emission of radiation by air and clouds between the target and the receiver.

It seems therefore quite helpful for the forthcoming discussions to review briefly these interactions and state parameters of the materials involved: the atmosphere and the oceans.

3 Radiative transfer theory

3.1 Interactions of radiation with matter

Electromagnetic waves travelling through gases or any other materials exhibit usually changes in their phases, amplitudes and directions due to <u>absorption</u> and reflection (scattering) processes. Absorption reduces only the amplitudes and may be responsible to convert the electromagnetic wave energy into heat. <u>Reflection</u> or scattering - processes as well as <u>refraction</u> may occur at discontinuities where the dielectric properties of the material changes. One may express these properties by the complex refractive index

$$n = n_r - in_i \tag{1}$$

where $n_{\bf r}$, the real part, is responsible for changes of the phase velocity and $n_{\bf i}$, the imaginary part, is responsible for absorption. All other parameters describing the radiative transfer properties of materials might be referred back to this quantity. For instance the volume absorption coefficient $\sigma_a(m^{-1})$ is related to $n_{\bf i}$ by

$$\sigma_{a} = 2\pi n_{i}/\lambda \tag{2}$$

where λ is the wavelength. The refractive index of many gases and materials - also of water shows generally an increase with decreasing wavelength (normal dispersion). But inside of absorption lines and bands also "anomalous dispersion" occurs. From this result strong spectral variations of absorption and reflection properties of various materials.

Emission and absorption of radiation by gases are connected with changes in electronic, vibrational and rotational energy levels. They may also occur in combined versions and cause a rather complex spectra consisting of single lines, line groups or bands.

3.1.1 Basic laws

The spectral radiance $L(\lambda)$ of a beam incident into a scattering and absorbing volume of air or water is reduced by the amount of $dL(\lambda)$ after its passage, which is related to the extinction properties and length of this volume by the law of Bouguer:

$$dL(\lambda) = -\sigma_{R}(\lambda) \cdot L(\lambda) \cdot ds$$
 (3)

where λ = wavelength, ds = geometric path length, $\sigma_e(\lambda)$ = spectral volume extinction coefficient (in m⁻¹). If ds is very small, perhaps of the order of one wavelength, one can assume, that the absorption and scattering processes along ds occur independently, thus

$$\sigma_{e}(\lambda) = \sigma_{s}(\lambda) + \sigma_{a}(\lambda) \tag{4}$$

where $\sigma_{\rm S}(\lambda)$ = spectral scattering coefficient, and $\sigma_{\rm a}(\lambda)$ = spectral absorption coefficient ($\sigma_{\rm a}$ = 2N $n_{\rm i}/\lambda$, Eq.(2)). The optical depth of a medium is τ = $\sigma_{\rm e}$. ds.

Functional relations on the absorption coefficients for the various atmospheric gases, such as water vapour, carbon dioxide, oxygen, ozone, methan and other minor constituents can now be obtained from standard table-works with a sufficient degree of accuracy and various degrees of complexity; also for liquid water.

The scattering and absorption coefficients for particles etc. can be calculated with the elegant theoretical framework developed originally by G. MIE (1908) for single scattering events of electromagnetic waves at spheres. Into formulae describing this process the following quantities may enter: wavelength, and the index of refraction and the size distribution and concentration of particles. Solutions have been elavorated now in a straight-forward manner and may be obtained even with library programs of major computer companies. Since the scattering occurs into all possible direction, $\sigma_{\rm S}$ is the integral over the phase function or scattering indicatrix, describing this directional dependence.

$$\sigma_{S}(\lambda) = \frac{1}{4\pi} \int p(\omega) d\omega$$
 (5)

where dw = angular element and $p(\omega)$ is the above mentioned phase function, which may be interpreted as a probability function. Only if particles are extremely small, if compared with wavelength, the phase function is nearly isotropical (Rayleigh-Scattering), and $\sigma_{\rm S}$ is proportional to λ^{-4} . In most other cases the forward scattering may be several orders of magnitudes larger than the side- and backward scattering and $\sigma_{\rm S}(\lambda)$ may vary very complex with wavelength. The single scattering theory may also be applied to water probes. It describes also all known polarization phenomena. The multiple scattering phenomena, occuring in reality, require for their explanation the application of the more complex radiative transfer theory.

3.2 The general equation for radiative transfer

3.2.1 The differential equation

To describe theoretically the radiation fields occuring in the atmosphere and upper ocean layers, one may make use of well-known Monte-Carlo schemes, which in principle enable a rather complete modelling of three-dimensional inhomogeneities. But they require prohibitive long computational times.

Therefore most studies are done with the "classical" differential equation for radiative transfer, in a horizontally uniform and parallel medium, with inhomogeneities only in the vertical direction. This approximation serves quite sufficiently for most applications in atmosphere-ocean systems.

In a scattering, absorbing and emitting volume of the optical thickness $\mathrm{d}\tau(=\sigma_{\mathrm{e}}(z)\mathrm{d}z)$, where z is the vertical coordinate counted from the top of the atmosphere vertically downward, the radiative transfer equation (RTE) describes the radiation budget of a volume element:

$$\mu \frac{dL(\tau, \mu, \phi)}{d\tau} = -L(\tau, \mu, \phi) + J_{\mathbf{g}}(\tau, \mu, \lambda) + J_{\mathbf{e}}(\tau, \mu, \phi)$$
 (6)

Here are μ (= cos), ϕ the directional coordinates with respect to the geometry of the planparallel medium

(ϕ = azimuth angle, = zenith angle) and a light source, e.g. the sun. L is the radiance of a beam passing a slab of the optical thickness d τ , J_s is the radiance scattered inside that slab into the directions μ , ϕ , due to direct solar radiation and / or also to radiation incident from all directions.

 J_e is the radiance emitted into the direction μ , ϕ .

This equation is valid for each narrow spectral interval $d\lambda$ centered at λ . The spectral index λ has been omitted here—for convenience.

3.2.2 Special cases:

In the earth-atmosphere system one may consider the contribution of $J_{\rm e}$ to the total budget, expressed in Eq.(6), to be negligible against the solar radiation in the wavelength region λ < 3.5 µm, since the amplitude of Flanck's function for terrestrial temperatures (T < 320K) is then small compared with incident solar radiation. Contrarily, for λ < 3.5 µm the contribution of solar radiation can be neglected. For a cloudfree atmosphere the fields of thermal radiation can be calculated with high accuracy neglecting all scattering events.

3.2.3 Formal solutions and boundary conditions

The differential equation (2) can be solved formally for downward and upward radiances:

upward
$$L^{+}(\tau,\mu,\phi) = L_{0}^{+}(\tau,\mu,\phi) \cdot e^{\frac{-(\tau_{0}-\tau)}{\mu}} + \int_{0}^{\tau_{0}-\tau} \frac{t-\tau}{\mu} (J_{s}(t,\mu,\phi)+J_{e}(t,\mu,\phi))dt$$
 (7)

downward
$$L^{-}(\tau,\mu,\phi)=L^{-}(\tau,\mu\phi)\cdot e^{-\tau/\mu}+\int_{0}^{\tau_{\theta}}e^{-t/\mu}(J_{s}(t,\mu,\phi)+J_{e}(t,\mu,\phi))dt$$
 (8)

where τ_0 = optical thickness of the entire medium (e.g. the atmosphere) and L_0^+ and L_0^- are radiances at lower and upper boundaries, to be determined by boundary conditions. The second term in each equation contains also multiply scattered light.

Boundary conditions are parallel solar beams incident at the top of the atmosphere, and the reflection and emission properties of the ground. Over oceans, solar light of the spectral range between 0.4 and 0.65 μm can penetrate into layers deeper than 50 meters. There, one has to consider the transmission of ocean surface for light incident from both sides. The transmission and reflection functions can be highly anisotropically, containing a strong specular component.

If, instead only of the unpolarized radiance, the polarisation due to scattering and reflection is taken into account, in the above mentioned equations the radiances and phase functions (included in J) must be replaced by a vector and matrix, respectively. The four-dimensional vector notation, postulated by Stokes for the description of the state of polarisation of light has been found adequate for this purpose.

A large variety of computational methods has been developed to solve these formal solutions. If the radiation fields are be considered in each angular detail they require long computation times, but yield to results comparable with observations. A variety of flux approximation neglecting any angular details is in use for computations for up- and downward fluxes only.

Such an approximation yields also sufficiently good results for interpretations of measurements of underlight penetrated from subsurface water layers back into the atmosphere. It has been proposed for planckton measurements from multi-spectral satellite-borne imagery.

4 Radiative transfer parameters of the atmosphere and ocean

4.1 Some basic quantities

Radiative transfer parameters describe those properties of the atmosphere, ocean and their interface, which affect the transfer of electromagnetic wave. Via the definitions mentioned above these properties enter the optical thickness τ_0 or boundary conditions of the RTE. Some definitions are summarized below:

volume absorption coefficient:
$$\sigma_a = \rho k_a$$
, (m^{-1})

$$\rho = \text{density of an absorbing medium } (gm^{-3})$$

$$k_a = \text{mass absorption coefficient } (m^2 g^{-1})$$

volume scattering coefficient: $\sigma_s = \rho k_s (m^{-1})$

 k_{s} = mass scattering coefficient

black body radiance: $B(\lambda,T) = c_1\lambda^{-5} (\exp(c_2/\lambda \cdot T) - 1)^{-1}$

T = absolute temperature (K)

λ = wavelength

c₁,c₂ = universal constants

reflectance: $\rho = \frac{M_r}{M_r} \quad (0 < \rho \le 1)$

 $M_{r,i}$ =reflected and incident flux density,

emissivity: $\varepsilon = \frac{M}{M} \frac{\varepsilon}{\varepsilon - 1} \quad (0 < \varepsilon \le 1)$

 $M_{\varepsilon=1}$ = emmitted flux density of a black body.

 k_a and k_s are material characteristics and depend on the optical properties, as for instance described by the refractive index m (Eq.(1)), only, while ρ is a measure for the concentration of each participant.

4.2 Atmosphere

4.2.1 Radiative transfer constituents of the atmosphere

In the atmosphere participate various gases, the aerosols and all cloud particles actively in the transfer of radiation. These gases are 0_2 , 0_3 , 0_2 , 0_2 , 0_3 , 0_2 and minor constituents. 0_2 and 0_2 occur in the atmosphere up to 10 km altitude with constant mixing ratio of 79 and 0.03 per cent per volume, respectively, while 0_2 0 and 0_3 2 show strong geographical variations. These gases dominate the transfer by absorption and emission of radiation. Their major absorption band regions are created in the spectral region between 0.2 and 0.20 and 0.20 and 0.21 and 0.22 and 0.23 and 0.24 and 0.25 and 0.2

All air molecules participate in the scattering of light may be described with Rayleigh's approximation. It dominates the transfer at ultraviolett wavelengths and is almost completely negligibly at wavelengths larger than 2 mm.

Aerosols, whose particle size distribution may be approximated by a power law (e.g. the JUNGE-distribution) and may range from radii of less than 0.01 mm to 10 mm, consist of ground materials, sea salt, ions and also volcanic ashes. Their index of refraction ranges in its real part between values of 1.3 to 1.5 and in its imaginary part from 0 to 0.2, depending on the water vapour content and the wave length of interest.

Vertical and horizontal distributions of aerosol concentrations vary considerably over various climatic regions and during the seasons due to the vertical missing activity within the atmosphere. Vertical profiles may range from several thousand particles per cm³ near ground to only 1 - 10 particles per cm³ in upper tropospheric and stratospheric layers, with usually a sharp decrease of the aerosol concentration in layers above the planetary boundary layer (1-2 km altitude). SHETTLE and FENN

(1975) compiled an extensive table work on mean vertical aerosol profiles and also their scattering and absorption coefficients for the entire spectrum between the visible and for infrared (in the microwave region aerosols can be neglected) for easy use in computational models.

In water clouds the particle size distribution is usually bimodal, with one maximum near 0.1 µm due to "nonactivated" aerosols and another at much larger radii (20 µm) due to water droplets. These particle size distributions vary considerably within one single cloud and nevertheless between individual clouds. Further the liquid water content may range from values of 0.05 gm⁻³ for thin status to more than 0.4 gm⁻³ for nimbo-stratus. With various assumptions ranging from pure water spheres to water shells around particles the scattering and absorption properties of a volume of cloud air can be calculated with single scattering theory according G. MIE (1908). The values obtained are as uncertain (by 10 - 20%) as the input parameters on microphysical cloud properties are. Their direct measurements with particle-counters and other equipment are very difficult and can be done only sporatically. There is not yet a method available to derive these parameters from cloud fields observable on satellite photographs or any other imagery, other than dedication of some mean tabular values to an identified cloud species.

4.2.2 A brief survey of the general circulation patterns

A brief survey of the general circulation patterns in the troposphere and stratosphere may help to understand the vertical and horizontal distributions of the atmosphere's radiative transfer properties.

In the troposphere, the lowest partion of the atmosphere, the temperature decreases with a mean lapse rate of - 6.5° C/km. It extends from ground to nearly 7 (polar region), 10 (mean latitudes), 15 km (tropics) altitude. In the stratosphere above, which is usually coldest in the tropics, the temperature increases to about 0° C at 50 km, the stratopause.

In the lowest part of the troposphere up to 1 - 2 km altitude, in the planetary boundary layer (PBL), the frictional, convectional and radiative enforced heating may alter considerably this general temperature structure. Near the ground, but also at the top of the PBL temperature inversions may occur which affect considerably the microwave transfer along quasi-horizontal paths.

To the general wind systems are strongly related locations of the major cloud systems. Low level trade winds in the subtropics cause convergence and thus convective cloud formations near the equator, and divergence over the subtropical high pressure cells connected with cloud dissipations. In the middle latitudes, where the temperature contrast between cold polar air and warmer subtropical air is greatest, westerly winds dominate throughout the entire troposphere transporting strong disturbances eastward which contain the major cloud fields and cause precipitation. These westerly winds are very strongand nearly zonal over the southern hemisphere, where interferring continents are missing. Over the polar region strong subsidence occurs due to radiatively inforced sinking with some easterly outflow. During summer time the mean latitude disturbances extend into the polar region transporting into them water vapor which causes the formation of strong stratus.

Within the stratosphere the wind regime over the poles changes semiannually in direction with strong easterlies in summer and westerlies in winter. In the tropical stratosphere there is a strong quasi-biannual variation of the wind direc-

tion. The annual wave of extratropical stratosphere circulation patterns is radiatively enforced. Imbedded in it are wavelike structures of steady and transient nature and turbulent elements.

All atmospheric layers between 50 and about 85 km altitude belong to the mesosphere, where the stratospheric circulation patterns prevails. But the temperature decreases gradually from stratopause values of about -10° C to values between -80° C and -150° C at the mesopause.

Within the troposphere and stratosphere, where besides of $\rm H_2O$ and $\rm O_3$ all gases are well mixed, local thermodynamical equilibrium prevails for almost all spectral regions. This allows remote soundings of the temperature fields and of various gas species in the atmosphere.

4.3 The oceans

4.3.1 Radiative characteristics of water

Liquid water like in its gaseous phase has typical bands in the infrared and also ultraviolet portion of the spectrum. Only in the blue-green region of the visible (0.48 - 0.60 μ m), solar radiation can penetrate into deeper layers of oceans and lakes depending on their content of other contanimating materials. In clear waters the penetration depth may reach several tenth of meters. All the radiation of longer wavelengths than 0.65 μ m heats the upper most water layers. Water is also transparent for radiation in the centimeter region.

The density fluctuations in water, which are equivalent to fluctuations of the refractive index particulate matter suspended in it and also air bubbles scatter the incident radiation like in a turbid atmosphere dominantly into the forward direction. Thus the upwelling underlight underneath the water surface may reach only values of less than 10% of the incident radiation. In the most transparent part of the spectrum at about 0.47 µm the light which can be observed at depth of 10 m and more has been scattered several times in water layers above.

The real part of the index of refraction of water ranges from values of around 1.3 in the visible and infrared to **9** in the microwave region; while that for air is very close to 1.0004 throughout the whole spectrum. Therefore parts of the radiation incident from both sides onto the air-water interface are reflected back. For a flat water surface this can be described according to Fresnel's laws, where also the strong polarisation can be computed.

Ocean waves of the wavelength from a few millimeters to meters and longer, foam and perhaps also particles cause a strong scattering. Reflection and transmission functions can be calculated with a sufficient degree of accuracy for a Gaussian distribution of wave slopes. Otherwise spatial coherence spectra of reflected beams can be used to infer the wavepatterns.

4.3.2 Physical ocean properties

About seven tenths of the earth's surface are covered with open oceans, which exchange intensively energy and momentum with the atmospheric layers above. Oceans are, therefore, considered to be an essential part of the total system forming the climate, climatic regions etc. on earth. Their physical properties are closely linked to them, i.e. ghe general atmospheric circulation.

Ocean water generally contains between 30% and 40% of salt, which consists of a mixture of NaCL, MgCl and several other chlorides. The surface temperature patterns

is closely linked to climate zones and water currents, the latter are primarily driven by surface winds.

The salt content (salinity), the pressure and the temperature determine the water density, which varies only by small fractions. But these small fractions are dominant responsible for the development of turbulent exchange processes of various scales in space and time.

The typical vertical temperature profile at middle latitudes shows the following general structure: Due to permanent mixing the upper layers of several tens of meters are nearly isothermal with a strong annual variation. Below that layer the temperature then may sharp decrease to values around +1 to $\pm 4^{\circ}$ C, where water has its largest density.

For continuous surveillance of interest are the contents of organic materials (planckton etc.) and anorganic contamination in the subsurface layers, oilslicks and the wavepatterns at the water surface. Several satellite techniques have been found useful for these purposes.

5 Some closing remarks

It has been tried in this paper to describe briefly our present knowledge of the physical properties of the earth's atmosphere and oceans and their interactions with electromagnetic waves used for surveillance and remote sensing purposes. This lecture had the special purpose to recall many facts which are already familiar to the audience. In the forthcoming papers the various special problems involved with the surveillance will be stressed in much closer detail.

6 Some literature

Bean, B.R., Dutton, E.J.: Radio Meteorology, Dover, New York, 1966

Dietrich, G. et al.: Allgemeine Meereskunde, 3. Aufl., Gebr. Borntraeger, Berlin, 1975

Irvine, W.M., Pollack, J.B.: Infrared optical properties of water and ice spheres, Icarus, 8, 324-360, 1968

Lorenz, E. N.: The Nature and Theory of the General Circulation of the Atmosphere, WMO-No. 218.TP.115, 1967

Mie, G.: Beiträge zur Optik trüber Medien, Ann. d. Physik, 8, 377.745, 1908

Neumann, G., Pierson: Principles of Physical Oceanography, Prentice-Hall, Inc., 545 pp, 1966

Newell, R.E. et al.: The General Circulation of the Tropical Atmosphere and Interactions with Extratropical Latitudes, The MIT Press Cambridge, Mass.and London 1974

Preisendorfer, R. W.: Hydrologic Optics, Vol. I-VI, Honolulu, Hawaii, 1976

Shettle, E.P., Fenn, W.: Models of the atmospheric aerosols and their optical properties, AGARD conference Pre-Print No. 183 on Optical Propagation in the Atmosphere, 2-1-2-9, 1975

Thompson, W.I., ed.: Atmospheric Transmission Handbook, Transport Systems Center, Cambridge, Mass., 1971, Report No. DOT-TSC-NASA-71-6

Valley, S. L., ed.: Handbook of Geophysics and Space Environments, McGraw-Hill, New York, 1965 Vande Hulst, H.C.: Light Scattering by small Particles, Wiley, New York, 1957
Wolfe, W.L., ed.: Handbook of Infrared Military Technology, Office Naval Res.
Wash. D.C., 1965

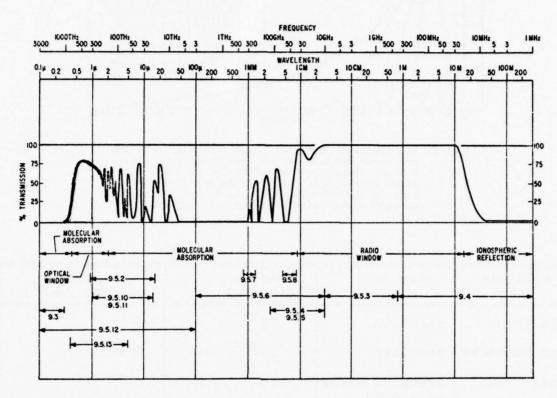


Fig. 1: The electromagnetic wavespectrum for remote sensing of ocean properties ranges from 0.2 μm to several meters. However the absorption by several atmospheric gases (0, 0, H₂0, CO₂) allows such observations only in narrow spect5al ranges (from Thompson).

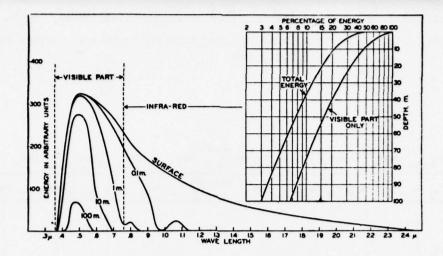


Fig. 2: The spectrum of direct solar radiation reaching the ocean surface ranges from 0.35 μm to about 2.5 μm . The selective absorption by water molecules allows only radiation in the blue-green part of the spectrum (0.5 μm) to penetrate to greater depths (from Neumann and Pierson).

Particle	Nature	Radius (microns)	Number -3)
electron	electron	10 ⁻⁹	
air molecule	molecule	10-4	2.7x10 ¹⁹
small 'ion'	group of water molecules	10 ⁻³	
combustion product	hygroscopic	10 ⁻² to 10 ⁻¹	104
sea-salt mucleus	hygroscopic and soluble	0.1 to 0.3	50 to 400
dust	generally in- soluble	0.1 to 10	highly variable
haze	water droplet	0.3 to 3	50 to 400
fog	water droplet	1 to 30	1 to 100
cloud	water droplet	1 to 30	50 to 500
rain	water droplet	3 to 3,000	highly variable
hail	ice particle	highly variable	•
snow	ice particle	•	,

Fig. 3: Particles and molecules in the atmosphere affecting the transfer of electromagnetic waves (from Thompson).

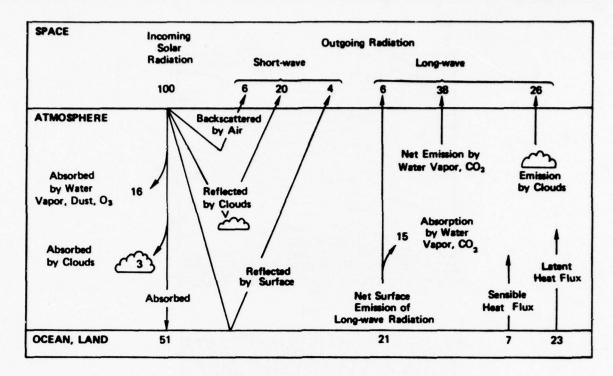


Fig. 4: The mean radiation budget of the land-ocean-ice-land-atmosphere system. All numbers are fractions in percent of the incident solar radiative energy, the only heat source of the system. Arrows in the lower right corner indicate heat transports from the earth into the atmosphere due to turbulent fluxes of sensible and latent heat (from National Acad. of Science, 1975; "Understanding Climate Change").

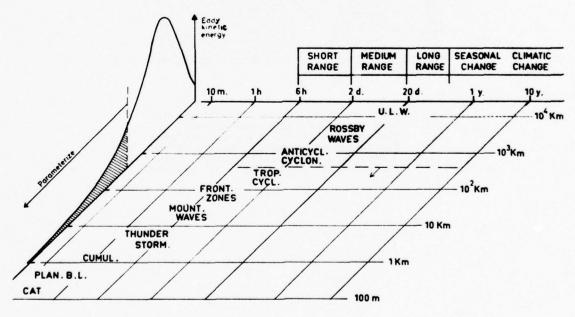


Fig. 5: Mean horizontal extensions and lifetimes of motions in the atmosphere and the spectrum of their eddy kinetic energy. The upper scale indicates the range of their predictability (from GARP Publication Series, No. 11, 1973; WMO-Genève).

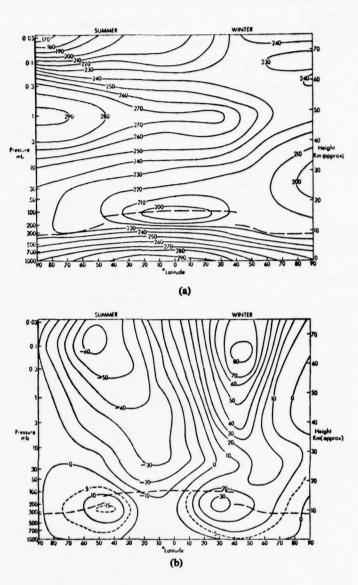


Fig. 6: Zonal averages of the temperature and wind speed (negative: easterlies) vs. pressure (altitude) and latitudes over the summer and winterhemisphere (after Murgatroyd, 1969, in "The Global Circulation of the Atmosphere", ed. by Corby)

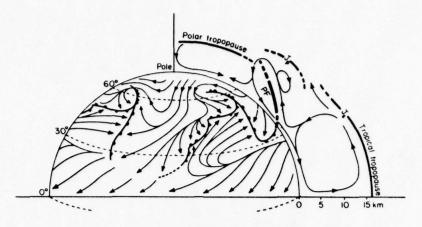


Fig. 7: Sketch of the surface winds and mean vertical circulations over one hemisphere (from Palmèn and Newton, 1969).

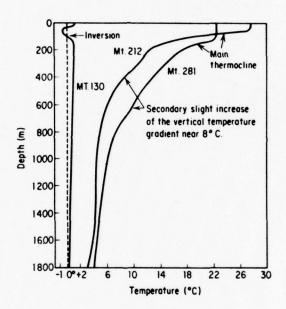


Fig. 8: Characteristic temperature profiles in the polar (left) and tropical (right) oceans (from Neumann and Pierson, 1966).

MICROWAVE SCANNING RADIOMETRY

James P. Hollinger
Advanced Space Sensing Applications Branch
Space Science Division
U. S. Naval Research Laboratory
Washington, D. C. 20375 USA

SUMMARY

Microwave scanning radiometry has the advantages for surveillance over active microwave devices of being completely passive and thus emitting no radiations, using little power and being covert and difficult to jam and, as compared to passive sensors at infrared, optical and ultraviolet wavelengths, of allowing all-weather, day or night operation and the detection of non-radiating metal objects. The basic principles of microwave radiometry including a description of antenna properties, a definition of antenna temperature, brightness temperature, and system temperature and a discussion of measurement techniques and accuracies are briefly presented. Then the microwave signals to be expected from calm and rough seas, sea ice, ships and ship wakes, oil slicks, and terrain as well as the attenuation and radiation from the atmosphere are described. Detailed descriptions and the specifications and performance of existing aircraft-borne scanners including the National Aeronautics and Space Administration PMIS, the U. S. Coast Guard AOSS-PMI, the Naval Weapons Center MICRAD, and the Naval Research Laboratory MWIS, and the satellite systems of ESMR on NIMBUS 5 and 6, SCAMS on NIMBUS 6 and the SMMR being developed for NIMBUS G and SEASAT are given. Selected measurements from these imaging systems are presented to demonstrate their application to the delineation of the ice-ocean edge, the determination of ice type, age, and thickness, snow cover, the location and distribution of fronts, convective zones, storms and areas of precipitation, the detection and quantification of marine oil spills, and microwave images of ships, ship wakes, beaches, field and vegetation boundaries, roads, railroads and commercial, industrial and residential areas.

INTRODUCTION

Microwave scanning radiometry has proven to be of great value for the remote sensing of the environment and for the remote surveillance of man-made objects against the environmental background. It has the advantage of being completely passive and emitting no signals; thus being covert, difficult to jam and using relatively little power compared to active microwave devices. Further it offers several potential advantages for remote surveillance over passive sensors operating at infrared, optical, and ultraviolet wavelengths. Perhaps most important, it allows all-weather, day and night operation. It provides the capability to detect and track objects moving on or near the surface below a cloud cover. Further, it is possible to detect metal objects which appear cold, since they emit no microwave radiation and reflect principally the low radiation from space and the atmosphere, against the relatively hot earth background. This makes it possible to detect and track a missile even after burn out resulting in more accurate and current trajectory determination.

The major disadvantage, by far, of a microwave imager is that, to obtain the necessary resolution and signal-to-noise, relatively large aperture, high-gain antennas with narrow beams are required. The higher the altitude and the larger the areas to be searched in short periods of time, the more severe the difficulty. Satellite-borne systems would require nearly impossibly large multiple-beam antennas. In order to detect objects the size of aircraft or ships from satellite altitudes, structures with dimensions of at least 10 or 10 wavelengths and a precision of 10 wavelengths would be needed. However applications over tactical distances of tens of kilometers are feasible with current instrumentation.

Microwave radiometry offers a broad range of applications and a wealth of information due to the wide variation of the emission, absorption and reflection properties of matter with the observational frequency, polarization, and viewing angle. Passive microwave scanners aboard aircraft and satellites have been used to detect ships, aircraft, trucks, buildings, roads, railroads and commercial, industrial, and residential areas. They have been used to delineate the ice-ocean edge; to locate icebergs, polynyas and leads; to identify and map ice type, age, thickness and coverage; to infer the thickness and water content of clouds; to map the location and distribution of weather fronts, covective zones, storms and areas of precipitation; to detect and quantify marine oil spills; to provide information on soil moisture and locate field and vegetation boundaries. In addition maps of agricultural, geological and geographical features have been obtained at night through a snow cover and forest fires have been defined through a heavy smoke cover.

The basic principles of microwave radiometry including a description of antenna properties, a definition of antenna temperature, brightness temperature, and system temperature and a discussion of measurement techniques and accuracies are briefly presented. Then the microwave signals to be expected from calm and rough seas, sea ice, ships and ship wakes, oil slicks, and terrain as well as the attenuation and radiation from the atmosphere are described. Detailed descriptions and the specifications and performance of existing aircraft-borne scanners including the National Aeronautics and Space Administration Passive Microwave Imaging System (PMIS), The U. S. Coast Guard

Airborne Oil Surveillance System Passive Microwave Imager (AOSS-PMI), the Naval Weapons Center Microwave Radiometric System (MICRAD), and the Naval Research Laboratory Millimeter Wave Imaging System (MWIS), and the satellite systems of Electrically Scanning Microwave Radiometer (ESMR) on NIMBUS 5 and 6, Scanning Microwave Spectrometer (SCAMS) on NIMBUS 6 and the Scanning Multichannel Microwave Radiometer (SMMR) being developed for NIMBUS G and SEASAT are given. Selected measurements from these imaging systems are presented to demonstrate their application to the delineation of the ice-ocean edge, the determination of ice type, age, and thickness, snow cover, the location and distribution of fronts, convective zones, storms and areas of precipitation, the detection and quantification of marine oil spills, and microwave images of ships, ship wakes, beaches, field and vegetation boundaries, roads, railroads and commercial, industrial and residential

MICROWAVE RADIOMETRY

The power P received, per unit frequency interval, from a source whose polarized radiation intensity is specified by the Stokes parameters [I $_{a}(\theta,\phi)$, Q $_{a}(\theta,\phi)$, U $_{a}(\theta,\phi)$, V $_{a}(\theta,\phi)$], by an antenna with polarized reception properties described by the Stokes parameters [I $_{a}(\theta,\phi)$, Q $_{a}(\theta,\phi)$, U $_{a}(\theta,\phi)$, V $_{a}(\theta,\phi)$] is given by

$$P = (A_e/2) \int_{4\pi} [I_s I_a + Q_s Q_a + U_s U_a + V_s V_a] d\Omega , \qquad (1)$$

where the antenna Stokes parameters have been normalized such that $I_a(0,0)=1$ and A_e is the effective area of the antenna [1]. The effective area may be found from the normalized antenna response pattern and a measurement of the radiation efficiency η of the antenna or a measurement of the maximum gain of the antenna G_o where

$$A_{e} = \eta \lambda^{2} / \int_{4\pi} I_{a} d\Omega = \eta \lambda^{2} / \Omega_{a} = \lambda^{2} G_{o} / 4\pi$$
 (2)

 λ is the observational wavelength and Ω_a is the effective solid angle of the antenna. Measurement of η is generally very difficult in practice and, since it is usually very close to unity, it is often taken to be one.

The power received by the antenna is conveniently specified in terms of a ficticious antenna temperature \mathbf{T}_a by the use of Nyquist's theorem [2]. This is the temperature to which an impedance, equal to the impedance of the antenna, would have to be raised in order that when it is substituted for the antenna it delivers the same power to the input of the receiver, as does the antenna. The antenna temperature is related to the power received per unit frequency interval by

$$T_{\lambda} = P/k \qquad . \tag{3}$$

The utility of doing this comes about because the radiation intensity of the source may be specified in terms of its effective blackbody temperature. All objects at temperatures above absolute zero radiate electromagnetic waves; the amount they emit, absorb, and reflect depends upon the properties of the material and the character of the surface. A perfect absorber which absorbs all the energy falling on it, reflecting none, is also a perfect emitter with an emissivity of unity. Such a body is called a blackbody and emits according to Planck's Law. Perfect blackbodies do not exist, though some approach it very closely. In general, materials are "grey" bodies with emissivities less than one.

The intensity emitted by a grey body is given by

$$I_{GB} = \varepsilon I_{BB} = \varepsilon \left(\frac{2h\nu}{\lambda 2}\right) \left[e^{(h\nu/KT)} - 1\right]^{-1} , \qquad (4)$$

where ϵ is the emissivity and I $_{BB}$ is Planck's blackbody law. Define an effective blackbody or brightness temperature T_B for any arbitrary source as

$$T_{B} = \frac{\lambda^{2}}{2K} I_{BB} = \left(\frac{h\nu}{K}\right) \left[e^{(h\nu/KT)} - 1\right]^{-1} \qquad (5)$$

In the case of purely thermal sources, such as grey and blackbody sources, T is the physical temperature of the body. However this definition can also be applied to any nonthermal source, such as man-made radiations from radio, radar or ignition noise or to gas discharges or plasmas which are not in thermal equilibrium. In the case of a nonthermal source, T is a ficticious temperature chosen such that a blackbody at this temperature would radiate, in the frequency interval $\Delta \nu$, the same intensity as does the nonthermal source. In this case, T is in general a function of frequency. Now when kT >> h ν , as is generally the case at microwave frequencies for earth environment observations, the Rayleigh-Jeans approximation to Planck's Law applies and $T_p = T$. Thus $T_{cb} = \epsilon T$ and the intensity of all thermal sources is directly proportional to their thermodynamic temperature; the proportionality constant being the emissivity of the source. Combining the above equations for a thermal source

$$T_{A} = \int_{A\pi} \varepsilon T I_{a} d\Omega/\Omega_{a} . \tag{6}$$

If the source is uniform over the entire antenna reception pattern, $T_A = \varepsilon T$. If the source is very small compared to the antenna beam, the antenna temperature is reduced by the ratio of the solid angle of the source to Ω_A . In general the antenna smooths and averages the source brightness distribution. An accurate knowledge of the antenna reception pattern allows a partial correction for antenna affects and restoration of the brightness distribution [3].

Since the source radiation is specified in terms of brightness temperature and the power received by the antenna in terms of antenna temperature, it is convenient to define the unwanted noise power generated by the receiver in terms of a system noise temperature by the use of Nyquists theorem as in equation (3). The RMS fluctuation ΔT_N of the output of the receiver is given by,

$$\Delta T_{N} = C \left[T_{R} + T_{a} \right] / \left[\tau \Delta \nu \right]^{1/2}$$

$$(7)$$

where C is a constant ranging from about 1 to 3 depending upon receiver design, T_{R} represents the unwanted noise generated by the receiver referred to the receiver input and τ is the time interval over which the signal is averaged. since most sources have a relatively flat spectrum, $\Delta\nu$, the passband of the receiver is generally made as large as possible; typically hundreds of megahertz. Even for a perfect receiver $(T_{R}=0)$ the numerator of equation (7) will be between 100 to 300 K for an earth viewing system depending upon frequency and whether the background is land or sea. Thus, improving receivers to have noise temperatures below a few hundred degrees pays diminishing returns. Values of about 10^{-1} to 10^{-2} K can be achieved for ΔT_{N} for a τ of one second depending upon frequency. The output noise, then, basically depends directly upon the square root of the number of resolution cells to be observed per second. This in turn is governed by the field of view, the resolution desired and the speed of the platform carrying the imager.

The radiometer is often calibrated by switching the input of the receiver from the antenna to one or more reference terminations whose temperatures are accurately known. A reference noise signal, with a spectrum similar to the signal spectrum, and which has been accurately calibrated in terms of power at the antenna terminals, can also be injected periodically for calibration. In addition the antenna or a reference antenna may be occulted by a highly absorbing material (a blackbody) or directed away from the earth to a position where the temperature is well known. In all of the calibration schemes, the signal from the antenna is determined by a comparison with an accurately known standard. With careful design, it is possible to measure the antenna temperature to an absolute accuracy of less than 1 K.

To obtain the source brightness distribution from the measured antenna temperature distribution, it is necessary to correct for the smoothing effects of the antenna, which acts as a spatial filter. For carefully designed antennas with high-beam efficiencies and low side lobe levels, it is possible to reconstruct the brightness distribution from the antenna temperature distribution to an absolute accuracy of 1 K or better. The reconstruction can only be performed for those spatial frequency components passed by the antenna. The high spatial frequency detail beyond the resolution of the antenna is irretrievably lost [3].

SOURCE RADIATIONS

The microwave radiation received from the earth's surface is composed of the radiation emitted by the surface, the radiation emitted by the atmosphere between the observer and the surface and the downwelling atmospheric and cosmic background radiation reflected or scattered from the surface to the observer. Further, the radiation emitted and reflected from the surface is attenuated by the atmosphere between the surface and the observer.

The emission, absorption, and scattering of the atmopshere is primarily dependent upon the gases, of molecular oxygen and water vapor and the hydrometeors of fog, clouds, rain, hail, and snow. The absorption and emission of water vapor at microwave frequencies is due to resonance lines at 22.235 and 183.3 GHz plus the far wings of higher frequency lines [4],[5],[6]. It is, of course, highly variable and most important at frequencies above 10 GHz. Absorption by oxygen results from a blend of lines between 50 and 70 GHz, of which 40 or so are significant and a single line at 118.8 GHz [7],[8],[9]. It is relatively constant and does not change much with time of year or latitude. The water droplets in fog and clouds are of the order of 0.1 mm or less in diameter so that for frequencies below about 100 GHz scattering is negligible and the extinction of radiation is due primarily to absorption [10]. Further the absorption is proportional to the total mass of water along the path of propagation and is independent of the drop size distribution. The loss in ice is very much less than in water and the absorption of hail, snow or ice clouds is generally negligible except for wet snow where the loss may be as large or larger than for rain. However scattering can be significant, especially for hail.

The zenith attenuation of the atmosphere (1 neper = 4.343 dB) is given in Figure 1 as a function of frequency for the atmospheric constituents of molecular oxygen, water

vapor and two types of clouds using a standard model atmosphere. The attenuation due to water vapor was calculated for 3 gm/cm of precipitable water. Although this is a typical value, it may range from twice as large, under hot humid conditions, to almost nothing for dry cold polar air. Therefore the attenuation due to water vapor varies from negligible to twice or more than that shown. Seventy five percent of clouds contain less liquid water than 0.015 gm/cm, labeled light cloud, and ninety five percent less than 0.45 gm/cm, labeled heavy cloud in Figure 1. Atmospheric windows occur below about 18 GHz and in the vicinity of 30, 90, 140, and 220 GHz.

The size distribution of rain drops depends upon the rain rate but the mean diameter is usually near one to a few millimeters. Therefore scattering is very important at microwave frequencies [10]. Calculations of the total extinction including both absorption and scattering losses for rain using an exponential rain drop size distribution and Mie scattering theory is shown in Figure 2 for different rain rates for several different microwave frequencies. The extinction due to rain is usually the predominant atmospheric effect and can be total especially at the higher frequencies.

The brightness temperature of the sea for both vertically and horizontally polarized radiation and for a diffusely scattering surface such as grass or vegetation as viewed from just above the surface at 37 GHz was calculated as a function of viewing angle, using the standard atmosphere and light clouds of Figure 1, and is shown in Figure 3. These calculations are for a calm, smooth sea. However the brightness temperature also depends upon the ocean surface roughness [11],[12],[13],[14]. The horizontal component is most sensitive; increasing with viewing angle to roughly 1 K per (M/sec) of wind speed at about 50 degrees incidence angle. The vertical component is nearly independent of surface roughness in the vicinity of 50 degrees and decreases with increasing wind speed at viewing angles greater than this. The roughness dependence arises from two effects. The first effect results from the increasing roughness of the compact water surface and the second effect from the increasing coverage of white caps and sea foam streaks with increasing wind speed. Both effects increase with wind speed and frequency and depend upon the incidence angle and polarization. The surface roughness effect is closely coupled to the local wind field; rapidly responding to changes in the local wind and hence is relatively insensitive to the energy content of low frequency gravity waves. Evidence indicates that it is primarily dependent upon the mean square surface slope and is thus due to surface waves of dimensions comparable to and shorter than the observational wavelength. The sea foam effect results from the increase in the effective microwave emissivity caused by the distortion of the surface by the foam bubble structure, and its increasing coverage with wind speed. The determination of the wind speed dependence is complicated by the fact that the foam coverage of the sea surface and the roughness effect depend, not only on the local wind, but also on the air-sea temperature difference, the duration and fetch of the wind, as well as on the history of the wave spectrum of the sea area being observed. Note also the large reflected sky component near the horizon for horizontally polarized radiation from the sea. The brightness temperature of the diffuse land surface is very nearly equal to the physical temperature of the surface and is nearly independent of viewing angle and polarization. This high emissivity is typical of grass, weeds, forests, and vegetation covered surfaces [15].

The microwave signal of the turbulent wake from a ship is similar to that from sea foam. The greater radiation from the wake is due to the disruption of the surface and the resulting somewhat tapered interface providing a less abrupt transition from the air to the high dielectric constant of the sea. This provides a better "match" between the sea and free space, increasing the radiation above that from the undisturbed sea.

Oil on the surface of the sea damps out the small scale wave structure and results in a reduction in the microwave signal. The magnitude of the reduction depends upon the marine wind speed and observational frequency, polarization, and viewing angle but usually is less than about 5 K. Thus the oil slick will appear as a slightly colder region unless the oil film has a thickness approaching a small fraction of the observational wavelength in the oil; a few tenths of a millimeter or so. In this case the oil film, with a dielectric constant between air and sea water, acts as a matching layer and increases the microwave radiation from the sea by an amount depending upon the thickness of the film and the observational wavelength. The thick regions then appear as bright spots on the slick area and it is possible to estimate the volume of oil present by the magnitude of the signal [16].

The microwave signal from snow fields, glaciers [17], and sea ice [18] is dependent upon multiple internal scattering. Snow depth, crystal sizes, degree of melting, ice roughness and age, which is related to the brine content of the ocean ice, all play a part in determining the brightness temperature. However it is generally much higher than the sea and icebergs and sea ice appear in strong contrast against the sea background and polynyas and leads in the ice are easily located. It is possible to interpret the microwave signals in terms of snow accumulation, ice age and type, and ice concentration which governs the heat loss through the ice pack and is of great importance in weather prediction.

The brightness temperature of the ocean at nadir as viewed from above the atmosphere was calculated as a function of frequency using the standard atmosphere and light clouds of Figure 1 and is shown in Figure 4. The contributions of the atmosphere and ocean are also shown separately. Ocean roughness effects will increase the brightness temperature roughly 1 K per m/sec of wind speed. Although the emissivity is different for various terrain and man-made features, it is usually close to unity compared to water and thus the brightness temperature of the land is generally more nearly equal to the physical

A metal object will emit no microwave radiation but will reflect the atmospheric radiation, or if it is above the atmosphere, the galactic and extragalactic radiation [1], incident upon it and will appear cool in contrast to the earth background. The incremental brightness temperature of a reflecting target above the atmosphere is, except at frequencies below a few GHz, where the effects of the ionosphere become significant, the difference between the cosmic background [19], 2.8 K, and the brightness temperature of the surface below. Thus the incremental temperature is between 100 and 300 K depending upon frequency and the background. The incremental brightness temperature for a reflecting target near the surface below the atmosphere over both land and ocean was calculated using the standard atmosphere and light clouds of Figure 1 and is shown in Figure 5. In this case the target signal decreases rapidly for frequencies above 100 GHz and is increasingly weather dependent for frequencies above about 18 GHz. However the higher frequencies would be very effective in the polar regions and would still provide some measure of weather penetration below polar latitudes.

Detailed measurements of the microwave emission from rocket exhaust plumes as a function of frequency, fuel type, thrust and altitude are not available. Transmission measurements through the plume at 0.4, 1.6, 2.2, 10 and 35 GHz and emission measurements at 0.4, 1.6 and 2.2 GHz of the plume for approximately 800 pound thrust rocket motors have been made by Balwanz and Lee [20],[21]. The absorption measurements show attenuation of greater than 30 to 40 dB at frequencies of 10 GHz and below but no appreciable signal loss at 35 GHz. The emission measurements indicate an equivalent blackbody temperature of 2000 K to 3000 K; comparable to the burn temperature in the plume. Earlier measurements by Balwanz indicated an equivalent blackbody temperature of 20,000 K at 10 GHz. The lower equivalent temperature of the recent measurements may be due to a more dense plume which becomes opaque, at the measurement frequencies, in cooler surface regions before inner, higher temperature gas, observed previously in a less dense plume, was reached. Electron densities of approximately 10 (cm 3) are inferred from the absorption measurements. This electron density probably persists to altitudes of 40 miles or more for although the ionized region grows from approximately the size of the rocket at sea level to perhaps thousands of feet in length at high altitudes the recombination rate decreases.

Although the burning plume is not necessarily in thermodynamic equilibrium and hence emission and absorption may not balance at each frequency, in the absence of anything better, we calculate the emission based on thermodynamic equilibrium. The brightness temperature of a uniform, ionized gas is given by

$$T_{B} = T_{e}(1 - e^{-\tau}),$$
 (8)

where T_{α} is the electron temperature and τ , the optical depth, is given by

$$\tau = \int \frac{9.8 \times 10^{-3} \text{N}^2}{\text{T}_2^{3/2} \text{V}^2} \left[19.8 + \ln \frac{\text{Te}^{3/2}}{\text{V}} \right] dx.$$
 (9)

Here N is the number of electrons per cm 3 , v.is the frequency in Hz, and x is in cm. The brightness temperature calculated for N = 10^12 and 10^13 cm $^{-1}$ by taking T = 2500 K and the thickness of the plume as 100 cm $_is$ shown as a function of frequency in Figure 6. An electron density of 3.7 x 10^{12} cm $^{-3}$ and the above conditions result in 40 dB or more attenuation at 10 GHz and lower frequencies and less than 3 dB attenuation at 35 GHz; consistent with the absorption measurements of Balwanz and Lee. It is also consistent with the equivalent blackbody temperature measured at the lower three frequencies.

MICROWAVE SCANNING SYSTEMS

The National Aeronautics and Space Administration (NASA) Passive Microwave Imaging System (PMIS) [22] operates at 10.69 GHz and is mounted in the bomb bay of the Lockheed Electra NP3A (NASA 927) aircraft behind a carefully designed low loss radome. The antenna is a dual-polarized, two-dimensional, phased array antenna 1.0 m by 1.1 m in size. The array is electronically stepped to provide a conical scan of the beam in the forward direction, at a constant angle of incidence on the surface of 49.5 degrees, to scan limits of 35 degrees in azimuth on either side of the along-track direction. Two orthogonal linear polarizations, lying in, and perpendicular to, the plane of incidence at the center scan beam position, but rotating with scan angle, are received. The beam varies in size from 1.8 degrees in the azimuth direction by 3.0 degrees in elevation at the scan center position to 2.7 degrees by 3.0 degrees at the scan edges. This results in an elliptical projection on the surface and about 22 independent beam positions or resolution cells across the swath width. The minimum practical operational altitude for which contiguous scans and an acceptable signal-to-noise are achieved is about 500 m at an aircraft speed of 100 m/sec. This requires 1.6 scans/sec and provides a swath width of 670 m and a surface resolution of 30 m cross-track and 62 m in the along-track direction. The receiver RMS noise output, ΔT_{N} , integrated over each resolution cell for the above conditions is about 1.5 K. The instrument undergoes a short calibration sequence at the end of each scan.

The U. S. Coast Guard Airborne Oil Surveillance System Passive Microwave Imager (AOSS-PMI) [23] operates at 37 GHz and is mounted in a U. S. Coast Guard C-130 aircraft. The antenna is a dual-beam, phased array approximately 0.20 m by 0.43 m in size. The two beams are identical and are opposed to each other at 44.6 degrees to the array normal. The antenna is mounted in the aircraft with the array normal directed at nadir and the antenna is mechanically scanned by spinning about this axis causing the dual beams to rotate in a conical fashion and provide a circular scan on the surface. The receiver input is continually switched to the forward antenna beam in synchronism with the antenna rotation. The beam width is 2.8 degrees in azimuth and 2.0 degrees in elevation providing a circular beam spot on the surface. The instrument is calibrated during the 18 degree portion at both ends of the hemicircular scan and measurements are made during the 144 degree central portion. There are 27 independent resolution cells across the swath width. The minimum altitude for which contiguous scans are achieved at an aircraft speed of 100 m/sec is 500 m, which corresponds to an antenna rotation speed of 88 revolutions/min or 2.9 scans/sec. This results in a swath width of 940 m and a surface resolution of 34 m. The RMS noise per resolution cell under these conditions is about 2.0 K.

The Naval Weapons Center Microwave Radiometric System (MICRAD) [24],[25] operates at 33.6 GHz and has been mounted in both an OV-10 and a C-130 aircraft. The antenna system is composed of three cassegrain parabolas, with a 0.61 m diameter, mounted 120 degrees apart on a rotating axis which is installed at an angle of 30 degrees to the horizontal in the aircraft. A switching matrix alternately connects the receiver input to each successive antenna in turn to provide a continuous mechanical 120 degree sector scan, about the rotation axis, centered on the aircraft ground track. The angle of incidence of the scanned beam on the surface varies from 30 degrees at the scan center to 64 degrees at the ends of the scan. This 120 degree scan about the rotation axis projects to a scan width on the surface of 148 degrees in azimuth centered on the flight direction. The beam width is 1.1 degrees, projecting 109 elliptically shaped resolution cells across the swath on the surface. Because of the greater slant range and incidence angle, the surface resolution degrades by about a factor of two along the track and by about a factor of four in the cross-track direction as the scan edges are approached. The maximum antenna rotation rate is 240 revolutions/min or 12 scans/sec. At an aircraft speed of 100 m/sec contiguous scans can be obtained at altitudes as low as 325 m. This provides a surface resolution of 7.2 m cross track and 8.3 m along the track in the central portion of the The RMS noise per resolution cell under these conditions is about 2.6 K.

The Naval Research Laboratory Millimeter Wave Imaging System (MWIS) [26] is very versatile since it incorporates an oscillating mirror and interchangeable antenna/radiometer units making it particularly adaptable to variations in its operational frequency, polarization, and resolution. It was flight-tested using the NASA/Wallops C-54 aircraft (NASA 427) and is currently installed in the Naval Research Laboratory P3-A aircraft (BUNO 149670). It has been operated at 90 GHz, simultaneously at 22 and 31 GHz, using a dual frequency antenna/radiometer, and will be used at 140 GHz in the near future. An oscillating elliptically shaped mirror, mounted at an angle of 45 degrees to its rotational axis, is used to scan the beam of the antenna at a constant angular rate. The rotational axis is aligned with the keel of the aircraft thus the antenna beam is scanned back and forth perpendicular to the flight direction and generates a zigzag raster on the ground with aircraft motion. The uniform rate zigzag is preferred over the more easily implemented sinusoidal scan because the time required to scan each resolution cell over the entire scan width is the same; whereas, the sinusoidal scan moves at a $\pi/2$ greater rate at the scan center, where optimum measurement is desired, than at the scan edge. The mirror can be scanned at rates up to 640 degrees/sec and it reverses direction in less than one millisecond. The scan width is 64 degrees centered on the ground track resulting in a maximum of 10 scans/sec. The 90 GHz radiometer uses a horn-lens antenna with a 2 degree beam providing 32 resolution cells across the scan. The projected beam spot increases slightly in size and varies from circular at center scan to slightly elliptical at the scan edge. Both the reduction in resolution and departure from circularity are less than 18 percent. In order to obtain contiguous beam spots at the edge of the zigzag scan, the scans must be spaced at one-half beam spot intervals at the center of the scan. Thus the effective scan rate is 5 scans/sec. At an aircraft speed of 100 m/sec, this corresponds to a minimum altitude of 570 m and a surface resolution of 20 m at scan The RMS noise per resolution cell under these conditions is about 2.5 K.

The Electrically Scanning Microwave Radiometer (ESMR) [27] was launched on the NIMBUS 5 satellite in December 1972. The system operates at 19.3 GHz and uses a planar phased array antenna with an aperture area of 0.83 m by 0.86 m. The antenna is linearly polarized in a direction parallel to the spacecraft velocity vector. It is mounted horizontally and electrically scanned perpendicular to the spacecraft velocity vector from 50 degrees to the left of nadir, through nadir to 50 degrees to the right of nadir in 78 discrete steps every four seconds. The beam-width is 1.4 degrees by 1.4 degrees at nadir but degrades to 2.2 degrees cross-track by 1.4 degrees in the along-track direction at the scan edges. This results in about 57 independent resolution cells across the 100 degree swath width. At an altitude of 1100 km the swath width is 3300 km and the surface resolution varies from 27 km by 27 km near nadir to about 49 km along-track by 175 km cross-track at the scan edge. The RMS noise per resolution cell is approximately 1.5 K.

A second ESMR operating at 37.0 GHz is part of the NIMBUS 6 [28] satellite launched in June 1975. It also uses a planar phased array antenna but both the vertically and horizontally linearly polarized components are measured. The array is mounted nearly vertically in the satellite, facing forward. The beam is electrically scanned ahead of the spacecraft, along a conical surface, ± 35 degrees in azimuth in 71 discrete steps. The angle of incidence on the surface is nominally 50 degrees but varies about ± 0.6

degrees across the scan. The beam-width varies from 0.95 degrees in azimuth by 1.00 degrees in elevation at the scan center to 1.17 degrees by 0.84 degrees at the scan edges. There are roughly 42 independent resolution cells across the scan width. At an altitude of 1100 km the swath width is 1200 km and the surface resolution varies from about 42 km along track by 26 km cross-track at center scan to 36 km by 32 km at the scan edge.

Also on NIMBUS 6 is the five-channel Scanning Microwave Spectrometer (SCAMS) [29] operating at 22.235, 31.650, 52.850, 53.850, and 55.450 GHz. This system uses three corrugated horn antennas; one each for the 22.235 and 31.650 GHz channels and one for the three 50 GHz channels. The beams are scanned mechanically by rotating mirrors in front of each horn. The mirrors are inclined at 45 degrees to the electrical axis of the horns and this axis is aligned with the spacecraft velocity vector; thus the beams are scanned cross-track, through nadir and around through zenith. A 360 degree scan requires 16 seconds. Thirteen earth data samples, each taking one second, are taken in 7.2 degree steps between ±43.2 degrees of nadir. During the remaining portion of the scan the beams view cold outer space and an absorbing disc mounted in the spacecraft for calibration. All of the antenna beam widths are 7.5 degrees given 13 resolution cells over the swath width. At an altitude of 1100 km the swath width is 2600 km and surface resolutions of approximately 145 km at nadir and 220 km along-track and 360 km cross-track are obtained. The RMS noise per resolution cell varies from about 0.2 K for the 22 and 31 GHz channels to about 0.5 K for the three 50 GHz channels.

A Scanning Multichannel Microwave Radiometer (SMMR) [30] is scheduled to be launched on both the SEASAT satellite in May 1978 and on NIMBUS G in October 1978. The system will operate at 6.6, 10.69, 18.0, 21.0, and 37.0 GHz. It will use a single multifrequency corrugated horn to illuminate an offset parabolic reflector. The reflector is elliptically shaped, measuring 1.10 m by 0.79 m, and will rotate about a vertical axis resulting in a conical scan pattern with the angle of incidence on the earth's surface constant at 50.3 degrees. On NIMBUS G the scan will be ± 25 degrees in azimuth centered on the satellite ground track to produce a swath width of about 800 km. The scan will be offset on SEASAT. The beam width will range from 4 degrees at 6.6 GHz to 0.7 degrees at 37 GHz producing surface resolutions of about 100 km cross-track by 150 km along-track at 6.6 GHz to 17 km by 27 km at 37 GHz.

ACKNOWLEDGMENTS

I wish to thank the Goddard Space Flight Center and the Johnson Space Center of the National Aeronautics and Space Administration, the U. S. Coast Guard, and the Naval Weapons Center for providing me with photographs of their microwave systems and examples of their measurements and results.

REFERENCES

- [1] Kraus, John D., "Radio Astronomy," McGraw-Hill Book Company, New York, p. 123, 1966.
- [2] Van Der Ziel, A., "Noise," Prentice-Hall, Inc., New York, p. 8, 1954.
- [3] Bracewell, R. N., "Radio Astronomy Techniques," Handbuch der Physik, vol. 54, pp. 42-129, 1962.
- [4] Staelin, David H., "Measurements and Interpretation of the Microwave Spectrum of the Terrestrial Atmosphere near 1-Centimeter Wavelength," Journal of Geophysical Research, vol. 71, pp. 2875-2881, 1966.
- [5] Barrett, A. H., and Chung, V. K., "A Method for the Determination of High-Altitude Water-Vapor Abundance from Ground-Based Microwave Observations," Journal of Geophysical Research, vol. 67, pp. 4259-4266, 1962.
- [6] Van Vleck, J. H., "Absorption of Microwaves by Water Vapor," Physical Review, vol. 71, pp. 425-432, 1947.
- [7] Rosenkranz, P. W., "Shape of the 5 mm Oxygen Band in the Atmosphere," IEEE Trans. on Antennas and Propagation, vol. AP-23, no. 4, July 1975.
- [8] Gordon, R. G., "Semiclassical Theory of Spectra and Relaxation in Molecular Gasses," J. Chem. Phys., vol. 45, pp. 1649-1655, September 1, 1966.
- [9] Van Vleck, J. H., "Absorption of Microwaves by Oxygen," Physical Review, vol. 71, pp. 413-424, 1947.
- [10] Paris, J. F., "Transfer of Thermal Microwaves in the Atmosphere," Thesis, Department of Meteorology, Texas A&M, 1971.
- [11] Stogryn, A., "The Apparent Temperature of the Sea at Microwave Frequencies," IEEE Trans. on Antennas and Propagation, vol. AP-15, pp. 278-286, March 1967.
- [12] Hollinger, J. P., "Passive Microwave Measurements of Sea Surface Roughness," IEEE Trans. on Geoscience Electronics, vol. GE-9, pp. 165-169, July 1971.

- [13] Nordberg, W., Conaway, J., Ross, D. B., and Wilheit, T., "Measurements of Microwave Emission from a Foam-Covered Wind Driven Sea," J. Atmos. Sci., vol. 28, pp. 429-435, 1971.
- [14] Ross, D. B., and Cardone, V. J., "Observations of Oceanic Whitecaps and Their Relation to Remote Measurements of Surface Wind Speed," Journal of Geophysical Research, vol. 79, pp. 444-452, 1974.
- [15] Peak, W. H., "Interaction of Electromagnetic Waves with Some Natural Surfaces," IRE Trans. on Antennas and Propagation (Special Suppl.), vol. AP-7, pp. S324-S329, December 1959.
- [16] Hollinger, J. P., and Mennella, R. A., "Oil Spills: Measurements of Their Distributions and Volumes by Multifrequency Microwave Radiometry," Science, vol. 181, pp. 54-56, July 1973.
- [17] Chang, T. C., Gloersen, P., Schmugge, T., Wilheit, T. T., and Zwally, H. J., "Microwave Emission from Snow and Glacier Ice," Journal of Glaciology, vol. 16, pp. 23-39, 1976.
- [18] Gloersen, P., Nordberg, W., Schmugge, T., and Wilheit, T. T., "Microwave Signatures of First-Year and Multiyear Sea Ice," Journal of Geophysical Research, vol. 78, pp. 3564-3572, June 1973.
- [19] Thaddeus, P., "The Short-Wavelength Spectrum of the Microwave Background," Annual Review of Astronomy and Astrophysics, vol. 10, pp. 305-334, 1972.
- [20] Balwantz, W. W., Weston, J. P., and Lee, S. L., "Turbulent Burning in Rocket Exhaust Streams," Proc. Eighth Plume Tech. Meeting, Colorado Springs, Colorado, pp. 1-18, July 1974.
- [21] Balwanz, W. W., and Lee, S. L., "Plume Properties," to be published.
- [22] "NASA 927 (NP3A) Aircraft Sensor System," Johnson Space Center, Houston, Texas.
- [23] "An Airborne Multisensor System with Multimission Capability for U. S. Coast Guard," TN 6900-1, October 1974, Aerojet Electrosystems Company, Azusa, California.
- [24] Hoover, M. C. and Moore, R. P., "An Airborne Ka-Band Microwave Radiometric Measurement Mapping System," Naval Weapons Center, China Lake, California.
- [25] Moore, R. P., Hoover, M. C., and Patterson, W. V., "Microwave Radiometric Imager Design for Pods and Aircraft," Proc. Soc. Photo-Optical Instr. Engr., vol. 79, pp. 124-131, March 1976.
- [26] Hollinger, J. P., Kenney, J. E., and Troy, B. E., "A Versatile Millimeter Wave Imaging System," IEEE Trans. on Microwave Theory and Techniques, vol. MTT-24, no. 11, pp. 786-793, November 1976.
- [27] Wilheit, T., "The Electrically Scanning Microwave Radiometer (ESMR) Experiment," in: The NIMBUS-5 User's Guide, pp. 59-105, NASA Goddard Space Flight Center, Greenbelt, Maryland, 1972.
- [28] Wilheit, T., "The Electrically Scanning Microwave Radiometer (ESMR) Experiment," in: The NIMBUS-6 User's Guide, pp. 87-108, NASA Goddard Space Flight Center, Greenbelt, Maryland, 1975.
- [29] Staelin, D. H., Barrett, A. H., Rosenkranz, P. W., Barath, F. T., Johnson, E. J., Waters, W. J., and Wouters, A., "The Scanning Microwave Spectrometer (SCAMS) Experiment," in: The NIMBUS-6 User's Guide, pp. 59-86, NASA Goddard Space Flight Center, Greenbelt, Maryland, 1975.
- [30] "NIMBUS-G Data Application System Data Plan," Revision 1, April 1977 prepared for NASA Goddard Space Flight Center, Greenbelt, Maryland under contract NAS5-22420 by OAO Corporation, Beltsville, Maryland.

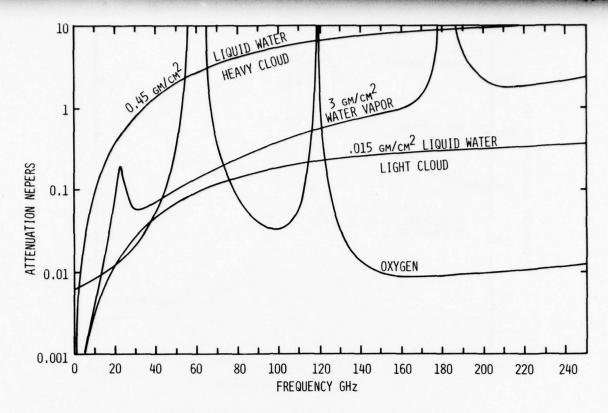


Fig. 1 Zenith microwave opacity components for a standard atmosphere, 3 gm/cm² columnar water vapor density and two clouds

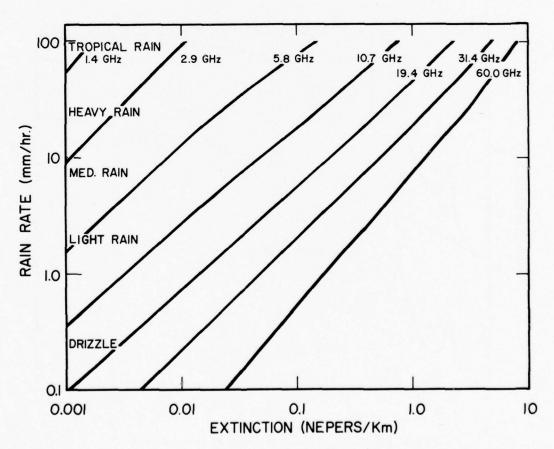


Fig.2 Microwave extinction due to rain

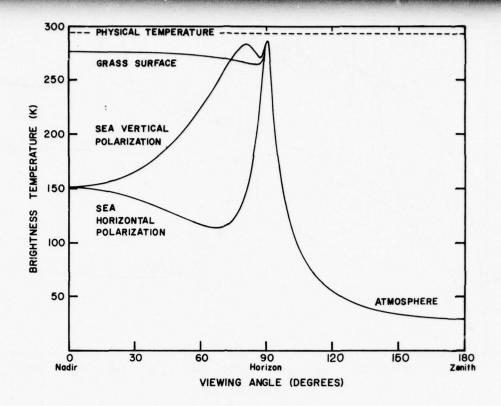


Fig.3 Brightness temperature of the sea, grass covered surface and a standard atmosphere with light clouds at 37 GHz

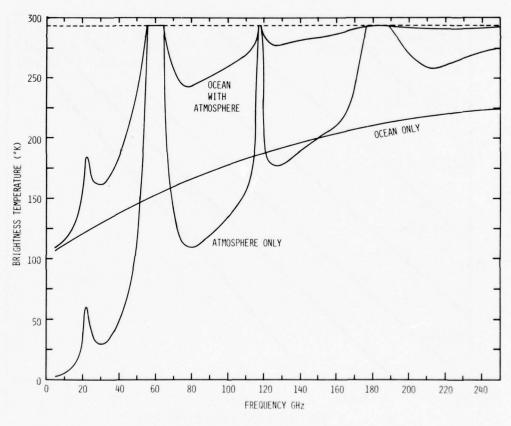


Fig.4 Brightness temperature of a standard atmosphere with light clouds and of a smooth ocean at nadir

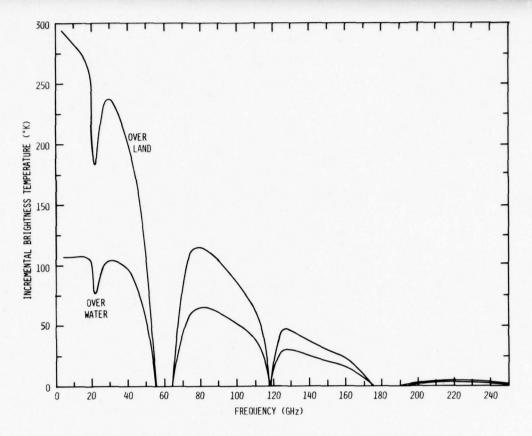


Fig.5 Incremental brightness temperature of a reflecting target over land and water

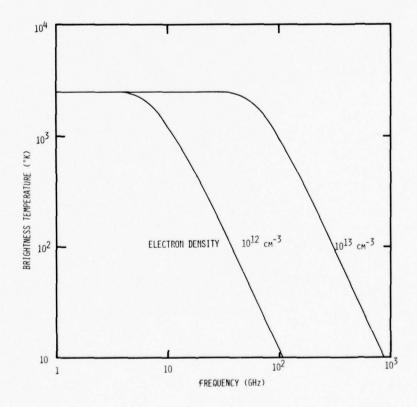


Fig. 6 Brightness temperature of a uniform one meter thick ionized gas in thermodynamic equilibrium at 2500° K

MICROWAVE SCANNING RADIOMETRY (APPLICATIONS)

by

E.P.L.Windsor, BSc. and H.McD.Mooney, MSc. BRITISH AIRCRAFT CORPORATION LIMITED SPACE SYSTEMS BRISTOL, UK

CONTENTS

		Page					
1.	INTRODUCTION	5-2					
2.	CHARACTERISTICS OF A SATELLITE BORNE PMR SYSTEM						
	2.1 General	5-2					
	2.2 Basic Variables of the Satellite/PMR						
	2.2.1 Brightness Temperature Resolution.	5-3					
	2.2.2 Spatial Resolution	5-4					
	2.2.3 Scanning Geometry	5-6					
	2.2.4 Orbit Characteristics	5-10					
3.	DESCRIPTION OF A POSSIBLE SATELLITE BORNE PMR SYSTEM						
	3.1 Background	5-15					
	3.2 System Aims	5-16					
	3.3 Description of System Options	5-17					
	3.4 Assessment Criteria	5-22					
	3.5 Performance Comparison	5-24					
4.	POSSIBLE CHARACTERISTICS OF AN AIRBORNE PMR SYSTEM FOR SURVEILLANCE						
	4.1 General	5-24					
	4.2 An Airborne 'Satellite' PMR	5-24					
	4.3 Conclusions	5-25					

1 INTRODUCTION

In the previous paper the basic principles of Microwave Radiometry applied to ocean survellance applications have been described, together with the characteristics of the imaging hardware that has been developed and examples of the outputs which they are capable of producing.

In this paper the characteristics of satellite borne PMR systems which have been studied by BAC Space Systems will be described in terms of their potential sensitivity in measurement of physical parameters together with the spatial resolution and global coverage achievable. The application of similar techniques to aircraft borne systems is also discussed.

BAC Space Systems Group has been involved on the study and application of remote sensing techniques to earth resources surveys for a number of years. The most relevant are:

- SARSAT and SARLAB Studies for ESA of (1973-74) Synthetic Aperture Radar (with Thomson-CSF).
- SKYLARK Sounding Rocket programmes carrying visual sensors for earth resources surveys (1972-73).
- PAMIRASAT Studies of Satellite borne Passive Microwave Radiometers (1975-77).
- Nimbus-G SMMR Experiment team, participation in Algorithm development and ground truth data collection.

It is the experience and results of the latter two that will be largely used for the material presented in this paper, and the authors thank ESA, NASA the UK Department of Industry, and BAC for permission to publish this material. Neverthe less, the views expressed in this paper are solely those of the authors.

2 CHARACTERISTICS OF A SATELLITE BORNE PASSIVE MICROWAVE RADIOMETER SYSTEM

2.1 GENERAL

The satellite borne systems studied have been aimed at global sensing of the Earth's surface and of the atmosphere, with particular emphasis on the remote measurement of the characteristics of the oceans, polar ice caps and the atmosphere for:

- Meteorology
- Climatology
- Oceanography
- Applications (Ice Mapping, Ship Routing, Wave Data Collection and Forecasting, etc.).

Although the requirements of any system designed for ocean survellance differ considerably from those for the types of mission above, primarily in respect of spatial resolution, the basic characteristics of a satellite borne passive microwave system remain relevant.

These characteristics may be varied considerably to match the required mission objective, and in this section the way in which the system variables interact will be studied so that possible options can be identified.

The system essentially consists of three elements:

- Satellite
- Sensor Payload
- Ground Segment (including Satellite/Ground Link.)

Although the latter is an essential part of the system and in many ways has the most immediate impact on the user, the first two parts of the system are highly interactive and have the most significant effect on the overall system performance and hence receive prime attention in this short review.

In principle, observations of the thermal emission from bodies or media in the natural environment can be made in the 'radio' band over an extremely wide wavelength or frequency range. This range can extend from the VHF, through the UHF and microwave to the fringes of the infra-red portions of the spectrum.

There are two main factors which, for spaceborne PMR systems, will limit the usable extent of the above spectrum to a relatively well defined region in the microwave. These are:-

- Atmospheric absorption
- Antenna dimensions

Emissions from the Earth's surface at wavelengths smaller than 0.75 cm (i.e. in the microwave band at frequencies above 40 GHz) are increasingly absorbed by various atmospheric media as they pass to outer space. The main contributors to this absorption are $\rm H_2O$, $\rm O_2$ and $\rm O_3$.

At wavelengths greater than 0.75 cm, the neutral atmosphere is relatively transparent and can be utilised for surface observation from space. However, due to the long observation ranges involved in spaceborne remote sensing the antenna dimensions (see 2.2.2) become increasingly large for a given spatial resolution on the Earth's surface. Because of this the practicable upper wavelength limit to PMR observations from space is around 30 cm (frequency - 1 GHz) and in general observation channels in the 0.75 cm to 6 cm band are utilised.

Wavelengths shorter than 0.75 cm can, of course, be used for atmospheric, rather than surface, observations - there being many gaseous spectral line emission features below this wavelength which are of interest to practical meteorology and the atmospheric sciences.

An essential characteristics of the satellite/payload system to be studied is the use os a multispectral technique to obtain quantitative measurements of the physical parameters of interest to the user.

The basic system variables considered are:

- Brightness Temperature Sensitivity
- Spatial Resolution
- Scanning Geometry (Swath Width, 'look' Angle, type)
- Satellite Altitude/Speed
- Orbit/Coverage/Repetition Rate
- Time of Day

The fundamental way in which these variables interact are discussed in the following sections.

2.2 BASIC VARIABLES OF THE SATELLITE/PMR

2.2.1 Brightness Temperature Resolution

A radiometer antenna orientated towards a remote body which is emitting thermal radiation will, as far as the input signal to the radiometer receiver is concerned, appear to have assumed a radiation temperature Ta whose value directly corresponds to the level of radiation intercepted by the antenna. Measurement of Ta by an appropriately calibrated receiver will then allow the remote 'emitter' to be assigned a 'brightness temperature' this being the temperature at which a perfect, black-body within the IFOV (Instantaneous Field of View) would have to exist to give the same level of intercepted radiation. Knowing the emission characteristics of the remote body it should then be possible to invert the measurement and associate the measured brightness temperature with particular aspects of the body's physical state.

The maximum achievable thermal resolution (ΔT) of the radiometer is generally defined as that change in Ta which produces a corresponding dc-signal change in the radiometer output equal to the latter's rms noise voltage. This resolution can be shown to be given by:

$$\Delta T = \frac{K (Ts + Ta)}{\sqrt{\beta \tau}}$$
 2.1

where Ts = receiver system noise temperature

 β = receiver RF bandwidth (Hz)

τ = integration time (secs)

K = a constant whose value depends on radiometer type

As is obvious, the smaller the <u>value</u> of ΔT then the more sensitive is the radiometer. Thus, highly sensitive radiometers will be designed to have low values of Ts, wide predetection bandwidths (β) and/or long integration times (τ) over which the IFOV dwells on a particular emitting region.

Current space-flyable technology using non-cooled solid state techniques may allow the achievement of receiver system noise temperatures in the PMR band of between a few hundred to a thousand or so degrees K. Appreciably better (i.e. lower) values of Ts could be obtained by use of cooled or non-cooled parametric amplifiers.

The value of the selected predetection bandwidth (β) will be both a function of electronic design constraints and the need to avoid those busy regions of the GHz spectrum in which unwanted reception of man-made signals (e.g. from ground-based radars) may occur. Generally the latter is the most dominant influence with the

most suitable channels for spaceborne PMR being those 'quiet' but narrow bands reserved for the exclusive use of the radio astronomy service. There are approximately 10 or so such bands in the 5 to 40 GHz region, their main disadvantage being simply their narrowness (generally a few 10's of MHz).

The integration time τ is a function of the mode of observation employed (e.g. scanning or non-scanning) and the dimensions of the IFOV. The constant K usually assumes a value of 2 for most suitable receiver designs.

Given the above, achievable values of ΔT within the PMR band generally range from a few tenths of a degree K to several degrees K.

2.2.2 Spatial Resolution

The spatial resolution of a radiometer is generally defined as the diameter of the ground 'footprint' generated by the radiometer's instantaneous field of view (IFOV). This is obviously determined by the beamwidth of the antenna used on the radiometer with the 'footprint' contours usually taken as being those at the half-power (-3db) limits of the antenna's reception beam-pattern.

At the above limits, we have, very approximately:

$$F = \frac{1.2\lambda d}{D}$$
 2.2

where

F = footprint diameter (km)

D = antenna diameter (metres)

d = observation range (km)

 λ = observation wavelength (metres)

Examination of the implications of this very basic relationship clearly indicate that PMR can only realise resolution levels which are measureable in kilometres. This contrasts strongly with the metre-level resolutions which are obtainable by current spaceborne surveillance sensors which either operate in the visible region of the spectrum or utilise active microwave techniques which are able to synthesize extra large apertures through coherent processing.

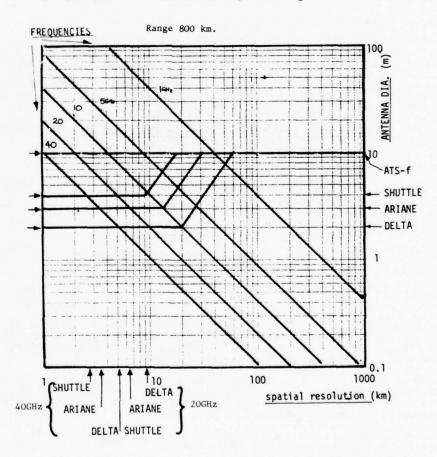
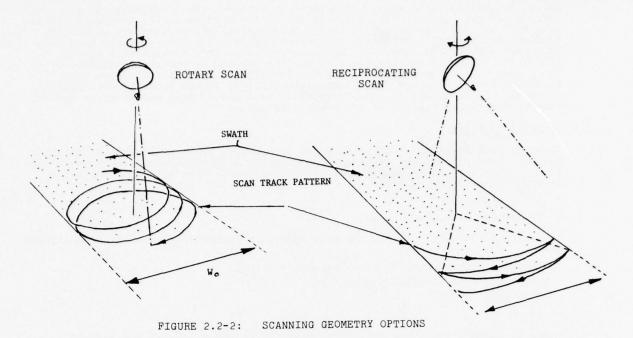


FIGURE 2.2-1: SPATIAL RESOLUTION CHARACTERISTICS



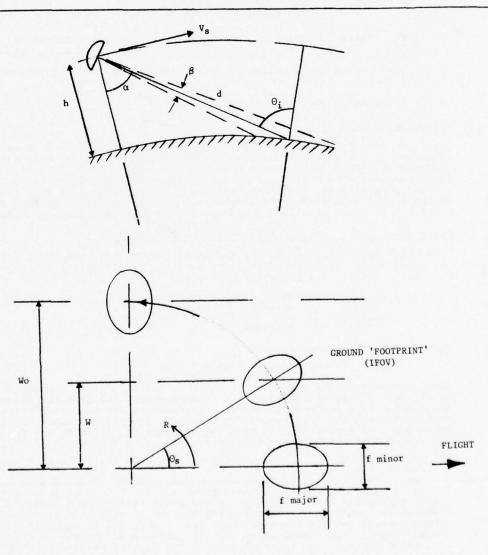


FIGURE 2.2.3:

SCANNING GEOMETRY (Conical Scan)

While, in principle, it would be possible to utilise very large antennas to improve PMR resolution a limitation is set by the need to employ antenna surfaces of a reflectivity high enough to ensure good radiometric performance within the 'radiometry' band (5 - 40 GHz). This means that solid surface, rather than mesh (and thus deployable), antennas must be used. With this constraint a strong limitation to usable antenna diameter will be imposed by the shroud dimensions of the launch vehicle used in the mission. The effects of this imposition are clearly shown in Figure 2.2-1 which relates typical launch vehicles with practicable antenna diameters and thence to achievable ground resolutions at an 800 km observation range, typical of an in-orbit situation.

2.2.3 Scanning Geometry

In order to generate an image with a PMR instrument, it is necessary to phyically scan the antenna over the angle subtended by the swath desired on the Earth's surface. There are two principal ways of effecting this scan with dish reflector antennas* (see Figure 2.2-2):

- 360° rotary scan
- Sector reciprocation

Given these scanning options, the scan-related parameters which must be considered are:

- Scan characteristics (continuous/reciprocating).
- Observation and incidence angle
- Scan rate
- Swath width.

These parameters are shown diagrammatically in Figure 2.2-3 for the case of a reciprocating conical scan. Their importance stems from the way that they impact upon:

- The radiometer integration time (τ) and hence system sensitivity.
- The global coverage rate and thus the observation repetition rate.
- The engineering implications of incorporating the scanning antenna on the spacecraft.

Let us investigate the above in more detail:

Linear vs Conical Scan

Since the radiometric 'appearance' of emitting surfaces can be shown to be strongly dependent on the angle of observation, it is usual to employ only conically scanning systems. This ensures that the observation angle (θ_i) is a constant, thereby removing the influence of one variable from the observation process. The problem remaining is, of course, related to the selection of that conical angle which is an acceptable compromise between the optimum observational needs of a range of potential observables and the achievement of a usefully wide swath width.

Observation and Incidence Angle - Antenna Footprint

Given the conical scan geometry, the antenna IFOV footprint will, for an antenna pattern of circular cross-section, be very nearly elliptical in shape. The major and minor axes of this footprint will be:

f minor =
$$\frac{\lambda d}{D}$$
 2.3
f major = $\frac{\lambda d}{D}$ sec Θ_1 2.4

where D = antenna diameter

d,0; are as shown in Figure 2.2-3.

Given an orbit altitude of h, then the observation angle α determines the values of all the factors mentioned above. Consequently, the selected value α must necessarily be a compromise between the observational characteristics of all observables and the requirement for a certain footprint dimension. Generally, a value for α of around 400 has been taken. This is, in fact, the value selected for the NIMBUS-G Scanning Multifrequency Microwave Radiometer (SMMR).

Values of d and $\Theta_{\dot{1}}$ for a range of altitude and observation angles are shown in figures 2.2-4 and 2.2-5.

^{*} It should be noted here that phased array antennas would be able to effect the scanning function electronically thereby potentially easing some of the problems involved in incorporating scanning PMR systems on sattlelite platforms. However, arrays possess certain other features features which, in comparison with reflector antennas, make them unattractive for the purposes of spaceborne PMR. These features are, among others, high internal complexity, limited multi-frequency capability, relatively high system noise levels and relatively low reliability.

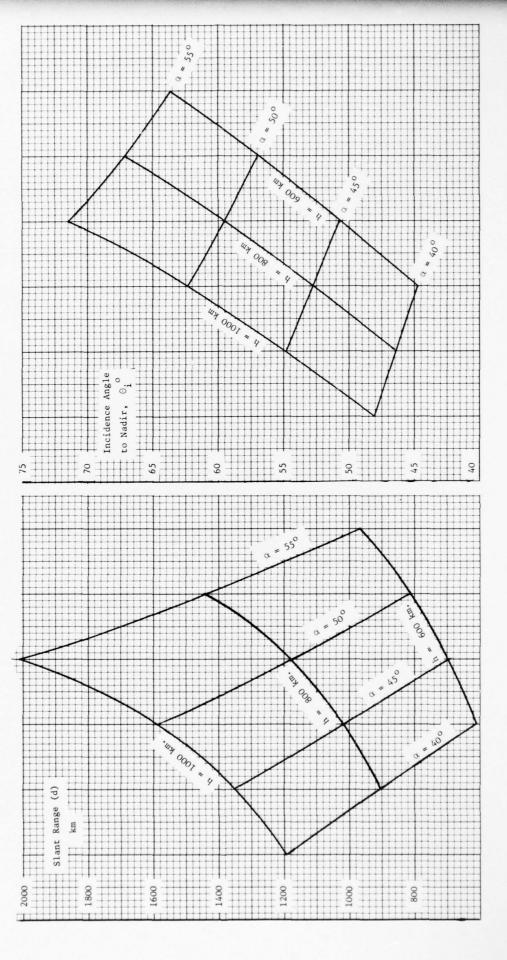


FIGURE 2.2-4: SLANT RANGE VS ALTITUDE, LOOK ANGLE

ANGLE ANGLE ANGLE VS ALTITUDE, LOOK

Scan Rate

To generate a complete image, the rate of scan must be chosen to synchronise with the satellite ground velocity such that consecutive scans provide a contiguous coverage pattern. The limiting contiguity conditions is at the midpoint of scan, along the satellite velocity vector.

We have, for rotary and reciprocating scan:

- Rotary Scan:

Here the antenna rotates through 360°

Scan Rate R =
$$\frac{\text{Vss D}}{\lambda \text{d sec0}_{\dot{1}}}$$
 2.5

where R = scan rate (revs/second)

Vss = Satellite ground velocity

Hence, the integration time τ for each IFOV is given by:

$$\tau = \frac{\lambda^2 d \sec 0}{D^2 2\pi Vss \sin \alpha} (secs)$$
 2.6

- Reciprocating Scan:

In the conical case above, the swath width W is very nearly:

Let us assume a reciprocating scan operating over the same swath width with an observation angle α' and the associated d',0'i and D'.

We have $\alpha' > \alpha$ (otherwise we would not reach the limits of the desired swath).

and thus d' > d

0'i > 0i

 $D^* > D$ (to ensure the same footprint dimensions at the longer range).

It can be shown that:

R (mean value) =
$$\frac{VssD}{\lambda d sec0}$$
, $\frac{4 sin^{-1}}{i}$ $\frac{W}{2H tan\alpha}$ (rad/sec)

and
$$\tau = \frac{\lambda^2 d^2 \sec \theta i}{D^2 4H Vss \tan \alpha \sin \theta (\frac{W}{2H \tan \alpha})}$$
 (secs)

R and τ for reciprocating and rotary systems, can, in fact, be shown to be equal for the same swath width and footprint dimensions irrespective of the value of α .

However, the value of the mean scan rate R for the reciprocating systems is inversely dependent on the major axis dimension of the footprint. Thus, as spatial resolution increases, R, from the engineering design point of view, may reach unacceptably high values. This is so since the scan direction must be reversed at each limit of scan. With a high R, large inertial loadings may be imposed on the antenna structure and bearing assembly and significant perturbations injected into the satellite platform. Therefore, as the proposed level of spatial resolution for a PMR system is increased a point will be reached where the only practicable scanning solution will be a rotary one since a system based on pure rotation will only product a constant level of angular momentum with no accelerations or perterbing forces. For example, examinations conducted within the PAMIRASAT study (see Section 3) indicated that for a PMR system intended for ground spatial resolutions of the order of 10 Km a rotary solution was strongly preferred.

Obviously, the values desired for τ and W, the resultant value for R and the selection of optimum scanning solution are all closely inter-related. Since, for both rotary and reciprocating solutions the value of τ is strongly, but inversely, dependent on W then the required Earth coverage characteristics, which are determined by the value of W and the orbit repetition rate (see 2.2.5), must also be brought into consideration. Generally speaking, analysis has indicated that values for W should not significantly exceed 1,000 km for realisation of usable performance.

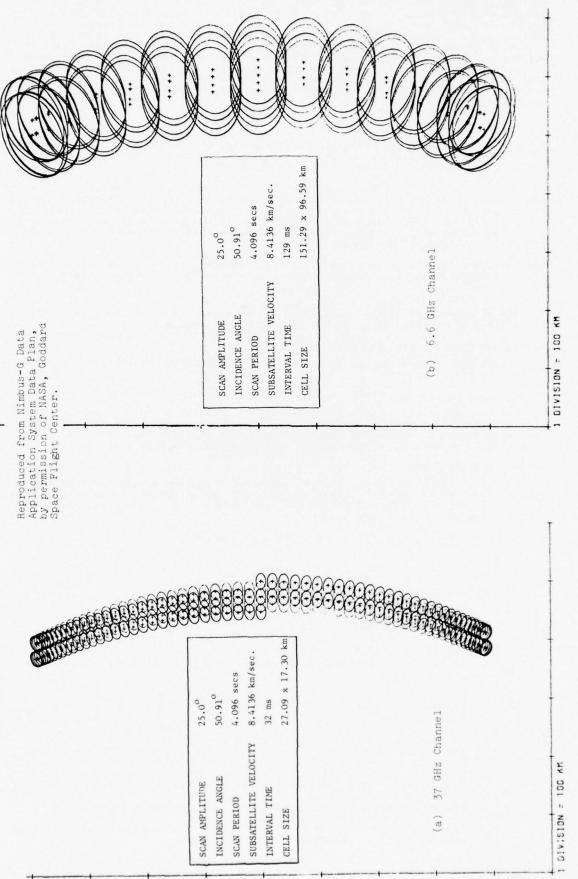


FIGURE 2.2-6:

Figures 2.2-6(a) and (b) are included to illustrate the footprint scan pattern for the scanning PMR on NIMBUS-G. Since the instrument is a multi-frequency one using a single antenna (a) and (b) show the scans for the highest (37 GHz) and lowest (6.6 GHz) frequency respectively. As will be further discussed in Section 3, in such multi-frequency instruments, the scan rate must be selected on the basis of the smallest footprint dimension to ensure that a complete image is obtained at all observation frequencies. This does mean, however, that the rate of scan is 'too high' or non-optimum for all but the highest frequency channel and that the integration time on any lower frequency channel is not as high as it could be if the rate were selected on the basis of the footprint dimension obtained on that channel.

2.2.4 Orbit Parameters

The orbit selected for a particular Earth observation mission will be the result of careful consideration of user requirements and the need to avoid excessive air drag effects on the fringes of the atmosphere.

For missions intended for relatively lengthy life times (several years) the air drag consideration will impose a lower altitude limit to orbit selection of around 500 km and for the general class of mission to which spaceborne PMR is likely to apply an upper altitude limit would be expected to be around 1,000 km. This upper limit is particularly significant since achievable spatial resolution decreases directly with increasing altitude.

The precise orbit characteristics will depend on the mission requisites of potential system users who will express their requirement in the following terms:

- Geographical Coverage:
 - This is determined by the inclination selected for the orbit. Highly inclined (i~ 90°) orbits will allow global or near global coverage.
- Maximum Time Interval (I) Between Observations:

 This is the maximum time acceptable between consecutive observations of a given Earth surface location.
- Rate of Area Coverage:

This is a factor closely related to I and is the rate at which coverage of an extensive geographical area is built up. If sensor swaths were very wide with a high degree of day-to-day overlap it might be possible (see below) to cover a sizable percentage of the Earth's surface in periods much less than I.

- Ground Track Pattern:

For low altitude orbits the ways in which the satellite ground track pattern envelopes the terrestrial sphere are many and varied and will completely determine the coverage characteristics mentioned above. The two orbital parameters which are of interest here are:

. The orbit period P where, for a circular orbit:-

$$P = 2\pi \sqrt{\frac{R^3}{GM}} \qquad \qquad 2.10$$

in which R = orbit radius

G = gravitational constant

M = Earth's mass

. The orbit inclination i

Given an orbit with particular values of P and i two important conditions can arise. These are:

(i) Synchronism between the developing satellite ground track and the terrestrial rotation rate r (= $2\pi/T$ where T is the length of a Sidereal day).

As one varies P and/or i then it is found that the orbital ground track goes 'in and out' of synchronous relationship with the period of the rotating Earth. At points of synchronism the subsatellite track will be repetitive, or recurring, over the interval of time I (see above). When there is no such synchronous relationship then the track will be disordered in time and will not be repetitive with fixed ground locations being overflown at widely variable intervals.

(ii) Synchronism between the precession of the orbit plane in space and the rate of Earth's revolution around the Sun.

Since the Earth is not perfectly spherical in shape, the slightly distorted terrestrial gravitational field causes the plane of any

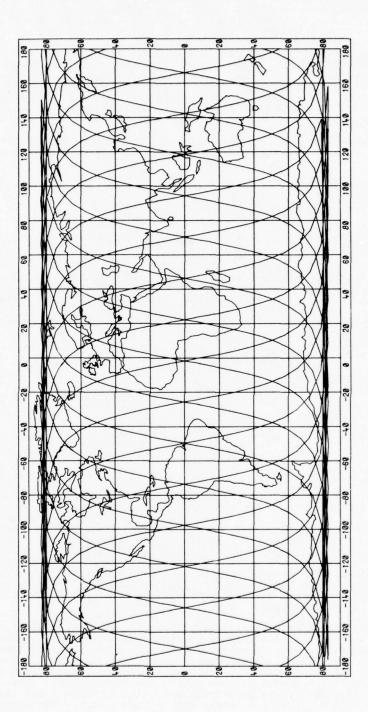


FIGURE 2 2-7: SUN-SYNCHRONOUS ZERO-DRIFT ORBIT TRACK (γ_z = 15 orbits/day; altitude 565 km).

satellite orbit to rotate (i.e. precess) in inertial space with the rate of this precessional rotation depending predominantly on R and i. For low altitude orbits (say, below 1,000 km) with inclinations near to 90° it is found that the precessional rate can be made equal in magnitude but opposite in sign to the Earth's motion around the SUN. Such orbits are termed SUN-SYNCHRONOUS. The effect of this synchronism is to cause the solar direction with respect to the orbit plane to remain constant throughout the year, thereby ensuring that the subsatellite times-of-day experienced during a single orbit are fixed for all time and for all subsequent orbits. Thus, for example, it is possible to stabilise the orbit such that it always passes across the equator at noon in one direction (say, south-going) and midnight in the other (north-going). Apart from ensuring a constant set of illumination conditions for any remote sensors which require solar illumination (not FMR), the solar aspect variations with respect to the satellite platform itself are minimised, thereby making satellite design an easier proposition compared to the non Sun-synchronous case in which, over a period of time, the solar aspect vector as seen from the satellite can swing about in 3 axes.

If we make the justifiable assumption that mission 'users' will require a recurring, circular orbit with a repetition period of a specified N days, then we may write:

 $2\pi N = r I + \delta \gamma \qquad \qquad . \qquad . \qquad 2.11$

where

 $2\pi N$ = total Earth rotation in time interval I

 δ = precessional rate (radians per orbit)

 γ = total integer number of orbits in interval I (i.e. I = P γ)

N = integer 1, 2, etc.

Thus, the total effective terrestrial rotation under the orbit is jointly a function of P and the rate of orbit precession. To achieve recurrence this rotation must be equal to $2\pi N$ radians exactly, where N is integer valued.

From 2.6 and 2.7 it is possible to derive an expression for orbit inclination i; thus:

$$i = cos^{-1}$$
 $\frac{R^{3/2} - A}{B R_{e}^{2}}$ 2.12

where $A = \frac{N}{Yr} \checkmark GM$

 $B = \frac{3 J_2 \sqrt{GM}}{2 r R^2}$

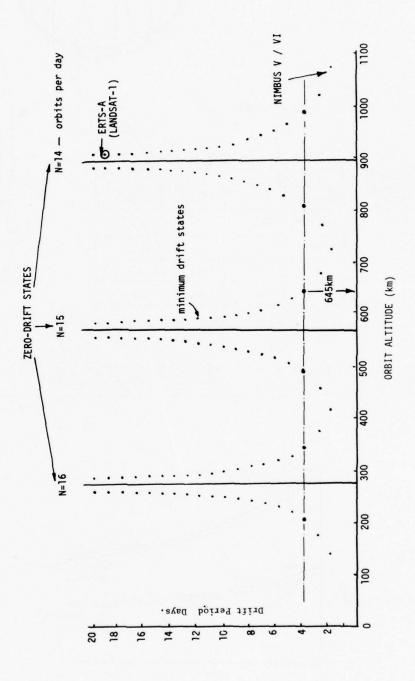
Re = Earth's radius

 $\rm J_2 = J_2$ coefficient in spherical harmonic expansion of Earth's gravity field - value depends on I and R.

Given values for N and γ and having specified a preferred range of orbit attitudes then the corresponding range of values for i can be determined. The recurrence interval I, as stated above, represents N integer multiples of effective terrestrial revolution, the precise value of I being dependent on the precessional rate of the orbit plane. For sun-synchronous orbits, for example, I is N multiples of a 'day' of exactly 24.00 hours duration (i.e. a solar day). For other than sunsynchronous conditions, the day will not equal 24.00 hours, although it will have a duration close to this figure.

When N = 1, then the orbit ground track pattern repeats itself within the minimum possible interval (approximately equal to 24 hours). This is known as the zero-drift state, the values of γ corresponding to this stage being integer-valued (equal to 15, 14, 13, etc.) and denoted by γ_Z^* in the discussion below. For an Earth observation satellite such an orbit will give the highest coverage frequency for any location in the ground pattern within the sensor swath. However, because the described track pattern is relatively sparse in coverage terms (see Fig.2.2-7) then the total extent of Earth coverage may be incomplete if the sensor swath cannot span the gap between adjacent subsatellite tracks. In fact, sensor swath widths of approximately 2,500 km would be required to do this, whereas it is not contemplated that the swaths of spaceborne PMR systems will be much more than 1,000 km maximum. Obviously, zero, drift orbits will not be suitable for PMR missions which demand complete global coverage.

^{*} γ_Z must be less than 16 for 'sensible orbit' - i.e. above Earth's atmosphere.



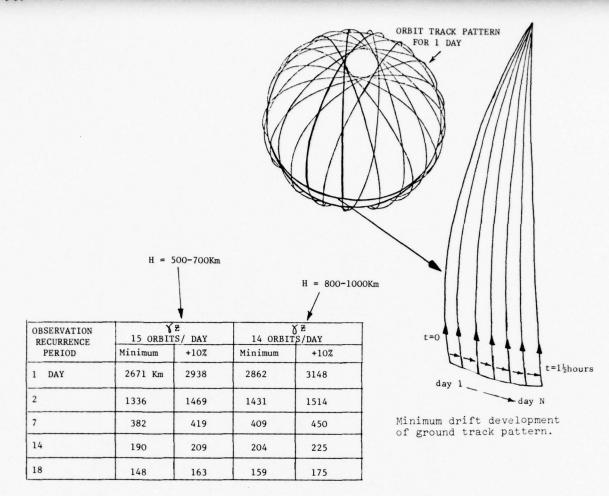


FIGURE 2.2-9: MINIMUM SWATH WIDTHS FOR VARIOUS RECURRENCE PERIODS

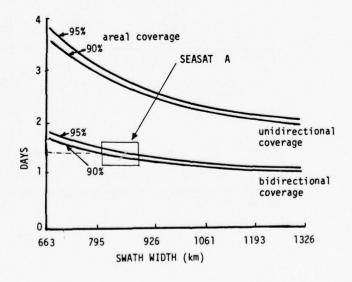


FIGURE 2.2-10: FOUR-DAY ORBIT : COVERAGE CHARACTERISTICS

When N is greater than unity, (i.e. the orbit exhibits and recurring pattern every N 'days') two significant states can arise depending on whether or not the condition:

$$\gamma = \gamma_Z \times N \stackrel{t}{=} 1 \qquad \qquad \dots \qquad 2.13$$

is satisfied by the orbits parameters. Once again, γ is the number of orbits executed within the recurrent interval I and γ_Z the number of orbits corresponding to a zero drift condition (i.e. γ_Z = 15, 14, 13, etc. depending on altitude).

The orbits for which the above condition holds true are, from equations 2.6 to 2.9, obviously distributed in altitude around that altitude at which γ_Z has a particular integer value. Their principal characteristic it that the subsatellite tracks are adjacent on a daily basis the pattern of these tracks being built up in an orderly fashion to pattern completion every N days. Such orbits are termed minimum drift and are used extensively in Earth observation missions to allow Earth coverage to be obtained in an orderly and progressive way. If the orbit and sensor swath width are correctly adjusted then one can, in fact, make the daily adjacent swaths associated with the subsatellite tracks contiguous or overlapping thereby allowing unbroken and complete Earth coverage. Figure 2.2-8 illustrates the distribution of low altitude zero-drift and minimum-drift orbits which are also sun-synchronous. Figure 2.2-9 gives the values of swath width W necessary to provide contiguous Earth coverage for several selected recurrence periods. Note the slight difference in swath width for different values of the associated γ_Z (14 and 15).

If the condition in 2.9 does not hold then the above minimum drift pattern does not develop. Given any ground location, then the satellite ground track (and sensor swaths) will appear to 'jump' easterly or westerly on a 'daily' basis and the N 'day' recurrence pattern will not be built up in a progressive, daily adjacent pattern. There are many such orbits for sun-synchronism conditions or otherwise. So far, studies have not revealed any particular demand for this type of recurring orbit. The possibility of their use is not ruled out, however.

Given that for the PAMIRASAT system a sun-synchronous, minimum drift orbit has been selected, then the choice of repetition period must be a compromise between the dynamic behaviour of the intended observables and the spatial and radiometric resolution required from the spaceborne PMR instrument. For example, a very brief repetition period of say, two days would demand wide sensor swaths (1300 - 1500 km). Since a PMR scanner would have to operate (i.e. scan) very rapidly to cover this swath width in a continuous fashion as the spacecraft moved over the Earth's surface then the integration times per resolution cell may be unacceptably low (see 2.2.3). Relaxation of achieved spatial resolution may then be the only way of retaining usable radiometric performance. In the PAMIRASAT case an N = four days orbit was selected.

This orbit has its ground track crossing the equator at a distance of 2,650 km apart, with the pattern advancing by 660 km each day. This giving total global coverage after four days with a sensor swath width of 660 km. However, due to the overlapping of swaths at non-equatorial latitudes much of the Earth is seen at more frequent intervals, particularly if both ascending and descending tracks are used (day and night). This effect becomes even more pronounced if a swath wider than 660 km is used, and this effect is shown in Figure 2.2-10. From this it can be seen, for instance, that for a 900 km swath width, using ascending and descending passes, 97% of the Earth surface will be seen approximately in 1.5 days.

It should be noted, of course, that there is no way, without going to geosynchronous altitude, whereby one part of the Earth's surface can be given increased coverage at the expense of other parts. The only way, therefore, to get very frequent surveillance of a particular area is by the use of repeated imaging using a multi-satellite system.

3 DESCRIPTION OF A POSSIBLE SATELLITE BORNE PMR SYSTEM

3.1 BACKGROUND

In 1974 BAC, in association with the Technical University of Denmark (TUD), was awarded a contract by ESA (European Space Agency) for a preliminary study of a possible operational spaceborne PMR system (PAMIRASAT - PAssive MIcrowave RAdiometry SATellite). A further study contract was awarded on completion of the above with work finally being completed on December 1976.

The principle aim of these activities was to assess the future potential for spaceborne PMR systems and to assess the mission, instrument design, technology and developmental consequences of system which represented a significant performance advance on the SMMR instrument to be carried on NASA's NIMBUS-G (launch 1978) and SEASAT-A (Launch 1979).

This paper utilises some of the results of the above PAMIRASAT Studies to illustrate the following:-

- (a) The ways in which the system variables described in the previous section have been reconciled to meet a particular mission aim and to briefly illustrate some of the considerations which designs at system level must take into account.
- (b) To show the potential performance of such a system.

It must be stressed that the aim of the system was measurement of ocean, ice and atmospheric parameters with the object of providing data for global weather and climate models to improve short and long term weather forecasting. While this does not strictly fall within the scope of 'surveillance', it serves as an example of the potential and limitations of Spaceborne PMR. Moreover, because of the strictly limited spatial resolution available, this is probably the most realistic application of PMR; the characteristics of such a system using an aircraft platform are discussed briefly in the final section of this paper.

3.2 SYSTEM DESIGN AIMS

As indicated above the aim was to derive a system having a performance significantly better than those planned, and which would provide data for world meteorology not otherwise obtainable on an all weather basis. Quantified, these aims could be stated as:

- Achievement of high area coverage rates compatible with useful observation of Earth's oceans and atmosphere, say every 1-2 days.
- 2. Incorporation of multi-channel reception necessary for the recognition of the complex microwave signatures associated with ocean and atmospheric media and to make measurements of their physical state.*
- Achievement of high spatial resolution to permit a wide range of potentially useful Earth observation missions, e.g.
 - of the order of 10s of kilometers for measurements of sea surface temperature and wind speed.
 - to make measurements of sea ice boundary to an accuracy of 10 km.
 - to make measurements of atmospheric water vapour, liquid water and temperature profile at a resolution of some hundreds of kilometers (200-300).
- 4. Achievement of high radiometric sensitivity to allow a usefully wide measurement capability within the range of potential missions: e.g.
 - Measurement of sea surface temperature to an accuracy better than $1^{\circ} {\rm K}$ over a wide range of weather conditions.
 - To measure wind speeds (not direction) with an accuracy of 1-2 m/sec (over ocean surfaces).

Of the above aims it is considered that 1 and 2 are basic to any useful oceans/ atmosphere survellance PMR and thus must generally be met, irrespective of the precise system design. Although aims 3 and 4 should also be met simultaneously, it is not easy to achieve this ideal in the real world since they tend to imply conflicting engineering demands. The reasons for this conflict have been outlined in Section 2, but specifically:

- AIM 3: The achievement of high spatial resolution requires narrow antenna beam widths and thus large antennas. To preserve contiguity of scans for retention of complete imaging performance, a high scan rate would be necessary and this implies a lower dwell or integration time per resolution cell. Thus, increasing spatial resolution will tend to degrade achievable radiometric sensitivity.
- AIM 4: Examination of the fundamental radiometer equation (Eq.2.1.) will show that improved radiometric sensitivity (a numerical decrease in $\Delta T)$ can be achieved by increase in bandwidth β improvement in receiver noise figure T_S or increase in integration time $\tau.$ Now, the upper value to β may be constrained by limitations to usable channel width (to the quiet but narrow radio-astronomy bands) and reduction in T_S limited by available, space-qualified technology. Improvement in integration time is thus the most readily available strategem open to designers. It is clear therefore that this can be achieved by reduction in antenna scan or rotation rate.

^{*} Analysis has indicated that up to five frequency channels are necessary in the 5 to 40 GHz band for satisfactory measurement of ocean and atmospheric observables. A provisional selection has indicated channels centred about the following frequencies - 4.995, 10.69, 15.375, 23.8 and 31.4 GHz. These channels were selected both on their inherent applicability to measurements of the desired observables and the fact that they coincide with the quiet radio-astronomy bands (see Section 2.2.2). Dual polarisation reception is generally required on each channel.

Since we have elected to adhere to the overall requirements for good Earth surface coverage rates at full imaging performance then we can only meet the need by relaxing achievable spatial resolution demands - contrary to the 3rd design aim.

By virtue of the incompatible requirements implicit in 3 and 4, we will tend to produce two categories of radiometer design for achievement of enhanced spatial resolution on the one hand and enhanced radiometric performance on the other. The engineering problem is, on the face of it, to produce designs which represent acceptable compromises.

3.3 BASIC DESIGN ALTERNATIVES

3.3.1 Introduction

The conclusion in 3.2 can best be illustrated by attempting to evolve design options which are biased towards either the achievement of high spatial resolution or the retention of high radiometric sensitivity with the overall constraints being the need to achieve each of these with practical, spaceflable systems. Let us take the most persuasive constraint to practicality as being a limitation as far as is possible to the number of separate antennas incorporated in the spaceborne PMR instrument. This is reasonable from the point of view of easing spacecraft configuration design. In addition, the system must be multi-channel in nature with swath widths in the region of 1000 km.

Consequently, Section 3.3.2 examines the capabilities of systems based on a single rotary or reciprocating scan antenna configured to achieve either high spatial resolution or high radiometric sensitivity.

3.3.2 Single Antenna Systems

The extremes of possible variation are displayed on Figure 3.3-1 and assume restriction to the available radioastronomy bandwidth and the use of receiver noise figures estimated as likely in the early 1980s.

The instrument designs are conditioned by either one of two factors:

- Achievement of high spatial resolutions of the order of 10 km (see Section 3.2). This is at least a factor of 2 better than the maximum resolution obtainable from the SMMR device on NIMBUS-G and SEASAT-A.
- Achievement of near $0.1^{\circ}k$ radiometric sensitivity (ΔT) on as many of the frequency channels as possible. Modelling work has indicated that such sensitivities are especially important for the lower frequencies in the band (particularly 4.996 GHz for sea-surface temperature measurement).

The radiometers conceived are necessarily multi-frequency in design and cover a 6:1 frequency range. Since a single antenna aperture is being utilised it is inevitable that there will be a similarly wide variation in antenna 'footprint' size (with frequency) on the sea-surface. This presents us with the problem of selecting the frequency at which the desired 10 km resolution level is to be achieved. It should be noted that the off-axis performance of antennas is limited and ideally the antenna feed should be a multi-frequency design capable of simultaneously generating a pattern of concentric, on-axis reception beams.

Examining Figure 3.3-1 we can state:-

OPTION A - High Spatial Resolution

From the point of view of practicality the 10 km spatial resolution is only achievable at the high end of the frequency band. Even so, this results in antenna diameters of the order of 2 metres - the antenna requiring solid not mesh construction to ensure adequate radiometric performance. Thus, achievement of 10 km resolution at 30 GHz implies only 60 km resolution at 5 GHz. The relatively poor radiometric performance, particularly at the higher frequencies, should be noted and an important additional point is that the antenna scan rate is based on achieving contiguity of scan lines at the highes frequency. This means that integration times at lower frequencies are less than optimum since in relative terms, the antenna is scanning 'too rapidly' for these frequencies (see Section 2.2.3).

OPTION B - High Radiometric Sensitivity

The aim is to achieve radiometric sensitivities of, or near, 0.1° K throughout the band and yet retain contiguity of scan lines at the highest frequency. These requirements result in the given design. Since the spatial resolution must be degraded to give slow scan rates then the antenna diameter is small (30 cm). The poor spatial resolution performance, particularly at the lower frequencies should be noted.

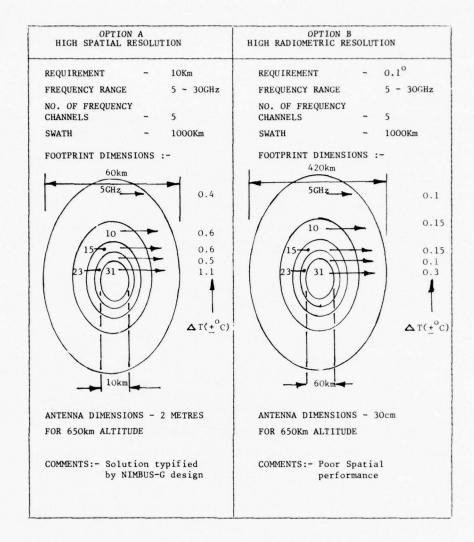


FIGURE 3.3-1: DESIGN EXTREMES FOR SINGLE ANTENNA SYSTEMS

Each of the two schemes above put emphasis on one aspect of performance rather than the other. In order to simultaneously realise acceptable spatial and radiometric levels it would be necessary to adopt Option A and to reduce antenna scan rates by incorporating multiple beams at each frequency. The effective footprint size used for deriving scan rates would not now be that of a single beam at the highest frequency but rather that of the larger footprint 'cluster'. If the number of beams perfrequency channel was chosen correctly and appropriate beam orientations were used then the scan rate could in fact be bought to, or near, optimum for each frequency. The penalty paid is, of course, greater feed complexity and the need to incorporate a great deal more receiver channels in the system.

Short of adopting the above tactic and/or significantly relaxing bandwidth constraints it must be accepted that designs which bridge the gap between the extremes discussed above will be based on the use of more than one antenna.

3.3.3 Multi-Antenna Systems

There are several possible approaches typical of which are based on:

(i) 'patching up the radiometric performance deficiencies in Option A (above) whilst retaining 'high' spatial resolution.

(ii) adopting designs which utilise more than one antenna in an attempt to equalise footprint dimensions throughout the frequency band thereby rendering an optimum integration time at each frequency for the spatial resolution levels selected. It is possible (see below) to obtain radiometric sensitivities similar to Option B (above) at much improved average spatial resolution.

As stated in 3.3.2, modelling work has indicated that for measurement of the important sea-surface parameters, radiometric sensitivities of, or near 0.1 K are highly desirable on the 4.995 channel. Consequently, in (i) above, the approach is to remove the 4.995 GHz channel from the large (2 metre) scanning antenna and incorporate it in a separate antenna or antenna system whose observational mode directly gives very good radiometric sensitivity. Thus, we have:

- OPTION C: OPTION A + profiling (non-scanning) reception at 4.995 GHz. A design has been proposed which utilises 3 fixed beams giving coverage strips distributed across the swath generated by the scanning, 2 metre, dish. Note that animage would not be obtained at 4.995 GHz. However, the extra high radiometric sensitivity obtained on the 4.995 GHz channel would allow improvements on sea-surface parameter measurements relative to the original Option A.
- OPTION D: OPTION A + separate slow scan antenna operating at 4.995 GHz to give an image covering the 1000 km swath at high radiometric sensitivity. This image would be superimposed on the multi-frequency image obtained by the remaining channels on the large scanning dish.
- OPTION E: This option derives from approach (ii) stated above. Through detailed modelling work it became evident that for useable measurement of the principal sea-surface parameters the effective spatial resolution achieved was weighted towards that resolution obtained on frequency channel contributing most effectively to the measurement.

For parameters such as sea-surface temperature and wind-speed this meant that the 10 km spatial resolution achieved at the higher frequency was relatively ineffective since the lower frequencies were more important to the quality of the measurement than the higher. This implied that even in Option A, sea-surface temperature distribution could only be mapped with spatial resolution nearing 60 or so kilometers since this was the spatial resolution obtained on the 4.995 GHz channel. This result suggested that a radiometer could be designed which utilised more than one antenna and gave a mean resolution of 60 km on each frequency channel. The scanning rate and thus the integration times would then be near optimum for all channels. A feasible solution has been shown to consist of two antennas of respectively 1.6 metres (4.995 and 10.69 GHz) and 0.5 metres (15.373, 23.8 and 31.4 GHz) diameter and which gives very high radiometric sensitivity on all channels. Since each antenna will continue to operate over several frequency channels the footprint dimensions will still be different. However the difference in dimensions will be much less than in Option A since the frequency band will be divided between the two antennas. The result is a much improved measure-ent performance for principal sea-surface parameters (temperature and wind field) relative to Option A (in terms of radiometric resolution) and Option B (in terms of spatial resolution). In addition there are advantages from the engineering point of view since unlike the other PMR options the high frequencies operate off the smaller antenna and the low frequencies off the larger. This makes antenna and feed design relatively easier. The penalty paid is the poor spatial performance for measurements of highly visible observables such as sea-ice which for mapping purposes in Option A based designs do not require the predominance of the lower frequency channel in the measurements and thus could successfully utilise the 10 km spatial resolution on the 31 GHz channel.

It is worth noting here, however, that if the PMR constituted part of a spaceborne ocean surveillance package which also contained, for example, a Synthetic Aperture Radar (SAR), the lack of the 10 km spatial resolution capability for sea-ice edge mapping by the PMR may not be a disadvantage since this function could be accomplished by the SAR to a resolution measurable in metres and much more applicable to the surveillance needs of navigation and related tasks. The PMR could then, as in the Option E, be optimised for other tasks for which the 10 km resolution was not so important.

The above radiometer options are illustrated in Figure 3.3-2 with Options A and B taken as the design starting points. Antenna dimensions and configurations are shown along with achievable radiometric performance.

Now it should be understood that, although all these options are based on firm prescriptions for observation mode, swath width, bandwidth and design approach, other possibilities do exist if we are prepared to relax the constraints. For example, starting from Option E, considerable improvements in directly achievably

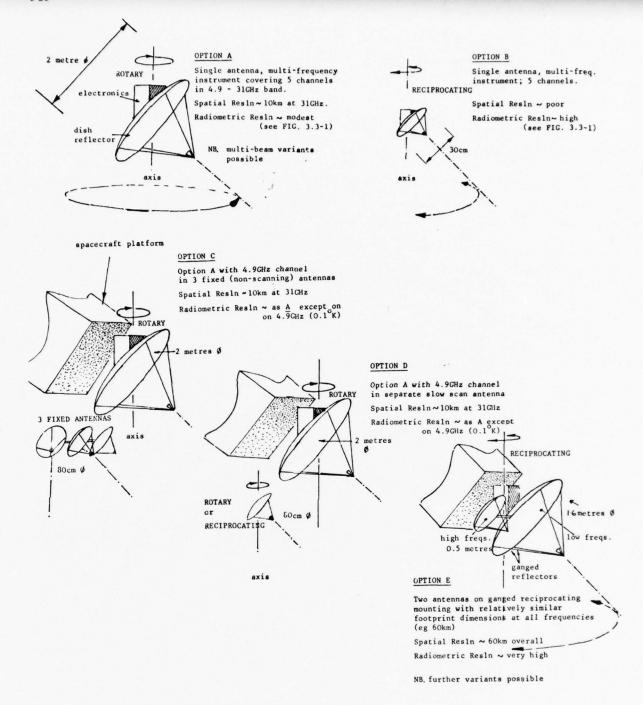


FIGURE 3.3-2: TYPICAL PMR OPTIONS

spatial resolution at similar radiometric sensitivities could result from application of the following:

- Increase in antenna size to allow narrower antenna beam widths.
- Incorporation of multiple beams (see 3.3.2) to minimise increases in required scan rate.
- Increase in receiver bandwidth retain good ATs
- Narrowing of swath width to minimise increases in required scan rate.

If we take, for example, a two-fold increase in β , narrow the swath from 1000 to say 650 km, and incorporate two receive beams per channel, spatial resolution performance could improve from the 60 km (mean) quoted above to around 25 km (mean). The high (0.1 k) radiometric sensitivity would be retained with the consequent high measurement performance for sea-surface parameters. If the same observation

Temperature o		5					20				
Wind	m/s	0	10	20	30	0	10	20	30		
Foam	7.	0	3.56	15.23	44.89	0	3.56	15.23	44.89		
OPTION A	Α	.587	.615	.692	.955	1.039	1.066	1.132	1.326		
	В	.834	.881	.985	1.273	1.480	1.531	1.616	1.779		
	C	1.561	1.640	1.806	2.212	2.775	2.839	2.943	3.111		
	D	4.590	4.669	4.787	5.016	8.710	8.671	8.528	8.223		
OPTIONS	A	.363	.374	.406	.513	.875	.875	.866	.828		
C & D	В	.528	.547	.590	.706	1.175	1.176	1.152	1.070		
	C	.934	.988	1.098	1.363	1.908	1.929	1.954	1.992		
	D	2.539	2.689	2.964	3.546	5.775	5.828	5.875	6.063		
OPTIONS	A	.161	.170	.195	.302	.305	.319	.361	.482		
B & E	В	.297	.315	.351	.447	.591	.628	.628	.722		
	C	.462	.477	.516	.632	1.033	1.038	1.038	1.063		
	D	1.541	1.612	1.751	2.030	3.280	3.283	3.240	3.105		

TABLE 3.5-1: STANDARD DEVIATION ON SEA-SURFACE TEMPERATURE ESTIMATION.

Temperature ^O C		5				20				
	ind m/s pam %	0	10 3.56	20 15.23	30 44.89	0	10 3.56	20 15.23	30 44.89	
At	tmos:									
OPTION A	A	1.144	1.179	1.410	2.741	1.982	1.992	2.263	3.787	
	В	1.562	1.623	1.950	3.662	2.905	2.935	3.299	5.167	
	C	3.061	3.156	3.734	6.642	5.838	5.807	6.361	9.444	
	D	9.575	9.518	10.407	15.547	19.387	18.705	19.309	25.789	
OPTIONS	A	.623	.636	.738	1.318	1.531	1.494	1.574	2.151	
C & D	В	.843	.868	1.025	1.845	2.114	2.064	2.156	2.883	
	C	1.580	1.655	2.020	3.814	3.731	3.677	3.963	5.784	
	D	5.166	5.348	6.302	10.900	12.758	12.470	13.185	18.892	
OPTIONS	A	.303	.308	.351	.652	.507	.518	.612	1.120	
B & E	В	.342	.358	.438	.888	.860	.896	1.053	1.652	
	C	.684	.699	.811	1.476	1.805	1.759	1.850	2.662	
	D	2.969	3.052	3.577	6.079	7.014	6.826	7.113	9.562	

TABLE 3.5-2: STANDARD DEVIATION ON SEA-SURFACE WIND SPEED ESTIMATION.

angle (40°) and orbit altitude (650 km) were retained antenna diameter would require increase by just over a factor of 2 to 3.2 metres (4.995 and 10.69 GHz) and 1 metre (15.375, 23.8 and 31.4 GHz) respectively.

Increase in diameters of less than this could be achieved if smaller observation angles were permissible. For example, reduction of observation angle α of say 27° would reduce the range by a factor of 1.6 and still allow a near 650 km swath width with either rotary or reciprocating systems. Antenna dimensions would then only increase by a factor of 1.2 relative to the 60 km resolution case and this would result in 'new' antenna diameters of 2 metres and 1.2 metres respectively.

In comparison with Option A, derived options and the NIMBUS-G SMMR the above design could result in a system which simultaneously gave considerably better spatial resolution and measurement accuracy.

Section 3.5 discusses the 'all weather' measurement performance of the above radiometers for sea-surface temperature and wind speed.

3.4 ASSESSMENT CRITERIA

In order to provide data which studies of the PAMIRASAT PMR could use in design optimisation the Technical University of Denmark modelled the complete sea/atmospheric/measurement system so that the performance of different combinations of radiometer characteristics could be assessed, particularly as regards provision of useful measurements in the presence of intervening 'weather'. In order to reduce this admittedly complex situation to something which could be tackled within the limitations of the study, four cases were selected as representing increasingly worsening weather conditions. These cases are specified in Table 3.4-1.

	State	Cloud Base km	Cloud Thickness km	Water gm/m ³	Rain mm/h	"Excess" Statistics Ascension Island
Α.	Clear Sky	-	_	0	0	90%
В.	Alto-Stratus	2500	1000	0.2	0	60%
C.	Nimbo-Stratus	500	3000	0.3	2	1%
D.	Cumulonimbus	1000	5000	0.6	10	0.1%

TABLE 3.4-1:

WEATHER STATES

The performances of the various radiometer packages, represented for the purposes of this paper by Option A to E, were assessed in terms of measurement capabilities for:-

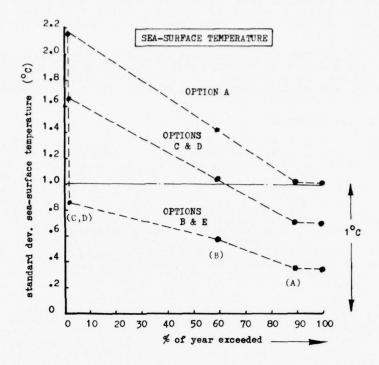
- (a) Sea-surface temperature
- (b) Sea-surface wind speed.

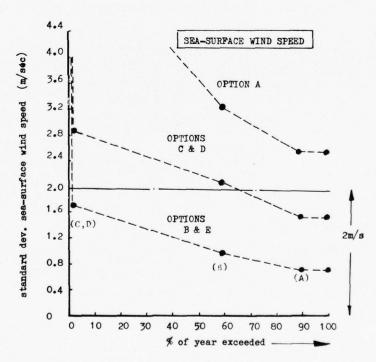
The hypothetical assessments were made assuming the presence of the above 'weather' states along the line-of-sight and were expressed as measurement standard deviations

In order to place the derived measurement accuracies into a weather context, the excess annual rainfall statistics of Ascension Island (representative of a mid-latitude, maritime location) were available and were used to convert the above four weather states into excess annual PMR measurement statistics. Obviously this approach has its limitations. There is no clear, quantificable correlation between rain-rate, cloud water content and atmospheric water vapour. Nevertheless, there is a strong correlative tendency between these factors.

The following were taken (see Table 3.4-1):

- Clear Sky Conditions (A):
 - The excess level for this lies somewhere between 100% and the mean cloud-cover value. Condition (A) verges on the 'idyllic', in terms of subjective weather assessment, and will therefore lie very near the 100% excess level (say 90%).
- Light Cloud (B):
 - The ocean area in the South Central Atlantic near Ascension Island has cloud cover in excess of 60% annually.
- Rain Conditions (C) and (D):
 - The excess measurement statistics for 2 and 10 mm/hr are equated in terms of occurrence to the excess rainfall statistics for the Ascension Island location (1% and 0.1% levels respectively).





ASSUMED CONDITIONS: Sea-Surface Temp. 15°C Sea-surface Wind 15m/sec.

FIGURE 3.5-1: SIMPLE PERFORMANCE ASSESSMENT OF OPTIONS A TO E

5-24

It should be emphasised that this tentative analysis is likely to be optimistic in its conclusions and does not, for example, include the influence of finite absolute accuracies. The usefulness lies in showing the relative merits of the various PMR options.

However, in addition to an assessment of performance in terms of measurement sensitivity, the value of spatial resolution, repetition rate and imaging versus profiling ability need to be assessed. The relative value of these have not been quantified, and therefore represent additional factors in assessing the overall 'figure of merit' for a given package.

3.5 COMPARISON OF PERFORMANCE

The results obtained from the simple performance assessment discussed in 3.4 are displayed on Figure 3.5-1 for Options A to E. The values taken for sea-surface temperature and sea-surface wind speed are, for this figure, 15°C and 15 metre/sec. Tables 3.5-1 and 3.5-2 list derived values of the measurement deviations for the PMR options A to E over a 5° to 20° sea-surface temperature range and a 0 to 30 metre/sec wind speed range. Note the inclusion of 'foam' as a percentage coverage. The incidence of foam is related to wind speed and has the effect of increasing sea-surface radiometric emissivity andthus apparent temperature. As would be expected, B and E give considerably better performances than A, C and D. In the sea-surface temperature case it is considered that measurement with standard deviations of greater than - 1°K rapidly decrease in potential useability as accuracy further diminishes. The 1°K level is therefore marked as a 'threshold' level. Likewise, the 2 metre/sec level is taken as 'the' threshold' in the wind speed measurement case.

The clear division of the various radiometer options into three groups should also be noted. In some senses this division is less real than apparent since one must bear in mind the mode of observation of each particular option. For example, Option D will give a better result than C since direct sea-surface temperature imagery is possible through the use of the 4.995 GHz. slow-scan antenna. This is not available on C with its fixed profiling dishes. In addition, between B and E, E is clearly the better since spatial res dution capabilities are maximised in relation to the achieved radiometric performance levels.

4 POSSIBLE CHARACTERISTICS OF AN AIRBORNE PMR SYSTEM FOR SURVELLANCE

4.1 GENERAL

As stated in Section 3, the resolution achievable from spaceborne PMR sytems will, certainly within the medium term, be measureable in terms of 10s of kilometers rather than in the 'metres' applicable to 'surveillance' in the strict military sense. Consequently, there appears no role for spaceborne PMR in the passive detection of military targets on the sea-surface on an all weather basis.

However, the situation may significantly change if we consider PMR systems operated from aircraft flying at altitude of 10 km or so.

In this section it is not intended to look in any detail at an airborne PMR system. Rather it is to 'scale' the satellite system described in the previous section and to try to indicate the principle resulting characteristics. Aircraft borne PMR systems have in fact been operated for several years, principally for scientific purposes. None of these have, however, been designed as an integrated system for an operational role, and few have carried radiometer at more than 2 frequencies.

4.2 AN AIRBORNE 'SATELLITE' PMR

In the brief analysis which follows, the rather sophisticated packages developed for the satellite borne system, will be examined to assess the effects of operating instead from an aircraft platform. The core of these packages is the large scanning antenna with multiple feeds at frequencies of 5 - 31 GHz. The effects of using an airborne platform for these packages are given below.

Assumptions

Scanning geometry and frequency coverage are assumed to be for the packages described in Section 3. The aircraft speed and altitude are assumed to be approximately 500 K TAS and 30,000' respectively. These are compared with the satellite values below:

	Satellite	Aircraft
Speed v	7 km/sec	0.26 km/sec
Altitude	645 km.	10 km

Spatial Resolution, Swath Width

These scale as the ratio of operating altitudes. Typical values of the principal antenna and scanning geometries considered are given below. (Scan cone angle 42°). Note that Option A based PMR packages are considered here.

	Satellite	Aircraft
Altitude (km)	645	10
Total Swath Width (km)		
(a) Full conical scan(b) 30° Reciprocating	1200 600	18.6 9.3
Spatial Resolution (km)		
2m dia. Antenna, 5 GHz 37 GHz	51 6.3	0.8
0.8m dia.Antenna, 5 GHz 27 GHz	128 15.8	2.0 0.24

Radiometric Temperature Resolution

From Equation 2.1, the radiometric brightness temperature resolution varies as:

1/т

where τ is the integration time for one IFOV.

For complete conical scan of rotation rate R, τ is given by Equation 2.6.

From the latter it can be seen that:

$$\frac{Ta}{TS} = \frac{da}{ds} \cdot \frac{vs}{va}$$

where suffix 'a' refers to aircraft and suffix 's' to satellite.

= 0.42, using the values assumed above, i.e. approximately half.

The values of Δ Ts for the airborne system will, therefore, be increased by a factor of approximately $\sqrt{2}$. That is, the system sensitivity will decrease due to the disproportionate changes in altitude and footprint dimension (and thus scan rate).

4.3 CONCLUSIONS

It can be seen that the spatial resolution achievable from an aircraft operating at typical altitudes of 10 km are much more likely to represent some possibility for use of PMR for ocean surveillance. For instance using the radiometer package (E) of Section 3 standard deviations of 0.50 and 1.00 sea-surface temperature measurements could be achieved under weather conditions (b) and 20 m/sec. surface wind speed, for water temperatures of 5° C and 20° C respectively. These measurements could be associated with a 1 kilometer footprint size. This type of performance might be capable of detecting local 'hot spots' generated by submerged submarines. Similarly, at the higher resolutions possible with larger antennae, it might be possible to detect the presence of ships as temperature anomalies, in spite of the rather poorer temperature sensitivity. For instance, a ship of 200 mm x 10 m appearing in the footprint of a 5 GHz antenna of 2 m dia. and having temperature difference of 50° K from the surrounding sea, would be indicated as a temperature anomaly of 0.25° relative to the footprints immediately adjacent to it. This would appear to indicate that a fairly large ship would be on the limits of detectability.

The latter would be improved by using a reciprocating scan of reduced swath width to increase integration time, possibly associated with an increased bandwidth. It is also probable with such targets that the mix of frequencies for best performance will be different to those developed for collecting basic ocean/weather data.

There is insufficient data to predict the detectability of such targets using PMR but the 'first order' assessment indicates that the system sensitivity is such as to warrant a more detailed study.

A final characteristic of such a system is the time required to sweep a given area Using the figures given earlier for speed and altitude, and a swath width of $18.6~\rm km$ (implying full conical scan) an aircraft borne system could cover an area of $17,400~\rm km^2$ in an hour. This would be reduced in the ratio of the swath widths if the reciprocating scan is used to increase integration time.

INFRARED RADIOMETRY AND VISIBLE SPECTROMETRY

Henri Hodara and Willard H. Wells
Tetra Tech, Inc., 630 North Rosemead Boulevard, Pasadena, California 91107

ABSTRACT

Measurements of very small temperature changes in the top millimeter of the sea surface by infrared radiometers are capable of indicating natural or man-made disturbances at some depth. We derive an equation that describes radiometric temperature fluctuations and identifies two major sources of error that mask the true sea temperature changes: humidity fluctuation in the air column between the sea surface and the radiometer, and reflected sky radiance from the rough sea surface. These masking effects are minimized by suitable design of the radiometer. Typical power spectra calculated from radiometric measurements are presented.

Visible spectrometry measures spectral changes in ocean upwelling radiance that take place on the sea surface and at some depth below it. We derive a general remote sensing equation and show how the two major sources of interference, sky reflection and atmospheric scattering are reduced by judicious selection of altitude and viewing angles. The results are applied to measure changes in upwelling radiance caused by man-made disturbances. Comparison and agreement with theoretical predictions are presented.

In this lecture we discuss the underlying principles and techniques of radiometric detection of man-made disturbances on the ocean surface. The disburbances, of a complicated nature, affect the upper layers of the ocean in various manners: changing the temperature of the top millimeter of the sea surface, altering the spectral transmissivity of sea water, hence its color. The physical mechanisms responsible for their generation are not the subject of these lectures; instead we concentrate on the principle of detecting them remotely and describe the implementation of the measurements.

Minute temperature changes of the order of millikelvins are detected with a sensitive infrared radiometer specifically designed for this purpose. A description of its operation, limitations and results of sea tests are given in Part I of this lecture.

The color changes are measured with a conventional narrow-band spectrometer that scans the visible spectrum continuously. Although the technique is more weather-limited than infrared, it does have the advantage of sensing at greater depths. The pertinent analyses and results of at-sea measurements form Part II of this lecture.

Part I: INFRARED RADIOMETRY

In what follows, we first discuss our approach to measurements at a distance of very small radiometric temperature fluctuations on the ocean surface. We proceed to analyze the source and magnitude of the errors introduced by the sea state and the atmosphere; finally we calculate the theoretical performance and fundamental limitations of an infrared radiometer capable of sensing temperature fluctuations of the order of millikelyins.

1.0 Sea Surface Radiometry

Let us describe first the type of instrument and mode of operation best suited for sensing small variations in sea surface radiometric temperature. The radiometer operates from a low altitude (as low as 100m) aircraft, at two wavelength bands centered at 10.6 μ m and 3.8 μ m; it has a temperature resolution of 10^{-3} K. At each wavelength the relative optical bandwidth is approximately 10%. The 10.6 μ m band extends from 10.0 μ m to 11.1 μ m; the 3.8 μ m from 3.6 μ m to 4.1 μ m. The bands are in those portions of the spectrum least affected by atmospheric absorption in the air column along the line

of sight of the instrument. As shown in Fig. 1, the 10.6 μm is chosen because it is least affected by atmospheric absorption; however, it is sensitive to fluctuations in water vapor and to compensate for it, the additional 3.8 μm band is used. Note that this band is also little affected by atmospheric absorption. Since an absorber is also a radiant emitter, the low absorption prevents the air temperature from masking that of the sea.

The temperature is measured by comparing the radiant flux received from the sea against a stable reference blackbody in the instrument. When the instrument looks at the sea, it cannot distinguish the various components of radiant flux collected by its aperture; in particular it cannot separate the flux emitted by the water and indicative of its surface temperature, from the sky flux reflecting off the water into the radiometer. As a result the radiometric estimate of the sea surface temperature is in error. To reduce the error, the radiometer looks sequentially at sea, sky and reference blackbody. The difference between sea and sky readings yields the net flux emitted by the ocean, provided one knows the sea reflectivity as a function of angle. The net flux is then converted to the equivalent blackbody temperature of the sea surface. We shall see in the next section that there are additional errors caused by fluctuation of water vapor and temperature along the line of sight, but they are negligible because the instrument optical bandwidth is sufficiently narrow to avoid the skirts of the atmospheric absorption bands. Narrow bandwidths are usually accompanied by decreased sensitivity; the latter is avoided by cooling not only the detector but also the instrument housing and optics. This is discussed further on.

We mentioned above that the sea surface temperature can be obtained from measurements of sea and sky flux provided that the water reflectivity is known. Other sensors such as lasers measure reflectivity and its dependence on angle and sea state. We shall see further on how the effects of sea state are taken into account; on the other hand the angular dependence of the sea reflectivity $\rho(\lambda)$ is well established, it is shown in Fig. 2. Note that the water emissivity, ϵ is simply

$$\varepsilon = 1 - \rho$$
 (1)

We shall use Fig. 2 and Eq. 1 in our future calculations.

2.0 Sources of Radiometric Temperature Errors

The effort reported here concentrates on two sources of error: fluctuation in sky radiance reflected from the sea surface, and temperature and humidity fluctuations in the air column between the radiometer and the sea. Errors due to water emissity or reflectivity changes caused by sea state and other factors can be accounted for by measuring the reflection coefficient as a function of angle with a laser reflectometer located in the airplane carrying the radiometer.

2.1 Fundamental Radiometric Equation

To derive the sources of error, we apply the fundamental radiometric equation to the geometry of the problem. The simplified geometry is shown in Fig. 3, with the three components of flux seen by the radiometer

$$\mathcal{N} = \mathcal{N}_{W} + \mathcal{N}_{S} + \mathcal{N}_{A} \tag{2}$$

The script \mathcal{N} denotes respectively water, sky and air radiance measured at the radiometer. Errors caused by fluctuations in sky and air radiance lead to the error equation:

$$\Delta N_{\rm p} = \Delta N_{\rm s} + \Delta N_{\rm a} \tag{3}$$

In the following we derive estimates of the magnitude of these errors; we shall see that the residual sky error is due to changes in cloud aspect angle, $\Omega_{\rm c}$

$$\Delta N_{s} = \frac{\partial N_{s}}{\partial \Omega_{c}} \Delta \Omega_{c}, \tag{4}$$

and air column errors are caused by air blobs of slightly different temperature $\mathbf{T}_{\mathbf{b}}$ and attenuation $\alpha_{\mathbf{b}}$ that are responsible for temperature and humidity fluctuations:

$$\Delta \mathcal{N}_{\mathbf{a}} = \frac{\partial \mathcal{N}_{\mathbf{a}}}{\partial \mathbf{T}_{\mathbf{b}}} \Delta \mathbf{T}_{\mathbf{b}} + \frac{\partial \mathcal{N}_{\mathbf{a}}}{\partial \alpha_{\mathbf{b}}} \Delta \alpha_{\mathbf{b}} = \frac{\partial \mathcal{N}_{\mathbf{a}}}{\partial \mathbf{T}_{\mathbf{b}}} \Delta \mathbf{T}_{\mathbf{b}} + \frac{\partial \mathcal{N}_{\mathbf{a}}}{\partial \alpha_{\mathbf{b}}} \frac{\partial \alpha_{\mathbf{b}}}{\partial \mathbf{w}} \Delta \mathbf{w}; \tag{5}$$

w stands for the water vapor content of the air column.

2.2 Air Column Errors

They are caused by fluctuations along the radiometer line of sight, between the aircraft and the sea surface. These fluctuations are primarily due to random variations in humidity and temperature. Humidity fluctuations induce a change in the path attenuation, $\alpha_{\rm b}$. The situation is depicted in Fig. 4; a blob of warmer air and higher absorptivity described by temperature $T_{\rm b}$ and attenuation $\alpha_{\rm b}$ crosses the radiometer line of sight. The radiometer senses a total radiance,

$$\frac{\mathcal{N} = \overline{\rho} N_{\mathbf{S}} \tau_{1} \tau_{2} \tau_{3} + \varepsilon_{\mathbf{B}} (T_{\mathbf{w}}) \tau_{1} \tau_{2} \tau_{3} + \varepsilon_{1} B (T_{\mathbf{a}}) \tau_{2} \tau_{3} + \varepsilon_{2} B (T_{\mathbf{b}}) \tau_{3} + \varepsilon_{3} B (T_{\mathbf{a}})}{\mathcal{N}_{\mathbf{a}}} \qquad (6)$$

The τ_i 's and ε_i 's are path transmittances and emittances, below the blob, through the blob and above it, respectively, and their derivation is given in Appendix A; $\bar{\rho}$ is the average water reflectivity that takes into account sea roughness. B is the blackbody function defined in Appendix B.

We recognize in the equation above the three components of flux of Eq. (2). The first term is the reflected sky radiance, \mathcal{N}_S measured by the radiometer. The second term, \mathcal{N}_W , is the sensed water radiance, and the last three terms make up the air radiance, \mathcal{N}_a . Since $\bar{\rho} \simeq .01 << \epsilon$, and sky radiance $N_S \leqslant B(T_W)$, (the water radiance given by the blackbody function at the water temperature T_W), \mathcal{N}_S is negligible compared to \mathcal{N}_W . Although sky reflections, as we shall see in the next section, contribute a large error when the sea is rough, their contribution to the air path error is swamped by the water signal, $B(T_W)$. Thus we can safely drop the first bracketed term in Eq. (6).

The path transmittances τ_1 , τ_2 and τ_3 can be written from inspection of Fig. 4:

$$\tau_{1} = e^{-\alpha [R - (r + \ell)]}$$

$$\tau_{2} = e^{-\alpha b^{\ell}}$$

$$\tau_{3} = e^{-\alpha r}$$
(7)

and the emittance of each path, as shown in Appendix A, is simply the total absorption for that path or one minus the corresponding transmittance:

$$\varepsilon_{1} = 1 - e^{-\alpha [R - (r + \ell)]}$$

$$\varepsilon_{2} = 1 - e^{-\alpha} b^{\ell}$$

$$\varepsilon_{3} = 1 - e^{-\alpha r}$$
(8)

The radiometric error due to air path fluctuations coming from changes in attenuation and temperature introduced by air blobs can be expressed as

$$\Delta \mathcal{X}_{\mathbf{a}} = \frac{\partial \mathcal{N}}{\partial \alpha_{\mathbf{b}}} \Delta \alpha_{\mathbf{b}} + \frac{\partial \mathcal{N}}{\partial T_{\mathbf{b}}} \Delta T_{\mathbf{b}}$$
(9)

Applying (9) to (6) after dropping the term $\bar{\rho}N_s$ we get

$$\Delta \mathcal{N}_{\mathbf{a}} = \left\{ \varepsilon \mathbf{B} \left(\mathbf{T}_{\mathbf{w}} \right) \left(-\ell \right) \tau_{1} \tau_{2} \tau_{3} + \varepsilon_{1} \mathbf{B} \left(\mathbf{T}_{\mathbf{a}} \right) \left(-\ell \right) \tau_{2} \tau_{3} + \varepsilon_{2} \mathbf{B} \left(\mathbf{T}_{\mathbf{b}} \right) \ell \tau_{3} \right\} \Delta \alpha_{\mathbf{b}} + \varepsilon_{2} \mathbf{B}' \left(\mathbf{T}_{\mathbf{b}} \right) \tau_{3} \Delta \mathbf{T}_{\mathbf{b}}$$

$$\tag{10}$$

We now introduce several simplifications into the preceding expression after expanding terms to first order.

$$\varepsilon \approx 1$$

$$\tau_{1} \approx \tau_{2} \approx \tau_{3} \approx 1$$

$$\varepsilon_{1} \approx -\alpha[R-r+\ell]$$

$$\varepsilon_{2} \approx -\alpha_{b}\ell$$

$$\varepsilon_{3} \approx -\alpha r$$

$$B(T_{w}) = B(T_{a}) + B'(T_{a}) (T_{w} - T_{a}) = B(T_{a}) + B'(T_{w}) (T_{w} - T_{a})$$

$$B(T_{b}) \approx B(T_{a})$$

$$\alpha_{b}\ell \approx \alpha\ell$$

$$(11)$$

After dropping second order products, $\alpha[R-(r+\ell)]$ $\Delta(\alpha_b^{\ell})$ small compared to $\Delta(\alpha_b^{\ell})$, and using the definitions

$$\Delta \alpha_{\mathbf{b}} = \alpha_{\mathbf{b}} - \alpha$$

$$\Delta T_{\mathbf{b}} = T_{\mathbf{b}} - T_{\mathbf{a}}$$
(12)

we have

$$\Delta \mathcal{N}_{\mathbf{a}} = \mathbf{B}' (\mathbf{T}_{\mathbf{w}}) \alpha \ell \left\{ \Delta \mathbf{T}_{\mathbf{b}} - \Delta (\alpha_{\mathbf{b}} \ell) (\mathbf{T}_{\mathbf{w}} - \mathbf{T}_{\mathbf{a}}) \right\}$$
(13)

Expressing the fractional change in α as an equivalent humidity change $\frac{\Delta w}{w}$,

$$\frac{\Delta \alpha_{\mathbf{b}}}{\alpha} = \frac{\Delta \mathbf{w}}{\mathbf{w}} \tag{14}$$

yields

$$\Delta \mathcal{N}_{\mathbf{a}} = \mathbf{B}' (\mathbf{T}_{\mathbf{w}}) \alpha \ell \left\{ \Delta \mathbf{T}_{\mathbf{b}} - (\mathbf{T}_{\mathbf{w}} - \mathbf{T}_{\mathbf{a}}) \frac{\Delta \mathbf{w}}{\mathbf{w}} \right\}$$
(15)

We shall express each change in radiance ΔN by an equivalent temperature change ΔT that would produce the same radiance change in a blackbody. This is convenient because the sea is almost black, and so we evaluate this conversion using the thermodynamic temperature of the first few feet of sea. Thus,

$$\Delta \mathcal{N} = \frac{\partial \mathbf{B} (\lambda, \mathbf{T})}{\partial \mathbf{T}} \Delta \mathbf{T} \equiv \mathbf{B'} \Delta \mathbf{T}; \tag{16}$$

The equivalent radiometric temperature fluctuation, ΔT , thus equals the change in radiance measured by the radiometer, divided by temperature derivative of the blackbody function, i.e.

$$\Delta T = \Delta \mathcal{N}/B' \tag{17}$$

Inserting (17) in (15), we obtain an expression for the radiometric temperature error caused by air path fluctuations

$$\Delta T_{a} = \alpha \ell \left\{ \Delta T_{b} - (T_{w} - T_{a}) \frac{\Delta w}{w} \right\}$$
(18)

Numerous experiments give the following typical values for the various parameters of Eq. (18):

$$\alpha_{3.8 \mu m} = 1.6 \times 10^{-5} \text{ ft}^{-1}$$
 $\alpha_{3.8 \mu m} = 1.6 \times 10^{-5} \text{ ft}^{-1}$
 $\alpha_{4.8 \mu m} = 6.6 \times 10^{-5} \text{ ft}^{-1}$

$$\alpha_{5.8 \mu m} = 6.6 \times 10^{-5} \text{ ft}^{-1}$$

$$\alpha_{5.8 \mu m} = 6.6 \times 10^{-5} \text{ ft}^{-1}$$

$$\alpha_{5.8 \mu m} = 1.6 \times 10^{-5} \text{ ft}^{-1}$$

$$\alpha_{5.8 \mu m} = 1.6 \times 10^{-5} \text{ ft}^{-1}$$

$$\alpha_{5.8 \mu m} = 1.6 \times 10^{-5} \text{ ft}^{-1}$$

$$\alpha_{5.8 \mu m} = 1.6 \times 10^{-5} \text{ ft}^{-1}$$

$$\alpha_{5.8 \mu m} = 1.6 \times 10^{-5} \text{ ft}^{-1}$$

$$\alpha_{5.8 \mu m} = 1.6 \times 10^{-5} \text{ ft}^{-1}$$

$$\alpha_{5.8 \mu m} = 1.6 \times 10^{-5} \text{ ft}^{-1}$$

$$\alpha_{5.8 \mu m} = 1.5 \times 10^{-5} \text{ ft}^{-1}$$

$$\alpha_{5.8 \mu m} = 1.5 \times 10^{-5} \text{ ft}^{-1}$$

$$\alpha_{5.8 \mu m} = 1.5 \times 10^{-5} \text{ ft}^{-1}$$

$$\alpha_{5.8 \mu m} = 1.5 \times 10^{-5} \text{ ft}^{-1}$$

$$\alpha_{5.8 \mu m} = 1.5 \times 10^{-5} \text{ ft}^{-1}$$

From (18) and (19) we get the following estimate of the error caused by air path fluctuation,

$$\Delta T_a \simeq 1 \text{mK}$$
 (20)

We shall see in the next section that the above error is negligible compared to that

due to sky reflections.

2.3 Sky Reflection Error

In order to calculate the error, we introduce several simplifications in the remote sensing Eq. (6), repeated below for convenience

$$\mathcal{N} = \overline{\rho} N_{s} \tau_{1} \tau_{2} \tau_{3} + \varepsilon B (T_{w}) \tau_{1} \tau_{2} \tau_{3} + \varepsilon_{1} B (T_{a}) \tau_{2} \tau_{3} + \varepsilon_{2} B (T_{b}) \tau_{3} + \varepsilon_{3} B (T_{a})$$

$$\mathcal{N}_{s} \qquad \mathcal{N}_{w} \qquad \mathcal{N}_{a} \qquad (6)$$

We note that air emissivities are much smaller than water emissivity

$$\varepsilon_1, \ \varepsilon_2, \ \varepsilon_3 << \varepsilon$$
 (21)

while blackbody radiances

$$B(T_{w}) \simeq B(T_{a}) \simeq B(T_{b}) \tag{22}$$

are all of the same order of magnitude; furthermore, since we are interested in transmittance fluctuation errors, call

$$\tau_1 \tau_2 \tau_3 = \tau \tag{23}$$

and neglect the small differences in the τ 's which are all close to unity.

We can simplify (6) with the help of (21), (22) and (23) for the purpose of estimating the error $\Delta \mathcal{N}_{\mathbf{S}}$ caused by sky reflection. Thus Eq. (6) reduces to

$$\mathcal{N} = \mathcal{N}_{S} + \mathcal{N}_{W} = \underbrace{\bar{\rho}\tau N_{S}}_{S} + \underbrace{\epsilon\tau B (T_{W})}_{W}$$

$$\mathcal{N}_{S} \qquad \mathcal{N}_{W}$$
(24)

In the following analysis we distinguish several cases, most of which have a removable error, as we shall see shortly.

Case 1: Glassy calm sea (specular reflection)

The error is totally removable. Refer to the geometry of Fig. 5a. When the radiometer looks down at the sea, it senses

$$\mathcal{N} = \underset{S}{\mathcal{N}} (\theta_r) + \underset{W}{\mathcal{N}}$$
 (25)

When it looks up at the sky, it senses the sky radiance, $N_S(\theta_r)$. If we multiply this reading by $\rho(\theta_r)\tau$, we obtain \mathcal{N}_S in (24); subtracting it from the sea reading \mathcal{N} yields the water radiance \mathcal{N}_W , with no error. Naturally we assume that ρ is measured independently, and at the low altitudes of concern, 300 m, τ is close enough to unity to neglect the difference.

Case 2: Rough sea, uniform sky

If the sky temperature is uniform, cloudless or totally overcast, the error is again totally removable.

Refer to the geometry of Fig. 5b. Because of rough sea, the radiometer sees more than the sky radiance in the direction $\theta_{\mathbf{r}}$, reflected from a horizontal facet of water; it receives flux from different portions of the sky, over incremental solid angles, $\Delta\Omega_{\mathbf{S}}$ and reflected from water facets having random orientations.

Thus for every sky direction, θ_s , ϕ_s , the radiance $\mathcal{N}_s(\theta_s,\phi_s)$ d Ω_s is reflected according to a distribution of reflectivities which follow the slope distribution of the water facets. If this random function of reflectivity is multiplied by the air path attenuation τ , we obtain a reflectivity blur distribution

$$G(\theta_r, \phi_r; \theta_s, \phi_s)$$

The reflected sky radiance seen by the radiometer and averaged over its angular resolution $\Omega_{\bf r}$ is therefore

$$\mathcal{N}_{s} = \frac{1}{\Omega_{r}} \int_{sky} G(\theta_{r}, \phi_{r}; \theta_{s}, \phi_{s}) N_{s}(\theta_{s}, \phi_{s}) d\Omega_{s}$$
(26)

The reflectivity blur distribution is the sky image blurring function and tells the extent to which each sky direction, $(\theta_{_{\rm S}},\phi_{_{\rm S}})$ reflects into the radiometer. Note that the G function is integrated over the angular resolution of the radiometer, thus depends on $\Omega_{_{\rm T}}$. Eq. (26) takes now the place of the first term in Eq. (24); the error again is totally removable provided that the sky reading is modified, according to (26) before it is subtracted from the sea reading.

Before we proceed with the next case, a few words about the blurring function are in order. This function G is measured with a laser reflectometer mounted on the same airplane as the radiometer. It can also be calculated from sea slope statistics, and its derivation is given elsewhere; *it is a function of the radiometer look angle, and its angular resolution, wind speed and direction.

In the calculations that follow we now avail ourselves of a useful analytical approximation. Refer to Fig. 6 which shows the radiometer look angle, θ_{r} with respect to zenith, z and asimuth ϕ_{r} measured with respect to the wind direction, x. If the blur function is expressed in terms of the angles ν and μ shown in the figure, in elevation and traverse planes respectively, it takes on the gaussian form given by

$$G = G_{Q}e^{-(v^{2}/2\sigma_{v}^{2} + \mu^{2}/2\sigma_{v}^{2})}$$
 (27)

Note that ν and μ are measured with respect to the direction $\theta_{\mathbf{r}}$, the specular reflection direction seen by the radiometer when the sea is flat. The variances, σ^2 depend on wind speed and radiometer look angle and are graphed in Fig. 7. Graphs of the calculated blur function given in Fig. 8 conform to the gaussian approximation.

Case 3: Non-uniform sky

If there are clouds and the sea is not glassy calm, we are faced with errors that are no longer removable. The geometry is depicted in Fig. 9. At position A, the radiometer picks up a cloud located at an aspect angle, $\theta_{\rm C}$ different from $\theta_{\rm r}$, the direction of specular reflection from the sea patch under inspection. The sky radiance measured by the radiometer is still given by Eq. (26). In order to facilitate calculations, assume that the solid angle subtended by the cloud is smaller than the blur variance, $\sigma_{\rm f}$ the blur function is essentially constant over the cloud area and (26) reduces to

$$\mathcal{N}_{\mathbf{S}} = \frac{1}{\Omega_{\mathbf{r}}} \left\{ \mathbf{G}(\theta_{\mathbf{r}}; \theta_{\mathbf{c}}) \, \mathbf{N}_{\mathbf{S}} \Omega_{\mathbf{c}}(\theta_{\mathbf{c}}) \right\} \tag{28a}$$

For simplicity we assume the cloud to be in the plane of Fig. 9, ϕ_r =0, and the cloud radiance to be uniform, $N_s(\theta_c)$ (lambertian emitter). These simplifying assumptions do not affect the order of magnitude of the error we seek. The cloud radiance can now be replaced by an equivalent blackbody function, $B(\lambda,T_c)$ at the cloud temperature T_c :

$$\mathcal{N}_{\mathbf{S}}(\theta_{\mathbf{C}}) = \frac{1}{\Omega_{\mathbf{r}}} \left\{ G(\theta_{\mathbf{r}}; \theta_{\mathbf{C}}) B(\lambda, T_{\mathbf{C}}) \Omega_{\mathbf{C}}(\theta_{\mathbf{C}}) \right\}$$
(28b)

When the aircraft reaches position B, the cloud falls within the angular resolution of the radiometer as it looks up at the sky. However, the aspect angle is now θ_{r} instead of θ_{c} . In order to remove as much of the error as possible, we blur the measured sky radiance, as the radiometer looks up to the sky according to (28) with one exception; since θ_{c} varies as the plane flies toward the cloud, the only known reference angle is θ_{r} , when the radiometer is looking up, and we can only blur the sky radiance measurement

^{*}A. Ashley and W. Wells, "Computations in Support of Sea Surface Radiometry", Applied Physics Laboratories/ John Hopkins University #600240, Nov. 1974

according to

$$\mathcal{N}_{\mathbf{S}}(\theta_{\mathbf{r}}) = \frac{1}{\Omega_{\mathbf{r}}} \left\{ G(\theta_{\mathbf{r}}; \theta_{\mathbf{c}}) B(\lambda, \mathbf{T}_{\mathbf{c}}) \Omega_{\mathbf{c}}(\theta_{\mathbf{r}}) \right\}$$
(29)

The error is the difference between measured $\mathcal{N}_s(\theta_c)$ from (28b) and estimated $\mathcal{N}_s(\theta_r)$, from (29)

$$\Delta \mathcal{N}_{S} = \mathcal{N}_{S}(\theta_{r}) - \mathcal{N}_{S}(\theta_{c}) \tag{30}$$

which no longer cancels because $\Omega_{\mathbf{C}}(\theta_{\mathbf{C}}) \neq \Omega_{\mathbf{C}}(\theta_{\mathbf{r}})$, since $\theta_{\mathbf{C}} \neq \theta_{\mathbf{r}}$. The error is then due to differences in aspect angle. In the foregoing we have neglected the path difference when the radiometer looks up and looks down since the cloud altitude greately exceeds the aircraft altitude.

Note that $\Delta N_{\rm S}$ follows from taking partial derivative of (28) or (29) with $\theta_{\rm C}$ as variable aspect angle,

$$\Delta \mathcal{N}_{\mathbf{S}} = \frac{\partial \mathcal{N}_{\mathbf{S}}}{\partial \Omega_{\mathbf{C}}} \Delta \Omega_{\mathbf{C}} = \frac{\mathbf{GB}}{\Omega_{\mathbf{r}}} \Delta \Omega_{\mathbf{C}}$$
(31)

The radiometeric temperature error follows from (17)

$$\Delta T_{S} = G \frac{B}{B^{*}} \frac{\Delta \Omega_{C}}{\Omega_{r}}$$
(32)

where

$$\Delta\Omega_{\mathbf{C}} = \Omega_{\mathbf{C}}(\theta_{\mathbf{r}}) - \Omega_{\mathbf{C}}(\theta_{\mathbf{C}}) \tag{33}$$

An estimate of the temperature error can be obtained from the value of $\Delta\Omega_{\rm C}$. An upper bound to the error is calculated as follows: Referring to Fig. 9, assume the radiometer is looking straight down at the sea surface, $\theta_{\rm r}=0$, then

$$v = \theta_{\mathbf{C}} \tag{34}$$

Furthermore, in order to simplify calculations choose

$$\mu = 0 \tag{35}$$

in Eq. 27. Going back to Fig. 9, suppose the radiometer sees a flat cloud of area, $a_{_{\rm C}}$ at altitude H imaged by reflection at range R from the sea patch under inspection; the cloud presents a solid aspect angle

$$\Omega_{\mathbf{c}}(\theta_{\mathbf{c}}) = \frac{a_{\mathbf{c}}\cos\theta_{\mathbf{c}}}{R^2} = \frac{a_{\mathbf{c}}}{H^2}\cos^3\nu \tag{36}$$

Because of (34) when the radiometer looks up at the cloud it sees a solid angle

$$\Omega_{\mathbf{c}}(\theta_{\mathbf{r}}) = \frac{a_{\mathbf{c}}}{R^2} = \frac{a_{\mathbf{c}}}{H^2} \cos^2 v \tag{37}$$

In principle, this error is removable since we can deduce from the airplane position and the collected data what value to assign to the variable angle $\theta_{\rm C}$ = ν , at all times. However, if the cloud shape is unknown, the error is no longer removable because we do not know the value of cos $\theta_{\rm C}$ needed to correct the error. This is well illustrated in the case where we erroneously assumed the cloud to be spherical, which yields a solid aspect angle in Eq. (36)

$$\Omega_{c}(\theta_{c}) = a_{c}/R^{2}$$
 (spherical cloud) (36a)

while it is actually flat for which the aspect angle is

$$\Omega_{c}(\theta_{c}) = a_{c} \cos \theta_{c} / R^{2}$$
 (flat cloud) (36b)

The error in aspect angle is therefore the difference between (36a) and (36b) or (36 and (37)

$$\Delta\Omega_{\mathbf{C}} = \frac{a_{\mathbf{C}}}{H^2} \cos^2 v (1 - \cos v) \tag{38}$$

and the corresponding temperature error

$$\Delta T_{s} = G_{o} \frac{B}{B^{T}} \frac{\Omega_{c}}{\Omega_{r}} \left[e^{-v^{2}/2\sigma_{v}^{2}} \cos^{2}v (1-\cos v) \right]$$
(39)

The largest error occurs when the bracketed expression of Eq. (39) is maximum. Assuming a fairly typical wind speed, we get the blur function variance from Fig. 7

$$W = 10 \text{ m/sec}, \sigma_{y}^{2} = .13$$

The angle ν that maximizes the bracketed expression in Eq. (39) yields the value

$$[] = .04, \ \lor \simeq 27^{\circ}$$
 (40)

We must now insert numbers for the other quantities in (39). Select λ = 3.8 μm for calculation. From Appendix B

$$B'/B \simeq c_2/\lambda T^2 \tag{41}$$

For an ambient temperature, T = 295K we get

$$B/B' = 23 \times 10^3 \text{ mK}$$
 (42)

To estimate $\Omega_{\rm c}/\Omega_{\rm r}$, refer to Fig. 10. The blur function, G, is sketched in polar coordinates and is shown to have an angular width, σ , equal to the angle subtended by the cloud. Note that σ is the standard deviation of the blur function in polar coordinates, i.e. $\sigma \simeq \sigma_{\rm c}/2$, so we have

$$\Omega_{C} = \sigma = \sigma_{V}\sqrt{2} = .51 \tag{43}$$

If the cloud subtends an angle $\Omega_{\rm c}^{>>\sigma}$, the sky will approach overcast and the error is removable. If $\Omega_{\rm r}^{<<\sigma}$, the error is negligible. Hence, Eq. (43) leads to a maximum error estimate. As we shall see in the section on radiometer design, the angular resolution of the instrument is

$$\Omega_{r} = .03 \text{ sr} \tag{44}$$

From (43) and (44) we obtain

$$\frac{\Omega_{\mathbf{C}}}{\Omega_{\mathbf{C}}} = \frac{.51}{.03} = 17 \tag{45}$$

Measurements as well as calculations (see Fig. 8) of blur functions give peak value

$$G_{\alpha} \simeq 10^{-3} \tag{46}$$

Inserting (40), (42), (45) and (46) in (39) yields the following non-removable temperature error caused by sky reflection

$$\Delta T_{g} = 10^{-3} \times 23 \times 10^{3} \times 17 \times .04 \approx 15 \text{ mK}$$
 (47)

Note that the estimated sky reflection error, Eq. (47), is more than an order of magnitude larger than the air column error of Eq. (20).

3.0 Measurements At Sea

Fig. 11 shows typical sky and sea signals at 3.8 µm and 10.6 µm obtained from a shipborne radiometer. The sky measurement shows unmistakably cloud images while the sea measurements exhibit the expected blurred reflection of the former. Let us try to remove the sky error by subtracting the sky measurement properly weighted by the blur

function from the sea signal. We choose for this exercise, the 3.8 μm data of Fig. 11 displayed on a different scale in the two bottom traces of Fig. 12. At the time of the sea measurements, no direct measurements of the blur function were made; instead we calculated it from the available data as follows:

The blur distribution function is described by ν , the angular position of the cloud. The geometry for the one-dimensional case is shown in Fig. 9 and redrawn in Fig. 13 for the purpose of this calculation. However, we only have time records for the radiometer measurements as it flies over the sea. To convert from time to angular position we need the relative velocity between clouds and aircraft and the cloud altitude. When the radiometer looks at the water at time t (Fig. 13), it senses an increment of blurred cloud reflection that comes from the sky radiance obtained when the radiometer looks up at some later time τ . Thus call the increment of sky signal received at time

$$s(\tau) d\tau$$
 (48)

The time difference τ -t is related to the angular coordinates by

$$\tan(\nu + \theta_r) - \tan(\theta_r) = \frac{v(\tau - t)}{H}$$
(49)

v being the relative velocity between clouds and radiometer. The incremental sky radiance modified by the blur function and summed over all time intervals yields the sea signal,

$$s_{W}(t) = \int h(\tau - t) s(\tau) d\tau$$
 (50)

Since the blur function is symmetrical

$$h(\tau - t) = h(t - \tau), \tag{51}$$

Eq. (50) is recognized as a convolution whose Fourier transform is

$$S_{\mathbf{W}}(f) = H(f) S(f)$$
 (52)

The quantities $S_w(f)$ and S(f) are calculated from the reflected sky radiance \mathcal{N}_S and direct radiance N_S seen by the radiometer in the down and uplooking mode respectively. However, the downlooking measurement \mathscr{N} includes the sea emission, \mathscr{N}_W , (Eq. (2), after neglecting \mathscr{N}_a) $\mathscr{N}(t) = \mathscr{N}_L + \mathscr{N}_S$ (53)

To extract \mathcal{N}_{S} we note that it only exhibits low frequencies (large clouds), so we take a long-term average (low pass filtering) or ensemble average of many records

$$\langle \mathcal{N}(t) \rangle = \langle \mathcal{N}_{S} \rangle + \langle \mathcal{N}_{W} \rangle \simeq \langle \mathcal{N}_{S} \rangle$$
 (54)

and the Fourier transform of $\langle N \rangle$ is identical to S(f), the transform of $\langle N \rangle$. Thus, H(f) can be calculated from (52)

$$H(f) = S_{tr}(f)/S(f)$$
 (55)

The inverse transform of $\mathbb{R}(f)$ yields the blur function h(t) in the time domain, shown in Fig. 14; it displays gaussian form like G(v), although the relation between v and t given by (49) is not linear. Using this function to blur the sky signal of Fig. 12 and subtracting the resultant curve from the sea yields the radiometric temperature of the sea, top trace of Fig. 12. Note that the temperature trace is consistent with our estimate of 15 mK, Eq. (47). If we now take the Fourier transform of $\mathcal{N}(t)$ in (53) without any filtering, we obtain the sea spectrum shown in Fig. 15. The low frequency hump is identified with the sky reflection. The high frequency roll-off can be shown to be the resolution limit of the instrument. The near flat portion of the spectrum is the true sea spectrum, the Fourier transform of \mathcal{N}_{w} ; any disturbance on the ocean surface, in order to be identifiable, must have a spectrum that falls in this intermediate region and exceeds the radiometric spectral background of the sea.

4.0 Temperature Resolution of a Cryogenic IR Radiometer

The heart of the radiometer is the detector. The detectors used at 3.8 μm and 10.6 μm are respectively InSb (indium antimonide) and Ge:Hg (mercury doped germanium).

To facilitate detector selection, manufacturers have established a figure of merit, the detectivity D. It is a measurable quantity, defined as the signal-to-noise ratio, S/N per incident flux,

$$D = \frac{I_s/I_n}{F} \qquad (watt^{-1} \equiv w^{-1})$$
 (56)

where \mathbf{I}_s and \mathbf{I}_n are respectively signal and noise currents at the detector output. The minimum detectable flux, \mathbf{F}_{\min} , corresponds to unity signal-to-noise ratio and equals the inverse of the detectivity. (The reason for the choice of D rather than \mathbf{F}_{\min} is to have a figure of merit that gets larger as detector sensitivity improves, i.e. is capable of detecting less flux.) The problem with this definition is that it depends on the detector area \mathbf{A}_d and the radiometer system electronic bandwidth, $\Delta \mathbf{f}$. This is readily seen by noting from the preceding equation that D varies inversely with noise, \mathbf{I}_n which for shot-noise corresponds to r.m.s. noise current

$$I_{n} = \sqrt{\langle i_{n}^{2} \rangle} = \sqrt{2eI_{S}\Delta f}, \tag{57}$$

where e is the electronic charge and I_s the average signal current. Thus D varies as $1/\sqrt{\Delta}f$; furthermore, average signal current I_s and incident flux are both proportional to the detector area, while the noise varies as $\sqrt{A_d}$; it follows that the detectivity

$$D \sim \frac{1}{\sqrt{A_{d} \Delta f}}$$
 (58)

is inversely proportional to the square root of the detectors area and the electronic bandwidth. In order to compare detectors of different area and systems of different electronic bandwidth, the specific detectivity D* (Dee-star) has been introduced, which eliminates the above dependence

$$D^* = D\sqrt{A_d\Delta f} = \frac{I_S/I_n}{F} \sqrt{A_d\Delta F} \quad w^{-1} cm \quad Hz^{1/2}$$
(59)

Note again that D* is simply the inverse of the minimum detectable flux F_{\min} normalized with respect to the square root of area-bandwidth product, $A_d \Delta f$.

Typical D* for a cooled Ge:Hg is $10^{+11}~\text{w}^{-1}\text{cm}~\text{Hz}^{1/2}$ at 10 μm .

4.1 System D_S^{\star} of Cold Radiometer in the Background Limit

The D* concept can be applied to optical systems. Cooling the optics as well as the housing results in a system D_S^* greater than the detector D^* . The system D_S^* is first derived, from which follows the achievable temperature resolution of the radiometer.

Refer now to Fig. 16 which shows the front of the radiometer with cooled detector, field stop and housing. To calculate D_s^{\star} , we need to know F_{\min} , the minimum detectable flux. We proceed as follows: the detector current and incident flux are related through the quantum efficiency, η and the photon energy hy by

$$I_{S} = \eta \frac{e}{h\nu} F$$

$$I_{n} = \eta \frac{e}{h\nu} F_{min}$$
(60a)

Substituting Eqs. (60a) and (60b) into (57) and solving for the minimum detectable flux gives

$$F_{\min} = \sqrt{\frac{2}{\eta} h_{\nu} F_{\Delta} f}$$
 (61)

The flux F seen by the radiometer is shown in Fig. 16; the instrument has solid angle resolution $\Omega_{\mathbf{r}}$ and collecting aperture $A_{\mathbf{r}}$. If the "scene" is 300K and the walls are cooled to cryogenic temperature, none of the wall radiation impinging on the detector, which by itself subtends a 2π solid angle, has any appreciable effect compared with the radiation received from the scene. Assuming the latter to be a blackbody function, we have from Appendix B

$$F = C_{T} \lambda^{-5} e^{-C_{2} / \lambda^{T}} \Omega_{r} A_{r \Delta \lambda} \qquad \text{watts}$$
 (62)

where $\Delta\lambda$ is the optical bandwidth of the radiometer. Recall that $\Delta\lambda/\lambda \simeq .10$ for both radiometer wavelengths; substituting (62) into (61) yields

$$F_{min} = C_1 \sqrt{\frac{\pi}{\pi c}} \frac{\Omega_r}{\pi} \frac{e^{-C_2/\lambda T}}{\lambda^5} \frac{\Delta \lambda}{\lambda} \sqrt{A_r \Delta f}$$
fractional relative subtense optical bandwidth background
$$C_1 = 1.19 \times 10^{-12} \text{w-cm}^2$$

$$C_2 = \text{hc/k} = 14,388 \ \mu\text{m-K}$$

$$k = 1.38 \times 10^{-23} \ \text{j/K}$$
(63)

Note that improvement in system D_S^\star comes about from the fact that while the detector accepts hot radiation over a 2π hemisphere, the cooled walls and stop of the radiometer limit "hot" radiation to Ω_r subtense.

From the definition of D* in terms of minimum detectable flux, F_{\min}

$$D^* = \frac{1}{F_{\min}} \sqrt{A_d \Delta f}$$

we obtain the theoretical system D*,

$$D_{s}^{\star} = 4.1 \times 10^{6} \sqrt{\eta \frac{A_{d}^{/A}r}{(\Omega_{s}/\pi) (\Delta \lambda/\lambda)} \lambda^{5} (\mu m) e^{c} 2^{/\lambda T}} w^{-1}_{Hz} 1^{/2}_{cm}$$
(65)

Putting in some numbers:

$$\lambda$$
 = 10 μm T = 300K
$$\Delta \lambda/\lambda$$
 = .10
$$\Omega_{\rm r}/\pi$$
 = 10⁻²
$$\Delta_{\rm d}/\Delta_{\rm r}$$
 = .5cm/20cm = 2.5 \times 10⁻²
$$\eta$$
 = .05 (includes all efficiencies)

We get for a cold radiometer

$$D_{s}^{\star} \sim 3 \times 10^{10} \text{ w}^{-1} \text{cm Hz}^{1/2}$$

We are now in a position to calculate the temperature resolution of the cold radiometer.

4.2 Temperature Resolution

Having calculated the system D* under background limited conditions, we turn to the problem of converting the corresponding minimum flux, F_{\min} to an equivalent temperature, ΔT_{n} . This is the minimum detectable temperature set by noise and it is the temperature resolution of the cryogenic radiometer. The minimum detectable flux, F_{\min} is the

smallest change in flux, ΔF that can be detected since it is equal to the photon noise caused by this flux. We simply write

$$F_{\min} \equiv \Delta F \equiv \frac{\partial F}{\partial T} \Delta T_{n}$$
 (66)

From (62) we have

$$\frac{\partial \mathbf{F}}{\partial \mathbf{T}} = \frac{\mathbf{h_C}}{\mathbf{k}\lambda\mathbf{T}} \frac{\Delta^{\mathbf{T}}\mathbf{n}}{\mathbf{T}} \mathbf{F} \tag{67}$$

It is useful to express the preceding equation in terms of the wavelength λ_T at which a blackbody of temperature T radiates maximum flux. It is readily done by differentiating the blackbody function with respect to T, setting it equal to zero and solving for λ_T^T . We get the Wien's displacement law,

$$\lambda_{\mathbf{T}} \mathbf{T} = 2897 \ \mu \mathbf{m} - \mathbf{K} \tag{68}$$

Note that for T \simeq 300K, peak wavelength is $\lambda_{\rm T}$ \simeq 10 $\mu m. The preceding expression can also be written in the convenient form$

$$\frac{hc}{k\lambda_{\mathbf{T}}T} \approx 5 \tag{69}$$

which substituted in (66) yields

$$F_{\min} = \Delta F \approx 5F \frac{\lambda_{T}}{\lambda} \frac{\Delta T_{n}}{T}$$
 (70)

From (65), (66) and (70) we get for the minimum resolvable temperature

$$\Delta T_{n} = \frac{T}{5} \frac{\lambda}{\lambda_{T}} \sqrt{\frac{1}{\pi \eta}} \sqrt{\frac{\Delta f \lambda / c}{A_{r} / \lambda^{2}}} \sqrt{\frac{e^{c} 2^{\prime} \lambda^{T}}{(\Omega_{r} / \pi) (\Delta \lambda / \lambda)}}$$
(71)

The radiometer described in the text has the following parameters:

$$\eta = 5\%$$

$$\lambda = 10 \mu m$$

$$\Delta f = 800 Hz$$

$$A_r = 20cm^2$$

$$\Omega_r = 3 \times 10^{-2} sr$$

$$\Delta \lambda / \lambda = .10$$

If the scene temperature T = 300K, the radiometer resolves according to (71)

$$\Delta T_{\rm p} \simeq 6 \times 10^{-5} \rm K \ at \ 10 \ \mu m$$

A plot of minimum resolvable temperature vs. wavelength is shown in Fig. 17. On the same graphs are shown temperature resolutions achieved in practice with this radiometer and indicated by triangles:

$$\lambda$$
 = 10 µm to 11.1 µm
$$\Delta T_n = 5 \times 10^{-4} \mathrm{K}$$

$$\lambda$$
 = 3.6 µm to 4.1 µm
$$\Delta T_n = 10^{-3} \mathrm{K}$$

We see that resolvable temperatures achieved in practice are less than an order of magnitude above theoretical limits. Figs. 18 and 19 show photographs of the radiometer and its operation on board ship.

Part II: VISIBLE SPECTROMETRY

Radiometry usually implies collecting flux over a relatively wide but fixed spectral band. The infrared radiometer described earlier measures flux at two fixed wavelengths, 3.8 μ m and 10.6 μ m with spectral bands of the order of 400 nm and 1000 nm. Each fixed wavelength scans a wide field of view with narrow angular resolution, 30 millisteradians; detection relies mostly on the spatial and temporal radiometric temperature of the sea surface.

Spectrometers, as opposed to radiometers, collect flux in narrow spectral bands over a wide spectral range. This is achieved by scanning the visible portion of the spectrum and slightly beyond it, from 300 nm to 700 nm in narrow bands of the order of 4 nm, with an angular resolution of the order of 20 millisteradians that coincides with its field-of-view. Information is mostly based on the relative spectral content of each band, i.e. ocean color. The instrument used for the measurements described further on is a commercially available, standard piece of equipment.

We now proceed to derive a remote sensing equation, illustrate some at-sea measurements and compare them with our theoretical prediction.

1.0 Remote Sensing Equation

The ocean color changes sensed by the spectrometer result from skylight penetrating the water, undergoing multiple scattering and re-emerging upwards with its spectral content modified by the spectral transmission characteristics of the water. The sky flux that travels downward in the water is called the downwelling flux, and the one that travels back up after scattering is the upwelling flux.

Sky light and water have markedly different spectral distributions and scattering functions; they are well known and shown in Figs. 20, 21 and 22.

To set up the remote sensing equation, refer to Fig. 23. At the ocean surface, two components of light flux travel towards the sensor, namely reflected sky radiance (sunglint avoided)

$$N_{sk}(\theta_r) = \rho(\theta_r) N_s(\theta_r)$$
 (72)

and transmitted upwelling radiance

$$N_{\mathbf{w}}(\theta_{\mathbf{r}}) = \tau_{\mathbf{u}}(\theta_{\mathbf{w}}) N_{\mathbf{u}}(\theta_{\mathbf{w}})/n^{2}$$
(73)

Note that ρ in Eq. (72) is an average reflectivity that takes into account the blurring caused by sea state as described by the blur function G of Part I.

 $N_{sk}(\theta_r)$ and N_w are measured at the sea surface; do not confuse them with the $\pmb{\mathscr{N}}$'s of Part I measured at the radiometer. $\tau_u(\theta_w)$ is the water surface transmissivity as a function of the refracted angle θ_w ; it relates to the spectrometer look angle θ_r , by

$$\sin \theta_r = n \sin \theta_w;$$
 (74)

n \simeq 1.34 is the refractive index of sea water and the factor n^2 in Eq. (73) follows from the fact that across two lossless media of different refractive index, radiances N are not preserved but rather N/n²

Note from Eq. (73) that $N_u(\theta_w)$ is the information-bearing signal. At arbitrary altitude H above the ocean, the atmospheric transmittance, T_θ reduces the above fluxes and the scattered sunlight introduces a masking flux, N_θ^* known as path radiance. By inspection of Fig. 23 we can write for the radiance received at the spectrometer

$$\mathcal{N}_{\theta} = N_{\theta}^{\star} + T_{\theta} \left[\underbrace{\rho(\theta) N_{s}(\theta)}_{N_{sk}(\theta)} + N_{\underbrace{u}(\theta_{w}) \tau_{u}(\theta_{w}) / n^{2}}_{N_{w}(\theta_{w})} \right]$$
(75)

We have dropped the subscript r from θ_r for simplicity.

2.0 Approach and Measurements At Sea

Measurements* were performed with the spectrometer mounted on a helicopter, looking at the nadir (θ_r = 0). The geometry is shown in Fig. 24. From this geometry, two simplifications in the remote sensing Eq. (75) follow:

- 1) The low altitude H = 500 feet to 2000 feet yields a transmittance T $_{\theta}$ $^{\sim}$ 1 to .84, essentially unity, for practical purposes.
- 2) The path radiance N $_{\theta}$ * at these low altitudes is negligible compared to N $_{sk}(\theta)$. This assumption was carefully verified
 - (a) by calculating the equivalent photometric brightness** (footlamberts) over the entire visible range and comparing it to the classical Scripps measurements of atmospheric path radiance
 - (b) by varying the helicopter altitude from 500 feet to 2000 feet and observing no change in spectral radiance as shown in the measurements of Fig. 26.

Taking these two simplifications into account, and the fact that θ_r = 0, Eq. (75) reduces to

$$\mathcal{N} = N_{sk}(0) + N_w(0) \tag{76}$$

Furthermore, as shown in Fig. 25, measurements of N $_{\rm sk}$ and N $_{\rm w}$ over a variety of waters in coastal zones indicate

$$N_{ck}(0) \ll N_{ck}(0) \tag{77}$$

over most of the visible spectrum. The simplification (76) and (77) when introduced in (75) yield the useable remote sensing equation

$$\mathcal{N} = N_{\omega} = \tau_{11} N_{11} / n^2 \tag{78}$$

In the water, the upwelling radiance, ${\rm N}_{\rm u}$ is related to the downwelling radiance ${\rm N}_{\rm d}$ by a reflection coefficient R so that

$$N_{ij} = RN_{d} \tag{79}$$

The downwelling radiance in water is related to the sky radiance, N_{sk} , according to the preservation of the quantity N/n^2 ; as in Eq. (73), we have

$$N_d = \tau_d N_{sk} n^2; \tag{80}$$

 $\mathbf{T}_{\mathbf{d}}$ is the downward transmissivity across the sea surface. After proper substitution, we end up with

$$N = N_{\mathbf{w}} = R_{\mathsf{T}_{\mathbf{u}}} \mathbf{d}_{\mathsf{sk}}$$
(81)

This is the basic remote sensing equation in the absence of surface disturbance. If a disturbance of spectral transmissivity, τ' appears on or near the surface of the water,

$$\tau_{\mathbf{d}}$$
 becomes $\tau_{\mathbf{d}}\tau'$ (one way trip) $\tau_{\mathbf{u}}$ becomes $\tau_{\mathbf{u}}\tau'$ (return trip)

as indicated in the sketch of Fig. 27. The spectral radiance from the disturbed area is therefore

$$\mathcal{N}' = R_{\tau}'_{\tau_u} \tau'_{\tau_d}^{N_{sk}}$$
(82)

so that the ratio of the radiances in the presence and absence of disturbance

$$\frac{\mathcal{N}'}{\mathcal{N}} = \tau^{*2} \tag{83}$$

equals the square of the spectral transmissivity of the disturbing material.

^{*}Measurements performed by NASA under Mr. Warren Hypes

^{**}Applied Optics, May 1964; Visibility Issue, S. Q. Duntley, Editor

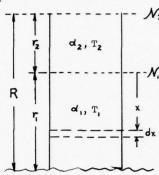
Our approach based on Eq. (83) requires building up a catalog of spectral transmissivity measurements, τ ' for expected disturbances such as oil slicks as a function of sea water concentration. Such measurements can be made at any time, independently of the remote observation, and stored as part of a data base. They are retrieved after the remote measurements of spectral radiance N' and N are performed over the disturbed and undisturbed areas respectively.

Supporting laboratory measurements of the transmissivity of an acid contaminant for various sea water concentrations is shown in Fig. 28; when combined with the observed spectral radiance \mathcal{N} in the undisturbed area, it yields the predicted radiance \mathcal{N} according to Eq. (82). The results shown in Fig. 29 are compared with the observed radiance in the same figure. The agreement is excellent and concentrations across the plume can be tracked as shown in Fig. 30.

EMITTANCE AND TRANSMITTANCE OF AIR COLUMN

Emissivity and transmissivity usually refer to radiative properties of surfaces where dealing with volumes we use the concepts of transmittance and emittance as defined below.

Consider, for simplicity, an air path made up of two different columns, each having absorption coefficients $\alpha_1(m^{-1})$ and $\alpha_2(m^{-1})$ and temperatures T_1 , T_2 as illustrated in the sketch below; let us calculate the flux emitted by the lower air column but received at the top of the upper column



The radiances at the respective interfaces are due to emission of the bottom column \mathcal{N}_1 and \mathcal{N}_2 . For homogeneous columns,

$$N_2 = N_1 e^{-\alpha} 2^r 2$$
 A-1

To calculate \mathcal{N}_1 we must relate it to a blackbody function and effective emissivity of the air column considered as an equivalent surface. Thus, an element dx in the lower column, contributes a fraction of the total radiance

$$dN_1 = \alpha_1 dx B(\lambda, T_1) e^{-\alpha} 1^X$$
 A-2

where $\alpha_1^{}$ dx is the effective emissivity of the infintesimal volume of thickness, dx, and B(λ ,T) is the blackbody function. The total radiance

$$\mathcal{N}_1 = B(\lambda, T_1) \alpha_1 \int_0^{r_1} e^{-\alpha} 1^x dx$$
A-3

The result is

$$\mathcal{N}_1 = (1 - e^{-\alpha} 1^r 1) B(\lambda, T_1)$$
 A-4

The quantity $1-e^{-\alpha}1^r1$ is recognized as the emissivity of the whole column. From A-4 and A-1 we have

$$\mathcal{N}_1 = (1 - e^{\alpha} 1^r 1) B(\lambda, T_1) e^{-\alpha} 2^r 2$$
 A-5

We call

$$1 - e^{-\alpha} 1^{r} 1 = \varepsilon_{1}$$
 A-6

emittance of the bottom column, and

$$e^{-\alpha}2^{r}2 = \tau_{2}$$
 A-7

transmittance of the upper column which reduces A-5 to

$$\mathcal{N}_1 = \varepsilon_1 B(\lambda, T_1) T_2$$
 A-8

Eq. (6) in the text is made up of terms built up in the same manner as A-8.

Appendix B

RADIOMETRIC TEMPERATURE EQUIVALENT OF RADIANCE

Radiance changes, $\Delta \mathcal{N}$ can be converted into equivalent temperature fluctuation of a blackbody function $B(\lambda,T)$ by the following expression

$$\Delta \mathcal{N} = \frac{\partial B(\lambda, T)}{\partial T} \Delta T = B'\Delta T$$
B-1

In calculating the changes, we often encounter the expression B'/B for which the approximation derived below is perfectly adequate.

The blackbody expression for radiance, B = $\frac{F/\Delta\lambda}{A_r\Omega_r}$ or flux F for unit wavelength, area and solid angle is

$$B(\lambda,T) = \frac{c_1/\lambda^5 (\mu m)}{e^{c_2/\lambda T} - 1} \quad \text{w/cm}^2 - \text{sr} - \mu m$$

$$B-2$$

where

$$C_1 = 2hc^2 = 1.19 \times 10^{-2} \text{ w-cm}^2/\text{sr} = 1.19 \times 10^4 \text{ w/cm}^2-\text{sr-}\mu\text{m}$$
 $c = 3 \times 10^8 \text{ m/sec} = \text{light speed}$
 $h = 6.6 \times 10^{-34} \text{j-s} = \text{Planck's instant}$
 $c_2 = 14,388 \mu\text{m-K}$

we find that for temperature T around 300K we can approximate the denominator of the preceding expression by $e^C 2^{/\lambda T}$ with an error of the order of 1% if we demand

$$e^{C_2/\lambda T} \ge 100$$

which corresponds to a wavelength

$$\lambda \le \frac{14,388 \ \mu mK}{4.61 \times 300K} = 10.4 \ \mu m$$

With the preceding approximation, expression B-2 becomes

$$B(\lambda,T) = C_1 \lambda^{-5} e^{-c} 2^{/\lambda T} \quad w/m^2 - sr - \mu m$$
 B-3

and

$$B'/B = c_2/\lambda T^2$$
B-4

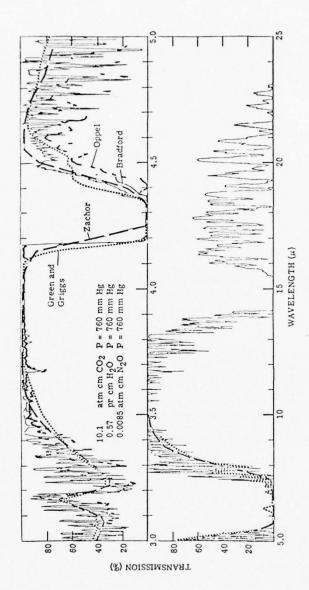
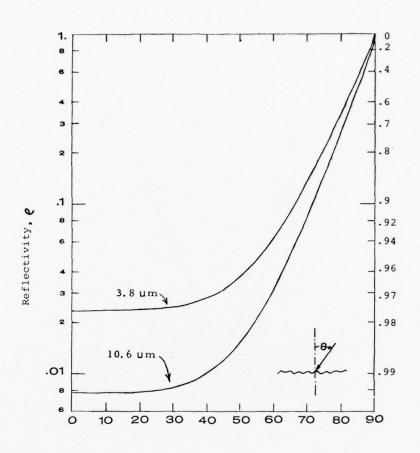


Fig. 1: Atmospheric absorption spectrum

Comparison of measured spectra of Yates and Taylor with computed spectra of Bradford, Green and Griggs, Oppel and Zachor. (NRL Report No. 5453, June 1960)





Incident Angle, θ (degrees)

Fig. 2: Reflection coefficient of sea water

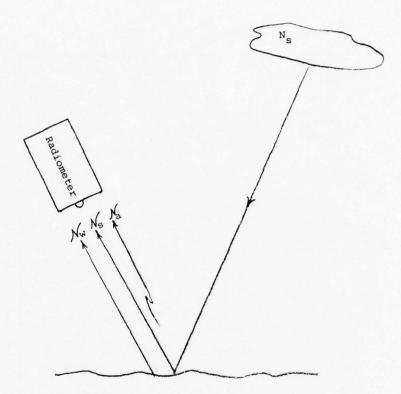


Fig. 3: Simplified geometry of radiant flux components seen by radiometer

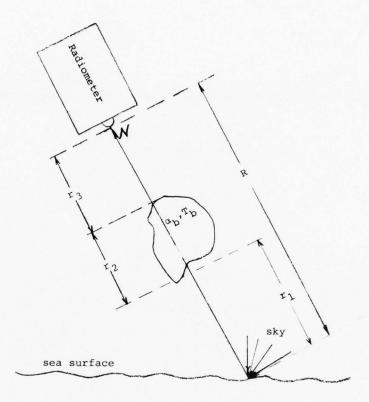
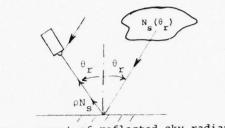
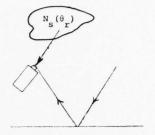


Fig. 4: Geometry of air path responsible for radiometric temperature errors





measurement of reflected sky radiance

measurement of direct sky radiance

a) Glassy calm sea (specular reflection)

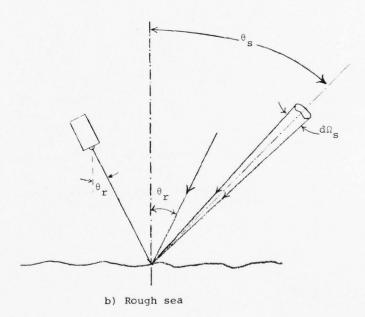


Fig. 5: Geometry for sky reflection errors

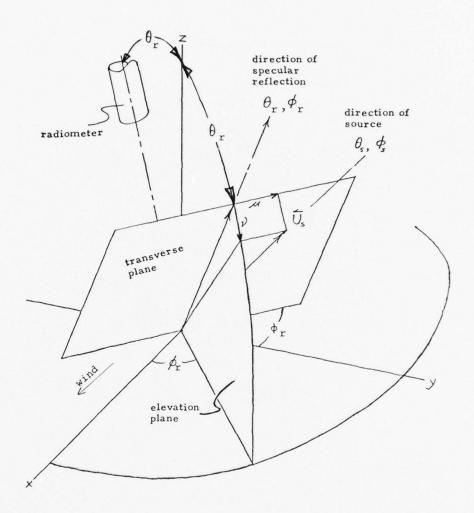


Fig. 6: Definition of angular coordinates μ,ν relative to reflected radiometer axis

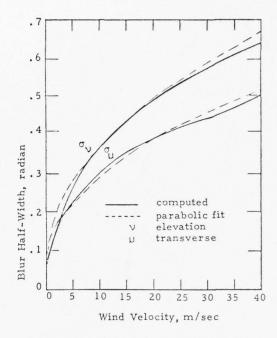
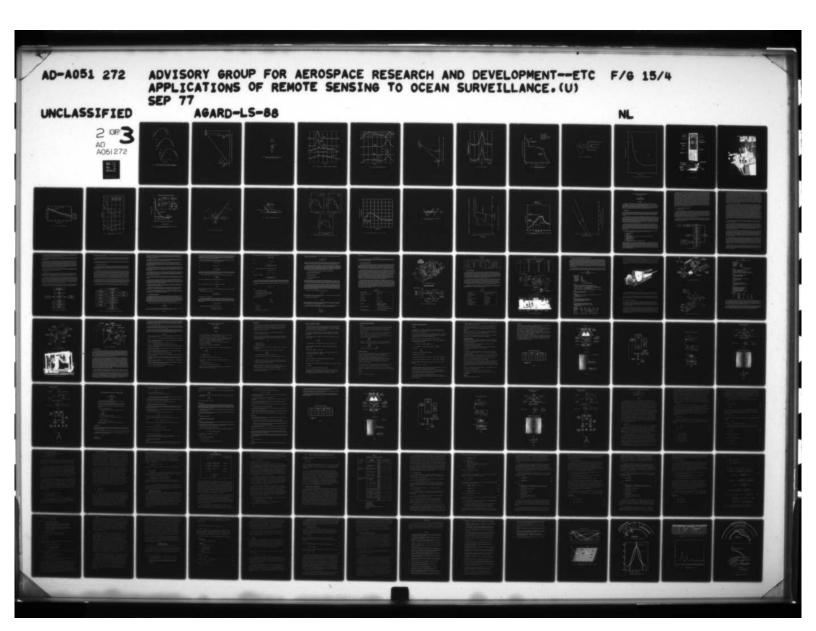
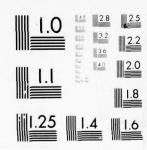


Fig. 7: Angular rms width of blur distribution as a function of wind speed. λ = 3.8 μm , $\theta_{_{_{\bf T}}}$ = 15*, $\phi_{_{_{\bf T}}}$ downwind.



20F3 AD A051272



MICROCOPY RESOLUTION TEST CHART NATIONAL BUREAU OF STANDARDS-1963-4

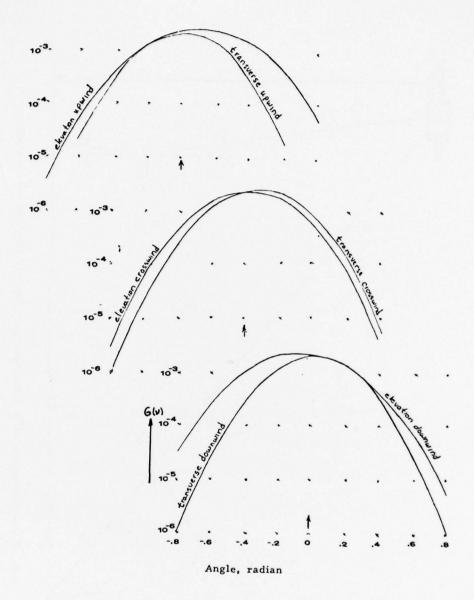


Fig. 8: Sections through sky reflection blur distribution, $\theta_{_{\bf T}}$ = 30°, λ = 3.8 $\mu m,$ W = 5 m/sec in all directions.

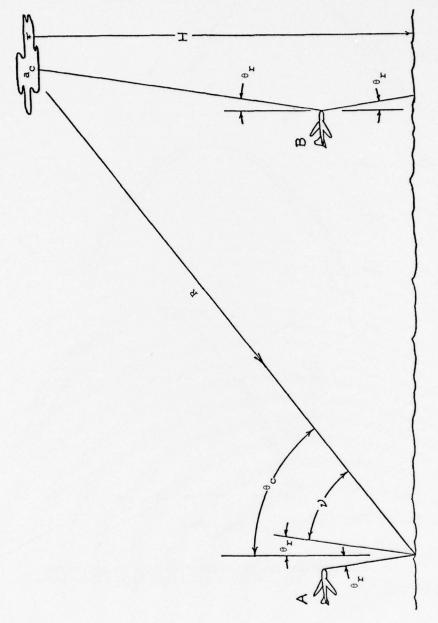


Fig. 9: Aspect angle of a cloud varying from one position to another.

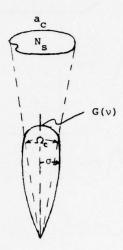


Fig. 10: Relationship between blur function angular width and subtended cloud angle

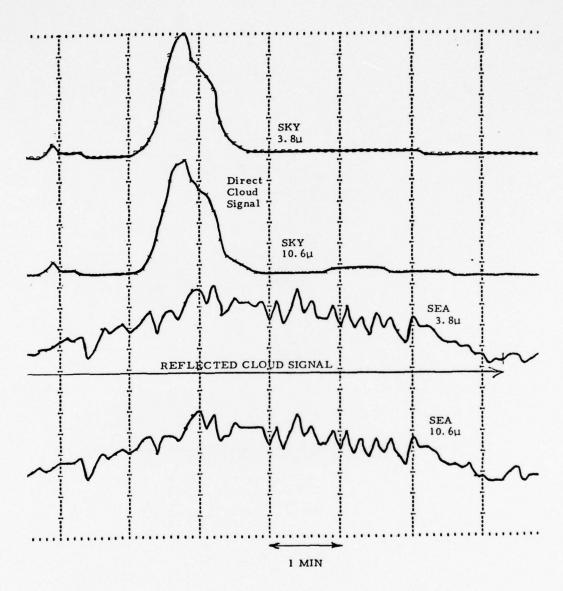


Fig. 11: Reproduction of signals from shipborne radiometer

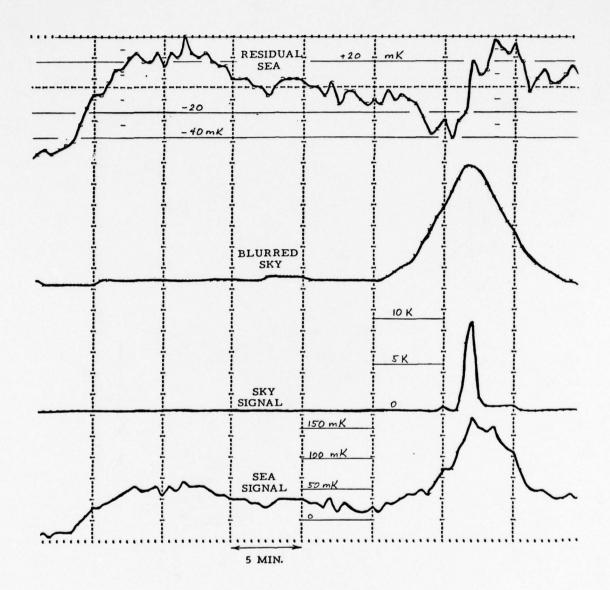


Fig. 12: Joint processing sea/sky 3.8 μm

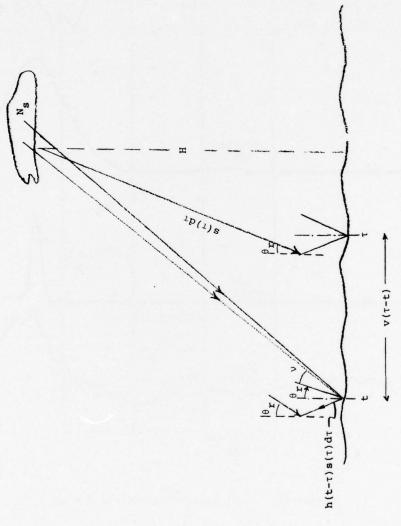


Fig. 13: Geometry for calculation of blur function Fourier transform

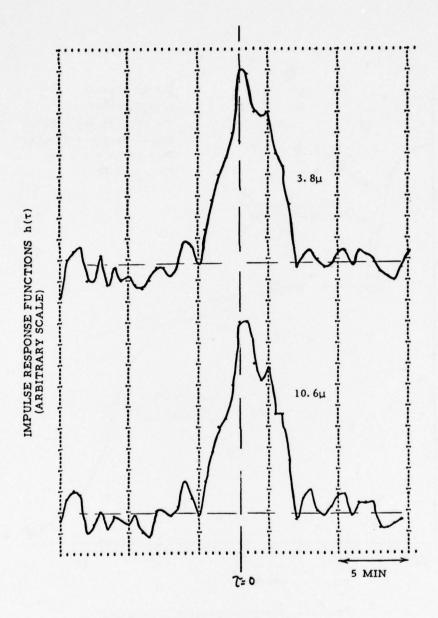


Fig. 14: Blur functions

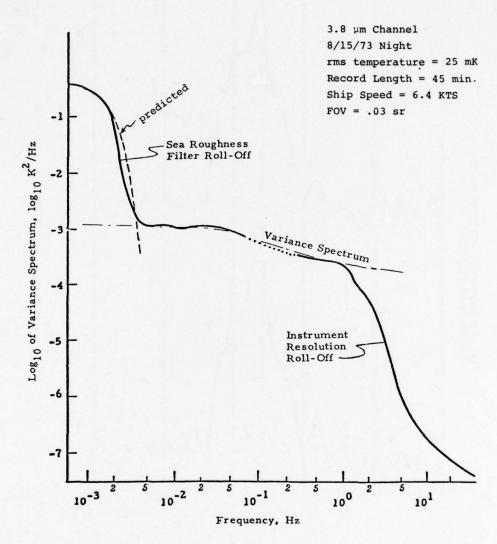


Fig. 15: Variance spectrum compared to sea surface filter effect

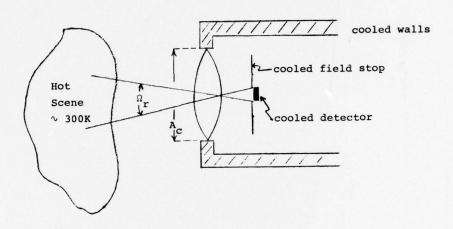


Fig. 16: Cooled radiometer

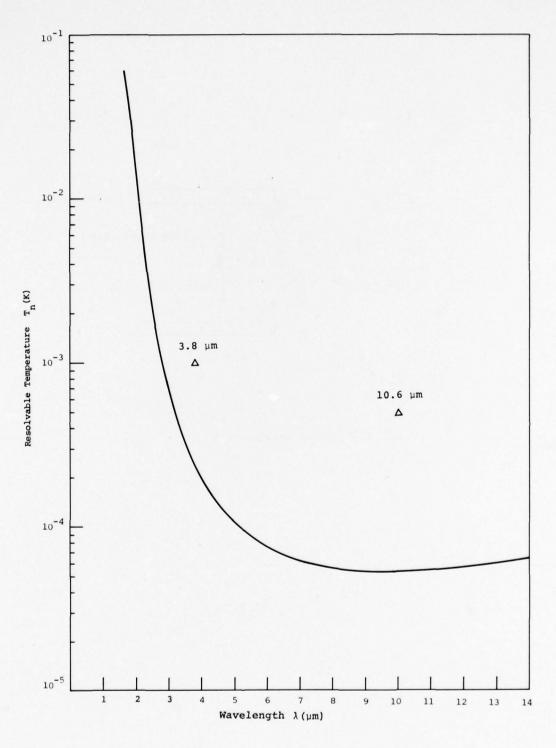


Fig. 17: Minimum resolvable temperature of cooled radiometer

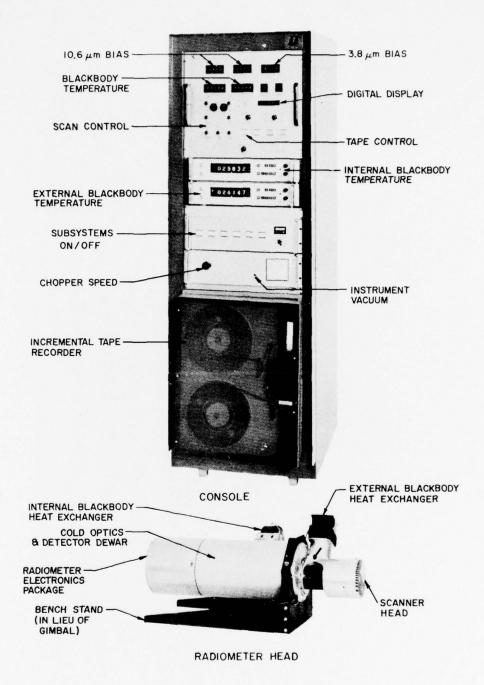


Fig. 18: Cooled radiometer

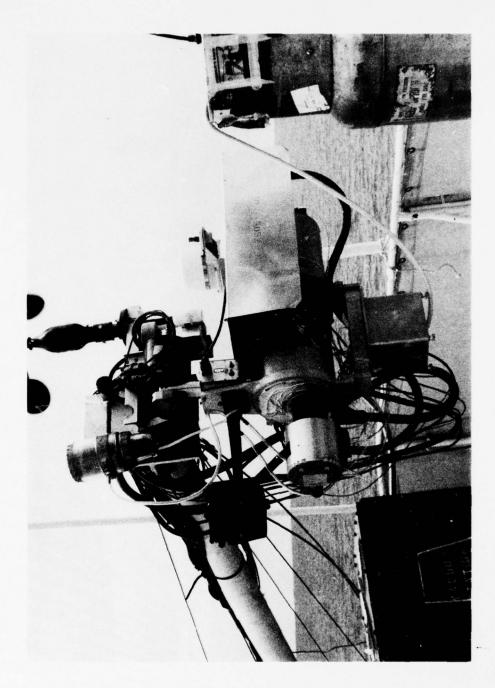


Fig. 19: Operation at sea

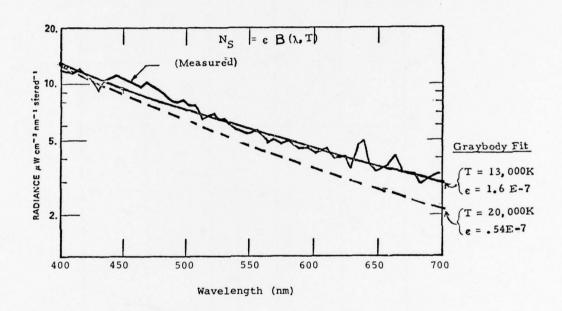


Fig. 20: Sky spectral distribution

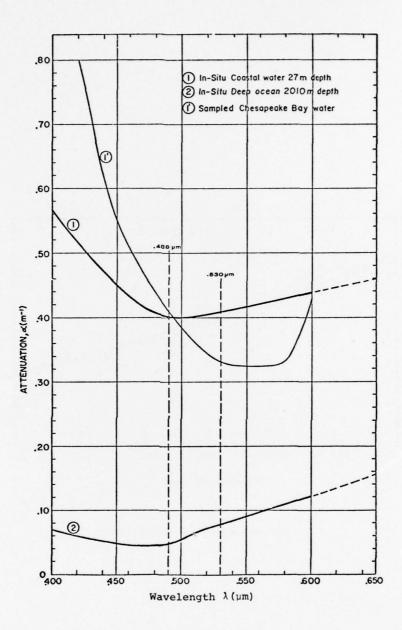


Fig. 21: Spectral attenuation of coastal waters and deep ocean

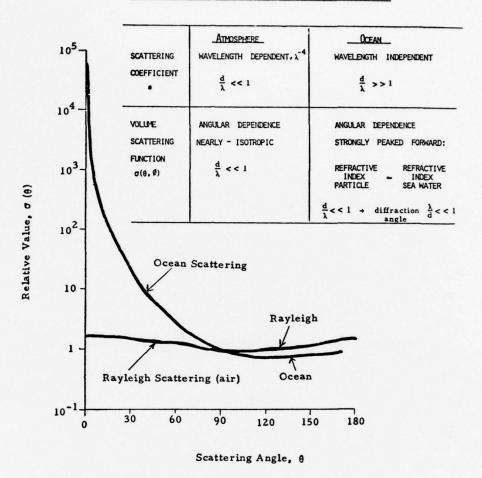


Fig. 22: Plot of relative value of volume scattering function in air and water, normalized at $90\,^{\bullet}$

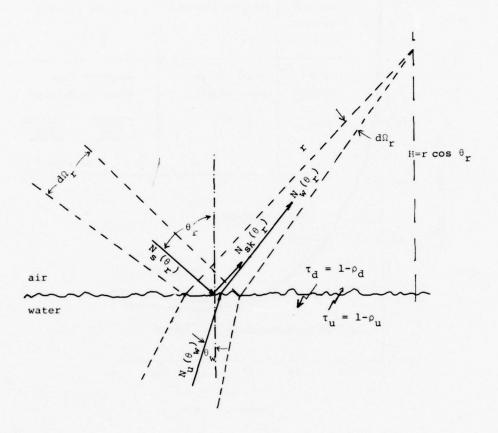


Fig. 23: Geometry of remote sensing

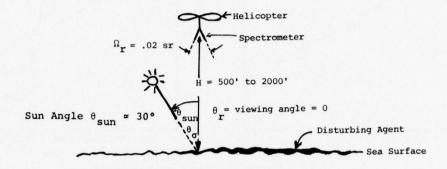
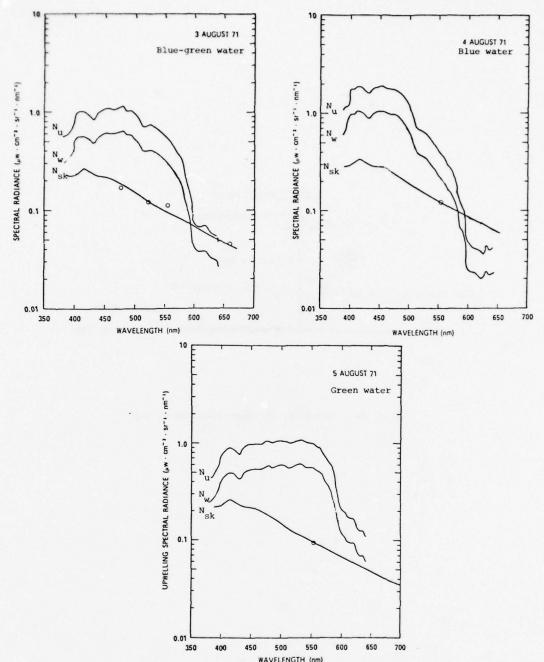


Fig. 24: Geometry of measurements at sea



WAVELENGTH (nm) Fig. 25: Relative magnitudes of reflected sky radiance, $N_{\rm sk}$, upwelling radiance in water, $N_{\rm u}$, and at water surface, $N_{\rm w}$, as measured by Scripps

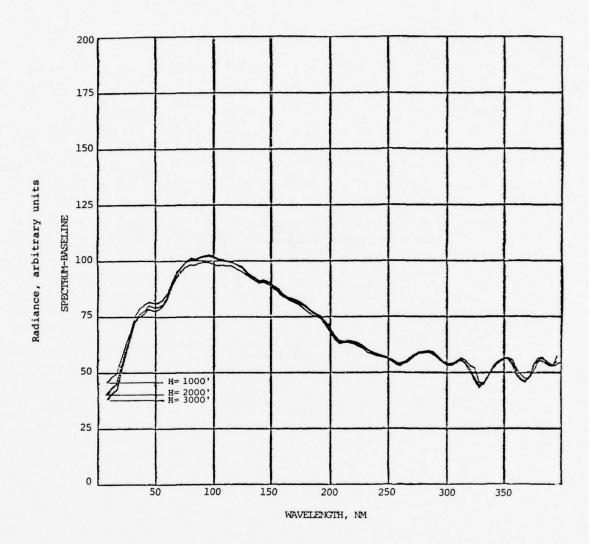


Fig. 26: Spectral radiance measured at 3000', 2000', and 1000'.

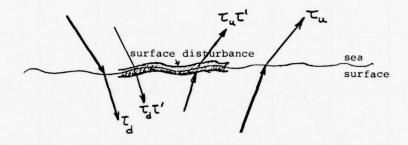


Fig. 27: Transmissivities across disturbed and undisturbed surface



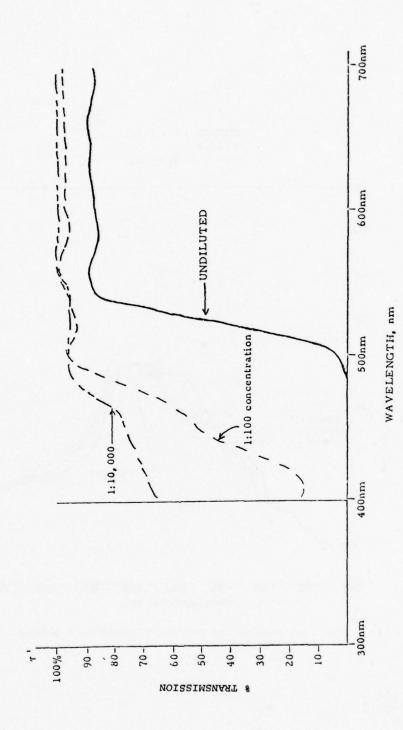


Fig. 28: Contaminant transmissivity for various concentrations

TIME = 8:48:54.52

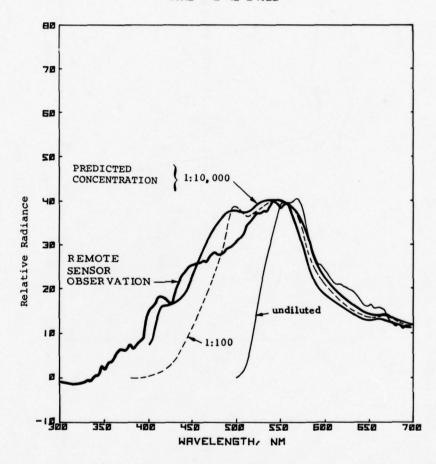


Fig. 29: Test results and predicted contaminant concentration by remote sensing.

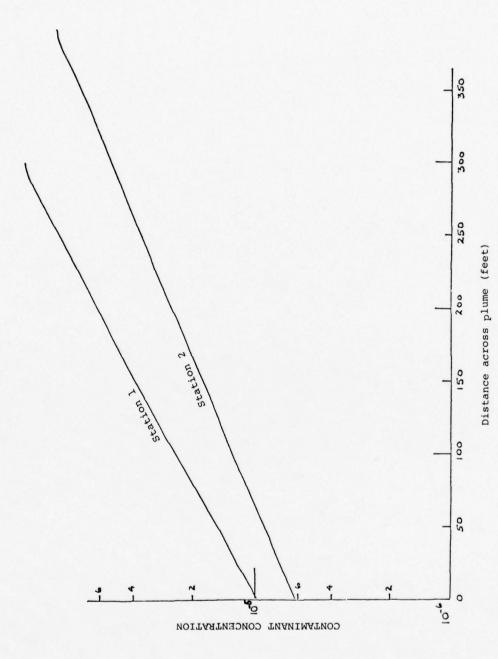


Fig. 30: Deduced contaminant concentration across plume

VISIBLE AND INFRARED IMAGING RADIOMETERS FOR OCEAN OBSERVATIONS

By

W. L. Barnes Goddard Space Flight Center Greenbelt, Maryland

ABSTRACT

This paper deals with the current status of visible and infrared imaging sensors designed for the remote monitoring of the oceans. Emphasis is placed on multichannel scanning radiometers that are either operational or under development. Present design practices and parameter constraints are discussed. Airborne sensor systems examined include the Ocean Color Scanner (OCS) and the Ocean Temperature Scanner (OTS). The Coastal Zone Color Scanner (CZCS) and Advanced Very High Resolution Radiometer (AVHRR), upcoming spaceborne sensors for oceanic applications, are reviewed with emphasis on design specifications, expected completion, and anticipated performance. Finally, recent technological advances and their probable impact on sensor design are examined.

I. INTRODUCTION

The development of imaging radiometers for the purpose of observing a wide variety of surface and atmospheric parameters from airborne or spaceborne platforms has been a rather recent phenomena, occurring almost completely within the last twenty-five years. The application of this technology to oceanography is even more recent with the first imaging visible and infrared radiometer dedicated to oceanography scheduled for launch during the upcoming year (1978).

Imaging the earth's surface was limited to airborne photography until the availability of infrared detectors with short time constants led to the development of thermal strip mappers in the early 1950's. These sensors used a single detector and a scanning mirror with the motion of the aircraft relative to the ground supplying the vertical scan motion. This technology developed rapidly and in November, 1960, the Medium Resolution Infrared Radiometer (MRIR) aboard TIROS II provided the first thermal images of the earth from a space platform. The primary interest in this data was meteorological. Applications to oceanography were minimal due to the 20 n. mi. spatial resolution. It was not until the data from the High Resolution Infrared Radiometer (HRIR) on NIMBUS I became available in 1964 that any meaningful study of the oceans was possible using data from space.

In the interim there has been a considerable research effort to determine which parameters of interest to the oceanographic community are discernable from aircraft or space platforms using visible and infrared radiometers. The two most important ocean parameters that lend themselves to remote sensing are surface temperature and ocean color. Sea surface temperature has received much more attention from the remote sensing community, due to its importance in the energetics of meteorology, than has been given to the study of ocean color. It has only been within the last few years that the study of ocean color from high altitude aircraft has sufficiently demonstrated the potentialities of this parameter to lead to a spacecraft sensor. This sensor, the Coastal Zone Color Scanner (CZCS) will be discussed later on.

The remote sensing of reflected solar and/or emitted thermal energy from the ocean has been used in a wide variety of studies with varying degrees of success. Topics that have been studied include:

- 1. Sea-surface temperature
- 2. Oceanic fronts
- 3. Currents
- 4. Coastal upwellings
- 5. Pollutants including oil slicks, acid dumps, thermal effluents, and industrial discharge
- 6. Sediment transport
- 7. Aquatic vegetation mapping
- 8. Shallow-water bathymetry
- 9. Fish location
- 10. Sea-state via glitter pattern
- 11. Chlorophyll and yellow substance (or gelbstoffe) concentration

Rather than becoming involved in a survey of the work done in each of these areas and the types of sensors used, this paper will first discuss the common elements of airborne and spaceborne systems, including the sensor, on-board data handling equipment, ground support systems, and ground data reduction. Secondly, equations for the design of visible and infrared imaging radiometers will be examined with emphasis on present practices and limitations. Then, two operational high-altitude airborne sensor systems and two spaceborne systems presently under development will be examined as examples of typical ocean surveillance designs. Finally, there will be a brief discussion of a few of the recent technological developments and their anticipated effect on the design and performance of visible and infrared radiometers through the mid-1980's.

Additional material on remote sensing of the ocean and the design and use of visible and thermal radiometers can be found in the literature and in several recently published books that survey the entire field of remote sensing. Outstanding among the latter is the Manual of Remote Sensing (1), a two volume 2100 page set of papers that address nearly every facet of remote sensing. The work was published in 1975 by the American Society of Photogrammetry and contains many references through 1973. Another excellent survey is Remote Sensing of the Environment (2) published in 1976 with over 1,000 references from the open literature, some as recent as 1975. Both the latter works and Remote Sensing of the Troposphere (3) published in 1972 contain excellent chapters on the remote sensing of the ocean that describe both recent research results and microwave, infrared, and visible sensors presently being used to conduct this research. Books specializing in infrared systems include Thermal Imaging Systems (4) by Lloyd and Infrared System Engineering (5) by Hudson. The former was published in 1975 and contains a very good discussion of all aspects of thermal imager design including detector arrays. The latter volume is more general in its approach and in addition, contains over 2100 references that are a comprehensive survey of the infrared literature prior to 1964. There are, of course, many additional books and articles concerned with remote sensors and their applications to oceanography, but these few references should provide sufficient background for someone new to the field to establish their bearings prior to moving on to the more specialized problem with which they may be concerned. Emphasis has been placed on publication dates in the above discussion due to the rapid pace with which the field is developing. In the short two-three years since some of these books were published, minor discrepancies have already appeared between discussed designs and current practices.

II. VISIBLE AND INFRARED IMAGING SYSTEMS

1. The Scanning Radiometer

The infrared scanning radiometer was developed principally because of the inability of film or image tubes to detect radiation of wavelengths greater than 0.7-0.8 micrometer and, as the need for visible and infrared radiometers arose, this type of sensor has been broadened to include visible channels thereby forming the class of multichannel visible and infrared scanning radiometers. Although these sensors ordinarily include both visible and infrared channels they may be designed to detect solely reflected solar or thermally emitted infrared energy, the most notable example of the former being the Multi-Spectral Scanner (MSS) of LANDSAT 1 and 2. This discussion will limit itself to those multichannel scanners in which the motion of the platform relative to the earth's surface provides one scan axis, thereby eliminating the two-axis scanners used with geostationary satellites.

Although, as a group, visible and infrared scanning radiometers consist of many varied designs, they, for the most part, do have certain common elements. Therefore it is possible to discuss in a general way the subsystems of a typical sensor. Such a collection of subsystems is shown in Figure 1. The following paragraphs are brief discussions of each of these subsystems.

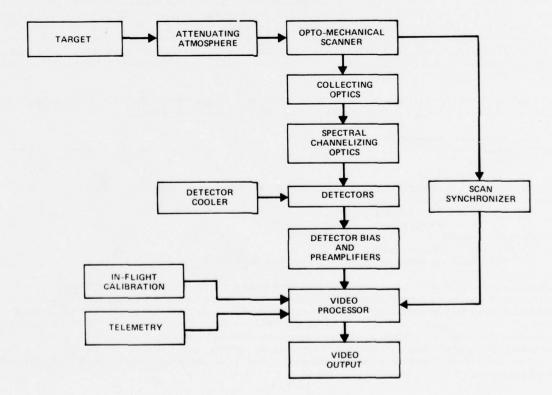


Figure 1. Scanning Radiometer Subsystems

The first two items shown, the target and attenuating atmosphere, are obviously external to the sensor. They are included because they are two of the dominant factors that govern the design of the radiometer. The target and the multi channel algorithm that will be used to separate out the parameters of interest in that target determine the required spectral position and width of the channels, the instantaneous-field-of-view (IFOV) and the required sensitivity of the sensor. However, the sensor design must also consider the contributions that the intervening atmosphere will have on the signal. In the thermal infrared portion of the spectrum the principal effect of the atmosphere on the upwelling radiation is molecular absorption. Therefore, in order to observe the surface, infrared channels are limited to "window" regions of the spectrum where there is very little water vapor (or trace constituent) absorption. The two major window regions are from 3.5-4.0 micrometers and 10.5-12.5 micrometers. For the visible portion of the spectrum, scattering of incident and reflected solar photons into the IFOV of the sensor by both aerosols and molecules is the primary atmospheric effect. Therefore, when observing the color of the ocean as many as 98% of the photons reaching the sensor come from the atmosphere instead of the ocean. However, since this sky radiance is essentially constant for a given solar zenith and viewing angle, it can be subtracted from the sensor signal in order to expand the dynamic range of the desired ocean color signal.

Ordinarily the first element of the imager is the opto-mechanical scanner. This is typically an object plane scan mirror located in front of the collecting optics, there are image plane scanners that scan in the focal plane of the collecting optics, but all of the examples discussed later use object plane scanners. The optical element(s) of the scanner can be passive (flat mirrors) or active (lenses or curved mirrors). Most of today's scanners use flat mirrors the majority either inclined at 45° to the axis of rotation or in the form of a polygon perpendicular to the axis of rotation. tion. Examples of both will be shown later. The major difference in these two systems is that with the inclined mirror system the projected image of the detector (or footprint) rotates as a function of twice the scan angle (measured from nadir). This is not very important unless the focal plane contains an array of detectors, then the relative orientation of their images on the surface will rotate with scan angle. Thus the footprint of a linear array with its long axis lying parallel to the direction of flight at nadir would be perpendicular to the flight direction at a scan angle of ±45°. This does not occur with the polygon scanner. It should, however, be recognized that both scan systems have geometrical distortions. Since the sensor is located at the center of a circle that is projected onto a flat or convex earth, the image will appear compressed near the edges. This effort can be compensated for by using a variable digital sampling rate, a variable speed scan mirror, or by correcting the data during processing on the ground. The latter is the usual solution. A second type of distortion is the increasing size of the footprint with scan angle. This is commonly referred to as the bowtie effect and can only be corrected by changing the IFOV with scan angle. This is not common but has been done. The scan mirror's speed of rotation is usually adjusted so that the along-track distance the surface nadir point moves is very nearly one IFOV per scan line period. Therefore, the lines are contiguous at nadir. However, due to the increasing size of the footprint with scan angle, the scan lines overlap at all other

The collecting optics generally consist of a reflecting cassegrain-type telescope. This serves as the entrance aperture to the sensor and, as shall be shown later, the area of the collecting optics plays a fundamental role in the sensitivity of the complete system.

There are two generally used methods to separate out that part of the spectrum desired for each channel; spectral reflectance or transmission filters and spatial dispersing elements such as prisms or interference gratings. Sensors having several channels in both the visible and infrared portion of the spectrum may use a combination of both methods. The sensors described later use both techniques. In addition to these spectral elements, the channelizing optics include the transfer optics used to direct the photons from the focal plane of the collecting optics to the spectral separation elements, and the condensing optics that focus the spectrally delineated energy onto the detectors. The former, due to their broad spectral requirements are commonly all reflective elements, whereas the latter can be spectrally tailored transmissive optics.

The detectors for the type of sensor under consideration are point or discrete detectors as contrasted to imaging detectors such as the vidicon. The two most commonly used visible detectors (actually visible and near infrared) are the photomultiplier tube and the silicon photodiode. The latter with usable spectral response from 0.4 to 1.0 micrometers has gradually replaced the photomultiplier for most remote sensing applications. Infrared quantum detectors have been the subject of an intense research effort over the last 20 years which has resulted in a technology that is capable of producing very nearly background limited (blip) detectors over much of the infrared spectrum from 3-30 micrometers. As stated earlier, the growth of this technology is directly responsible for the rapid development of the scanning infrared radiometer.

Infrared detectors operating at wavelengths greater than 1.5 micrometer must be cryogenically cooled. Typical temperatures required for infrared detectors operating in the atmospheric windows at 3.5 and 11 micrometers are 77-110K. The three most commonly used methods for detector cooling are open cycle coolers in which the heat from the detector evaporates a liquid cryogen which is stored in a thermally insulated dewar, closed cycle refrigerators which typically use a two-stage compressor and an expansion valve near the detector, and radiative coolers which use the 3K space background as a heatsink. The first two of these are most often used with aircraft sensors where cryogen supplies or the power to drive a compressor are no problem. The radiative coolers have proven to be quite effective with spacecraft sensors. Other methods that have occasionally been used include solid cryogens and thermoelectric coolers.

The detector preamplifiers are one of the most important elements in a visible and infrared radiometer. Their noise figure must be kept low enough for the limiting noise source of the system to be that of the detector, and this noise figure must be preserved through careful system design. Monolithic silicon detector arrays in which the preamplifier and the detector are part of the same silicon chip have very low noise figures. Similar infrared detector systems are under development.

The video processor amplifies the output from the detectors and preamplifiers, shapes the scan synchronizer pulse, blanks the signal from the preamplifiers during portions of the scan when it is not used, multiplexes the various ancillary signals onto the video, and outputs the analog video signal.

The scan synchronizer is a magnetic or optical encoder that is mechanically attached to the scan mirror shaft and serves as an indicator of the mirror's position. This is important both for internal timing in the video processor and for data reduction.

The rediometric accuracy of the imaging radiometer is limited by the accuracy of its calibration. It is especially important in the case of thermal channels that this calibration be updated periodically. This is accomplished by including the output of two or more blackbodies of known but different temperature in the video output. For an accurate calibration of the entire system these blackbodies should be viewed by the scan mirror and should fill the entrance aperture. Aircraft sensors ordinarily use two temperature controlled blackbodies that are viewed once each scan line. Spacecraft sensors typically use a single blackbody that is a portion of the base of the sensor and view space as a second calibration point. Since it is difficult to fabricate a uniformly diffuse visible source that will fill the entrance aperture of any sizable radiometer, the visible calibration is often performed by inserting the source at the focal plane of the collecting optics or by using laboratory calibration data.

Telemetry inserted into the video data stream is usually limited to that necessary for data reduction. Engineering telemetry is outputted via a separate data line. Typical video telemetry voltages include blackbody thermistor outputs, and staircase voltages to ascertain system linearity.

2. The Remote System

The scanning radiometer system, as mounted on the aircraft or spacecraft, includes important elements in addition to the sensor. These elements and their interrelation are shown in Figure 2. The multichannel scanning radiometer shown as the first element in this illustration includes the subsystems described in the previous section and diagramed in Figure 1. The following discussion will consider each of the subsystems of Figure 2.

The digitizer may be included as part of the radiometer or as a separate subsystem. There is usually a separate data line for each channel with all inputs to the digitizer being sampled simultaneously, at a predetermined rate converted by one or more A/D circuits, read into a buffer, and read out of the buffer serially, with a separate serial bit stream for each channel. The inputs to the buffers may be turned off during those portions of the scan in which there is no useful video data, thereby reducing the system data rate considerably. The possible reduction in data rate will be dependent on the scan efficiency of the mechanism used and the field of view. Thus for a rotating inclined mirror system that scans $\pm 45^{\circ}$ about nadir, the data rate can conceivably be reduced to nearly one-fourth the rate resulting from digitizing at a constant rate during the complete revolution of the mirror.

The digitizer/buffer serial data streams enter the multiplexer where the data is interleaved and divided into convenient sized frames each of which has a header consisting of several data words reserved for identification, time code, platform location and attitude, and any other information that will aid in data reduction and analysis. The

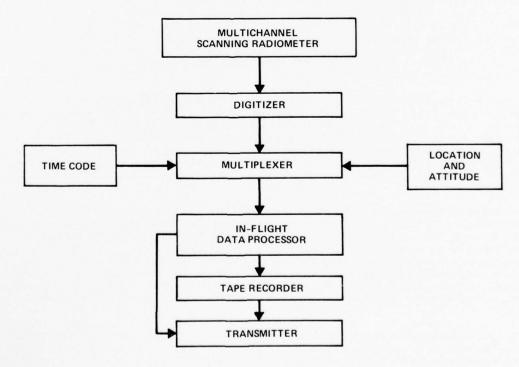


Figure 2. Scanning Radiometer Sensor System

location and attitude data can be supplied by an inertial navigation system for airborne systems or calculated from ephemeris data for spacecraft systems.

The in-flight data processor can either be a microprocessor system designed to perform certain predetermined tasks such as ratioing or differencing of channels or it may be a minicomputer that can be used to perform a wide variety of in-flight calibration and analysis tasks with the additional capability of being reprogrammed via ground commands.

The output from the processor can go either to a wideband tape recorder for storage or to a transmitter for relay to a ground station. Airborne data transmission can be used for real-time sensor performance checks and to aid in interaction with surface vessels.

3. Ground Equipment and Data Reduction

The typical scanning radiometer system described in the preceding two sections and diagrammed in Figures 1 and 2 requires a considerable amount of ground support equipment and a sophisticated data facility in order for the system to be maintained at the peak of its capability and to generate a useful end-product. The types of equipment required and the steps of a typical data calibration and analysis scheme are shown in Figure 3 and discussed in the following paragraphs.

The sensor calibration system includes secondary visible and infrared standard sources of a size to overfill the entrance aperture of the sensor. The most accurate visible source for this purpose is a large aperture integrating sphere suitably coated with a diffuse reflecting material and containing several quartz-iodide lamps that are shielded from a direct view of the sensor's entrance aperture (6). The spectral irradiance from the sphere is measured by comparison with a National Bureau of Standards calibrated quartz-iodide lamp using a spectrometer with a small integrating sphere and a thermopile detector. The infrared calibration source is a controlled, variable-temperature blackbody in a blackened cavity maintained at a temperature much less than the viewed surface. This source, which must also overfill the entrance aperture, is used to calibrate the in-flight blackbodies of the sensor which are, in turn, used to calibrate the data. Great care must be taken to make the surface a near-perfect emitter, to maintain a uniform temperature across the surface, and to measure the surface temperature with the required accuracy.

The thermal vacuum chamber serves to simulate the environment that the sensor will be subjected to including atmospheric pressure, temperature, and, in some cases, radiant sources. The chamber must be capable of holding both visible and infrared sources in order to ascertain the effects of environmental extremes on the sensor's performance. This is especially true for infrared sensors since a change in instrument temperature will result in a change in the radiant energy emitted to and reflected by the in-flight blackbodies, thereby changing their calibration.

Cryogenic equipment that may be required includes liquid cryogen storage and transfer gear for sensors with dewars and for cooling of vacuum chamber walls, closed-cycle liquid helium refrigerators with blackbody panels to

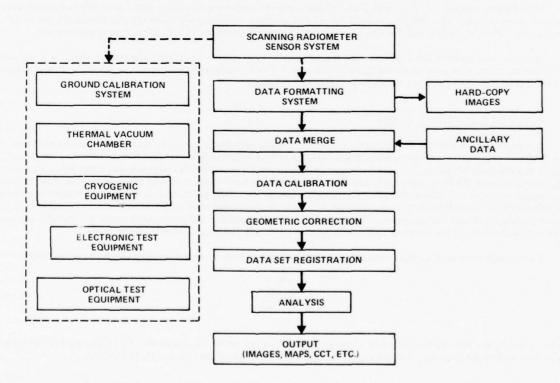


Figure 3. Scanning Radiometer Ground Equipment and Data Reduction Steps

simulate space for bringing radiative coolers to their operating point during vacuum chamber testing and to give a simulated space view which is used as one of the in-flight infrared calibration points, dewars to align and check infrared optics and detectors prior to mounting in the sensor, and clamp-on bench coolers for operating radiative coolers outside the vacuum chamber.

In addition to the normal electronic test equipment contained in any well-equipped laboratory, a remote sensing laboratory should also include a detector test console, digital test gear, time code generator/translator, and a computer-controlled test console for use during sensor testing and calibration.

The major piece of optical test equipment needed is an all-reflective optical collimator with an entrance aperture wide enough to fill all anticipated radiometers and a set of visible and infrared focal plane targets for measuring the modulation transfer function (MTF) of the sensor. A spectrally scanning source of nearly monochromatic radiation is also required in order to measure the spectral response of each channel. In most cases a grating spectrometer is adequate.

The first step in reducing the scanning radiometer data to a useful product is to reformat the multiplexed serial data into computer compatible tapes (CCT's). In the case of some aircraft sensors this step is performed by the inflight data processor. The CCT's can be used to generate an image tape which in conjunction with an electronic image processor can be used to generate images on a television screen, film, or photosensitive paper, in order to check the quality of the data.

Since the data rate of this type of sensor is often quite high, the data may have been recorded on several serial tracks of an in-flight or ground tape recorder. It is, therefore, necessary that these data sets be merged to form a single time-series of CCT's. This can be done as an integral part of the reformatting process or as a separate step. Also, at this point, other data sets such as surface-truth, calibration data, orbit information, and data from other sensors can be merged into the data set.

Data calibration consists of using the calibration information obtained during preflight calibration, from inflight calibration, and, in the case of airborne sensors, post-flight values to convert the digital counts to values of radiant intensity.

Geometric corrections are used to remove the distortions of the image caused by the inherent performance of the scan mechanism. As stated previously, these distortions can be eliminated by various modifications of the basic sensor design. However, these modifications complicate the sensor design to such an extent as to imperil reliability and are therefore not justified in most cases. Corrections performed by the ground data system can range from simple pixel averaging schemes to multi-dimensional interpolation.

The major reason for geometric fidelity is to allow the sensor data to be registered with other data sets such as that from other imagers, surface sensor data, and various parameter and feature maps. This process typically involves matching the sensor data to a digital base map.

Multichannel analysis is essentially converting a series of radiances measured at the sensor to a smaller set of surface parameters. This analysis is performed by algorithms developed via modeling and laboratory and field experiments. Several current schemes will be mentioned in the discussions of specific scanning radiometers.

After the data analysis has converted the sensor output to the required surface parameters, they, in turn, must be put into the form most conveneint for the ultimate user. Types of output include visual displays, radiance images, thematic images, maps, computer compatible tapes, and catalogs.

III. SCANNING RADIOMETER DESIGN

The application of remote sensing to the detection of oceanographic parameters that are of interest to the scientific, commercial, and/or military communities consists of four major phases; (1) problem delineation, (2) multichannel algorithm development, (3) sensor design and construction, and (4) data collection and reduction. This section, concerned with the first part of (3), assumes that (1) and (2) have taken place and have resulted in a set of spectral channel positions and half-widths, desired footprint and swath width, required sensitivity, and probable platform. This information, as shall be shown, is sufficient to enable the development of a preliminary system design. The following paragraphs will develop the sensitivity equations for both visible and infrared channels and thereby demonstrate which elements of the scanning radiometer govern its design and what tradeoffs can be made.

A commonly used performance criteria is the peak-signal to rms-noise ratio (SNR) which can be defined by

$$\frac{S}{N} \equiv \int_{\lambda}^{\lambda_2} \frac{P_{\lambda} d_{\lambda}}{(NEP)_{\lambda}}$$
 (1)

where λ_1 and λ_2 are the wavelength limits of the particular channel under consideration, P_{λ} is the spectral irradiant power received by the detector, and (NEP) $_{\lambda}$ is the spectral noise equivalent power. P_{λ} is given by

$$P_{\lambda} = aA\Omega \tau(\lambda) N_{\lambda} \tag{2}$$

where a is the albedo for reflected solar channels and the emissivity for thermal channels. The emissivity is assumed to be unity for thermal channels viewing water surfaces. A is the area of the entrance aperture of the sensor including losses due to obscuration of the primary mirror by the secondary. Ω is the solid angle subtended by the instantaneous field of view (IFOV). τ (λ) is the wavelength dependent transmission of both the atmosphere and the sensor optics, and N_{λ} is the spectral radiance from the IFOV.

If the spectral bandwidth of the channel does not include strong atmospheric absorption lines and the spectral response of the sensor is constant over the bandwidth, a valid assumption is that:

$$\tau(\lambda) = \tau_0 \text{ for } \lambda_1 \le \lambda \le \lambda_2$$

and

$$\tau(\lambda) = 0$$
 for $\lambda_1 > \lambda > \lambda_2$

Thus,

$$\frac{S}{N} = aA\Omega \tau_0 \int_{\lambda_1}^{\lambda_2} \frac{N_{\lambda}}{(NEP)_{\lambda}} d\lambda$$
 (3)

Equation (3) is true for both reflected solar and thermal channels. It is only when calculations are made for the noise equivalent power for channels in the different wavelength regions, which consequently necessitates different types of detectors, that the sensitivity equations begin to diviate from one another.

A sensitivity criteria used primarily with infrared detectors, the specific detectivity or D* is defined as

$$D^*(\lambda) \equiv \frac{(A_d \Delta f)^{\frac{1}{2}}}{(NEP)_{\lambda}}$$
 (4)

Where A_d is the area of the detector and Δf , the output bandwidth, is given by

$$\Delta f = \frac{1}{2t_d} \tag{5}$$

where td is the IFOV dwell time which, for scan lines contiguous at nadir, is given by

$$\mathbf{t_d} = \frac{\mathbf{h}\Omega}{2\pi\mathbf{v}} \tag{6}$$

where h is the altitude of the sensor platform, Ω is the solid angle subtended by the IFOV, and v is the surface speed of the sensor platform.

Equations (3) and (4) can be combined to give

$$\frac{S}{N} = \frac{A\Omega \tau_0}{(A_d \Delta f)^{\frac{1}{2}}} \int_{\lambda_1}^{\lambda_2} D^*(\lambda) N_{\lambda} d\lambda$$
 (7)

where the emissivity, a, is assumed as unity.

For the thermal infrared channels, the most commonly used sensitivity criteria, instead of the signal to noise, is the noise equivalent temperature difference (NETD). This quantity is usually defined as being that small change in temperature of a blackbody target which will result in a peak-signal to rms noise ratio of unity as measured at the output of the sensor. Since a small change in temperature is equivalent to a small change in radiance, N_{λ} of equation (7) becomes dN_{λ} and

$$dN_{\lambda} = dT \frac{dN_{\lambda}(T)}{dT} \approx \Delta T \frac{dN_{\lambda}(T)}{dT}.$$
 (8)

Combining equations (7) and (8) and the definition of NETD results in

NETD =
$$\frac{(A_d \Delta f)^{\frac{1}{2}}}{A\Omega \tau_0} \left[\int_{\lambda_1}^{\lambda_2} D^*(\lambda) \frac{dN_{\lambda}(T)}{dT} d\lambda \right]^{-1}$$
(9)

For $\lambda T < 4000 \ \mu m^{\circ} K$, Planck's law may be approximated by Wien's radiation law and

$$\frac{dN_{\lambda}(T)}{dT} = \frac{c_1 N_{\lambda}(T)}{\lambda T^2}$$
 (10)

where

$$c_1 = 1.4388 \times 10^4 \ \mu \text{m}^{\circ} \text{K}$$

Therefore

$$NETD = \frac{(A_d \Delta f)^{\frac{V_2}{2}} T^2}{A\Omega \tau_0 c_1} \left[\int_{\lambda_1}^{\lambda_2} N_{\lambda}(T) D^{\bullet}(\lambda) \frac{d\lambda}{\lambda} \right]^{-1}$$
(11)

For the case of photodetectors having theoretical performance such that

$$D^*(\lambda) = \frac{\lambda}{\lambda_p} D^*(\lambda_p)$$
 for $\lambda \le \lambda_p$

and

$$D^*(\lambda) = 0$$
 for $\lambda > \lambda_p$

equation (11) can be simplified to

$$NETD = \frac{(A_d \Delta f)^{\frac{1}{2}} T^2 \lambda_p}{A\Omega \tau_0 c_1 D^* (\lambda_p)} \left[\int_{\lambda_1}^{\lambda_2} N_{\lambda}(T) d\lambda \right]^{-1}$$
(12)

This form of the NETD equation is quite convenient. The integral is evaluated numerically. It should be kept in mind that the NETD is a function of T and that any specification of the NETD of a sensor without quoting the target temperature at which it was calculated or measured is meaningless. Typically the NETD is given for a 300K scene.

In the case of visible or near-infrared channels using silicon photodiodes, the noise-equivalent-power can be expressed as

$$NEP = \frac{1}{S} (i_s^2 + i_d^2 + i_r^2)^{\frac{1}{2}}$$
 (13)

where

S = diode responsivity in ampere/watt

 i_s = shot noise current due to signal flux on the detector

 i_d = photodiode leakage current noise when not illuminated

i, = load resistor Johnson noise current.

The noise currents are given by:

$$i_s^2 = 2eI_s \Delta f$$

$$i_d^2 = 2eI_d \Delta f$$

$$i_r^2 = 4KT \Delta f/R$$
(14)

where

I = signal current

Id = dark current

R = load resistor

 Δf = output bandwidth (see equations (5) and (6)).

Since in Eq. (14) only the signal current is a function of wavelength and it is calculated using the minimum detector illumination, equations (3) and (13) give

$$\frac{S}{N} = \frac{aA\Omega\tau_0 S}{\left(i_s^2 + i_d^2 + i_r^2\right)^{\gamma_2}} \int_{\lambda_1}^{\lambda_2} N_{\lambda} d\lambda \tag{15}$$

where N_{λ} is now the solar spectral radiance and the integral can be extracted from various solar constant tables such as Thekaekara (6), Johnson (7) or Labs and Neckel (8). Strictly speaking, a and S are also functions of λ , but an average value can be readily determined for a given spectral bandwidth with no appreciable loss in accuracy.

Equations (12) and (15) can be used to calculate the performance of the various channels of a visible and infrared scanning radiometer design and to adjust the parameters of that design if it fails to meet the sensitivity required for the desired sensor application. These equations however, assume certain ideal conditions that are modified by reality and neglect certain effects that tend to degrade the performance of the sensor. These effects can be put in the form of a degradation factor, α , which, when multiplied with the NEP, results in a decrease in the sensor sensitivity. Goldberg (7) has identified six multiplicative factors which may contribute to α . These include:

 α_1 - detector operating conditions other than those under which D* (or S) was measured.

 α_2 - effective noise bandwidth including $\frac{1}{f}$ noise

 α_3 - radiation or electronic chopping

 α_4 - electronic filter response

α, - system noise (primarily amplifier noise)

 α_6 - diffraction effects.

Obviously, some of these factors are not applicable to the type of sensor being considered. For instance, the Advanced Very High Resolution Radiometer (AVHRR) design (8), which will be examined in a later section, found that only α_2 and α_5 were significant and that these resulted in $\alpha = 1.6$. Goldberg (7) has demonstrated that in some cases, α may be as large as 13.9. For the type of sensor under discussion the value of α for the AVHRR is more typical.

Thus, equations (12) and (15) when modified by α should give a reasonably accurate estimate of sensitivity that can be expected for a particular sensor design. The sensor itself as was discussed in the preceding section, is only a portion of the complete sensor system and, therefore, the sensor design must be compatible with the total system. With the advent of multichannel scanning radiometers having more channels, smaller IFOV's and wider scan swaths, the factor that impacts system design the most is data output. In fact, in most cases the ability to store, transmit to the ground, and analyze the data from the sensor determines the system design limits rather than the design being governed by state-of-the-art sensor technology.

The data rate, d, from a scanning radiometer is given in bits/second by

$$d = \frac{ncb}{t_d} \tag{16}$$

where n is the number of channels, c is the number of samples/IFOV, b is the number of binary bits used to represent each analog sample, and t_d is the dwell time per IFOV.

Combining equations (6) and (16) gives

$$d = \frac{2\pi n cbv}{\Omega h}$$
 (17)

Since the Nyquist criteria calls for a minimum of 2.5 samples/cycle and since at least two IFOV are required for a complete cycle (black to white or hot to cold), a commonly used value for c is 1.4. The value of b is determined by the sensitivity and range of the sensor and is typically 8 or 10.

An example of the data rates resulting from today's scanners can be had by examining the Coastal Zone Color Scanner (9) slated for a 1978 launch aboard Nimbus-G. The parameters used with equation (17) are

n = 6
c = 1.4
b = 8
v = 6.45 km/sec.

$$\Omega$$
 = 7.48 × 10⁻⁷ st.
h = 925 km

or 2.4×10^{10} bits/orbit which is an order of magnitude larger than available space-qualified tape recorders. Thus, the data must be reduced by onboard processing or the on-time of the sensor limited to those periods that the space-craft is in contact with a ground station.

IV. OCEAN TEMPERATURE SCANNER

The Ocean Temperature Scanner (OTS) is a 5-channel scanning radiometer designed for use aboard medium and high altitude aircraft. The sensor was designed, fabricated, and tested by personnel of the National Aeronautics and Space Administration's Goddard Space Flight Center (10) and has been flow aboard a CV-990 and a U-2 aircraft at altitudes of 11 km and 19.8 km, respectively. This sensor is, in many aspects, a simulator of the Advanced Very High Resolution Radiometer Mod 2 (AVHRR/2) that will be discussed later and is presented here both because it is typical of airborne sensors used to develop spacecraft systems and because of several unique design characteristics.

Table 1 lists some of the design parameters of the OTS. The 3.5 or 7.0 milliradian field of view is determined by the appropriate transfer optics between the focal plane of the 12.5 cm diameter Dall-Kirkham telescope and the detector chips which serve as the limiting aperture for both the infrared and visible channels. Two IVOF's are used in order to achieve approximately the same 70-meter footprint from both medium and high altitude. The difference in scan speed and mirror speed in Table 1 is due to the use of the double-sided scan mirror shown in Figure 4. The scan mirror has its axis of rotation parallel to the direction of flight. As seen in Figure 4, the optical path is from the scan mirror, off a large folding mirror, into the telescope, through the transfer optics, and into the LN_2 dewar where the 4 infrared detector chips are located, each with a bandbass filter immediately in front of it. A two-dimensional view of the optics is shown in Figure 5, which also illustrates the location of the visible detector and its bandpass filter. The visible light is focused on the detector by using the first uncoated germanium relay lens as a concave mirror. The array of infrared detectors is arranged such that its long axis is along the scan line. Thus, the IFOV of the first detector is viewed by the following detectors a few milliseconds later.

Table 2 lists the spectral channels of the OTS and their function. Of principal interest are Channels 3 and 4, the two atmospheric windows in the thermal infrared. Although both of these channels are relatively free of water vapor absorption, the small amounts remaining are sufficient to cause errors in the range of 2-8 K in determining the sea surface temperature. Prabhakara et al. (11) have shown that the difference in absorption in Channels 3 and 4 can be used to linearly extrapolate the temperatures measured by these channels to zero absorption which is equivalent to the true surface temperature. Thus, these channels are included in the OTS in an effort to ascertain the accuracy of this correction and to support the AVHRR/2, which includes these same channels. It may well be that Channel 1 (3.5-4.0 micrometers), which is an atmospheric window with even less water vapor absorption than Channels 3 or 4, can serve as a third point for this extrapolation. Unfortunately, there is enough reflected solar energy in Channel 1 that it would probably be limited to nighttime use.

TABLE 1
OTS Design Parameters

Number of Channels	5 (4 IR, 1 Vis)
Instantaneous Field of View (IFOV)	7.07 or 3.53 mr.
Field of View	±30°
Scan Speed	3.12 Lines/sec
Mirror Speed	1.56 Hz
Range (adjustable)	230 - 330°K (IR)
	0-20% Albedo (Vis)
Sensitivity	NETD (7 mr) = 0.2K @ 300K NETD (3.5 mr) = 0.4K @ 300K (Channel - 4 measured)
In-Flight Calibration (IR)	(a) 35°C Regulated blackbody (Clamp)
	(b) Unregulated blackbody (variable temperature)
In-Flight Calibration (Vis)	Zero-level clamp on blackbody

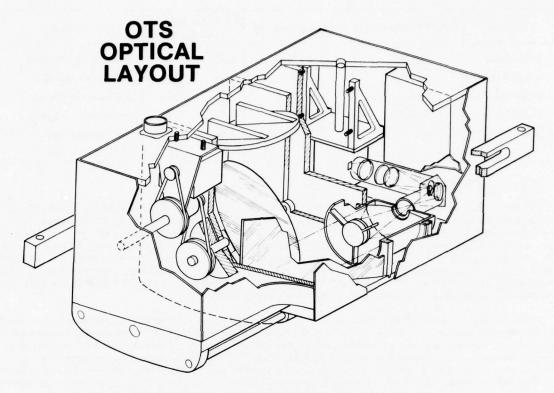


Figure 4. OTS Optical System Schematic

OCEAN TEMPERATURE SCANNER

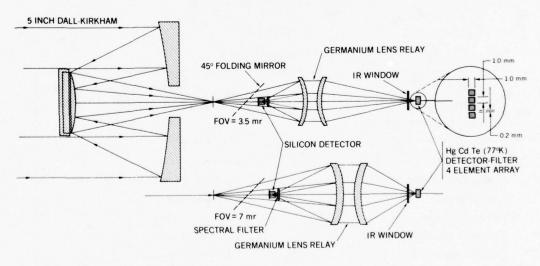


Figure 5. 3.5- and 7-Milliradian Transfer Optics

TABLE 2

OTS Channels

	Channel	Detector Material	Temperature Range		D (°K) ulated)	Purpose
1	3.6-4.1 μm	HgCdTe	280-330	0.33	0.72	atmospheric window
2	6.5-7.0 μm	HgCdTe	280-330	0.09	0.20	H ₂ O vapor detection
3	10.2-11.2 μm	Hg CdTe	280-330	0.05	0.11	atmospheric window
4	11.9-12.9 μm	HgCdTe	280-330	0.07	0.15	atmospheric window
5	0.5-0.9 μm	Silicon	S/N ≈ 1000	7 mr optics	3.5 mr optics	discern cloud contaminated data

V. OCEAN COLOR SCANNER

The Ocean Color Scanner (OCS)(12) is a 10-channel airborne scanning radiometer designed to image reflected solar energy in the range 0.4-1.0 μ m. As was the case with the OTS, this sensor was designed, fabricated, and tested by personnel of NASA's Goddard Space Flight Center. Three duplicate models of the OCS have been assembled to date; they have flown on an F-106, Lear jet, U-2, and Mystere-20 Falcon. The latter aircraft was used to support ocean color experiments by the Joint Research Center, European Communities, off the coast of Holland in the Summer of 1977. Problems that have been studied using data from the OCS include bioproductivity, acid waste dumps, sediment transport, oil spills, and red tide blooms. The sensor's major function is to support algorithm development for the Coastal Zone Color Scanner (CZCS)(9) slated for launch aboard Nimbus-G in 1978.

Tables 3 and 4 list some of the OCS design and performance parameters. The aircraft parameters are from the U-2, this being the platform used for the majority of the flights due to its ability to fly above most of the atmosphere and the synoptic coverage from these altitudes. Figure 6 is a schematic of the OCS optics. The 45° inclined scan mirror is not shown. From the focal plane of the 12.5 cm diameter Dall-Kirkham telescope, the light enters a grating spectrometer which has 24 bundles of glass fibers in its focal plane. Ten of these bundles, positioned so as to cover the spectral intervals shown in Table 4, go to order-isolating filters, optical relays, and silicon photodiodes. The 14 remaining spectral channels can be interchanged with any of the ten output channels as needed.

A photograph of the OES is shown in Figure 7, with the various components labeled. Nadir is towards the top of the photograph. During flight operations, the scanner is enclosed in a semi-cylindrical cover approximately 75 cm long and 25 cm diameter. The scanner mass is approximately 34 kg.

TABLE 3
Radiometer Data

Aircraft Speed	201 meter/sec (390 knots/hour nominal
Aircraft Altitude	19.8 kilometers (nominal)
Angular Resolution (IFOV)	3.5 mr
Footprint	70 m × 70 m
FOV	±45°, from nadir
Scan Rate (mirror speed)	2.727 revolutions/sec
Swath Width	39.6 kilometers
Output Voltage	0 volts to +5 volts
Scanner Information Output	0 volts to +4 volts
Output Bandwidth	0 to 2500 Hertz
Output RMS Noise Level	10 millivolts

 ${\bf TABLE~4}$ Optical Parameters of the Ocean Color Scanner Channels

Channel	Center Wavelength (nm)	Full Width at Half- Height Bandwidth (nm)	Radiance (Gain × 1) mw/cm ² μ
1	431	22.5	80.25
2	472	21.5	65.80
3	506	27.5	42.37
4	548	24.5	26.00
5	586	25.8	19.90
6	625	26.0	15.73
7	667	25.8	12.20
8	707	23.2	9.95
9	738	22.5	126.7
10	778	23.0	6.74

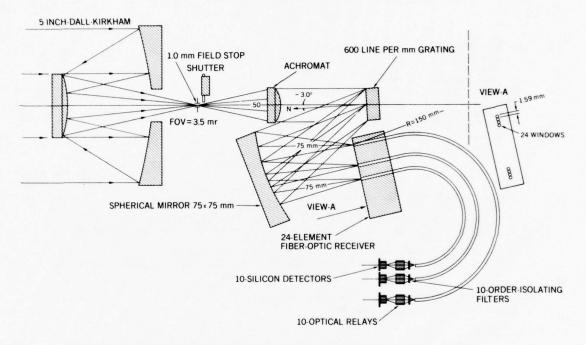


Figure 6. Ocean Color Scanner Optics

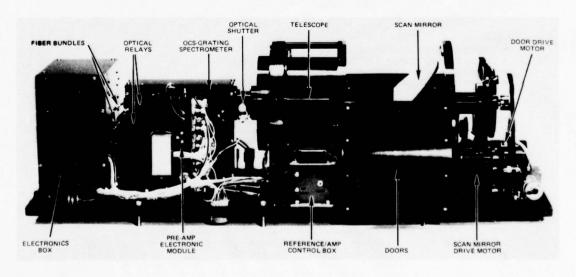


Figure 7. Airborne Ocean Color Scanner

VI. ADVANCED VERY HIGH RESOLUTION RADIOMETER - MOD 2

The Advanced Very High Resolution Radiometer (AVHRR) (13) is a 4-channel visible and infrared scanning radiometer slated for launch aboard the first of the TIROS-N spacecraft in 1978 (which shall be designated NOAA-A when turned over to the National Oceanographic and Atmospheric Administration as part of the operational meteorological system). The AVHRR/2 (8) is a 5-channel version of the AVHRR that will be aboard NOAA-C in 1979 and is expected to be the NOAA operational polar-orbiting visible and infrared imager through the mid-1980's. The AVHRR or AVHRR/2 will replace the VHRR and SR of the present NOAA series. The AVHRR/2 and the Coastal Zone Color Scanner (CZCS) (9), which will be discussed next, are state-of-the-art designs for spaceborne visible and infrared scanning radiometers and are presented here as solutions to specific problems and as examples of present technology. Different objectives may require radically different designs from these, but the discussion of Sections II and III will apply in most instances.

All of the pertinent details of the AVHRR/2 are given in Table 5 (14). The 450 nm orbit and 1.3 mr IFOV result in a 1 km footprint with, as noted in Table 5, all channels co-registered to within 0.1 mr in each axis. The first flight model of the AVHRR has completed all testing and has met the requirements (where applicable) listed in Table 5;

MISSION PARAMETERS

- ORBIT ALTITUDE 450 N. M.
 ORBIT INCL 98.8°
- ORBIT PERIOD 102 MIN. • ASCEND. NODE - 3:30 PM • EARTH ORIENTED - ±1 DEG
- GROUND SPEED 3.5 NM PER SEC • FIRST LAUNCH - NOAA-C 1979
- SUN ANGLE 0°-68° FROM PITCH AXIS

AVHRR/2 SYSTEM CHARACTERISTICS

GENERAL

- 5 CHANNEL SCANNING RADIOMETER, 8" OPTICAL SYSTEM, VIS AND IR CAPABILITY
- PHYSICAL: 30.75 × 14.5 × 11.5 INCHES, 65 POUNDS PER INSTRUMENT
- ELECTRICAL: 28.5 WATTS @ 28 VDC, + 10 VDC + 5 VDC (SCAN MOTOR IN HIGH POWER MODE)
- DATA OUTPUT: 10 BIT DIGITAL; S BAND: 600 kbps DAY, 300 kbps NITE, REAL TIME AND STORED VHF: APT TRANSMISSION
- THERMAL OPERATING RANGE: 10°-30°C; LOUVER CONTROLLED AT +15°C
- STATUS: FLYABLE PROTOFLIGHT AVAILABLE 2nd QCY 1978 MANUFACTURER ITT A/OD FT. WAYNE, IND.

SCANNER

- 360 RPM, 80 POLE HYSTERESIS SYNCHRONOUS, ≤ 17 µsec JITTER (~1/2 IFOV)
- ELLIPTICAL BERYLLIUM SCAN MIRROR

ELECTRICAL

- 10 BIT A/D CONVERTER, SIMULTANEOUS SAMPLE AND HOLD, SEQUENTIAL CONVERSION AND READOUT
- 28 COMMANDS
- 22 ANALOG HOUSEKEEPING PARAMETERS
- 14 DIGITAL TELEMETRY

COOLER

- 2 STAGE PASSIVE RADIANT COOLER FOR 3 IR DETECTORS
- DESIGN TEMP. 98° K; OPERATING TEMP. 105°K/108°K SELECTABLE
- DEPLOYABLE COVER/EARTH SHIELD SINGLE ACTION
- BENCH CHECK CAPABILITY @ 108°K

OPTICS

- 6 INCH AFOCAL, ALL REFLECTIVE, CASSEGRAINIAN TELESCOPE
- PRIMARY: PARABOLOID, 8 IN APERTURE, CERVIT, F_L = 10 INCHES
- SECONDARY: PARABOLOID, 1 IN APERTURE, CERVIT, 8 × MAG. OBSC. 6%
- INTERVERTEX DISTANCE 8.75 IN.
- POLARIZATION < 7%

PERFORMANCE	<u>CH 1</u>	CH 2	<u>CH 3</u>	CH 4	CH 5
SPECTRAL RANGE	0.58-0.68μ	0.725-1.0μ	$10.3 - 11.3 \mu$	3.55-3.93µ	11.5-12.5µ
DETECTOR TYPE	SILICON	SILICON	HgCdTe	InSb	HgCdTe
RESOLUTION	-				-
IFOV	-		1.3 MA X 1.3 MR		-
REGISTRATION	-	withi	N 0.1 MR IN EAC	H AXIS ———	-
S/N	3:1	3:1	$(@ \rho = 0.5\%)$		
NETD	N/A	N/A	-	< 0.12°K @ 300°F	
MTF (@ 1 IFOV)	-		0.30		-
DYNAMIC RANGE	← 0.5% to 100	% ALBEDO		- 4°K to 320°K-	-

it is not expected that the AVHRR/2 will have any difficulty in performing to these same specifications. A photograph of the AVHRR is shown in Figure 8 with nadir towards the top of the figure. Since AVHRR and AVHRR/2 are externally indistinguishable, this figure can serve for either. Figure 9 is an exploded view of the sensor broken down into its five basic modules. The black area on the baseplate serves as the in-flight calibration blackbody. The deep notch on the cooler side of the scan cavity allows the sensor to view deep space which serves as a second calibration point for the infrared channels and as a zero-clamp for both visible and infrared channels. The door on the passive cooler remains closed until 1-2 weeks after launch to prevent contamination of its heat-emitting surfaces by volatiles outgassed by the spacecraft and its sensors and then serves as a shield to prevent the cooler from viewing the earth or its atmosphere.

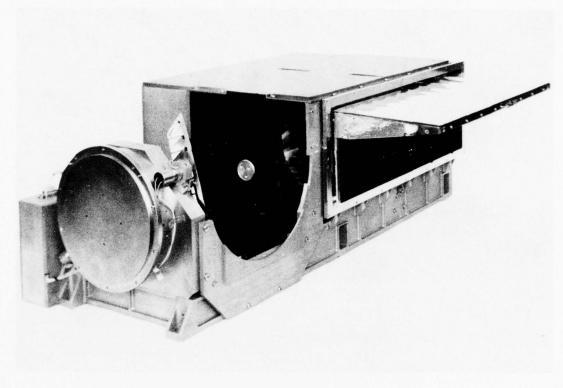


Figure 8. AVHRR

Figure 10 shows all of the optical elements of the AVHRR/2 except the scan mirror. Elements labeled M are mirrors, F are filters, W are windows, L are lenses, and D are dichroic filters. The box labeled "vacuum" is the back of the passive cooler which is operable in the laboratory by placing an evacuable ${\rm LN}_2$ cooler over its front surface.

The AVHRR/2 is destined to supply data for a wide variety of meteorological, hydrological, and oceanographic parameters, but the major reason for adding the fifth channel was to insure the AVHRR's capability of measuring global sea surface temperature to an absolute accuracy of less than 1.0 K using the technique discussed in Section IV.

VII. COASTAL ZONE COLOR SCANNER

The Coastal Zone Color Scanner (CZCS) (9) is a six channel scanning radiometer slated for launch aboard Nimbus-G in October, 1978 and is expected to make measurements in both coastal and open ocean for the purpose of observing chlorophyll concentrations, yellow stuff, surface vegetation, and surface temperature. The CZCS is the first spacecraft sensor dedicated to the study of biological oceanography. It differs from the AVHRR in that it is an experimental sensor and will therefore be used to develop new applications rather than as an operational data collector as is the case with the AVHRR.

A summary of the CZCS is given in the same format as was used with the AVHRR/2 in Table 6. A comparison of Tables 5 and 6 reveals many similarities between the CZCS and the AVHRR/2. Basically, however, the two sensors are quite different, the CZCS is predominately a visible energy detector using a grating spectrometer to spectrally delineate most of its channels whereas the AVHRR/2 has mainly infrared channels and uses interference filters to separate the channels. A unique feature of the CZCS design is the ability of the scan mirror to tilt ±350 mr. thereby shifting the scan lines fore or aft of the spacecraft nadir point. This is done in order to avoid the specular reflection of the sun from the water's surface commonly known as sun-glint. The amount and direction of this tilt is commandable from the ground.



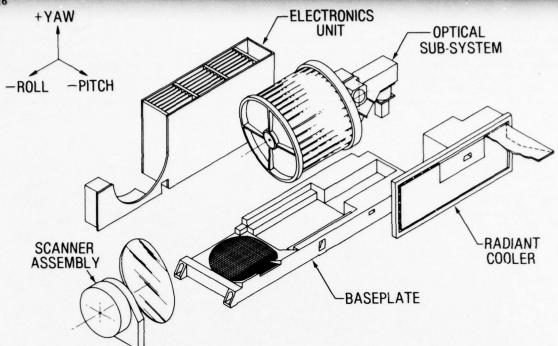


Figure 9. AVHRR/2 Basic Modules

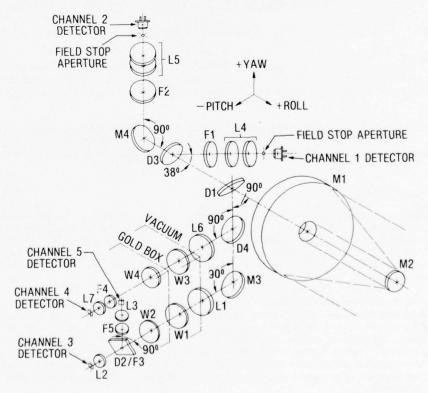


Figure 10. AVHRR/2 - Optical Elements

TABLE 6

SUMMARY - COASTAL ZONE COLOR SCANNER CZCS

MISSION PARAMETERS

ORBIT ALTITUDE - 955 KM
ORBIT INCLINATION - 99°
ORBIT PERIOD - 103.5 MIN.
SURFACE SPEED - 6.6 KM/SEC
SPACECRAFT - NIMBUS-G
LAUNCH - OCTOBER 1978

CZCS SYSTEM CHARACTERISTICS

GENERAL

6 CHANNEL SCANNING RADIOMETER, VIS AND IR CAPABILITY PHYSICAL: 69 x 43 x 26 CM, 25.8 KG ELECTRICAL: 24.3 WATTS AVG., < 40 WATTS PEAK DATA OUTPUT: 8 BIT DIGITAL, 3.94 \times 10^6 BITS/SEC (MAX), 8 \times 10^5 BITS/SEC (AVG.) MANUFACTURER: BALL BROTHERS RESEARCH CORP., BOULDER, COLO.

SCANNER

8.0 HZ, 80 POLE HYSTERESIS SYNCHRONOUS MOTOR ELLIPTICAL BERYLLIUM SCAN MIRROR ±350 MR TILT IN PITCH IN 540 STEPS

ELECTRICAL

8 BIT A/D CONVERTER, SIMULTANEOUS SAMPLE AND HOLD 22 ANALOG TELEMETRY POINTS 30 DIGITAL TELEMETRY POINTS 38 COMMANDS

COOLER

2 STAGE PASSIVE RADIANT COOLER FOR 1 CHANNEL 113K DESIGN TEMP., 120K OPERATING TEMP. COVER/EARTH SHIELD DEPLOYS OR CLOSES ON COMMAND BENCH OPERABLE

OPTICS

17.8 CM DIAMETER CASSEGRAIN F/4 TELESCOPE WADSWORTH TYPE GRATING SPECTROMETER (CHAN. 1-5) POLARIZATION SENSITIVITY < 1.5 PERCENT 0.865 MR IFOV, 0.83 x 0.83 KM FOOTPRINT SPATIAL RESOLUTION (MTF) > 0.4 FOR 1 IFOV CHANNELS REGISTERED WITHIN 0.15 MR ALL DIRECTIONS SCANNING FIELD OF VIEW ±700 MR

PERFORMANCE

CHANNEL	SPECTRAL RANGE	DETECTOR TYPE	S/N	NETD
1	.433453 μm	Si	217	NA
2	.510530 μm	Si	218	NA
3	.540560 μm	Si	201	NA
4	.660680 μm	Si	114	NA
5	.700800 µm	Si	308	NA
6	10.5-12.5 μm	HgCdTe	303	0.2K (270K)

A line drawing of the CZCS pointing out the major features is given in Figure 11, and a photograph of the scanner mounted on a laboratory test stand is shown in Figure 12. As discussed in Section III, the data rate of the CZCS is too large for a complete orbit's output to be stored using present tape recorders. Consequently, only a few minutes of data per orbit will be stored, using stored commands for preselection of target areas. The majority of the data will be obtained via direct transmissions while in view of ground stations. The location of these stations, however, does give extensive coverage of coastal areas in both North America and Europe.

Figure 13 is a diagram of the CZCS optical elements. A unique feature of this design is the pseudopolarizer consisting of two birefringent wedges that are located just prior to the concave 600 line/mm grating which is highly polorizing. Using these wedges and careful optical design, the polarization of the radiometer is kept at less than 2% for channels 1-4, thereby, preserving the radiometric accuracy of the sensor while viewing polorized scenes.

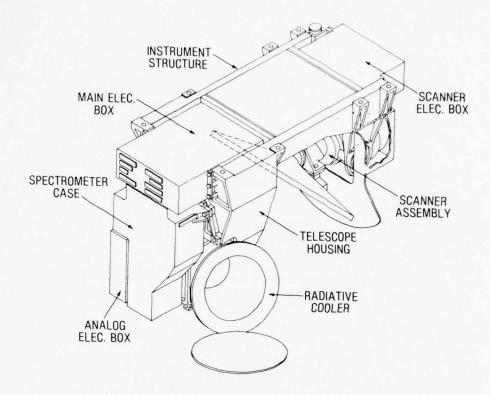


Figure 11. CZCS-Major Components

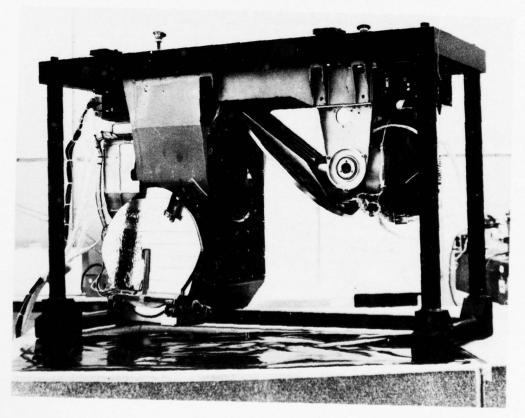


Figure 12. Nimbus-G CZCS

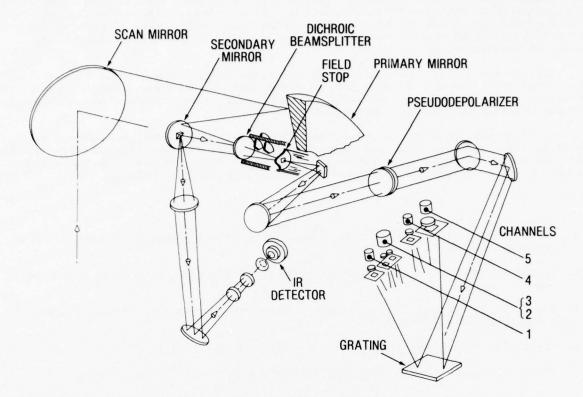


Figure 13. CZCS Optical Elements

VIII. NEW TECHNOLOGY

The preceding sections have examined the present status of scanning radiometer system design and have presented several existing spacecraft and aircraft sensors as examples of implementation of these design practices. Although the example sensors have either been in use for only a brief time or are still being fabricated and tested, their designs were finalized some 1-3 years back and, consequently, do not include some of the latest innovations. Therefore, this section will briefly examine present trends in visible and infrared imaging radiometer design and developments in various types of system hardware. This discussion is not intended to be comprehensive but is meant to sketch out probable trends in the development of this type of sensor over the next few years. The reader is urged to examine the current literature for detailed descriptions of individual topics.

From the discussion of Section III, it is apparent that among the major difficulties of scanning radiometry are the brief dwell time on each IFOV and the inherent complexity of mechanical scanners. Both of these problems are being addressed through the development of large detector arrays. For example, a linear array of a few hundred to several thousand detector elements can be used to form a single scan line whose image is swept along the surface by the motion of the sensor platform. Consequently, the need for a scan mirror is eliminated and the dwell time on each IFOV is increased by the number of elements in the array divided by the efficiency of the mechanical scanner and, using equations (5) and (7), the signal-to-noise increases by the square root of this factor. This increase in signal-to-noise can be traded for increased spatial or spectral resolution if so desired. One and two dimensional arrays of silicon detectors with integrated CCD readouts have been available for some time. The so-called "pushbroom" scanners using linear silicon arrays have been proposed for spaceborne applications and are presently under construction (15) for airborne use. Unfortunately, the development of integrated infrared detector arrays has proven to be a difficult task. The most promising results to date appear to be the hybrid arrays in which the multi-element detector chip and the integrated read-out electronics chip are hardwired together. This technology is available today but is rather cumbersome to implement for large numbers of detector elements.

The use of two-dimensional arrays can further increase the signal-to-noise and/or resolution of a radiometer. The usual mode of implementation for moving platforms is for the array to view a given scene on the surface for as long a period as necessary via image motion compensation. Preselected targets can be acquired by stored commands.

Another major problem of scanning radiometers, touched on briefly in the last part of Section III, is their enormous data output. For many applications, it is possible to reduce this flood of data by digital processing prior to transmission or storage. This processing can take the form of a simple averaging of several pixels as will be done with the AVHRR data or it may involve complex analysis. The means of carrying out this on-board processing can be a hardwired system or it can be a remotely programmable computer. The latter has the advantage that changes in the performance of spacecraft sensors can be adjusted for by reprogramming after launch. Such systems exist today, and there will probably be a marked increase in their data processing capabilities over the next few years.

Problems in data storage and transmissions are being attacked on two fronts. Solid-state mass storage devices have undergone intense development with the aim of using them to replace the present tape recorders and they appear to be nearing this goal. In addition, synchronous satellite systems such as the Tracking and Data Relay Satellite System (TDRSS) are being developed so that data from aircraft or orbiting satellite sensors can be relayed directly to a ground station from any spot on the globe.

Due to increasingly sophisticated radiometry requirements, the development of large arrays of infrared detectors, and the need to locate spectral channels in the far infrared, there is an ever-increasing need for larger capacity, lower temperature cryogenic coolers. These will take the form of large passive coolers, large capacity LHe dewars, and high thermal capacity and/or low temperature closed-cycle systems.

Finally, one of the greatest impacts on sensor design technology will probably arise from the advent of the Shuttle/Spacelab era. Not only will this provide a large spaceborne platform with direct scientist/operator control for the development of new remote sensing techniques, but, due primarily to its low orbit, it will make possible combined passive, and active visible and infrared sensors through the use of laser ranging and radiometry.

REFERENCES

- Reeves, R. G., Arson, A., and Landen, D., Editors, <u>Manual of Remote Sensing</u>, American Society of Photogrammetry, Falls Church, Va., 1975.
- Lintz, I, and Simonett, D. S., Editors, Remote Sensing of the Environment, Addison Wesley, Reading, Mass., 1976.
- 3. Derr, V. E., Remote Sensing of the Troposphere, U.S. Dept. of Commerce, National Oceanic and Atmospheric Administration, Boulder, Colo., 1972.
- 4. Lloyd, J. M., Thermal Imaging Systems, Plenum Press, New York, N. Y., 1975.
- 5. Hudson, R. D., Infrared System Engineering, John Wiley and Sons, New York, N.Y., 1969.
- McLean, J. T., "Operation Manual for 30-Inch Diameter Spherical Integrator Source for the AVHRR on TIROS-N," NASA/GSFC X-942-75-18, 1975.
- Goldberg, I. L., "A Very High Resolution Radiometric Equipment for ATS-F and G," NASA/GSFC Preprint X-622-68-26, Greenbelt, Md., 1968.
- 8. Juarez, D., "Advanced Very High Resolution Radiometer, Mod 2, Technical Description," Contract #NASS-23400, ITT Aerospace/Optical Division, Ft. Wayne, Ind., 1976.
- 9. Richard, H. L., Technical Officer Nimbus-G/CZCS, personal communication.
- 10. Barnes, W. L., and Escoe, D., "Ocean Temperature Scanner Experiment Plan," NASA/GSFC Preprint X-941-77-94, Greenbelt, Md., 1977.
- Prabhakara, C., Conrath, B. J., and Kunde, V. G., "Estimation of Sea Surface Temperature From Remote Sensing in the 11-13 μm Window Region," Journal Geophysical Research, Vol. 79, No. 33, Nov. 1974. pp. 5039-5044.
- 12. Barnes, W. L., Blaine, L. R., and Murphy, C. J., "Ocean Color Scanner Experiment," NASA/GSFC Preprint X-941-77-38, Greenbelt, Md., 1977.
- 13. Jaurez, D., "Advanced Very High Resolution Radiometer Technical Description, Revision B," Contract #NASS-21900, ITT Aerospace/Optical Division, Ft. Wayne, Ind., 1974.
- 14. Donohue, M. J., AVHRR and AVHRR/2 Systems Engineer, personal communication.
- 15. Ostrow, H., NASA/GSFC, personal communication.

RADAR A FAISCEAU LATERAL UTILISANT UNE ANTENNE SYNTHETIQUE

J.Genuist Thomson-CSF Malakoff,France

RESUME

Le radar à faisceau latéral, à antenne synthétique, permet d'obtenir une image de très grande résolution des terrains survolés par un avion.

La résolution en distance radar, suivant la direction perpendiculaire à la route de l'avion, est obtenue avec une émission-réception à impulsions très fines, réalisée avec la technique de compression d'impulsion.

La résolution longitudinale, suivant la route de l'avion est obtenue par traitement du signal Doppler.

Deux catégories de traitement ont été expérimentées :

- Traitement par simple filtrage qui conduit à une résolution théorique de la forme :

$$\sqrt{\frac{\lambda \ d_o}{2}}$$

λ : Longueur d'onde

d : Distance de la cible.

et à la notion d'antenne synthétique non focalisée.

- Traitement par corrélation qui conduit à une résolution théorique de la forme : $\frac{L}{2}$

L : Dimension de l'aérien.

et à la notion d'antenne synthétique focalisée.

Différents résultats expérimentaux sont présentés pour chacun des procédés en analysant les avantages et inconvénients.

1 - INTRODUCTION

Le radar aéroporté à faisceau latéral à antenne synthétique permet d'obtenir, par tous temps, une carte de définition suffisante pour identifier les détails topographiques naturels ou artificiels de la région survolée, et pour faire apparaître, entre deux vols successifs, les modifications éventuelles de la configuration de la zone surveillée.

La résolution transversale, suivant la distance radar perpendiculaire à la route avion, dépend du spectre émis.

La résolution longitudinale, suivant la route avion, obtenue par traitement du signal Doppler est bien meilleure que la résolution naturelle due au faisceau de l'antenne, définie par :

$$\frac{\lambda}{L} d_{o}$$

λ : Longueur d'onde

L : Dimension de l'aérien

d : Distance de la cible

Différents traitements du signal peuvent être envisagés que l'on peut classer en deux catégories :

- Traitements par filtrage simple du signal qui conduit à une résolution

$$\sqrt{\frac{\lambda d_o}{2}}$$

et à la notion d'antenne synthétique non focalisée,

- Traitement par filtre adapté ou par corrélation qui conduit à une résolution

$$\frac{L}{2}$$

indépendante de la distance et à la notion d'antenne synthétique focalisée. La planche I donne, pour une dimension d'antenne, les résolutions théoriques comparées pour quelques exemples de distance.

THOMSON-CSF a expérimenté différents types de traitement, mais seuls les résultats obtenus avec le traitement par filtres électriques ou par corrélation optique retiendront notre attention au cours de cette conférence.

Les cartes radar ne figurent pas dans les planches de ce document, elles seront projetées en cours de conférence.

2 - RAPPEL DE LA GEOMETRIE DU SYSTEME

La représentation de la géométrie du radar à faisceau latéral est donnée planche 2. Le faisceau d'antenne est orienté perpendiculairement à la route avion. Pendant la traversée du faisceau, la distance avion-cible varie et passe par un minimum do quand la cible est vue par le travers de l'avion.

A cette variation de distance est liée une variation de phase, mise en évidence par l'utilisation d'un radar cohérent qui conserve la référence de la phase de l'onde émise.

En prenant comme origine, l'instant où l'avion passe par le travers de la cible, on peut écrire :

$$d = d_0 + \frac{v^2 + v^2}{2 + d_0}$$

car le déplacement de l'avion est lié à sa vitesse par la relation X = Vt.

La phase du signal réfléchi comparée à la phase du signal émis, conservée en mémoire s'écrit :

$$\emptyset = \frac{4\pi - d}{\lambda} = \frac{4\pi}{\lambda} d_0 + \frac{2\pi}{\lambda d_0} V^2 t^2 = \emptyset_0 + kt^2$$

A la variation quadratique de la phase est liée une variation linéaire de la fréquence Doppler définie par la relation :

$$f_d = \frac{1}{2 \pi} \frac{d0}{dt} = Kt$$

La détection synchrone met en évidence un signal radar de la forme :

$$S_R(t) = S \cos \emptyset = S \cos (\emptyset_0 + kt^2)$$

La durée de ce signal est limitée au temps de traversée de la cible dans le faisceau :

$$T_{O} = \frac{2 \theta_{O} d_{O}}{V}$$

avec 2 $\theta_{_{\rm O}}$: ouverture angulaire du faisceau d'antenne.

Les équations précédentes définissent le signal radar d'une cible ponctuelle, en supposant que le système global (radar et traitement) est linéaire, on peut par superposition appliquer les résultats à une cible réelle complexe.

3 - TRAITEMENT PAR FILTRAGE PASSE BAS

Principe

Avec ce type de traitement, seule est conservée la partie du signal contenant les fréquences Doppler très basses (planche 3). Dans ces conditions, la cible n'est visualisée qu'un court instant quand elle se présente par le travers de l'avion.

L'affinage obtenu est limité à une valeur telle que l'enveloppe du signal se réduit à un spectre dont la largeur égale celle du filtre passe bas.

La valeur optimum de la constante de temps du filtre qui donne le meilleur contraste du signal après traitement est égale à :

$$\sqrt{\frac{\lambda \ d_o}{2\pi \ V}}$$

Par rapport à la résolution naturelle $\frac{\lambda}{L}$ d_o due à l'ouverture du faisceau d'antenne, le taux d'affinage du traitement par filtre passe bas est :

$$\sqrt{\frac{2\lambda~d_o}{L^2}}$$
 La largeur de l'écho affiné étant : $\sqrt{\frac{\lambda~d_o}{2}}$

Synoptique (Planche 4)

Le radar utilise un émetteur à magnétron dont la durée d'impulsion conduit à une résolution transversale homogène avec la résolution longitudinale. La phase du signal émis est mise en mémoire dans un oscillateur cohérent FI, synchronisé par l'impulsion magnétron après transposition en FI. Après détection cohérente, les signaux reçus sont inscrits dans un banc de filtres permettant de traiter autant de signaux S_R (t) qu'il y a de quanta de distance à obtenir pour la résolution transversale recherchée dans le domaine de terrain à visualiser.

A chaque récurrence radar, un commutateur adresse, successivement dans le temps, les signaux vers le filtre correspondant au quatum de distance à traiter.

Après filtrage, un commutateur de lecture permet d'envoyer la "vidéo affinée" vers un système de représentation constitué d'un indicateur et d'un système photographique associé.

Résultats

Présentation de quelques cartes radar.

4 - TRAITEMENT PAR CORRELATION OPTIQUE

Principe

Le signal S_R (t) est inscrit en transparence sur un film. On a pris soin de superposer à S_R (t) une composante moyenne S_0 telle que l'on puisse inscrire S_R (t) avec son signe (planche 5).

Cette inscription obtenue au moyen d'un tube cathodique devant lequel se déplace un film à vitesse constante transforme la fonction temporelle S_R (t) en fonction spatiale S_R (X) avec X = Vt (au facteur d'échelle près).

Plaçons ce film sur le chemin optique d'une onde plane (Planche 6).

Si E $_{o}$ cos ωt est le champ incident tombant sur le film, le champ transmis aura une répartition suivant X telle que :

$$S(X) = \frac{E_0}{2} \left[1 + \cos \left[k_1 X^2 + \emptyset_0 \right] \right] \cos \omega t$$

ω : est la pulsation de la lumière incidente $\left[ω$ = 2π f $_L$ = $\frac{2π c}{λ_L}\right]$

k, est égal à :

$$\frac{2 \text{ II}}{\lambda d}$$

La fonction S (X) est équivalente à trois ondes :

- Une onde plane α : $\frac{E_o}{2}$ $\cos \, \omega t$

- Une onde sphérique convergente, de centre 02, $\beta:\frac{E_0}{4}\cos\left[\omega t + k_1 x^2 + \emptyset_0\right]$

- Une onde sphérique divergente, de centre 01, γ : $\frac{E_o}{4}$ cos $\left[\omega t - k_1 X^2 - \emptyset_o\right]$

Le facteur d'échelle μ étant connu, on trouve alors pour 00 $_1$ et 00 $_2$ la valeur commune :

F =
$$00_1 = 00_2 = \mu^2 \frac{\lambda}{\lambda_1} \frac{d_0}{2}$$

La décomposition optique ainsi obtenue est liée à l'axe de symétrie de la fonction $S_{\mathbf{p}}$ (X) inscrite, donc à la position du film le long de X.

Une fente très fine F fixe, placée en 02, recevra un flux lumineux important.

Un film de sortie placé derrière cette fente inscrira un signal comprimé quand l'axe de symétrie de la fonction passera par la fente F.

Pour obtenir une représentation conforme des échos enregistrés, il suffit de faire défiler le film de sortie en synchronisme avec le film sur lequel la fonction S_R (X) est inscrite.

Ce signal comprimé a une dimension égale à la dimension de l'antenne portée par l'avion au facteur d'échelle μ près.

La fonction ainsi obtenue est la fonction de corrélation de S_R (X) [planche 7] . Pour obtenir une bonne dynamique, il faut éliminer la composante divergente parasite (onde γ). Ceci est réalisé en ajoutant une porteuse au signal Doppler enregistrê.

Comme on le montre planche 8, cette porteuse confère au système en effet prismatique et permet ainsi de recueillir la composante utilise (onde β) derrière une fente disposée en dehors des faisceaux des ondes parasites.

Tous les résultats précédents peuvent se retrouver en utilisant les phénomènes de diffraction qui font appel aux transformations de FOURIER.

Synoptique (planche 9)

Pour obtenir une résolution transversale homogène à la résolution longitudinale, le radar utilise une émission-réception d'impulsion très fine avec la technique de compression d'impulsions.

Après détection cohérente, les signaux Doppler sont envoyés à un système d'enregistrement photographique comprenant :

- un indicateur, équipé d'un tube cathodique flying-spot, modulé en lumière et balayé suivant une seule dimension : en distance radar,
- un objectif,
- une caméra qui fait défiler un film dans le plan image de la face avant de l'indicateur, perpendiculairement à la trace et à une vitesse proportionnelle à celle de l'avion.

La qualité du traitement par corrélation nécessite que la loi Doppler des signaux enregistrés soit aussi proche que possible de la loi de référence cos $(\cancel{p}_{\alpha} + kt^2)$.

Cette loi idéale est obtenue en considérant que l'avion porteur, décrit une trajectoire rectiligne horizontale d'un mouvement uniforme.

Tout écart par rapport à cette trajectoire idéale, introduit sur les signaux reçus des variations de phase parasites qui doivent être compensées en réception. Ceci est réalisé en effectuant, sur l'onde de référence du détecteur cohérent, des corrections de phase proportionnelles aux écarts de l'avion par rapport à la trajectoire idéale.

Le film des informations Doppler, enregistré en vol, est développé au sol, puis analysé dans le corrélateur optique.

Le film de sortie du corrélateur donne la carte radar exploitable.

Des photographies des différents éléments du radar sont présentées au cours de la conférence.

Résultats

Présentation de quelques cartes radar.

Conclusion

Les expérimentations effectuées avec l'affinage par filtre ou par corrélation ont permis de s'approcher des limites théoriques des résolutions.

D'autres types de traitement ont également été essayés mais présentent des inconvénients divers, tels que l'affinage par spot et le filtre adapté associé à une mise en mémoire des informations Doppler sur un tube à mémoire.

Grâce aux progrès technologiques, d'autres orientations sont désormais possibles, comme la corrélation électronique numérique qui permet l'obtention des cartes radar en vol, pratiquement en temps réel.

Nous terminons en remerciant le Service Technique des Télécommunications de l'Air qui a financé ces différentes études et autorisé cette présentation de résultats. Nous remercions également le Centre d'Essais en Vol de Brétigny qui a réalisé l'expérimentation de nos matériels.

LARGEUR THEORIQUE DES ECHOS EN ROUTE AVION

DISTANCE RADAR	SANS TRAITEMENT	AVEC TRAITEMENT	
		FILTRAGE VAdo 2	CORRELATION L
1 km	35 m	4 m	0,5 m
5 km	175 m	9 m	0,5 m
10 km	350 m	13 m	0,5 m

L = Longueur antenne = 1 mètre

 λ = Longueur d'onde = 3,3 cm

Planche 1

EFFET DOPPLER

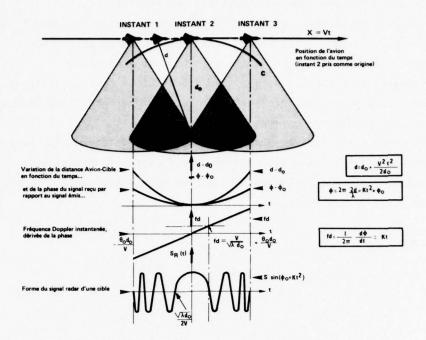


Planche 2

AFFINAGE PAR FILTRE

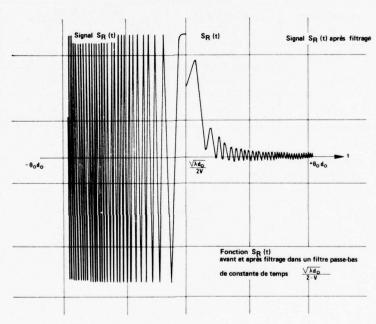


Planche 3

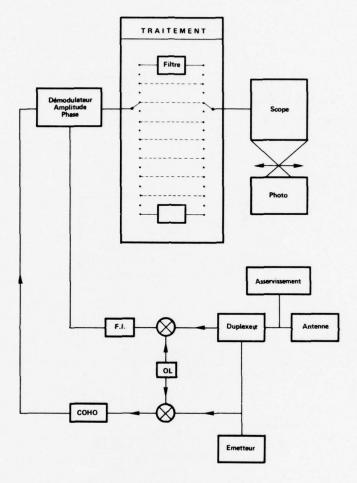
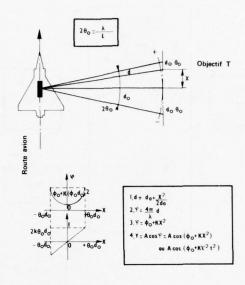


Planche 4

INFORMATION BRUTE INSCRITE A BORD DE L'AVION



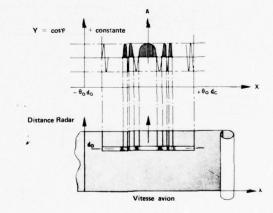
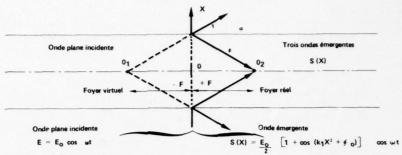


Planche 5

TRAITEMENT OPTIQUE DE LA FONCTION SR (X)

Point de vue de l'optique géométrique



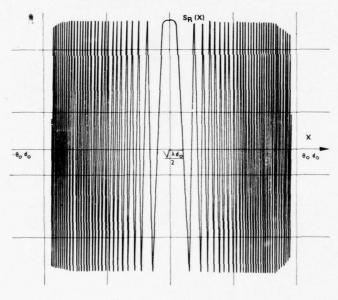
Echo Doppler inscrit en transparence sur le film $S_0^- + S_R^-(X) = -\frac{1}{2} - \left[1 + \cos^-(k_1 X^2 + f^-_0)\right]$

Distance focale : F $= \mu^2 \frac{\lambda}{\lambda_L} \frac{d_O}{2}$

 $S \ (X) \begin{cases} \text{Onde plane} \ \alpha \ : \ & \frac{E_0}{2} \ \cos \ \omega t \\ \\ \text{Onde convergente } \vartheta \ : \ & \frac{E_0}{4} \ \cos \ (\omega t + KX^2 + \phi_c \cos \omega t + KX^2 + \phi_c \cos \omega t) \end{cases}$

Planche 6

SIGNAL COMPRIME SRC APRES TRAITEMENT OPTIQUE



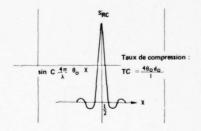
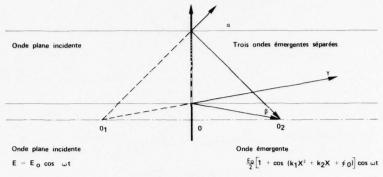


Planche 7

TRAITEMENT DE LA FONCTION S R (X)

INTRODUCTION D'UNE PORTEUSE



Echo Doppler inscrit en transparence sur le film

$$S_0 + S_R(X) = \frac{1}{2} \left[1 + \cos (k_1 X^2 + k_2 X + \phi_0) \right]$$

Planche 8

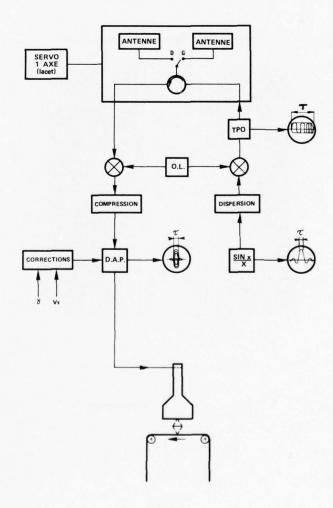


Planche 9

SIDEWAYS-LOOKING RADAR (SLR) USING A SYNTHETIC AERIAL

by

J.Genuist Thomson-CSF, Malakoff, France

SUMMARY

The sideways-looking radar (SLR) with synthetic aerial enables a very high resolution image to be obtained of the terrain overflown by an aircraft.

The radar range resolution along the direction perpendicular to the path of the aircraft is obtained with a very fine pulse transmission-reception, using pulse compression technique.

The longitudinal resolution, along the path of the aircraft is obtained by processing the Doppler signal.

Two categories of processing have been tried:

- Processing by simple filtering which leads to a theoretical resolution of the form:

$$\sqrt{\frac{\lambda d_0}{2}}$$

 λ : wavelength

do: range of the target,

and to the idea of an unfocussed synthetic aerial.

- Processing by correlation, which leads to a theoretical resolution of the form:

L/2

L: dimension of the aerial

and to the idea of the focussed synthetic aerial.

Different experimental results are presented for each of the processes, analysing the advantages and disadvantages.

1. INTRODUCTION

The airborne SLR with synthetic aerial enables a map to be obtained in all weather with sufficient definition for identifying natural or artificial details of the region overflown and to reveal, between two successive flights, any changes in configuration of the zone surveyed.

The transverse resolution, along the radar range perpendicular to the aircraft path, depends on the spectrum emitted.

The longitudinal resolution, along the aircraft path, obtained by processing the Doppler signal, is much better than the natural resolution, due to the aerial beam, defined by:

$$\frac{\lambda}{L} d_0$$

λ: wavelength

L: dimension of the aerial

do: range of the target.

Different processings of the signal can be considered which can be classified in two categories:

- Processing by simple filtering of the signal, which leads to a resolution

$$\sqrt{\frac{\lambda d_0}{2}}$$

and to the idea of the unfocussed synthetic aerial.

Processing by matched filter or by correlation, which leads to a resolution

1./2

independent of the range, and to the idea of the focussed synthetic aerial. Figure 1 gives, for one dimension of the aerial, comparative theoretical resolutions for some range values.

Thomson-CSF has tried different types of processing, but only the results obtained with processing with electrical filters or by optical correlation will receive our attention during this paper.

The radar maps do not appear in this document; they will be projected during the lecture.

2. RECAPITULATION OF THE GEOMETRY OF THE SYSTEM

The geometry of the SLR is represented in Figure 2. The aerial beam is directed perpendicularly to the aircraft path. During the traversal of the beam, the aircraft-target distance varies and passes through a minimum d_0 when the target is seen abeam of the aircraft.

With this range variation is associated a phase variation, revealed by the use of a coherent radar which preserves the reference of the transmitted wave phase.

Taking as origin the moment when the aircraft is abeam of the target, one can write:

$$d = d_0 + \frac{v^2 t^2}{2d_0}$$

since the movement of the aircraft is associated with its speed by the formula X = Vt.

The phase of the reflected signal compared with the phase of the transmitted signal, retained in a memory, is written:

$$\phi = \frac{4\pi - d}{\lambda} = \frac{4\pi d_0}{\lambda} + \frac{2\pi}{\lambda d_0} v^2 t^2 = \phi_0 + kt^2.$$

With the quadratic variation of the phase is associated a linear variation of the Doppler frequency, defined by:

$$f_{\rm d} = \frac{1}{2\pi} \frac{{\rm d}\phi}{{\rm d}t} = Kt.$$

The synchronous detection brings forth a radar signal of the form:

$$S_{R}(t) = S \cos \phi = S \cos(\phi_0 + kt^2)$$
.

The duration of this signal is limited to the time of traverse of the target in the beam:

$$T_0 = \frac{2\theta_0 d_0}{V}$$

with $2\theta_0$ the angular aperture of the aerial beam.

The above equations define the radar signal from a point target; assuming that the overall system (radar and processing) is linear, by superimposition the results can be applied to a real complex target.

3. PROCESSING BY LOW PASS FILTERING

Principle

With this type of processing only that part of the signal is retained containing the very low Doppler frequencies (Fig.3). In these conditions the target is displayed only for a brief moment when it appears abeam of the aircraft.

The improvement of display obtained is limited to a value such that the envelope of the signal is reduced to a spectrum whose width equals that of the low pass filter.

The optimum value of the time constant of the filter, which gives the best contrast of the signal after processing is equal to:

$$\sqrt{\frac{\lambda d_0}{2\pi V}}$$
.

Compared with the natural resolution $(\lambda/L) d_0$ due to the aerial beam aperture, the improvement ratio of the low pass filter processing is:

$$\sqrt{\frac{2\lambda d_0}{L^2}}$$

The width of the improved echo being: $\sqrt{\frac{\lambda d_0}{2}}$.

Synopsis (Figure 4)

The radar uses a magnetron transmitter whose pulse duration leads to a transverse resolution uniform with the longitudinal resolution. The phase of the transmitted signal is stored in a memory in an IF coherent oscillator, synchronised by the magnetron pulse after transposition into IF. After coherent detection, the received signals are written into a filter bank enabling as many signals, $S_R(t)$, to be processed as there are range quanta to be obtained for the transverse resolution sought in the terrain zone to be displayed.

At each radar recurrence a switching system applies in time succession the signals to the filter corresponding to the quantum of range to be processed.

After the filtering a read-out switch enables the "improved video" to be sent to a representation system formed of a display and an associated photographic system.

Results

Presentation of some radar maps.

4. PROCESSING BY OPTICAL CORRELATION

Principle

The $S_R(t)$ signal is written transparently on a film. Care is taken to superimpose on $S_R(t)$ a mean component S_0 so that $S_R(t)$ can be written with its sign. (Fig. 5)

The inscription, obtained by means of a cathode tube, in front of which a film moves at constant speed, transforms the time function $S_R(t)$ into a space function $S_R(X)$ with X = Vt (to within scale factor).

This film is placed on the optical path of a plane wave (Fig.6).

If $E_0 \cos \omega t$ is the incident field falling on the film, the transmitted field will have a distribution along X such that:

$$S(X) = \frac{E_0}{2} \left[1 + \cos[k_1 X^2 + \phi_0] \right] \cos \omega t$$

 ω : is the pulsation of the incident light $\left[\omega=2\pi f_L=\frac{2\pi C}{\lambda_L}\right]$

 k_1 is equal to: $2\pi/\lambda d_0$

The function S(X) is equivalent to three waves:

- a plane wave
$$\alpha$$
: $\frac{E_0}{2}\cos \omega t$,

- a convergent spherical wave, of centre O2,
$$\beta$$
: $\frac{E_0}{4}\cos[\omega t + k_1 X^2 + \phi_0]$,

- a divergent spherical wave, of centre O1, γ : $\frac{E_0}{4} \cos[\omega t - k_1 X^2 - \phi_0]$.

The scale factor μ being known, then for OO_1 and OO_2 is found the common value:

$$F = OO_1 = OO_2 = \mu^2 \frac{\lambda}{\lambda_L} \frac{d_0}{2}.$$

The optical break-down thus obtained is associated with the axis of symmetry of the written S(X) function, thus with the position of the film along X.

A fixed very fine slit F, placed at O2 will receive considerable light flux.

An output film placed behind this slit will write a compressed signal when the axis of symmetry of the function passes the slit F.

To obtain a representation corresponding to the echos recorded it is sufficient to pass the output film along, synchronised with the film carrying the function S(X).

This compressed signal has a dimension equation to the dimension of the aerial carried by the aircraft, to within the scale factor μ .

The function so obtained is the S(X) correlation function (Fig. 7).

To obtain good dynamics it is necessary to eliminate the interfering divergent component (γ wave). This is done by adding a carrier to the recorded Doppler signal.

As Figure 8 shows, this carrier confers on the system a prismatic effect and so enables the component used (β wave) to be collected behind a slit arranged outside the beams of the interfering waves.

All the preceding results can be obtained by using the diffraction phenomena which requires the use of Fourier transforms.

Synopsis (Figure 9)

To obtain a longitudinal resolution consistent with the transverse resolution, the radar uses a very fine pulse transmission-reception with pulse compression technique.

After coherent detection the Doppler signals are sent to a photographic recording system comprising:

- a display, fitted with a flying spot CRT, modulated in light and scanned along a single dimension: in radar range,
- a lens,
- a cine camera, in which the film passes in the image plane of the front face of the display unit, perpendicularly
 to the trace and at a speed proportional to that of the aircraft.

The quality of the processing by correlation requires that the Doppler effect law of the recorded signals be as near as possible to the reference law $\cos(\phi_0 + kt^2)$.

This ideal law is obtained by considering that the carrier aircraft describes a horizontal straight line with uniform motion.

Any deviation from this ideal path introduces on the received signals interfering phase variations, which have to be compensated in reception. This is done by applying corrections to the reference wave of the coherent detector, of phase proportional to the aircraft deviations from the ideal path.

The film of the Doppler signals, recorded in flight, is developed on the ground, then analysed in the optical correlator. The output film from the correlator gives the usable radar map. Photographs of the different elements of the radar are presented during the lecture.

Results

Presentation of some radar maps.

Conclusion

The trials made of improvement by filter or by correlation have enabled the theoretical limits of resolution to be approached.

Other types of processing have also been tested but present various disadvantages, such as enhancement by spot and matched filter associated with memory storage of the Doppler signals on a memory tube.

By means of technological advances other possibilities are henceforth offered, such as digital electronic correlation, which enables radar maps to be obtained in flight, practically in real time.

We conclude by thanking the Service Technique des Telecommunications de l'Air which financed these various studies and allowed this presentation of the results. We also thank the Centre d'Essais en Vol, Bretigny which carried out the trial of our equipment.

THEORETICAL WIDTH OF ECHOES IN AIRCRAFT PATH

RADAR RANGE	WITHOUT PROCESSING	WITH PROCESSING FILTERING CORRELATION	
		$\sqrt{\frac{\lambda d_0}{2}}$	2
1 km	35 m	4 m	0.5 m
5 km	175 m	9 m	0.5 m
10 km	350 m	13 m	0.5 m

L = Aerial length = 1 metra

 $\lambda =$ Wavelength = 3.3 cm

Figure 1

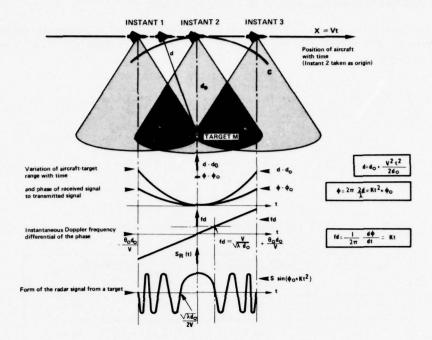


Figure 2



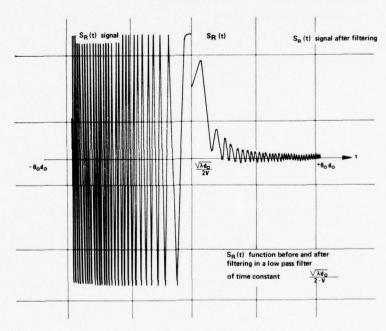


Figure 3

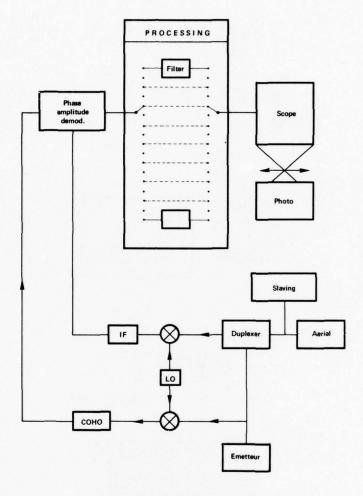
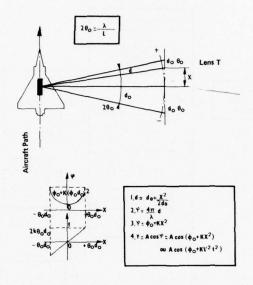


Figure 4



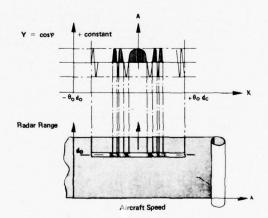
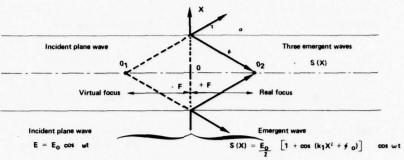


Figure 5

OPTICAL PROCESSING OF THE FUNCTION $S_{R}(X)$

Geometrical optical viewpoint



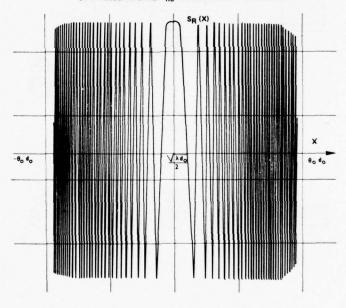
Doppler echo written transparently on film $S_0 \ + S_R \ \{X\} \ = \ \frac{1}{2} \quad \left[1 \ + \cos \ \{k_1 X^2 \ + \ \ \ _0\} \right]$

Focal length : $F = \mu^2 \frac{\lambda}{\lambda_L} \frac{d_0}{2}$

 $S(X) \begin{cases} \text{Plane wave } \alpha & : & \frac{E_O}{2} & \text{COS } \omega t \\ \\ \text{Convergent wave } \beta & : & \frac{E_O}{4} & \text{COS } (\omega t + KX^2 + \Phi_O) \\ \\ \text{Divergent wave } \gamma & : & \frac{E_O}{4} & \text{COS } (\omega t - KX^2 - \Phi_O) \end{cases}$

Figure 6

COMPRESSED SIGNAL $\,S_{RC}\,$ AFTER OPTICAL PROCESSING



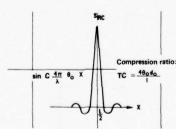


Figure 7

PROCESSING OF THE FUNCTION SR(X)

INTRODUCTION OF A CARRIER

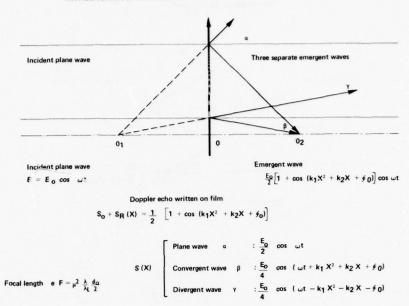


Figure 8

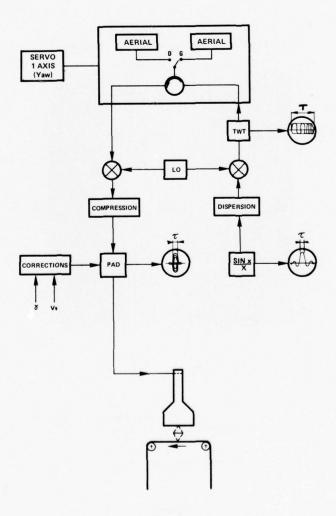


Figure 9

Giorgio Tacconi

ABSTRACT

The propagation of waves in layered media and the inherent possibilities of transferring information from one layer to another or within a layer, can be used for communications, detection, or evaluation of structural anomalies of the geological zones in which the propagation phenomenon takes place. ELF electromagnetic waves clearly obey the Maxwell equations but, because of the order of magnitude of their wave lengths, namely the relative skin depth, can also be used for practical applications in dissipative media, like sea water, where high frequency signals vanish too rapidly for any practical use. The paper, after a conceptual physical-mathematical introduction, taking into account the environmental structure of the natural man-made noise and the boundaries conditions, shows some practical applications in communications, detection and environmental studies. Features and properties for different scenarios of propagation are considered, together with limitations and the dependence on technology of the achievement of certain operational performances. The paper does not represent a complete or exhaustive compendium of the subject, but shows some experimental approaches intended to draw attention to problems that may, after appropriate changes, be solved by means of other instrumentation and methods.

1. INTRODUCTION

In general radio telecommunications have been effected by means of high-frequency electromagnetic waves, with the lowest limit being about 10 kHz. As a consequence, for the most part, electrical engineers are not familiar with the techniques applied to extra low frequency (ELF) telecommunications. Even though the fundamental physical mathematical model is the same, there are some implications that give rise to disorentation: for instance, the antenna sizes that result are relatively enormous.

ELF electromagnetic phenomena were first considered by Nicola Tesla [Ref. 1] at the beginning of this century when tests were made to transmit energy at ELF ranges. Over the past fifty years the interest in these frequency bands has considerably increased. For the most part this increasing interest is related to the improvement in analytical and technological tools. For instance, before the assessment of low-noise, semi-conductor amplifiers it was impossible to detect the Schumann mode resonances of the earth/ionosphere cavity, the ranges of which, in fact, start from about 7 Hz [Ref. 2].

^{*} Part of the scientific material used in this paper has been developed under CNR Contract No.12/CT/76

Also the availability of analytical tools such as the power spectral analysis, the Fast Fourier Transform (FFT), and the Maximum Entropy Method (MEM), together with the possibility of high-stability frequency standards for phase look-in detection, have considerably contributed to enlarging the scientific interest in the ELF phenomena. In addition, the development of high permeability magnetic materials for coils, special materials for electrodes, and parametric-resonance magnetometers (Josephson effect), have greatly contributed towards the development of more sensitive and reliable sensors. This is to mention just a few of the more important scientific and technical discoveries. More precisely, it should be said that the global progress of mathematics and technology has contributed to the present state of the scientific knowledge and technological know-how of ELF applications.

ELF communications and detection is a subject that covers a very large number of topics and it is not possible to give a complete and exhaustive compendium in this paper. The aim here is to give the fundamentals of telecommunications in such frequency ranges, and to present the physical phenomena from an operational point of view, taking into account present-day theory and technology, and probable future developments. For those whose interest has been stimulated by the topics that can merely be outlined in this presentation, a bibliography is included of the literature in which deeper treatment will be found.

2. SOME BASIC THEORIES

The theory of electromagnetic propagation at ELF ranges has been exhaustively developed by many authors [Refs. 3, 4 and 5]. However, without dwelling too much upon fundamentals it is worthy to first outline the Maxwell equations for an electromagnetic field:

$$\nabla \times \bar{E} = -\frac{\partial \bar{B}}{\partial t}$$
 (1a)

$$\nabla \times \overline{H} = \overline{J} + \frac{\partial \overline{D}}{\partial t}$$
 (1b)

$$\nabla \cdot \overline{\mathbf{B}} = 0 \tag{1c}$$

$$\nabla \cdot \mathbf{\bar{D}} = \rho \tag{1d}$$

where ρ = free charge density

 \bar{J} = electric current density

E = electric field intensity

D = electric displacement

 \overline{H} = magnetic field intensity

 \bar{B} = magnetic flux density

∀ = divergence operator

The solutions of such equations conveniently represent the field only in very simple cases. Consequently, it is necessary to introduce some auxiliary potentials and the fields will be obtained from these potentials by differentiations. The theory, which has been developed in a very clear way by Kraichman, Wait and others [Refs. 3, 4, 5, 6 and 7], demonstrates that it is possible to define the electromagnetic field in terms of a single vector function, namely the Hertz vector potential.

The general formulation of the Maxwell equations for an harmonic variation is given by:

$$\nabla \times \overline{E} = -j \omega \overline{B} \qquad (2a)$$

$$\nabla \times \overline{H} = \overline{J}_{O} + (\rho + j\omega \varepsilon) \overline{E}$$
 (2b)

$$\nabla \cdot \mathbf{\bar{B}} = 0 \tag{2c}$$

$$\nabla \cdot \overline{\mathbf{D}} = \mathbf{p}$$
 , (2d)

in which the derivative of \bar{B} with respect to time is represented by the harmonic factor j^{W} , and the electric current density \bar{J} is represented by a constant term \bar{J}_{o} and a term $\sigma \bar{E}$ representing an induced conduction current. The Eq. (2b) can be written as follows:

$$\nabla \times \vec{\mathbf{H}} = \vec{\mathbf{J}}_{\mathbf{O}} + \mathbf{j} \omega \varepsilon^* \vec{\mathbf{E}}$$
 (3)

 ϵ^* represents here the complex permittivity, in the case of a general conducting media, defined as

$$\varepsilon^* = \varepsilon \left(1 + \frac{\sigma}{jw\varepsilon}\right)$$
 ; (4)

evidently, when σ = 0 the medium is non-conducting.

The electromagnetic field in a conducting medium, generated by one activated electric dipole moment can be expressed in terms of an electric Hertz vector $\bar{\tau}$ as:

$$\bar{E} = \nabla \nabla \cdot \bar{\Pi} - \gamma^2 \bar{\Pi}$$
 (5a)

$$\overline{\mathbf{B}} = \frac{\mathbf{Y}^{\otimes}}{\mathbf{i}\mathbf{w}} \, \, \forall \, \, \mathbf{x} \, \, \overline{\mathbf{n}} \tag{5b}$$

$$\overline{D} = \varepsilon \overline{E} + \overline{E}_{O}$$
 (5c)

where the relation between $\overline{\mathbf{E}}_{o}$ and $\overline{\pi}$ is:

$$\nabla^{2} \vec{\pi} - Y^{2} \vec{\pi} = \frac{\omega^{2} \mu}{V^{2}} \vec{E}_{o} \tag{6}$$

in the same way it can be demonstrated that:

$$\bar{E} = -j\omega\mu \nabla x \bar{\pi}^*$$
 (7a)

$$\bar{H} = \nabla \nabla \cdot \bar{\pi}^* - \sqrt{2} \bar{\pi}^* \tag{7b}$$

$$\bar{\mathbf{B}} = \mu(\bar{\mathbf{H}} + \bar{\mathbf{M}}_{\mathbf{O}}) \qquad , \tag{7c}$$

where $\bar{\pi}^*$ = the magnetic Hertz vector

 \overline{M}_{O} = the activated magnetic dipole moment

 μ = the magnetic permeability

and the relation between \overline{M}_{0} and $\overline{\pi}^{*}$ is

$$\nabla^2 \cdot \vec{\pi}^* - \gamma^2 \vec{\pi}^* = -\vec{M}_0 \qquad . \tag{8}$$

The formal identity of Equations (5a) and (7b) is evident, and this shows that if both electric and magnetic activated dipoles are present the electromagnetic field can be obtained by means of a single superposition of the solutions for each type of dipole [Refs. 3, 6 and 7].

In the concept of propagation, the transference of "something" — whether this be matter, or energy, or information, or all three together — from one point in space to another is implicit. The basic formal mathematical approach for electromagnetic and acoustic (elastic) wave propagation is the same, and in both cases the behaviour and the structure of interfaces affect the propagation or, more precisely, the signal that has to be transmitted and received. In principle, it is impossible to omit telecommunication problems from any physical measurement, since any type of measurement can be considered a sort of "non- or quasi-semantic communication", i.e. passive detection is a communication of this type.

In a physical measurement, the information at the receiver is produced by making a comparison between the received signal and the original physical phenomenon; whereas in telecommunications a comparison is made between the received signal and the transmitted one. In both cases, however, a certain a priori knowledge of the expected signal is required. It is well established that electromagnetic perturbations in the ELF range propagate in that particular wave guide which is the earth/ionosphere gap, even at circumterrestrial distances. From the very general mathematical model the formula of the skin depth is deduced:

$$\delta = \sqrt{\frac{2}{\omega_{\varphi}\sigma}} \quad , \tag{9}$$

where μ is the relative permeability of the medium

w is the angular frequency

o is the electrical conductivity of the medium.

Electromagnetic ELF propagation presents a property of high penetrative power (relative to man-size operational scenarios and strategies) which, from the point of view of communications through dispersive media represents a remarkable advantage; ionosphere, earth's crust, and oceans are examples of such media.

The general theory of communications can be used also in the case of electromagnetic ELF links. A transmission channel can be considered, in the main, as a system of three elements: the transmitter, the medium, and the receiver. The medium is the element of the system that is normally outside the control of man; as a consequence, the most important problem of any type of communication is represented by the knowledge of the medium, namely those parameters of the medium which, with their fluctuations in non-uniformities of time or space, alter the transmitted signal. By the medium is meant the space surrounding the transmitter and the receiver, also including, of course, the boundaries that normally are not simple bi-dimensional immobile interfaces, but more frequently real, randomly fluctuating layers with non-uniform spatial structures.

One of the most simple transmission channels is that in which the receiver and the transmitter are placed in the same medium, bounded by two parallel infinite interfaces. If the geometry of the interfaces and the properties of the medium are changing in time and space, the transmission channel can be characterized by means of the scattering function concept, provided that the statistical distributions of time histories and space anomalies are known. The knowledge of this scattering function associated with the filter, representing the medium, can be used with remarkable advantage to build-up the optimal signal (in terms of frequency, bandwidths, repetition rate, etc.) to obtain the highest value of signal-to-noise ratio. The calculation of the scattering function under particular statistical conditions, i.e. Wide Sense Stationary Uncorrelated Scattering (WSSUS), is based on the solution of wave equations in such a way that the scattering function becomes a function of the time spreading, the frequency smear, and the position in space [Refs. 8, 9 and 10], namely:

 $R_{S}(\tau, \varphi, \underline{a}\underline{b})$

where + = time spreading

 φ = frequency smear

 $\underline{a}\,\underline{b}$ = spatial parameters.

The wave equations can be solved by means of the ray-tracing approach or normal modes. In the example given in Fig. 1(a) the ray-tracing approach has been used. In order to give a simple example of experimentally computed scattering function, Fig. 1(b) shows the scattering function of an underwater acoustic channel, in this case neglecting the spatial parameters [Ref. 11]. This example may at first appear inappropriate; on the contrary acoustic propagation in the ocean represents a very general model for communication studies, mainly with respect to the medium, which is bounded by time-and space-depending interfaces and/or layers and, in addition, the phenomenon of of volume scattering due to the non-uniformity of the medium is shown. In the electromagnetic ELF case, with particular sizes of layers, the ray-tracing approach

using the eikonal approximations is not sufficient to satisfactorily describe the propagation phenomena; the approach in terms of normal modes is required [Ref. 12 and 13]. In the ELF ranges the scattering effect of interfaces is not only due to the geometrical structure and fluctuations of boundaries, but also to the distribution of certain physical parameters of the medium in the boundary layer where the perturbation penetrates. The most important of these parameters for electromagnetic propagation is the electrical conductivity "o", which together with the frequency determines the skin depth. Using the formula

$$\delta = \left(\frac{2}{\omega_{\beta_0}\sigma}\right)^{\frac{1}{2}} \left[\left(\frac{\omega^2 e^2}{\sigma^2} + 1\right)^{\frac{1}{2}} - \frac{\omega \epsilon}{\sigma}\right]^{\frac{1}{2}}$$

$$\tag{11}$$

the skin depth can be computed as a function of frequency for various conductivities [Ref. 3].

4. THE ELF BOUNDARIES

The earth/ionosphere gap, in which ELF propagation phenomena take place, should be considered globally as a unique physical system. However, in order to simplify the problem the system shall be divided here into two parts:

- (i) The upper boundary: ionosphere and magnetosphere.
- (ii) The lower boundary: oceans and earth's crust.

This division is made purely for convenience, in reality there are many phenomena affecting the upper boundary that interfere with those of the lower boundary and viceversa.

Because of the wave lengths, the distances involved in ELF communications range up to thousands of kilometres. The interfaces of interest are, in the main, those shown in Fig. 2, where the principal boundaries involved, the upper boundary (ionosphere) and the lower boundary (earth's surface), are quite evident.

4.1 The Upper Boundary (Ionosphere)

The upper boundary is that region of the upper atmosphere situated between 50 km and 300 km above the earth's surface. The ionosphere conductivity varies between 1 and 20 mhos/m and, as calculated and reported in Refs. 3 and 14, the skin depth of an electromagnetic wave in a medium of such conductivity can be of the order of several hundreds of metres. A signal propagating through the ionosphere to reach the earth's surface is evidently influenced by the behaviour of conductivity in time and space. Obviously, the model of a layered medium in regular layers with a well-known conductivity behaviour is, in this case, quite far from reality. The behaviour of conductivity in the ionosphere is summarized in the formulae given in Table 1, from which it may be noted that conductivity is a tensor depending on time and related to the physics of plasma and hydrodynamics [Ref. 14].

IONOSPHERIC CONDUCTIVITIES

$$\sigma_{\mathbf{P}} = \begin{bmatrix}
\sigma_{\mathbf{P}} & \sigma_{\mathbf{H}} & 0 \\
-\sigma_{\mathbf{H}} & \sigma_{\mathbf{P}} & 0 \\
0 & 0 & \sigma_{\mathbf{H}}
\end{bmatrix}$$

$$\sigma_{\mathbf{P}} = \begin{bmatrix}
\frac{v_{\mathbf{en}} & w_{\mathbf{ce}}}{v^{2}_{\mathbf{en}} + w^{2}_{\mathbf{ce}}} + \frac{v_{\mathbf{in}} & w_{\mathbf{ci}}}{v^{3}_{\mathbf{in}} + w^{2}_{\mathbf{ci}}} \end{bmatrix} \frac{e \, Ne}{B} \qquad (PEDERSEN)$$

$$\sigma_{\mathbf{H}} = \begin{bmatrix}
\frac{w^{2}_{\mathbf{ce}}}{v^{2}_{\mathbf{en}} + w^{2}_{\mathbf{ce}}} - \frac{w^{2}_{\mathbf{ci}}}{v^{3}_{\mathbf{in}} + w^{2}_{\mathbf{ci}}} \end{bmatrix} \frac{e \, Ne}{B} \qquad (HALL)$$

$$\sigma_{\mathbf{H}} = \begin{bmatrix}
\frac{1}{m_{\mathbf{e}}} & v_{\mathbf{en}} + \frac{1}{m_{\mathbf{i}}} & v_{\mathbf{in}} \\
v_{\mathbf{in}} & v_{\mathbf{in}} & v_{\mathbf{in}}
\end{bmatrix}$$

$$\sigma_{\mathbf{C}} = \sigma_{\mathbf{P}} + \frac{\sigma^{2}_{\mathbf{H}}}{\sigma_{\mathbf{P}}} \qquad (COWLING)$$

$$v_{\mathbf{i}} = \text{collision freq.}$$

$$w_{\mathbf{e}} = \text{gyro freq.}$$

$$v_{\mathbf{i}} = \text{ion}$$

$$e = \text{electron}$$

If the ionosphere is considered a transmission medium, and since the most important parameter of such a medium is the conductivity, it is evident from previous considerations on transmissions (i.e., WSSUS hypoethesis) that a statistical evaluation of the fluctuations in time must be made. Some evaluations on the background noise and its distribution in the ELF ranges have been made by Bernstein et al [Ref. 15], and Fig. 3 gives an example of a typical ELF noise distribution compared with an assumed Gaussian noise. More specifically, in hydrodynamic turbulent velocity fields it is inadequate to assume a certain process as random, it must be statistically determined; Ref. 16 underlines the inadequacy of assuming randomness in many cases.

Plasma physics and ionosphere hydrodynamics can supply the needed information on the fluctuations and space distributions of conductivity that are useful in correlating the non-Gaussian distribution of noise with a physical predictable phenomenon.

Telecommunication theories and techniques can also supply useful diagnostic tools as shown in Fig. 4, which represents an ELF signal propagating through the earth/ionosphere gap and received at a distance of about 5 nanometres; the ripples represent anomalies related to magnetospheric phenomena.

The characteristics of natural ELF background noise have also been used as diagnostic tools in magnetospheric investigations [Refs. 17, 18 and 19]. The most evident and important characteristics of natural background noise at such a range are the

Schumann modes. These were theoretically envisaged by Schumann [Ref. 2], and experimentally detected by Balser and Wagner [Ref. 20] in the air and by others [Refs. 17, 18, 22 and 23] in the sea. These modes present a typical power spectral, density distribution [Fig. 5]. The centre frequency of each mode is given by the formula

$$f_{n} = k \sqrt{n(n+1)} Hz$$
 (12)

k depends from the condition of the ionosphere.

From a proper analysis of their fluctuations in time and space, it is possible to extract an evaluation of certain ionospheric and earth-surface parameters. Subsequently, with the SANGUINE-SEAFARER Project [Refs. 19, 24 and 25] the earth/ionosphere cavity has been artificially excited from 45 Hz up to 75 Hz, and as a consequence a variety of investigations have been carried out by many scientists in different parts of the world. Antenna design, statistical background-noise evaluation, sensor implementation, environmental hazards, signal codification and many other relevant arguments have been carefully investigated [Ref. 24 and 26]. The principle of artifical ELF excitation of the earth/ionosphere cavity is shown in Fig. 6 [Ref. 27].

ELF electromagnetic phenomena in the upper boundary are of great importance for long-range communication systems [Ref. 15]. From the many investigations made in connection with the SANGUINE-SEAFARER project on the influence of ionospheric phenomena on the ELF propagation, it was possible to estimate the structure in time and space of the noise and, consequently, to design an optimal signal processing system so as to maximize the signal-to-noise ratio [Ref. 24 and 27].

Antennas of this type of communication must, of necessity, be very small in comparison with the wave length; at 100 Hz the wave length is 3 Mm. Under such circumstances, transmitting systems are extremely inefficient [Ref. 27], consisting of a single large array transmitting to a number of receivers buried or submerged. The present situation with respect to power requirements and the reliability of communications even at low data rates, is improving not only because of its importance, but also because the technical advances in signal-processing coding and antenna design have considerably reduced the power requirements.

The basic calculations of a transmitting system at a given data rate R (bits/s) have been formulated by Burroughs [Ref. 27] as follows:

- (i) Coding/modulation scheme.
- (ii) Required message reliability/error rate (missed message rate).
 These two quantities determine the necessary ratio

$$\frac{E_{\mathbf{b}}}{N_{\mathbf{c}}}$$
 (13)

where E_b = required received signal energy (Joules)/per information bit. N_e = effective Gaussian noise power density (W/Hz) at the receiver.

Consequently, from the knowledge of $N_{\rm e}$, the required signal power $P_{\rm r}$ (watts) is deduced from the relation

$$\frac{P_{\Gamma}}{N_{e}} = \frac{E_{b}}{N_{e}} \cdot R \qquad (14)$$

Subsequently, by means of the propagation equations it is possible to relate the current moment of the transmitter with the needed signal power P_{Γ} , and finally, provided the particular configuration and size of the antenna are known, to determine the required input power.

Figure 7 shows a radio-signal system transmitted at ELF/VLF ranges from a satellite. These signals are propagated through the ionosphere to receiving antennas on the earth's surface [Ref. 28]. In this particular case for calculating a signal-to-noise power budget it is necessary to calculate the geometric spreading factor of the waves as they propagate through the ionosphere. This procedure is fundamentally based on geometrical optics and used in order to evaluate the scattering properties of the "layered boundary" which, according to the considerations made on the scattering function $R_{\rm S}$ of a transmission channel, is the ionosphere. Many works have been made in order to evaluate the ELF signal and noise variability on particular paths [Refs. 17 29, 39 and 31]. The SANGUINE-SEAFARER project has improved the possibilities of investigating the properties of the electromagnetic ELF transmission channel.

4.2 The Lower Boundary (Earth's Surface)

The lower boundary of the waveguide is the earth's surface. This consists of 71% in oceans and seas and the remainder in land. For the oceans similar considerations as made for the ionosphere can be applied. In this case, however, the behaviour of the conductivity is simpler and easily correlated to other physical parameters of the sea water (i.e., salinity, temperature, pressure). The conductivity of sea water ranges from 2.5 to 5 mhos/m and the skin depth can reach several hundreds of metres. Table 2 shows in synthesis the implications of interfaces in ELF ranges. The field components, represented in this Table by points, are different to each other and depend not only on the conditions of the boundaries, but also on the type of dipole (vertical electric, vertical magnetic, horizontal electric, horizontal magnetic), and on the range that implies the frequency (wave length). For practical application in ELF telecommunications, the particular cases summarized in Table 2 must be taken carefully into account. The calculation of the values of the various field components are reported in Ref. 3.

TABLE 2 SYNOPTIC FIELD COMPONENTS IN ELF RANGES

RANGE	PROPAGATION SCENARIO	DIPOLE TYPE	FIELD COMPONENTS
Far Field $(\rho \gg \lambda_0)$	Sub-surface/Free Space Sub-surface/Sub-surface	VED VMD HED HMD	E_{ρ} , E_{ϕ} , E_{z} , H_{ρ} , H_{ϕ} , H_{z}
	(U.O.A.D. propagation)	VMD HED HMD	
Near Field $\rho \ \ensuremath{\stackrel{\sim}{\approx}} \ \lambda_{O}$	Sub-surface/Free Space $h \le 0^+$ $z \ge 0^+$	VED VMD HED HMD	
	Free Space/Sub-surface $h \ge 0^+$ $z \le 0^-$	VED VMD HED HMD	
	Sub-surface/Sub-surface $h \le 0$ $z \le 0$	VED VMD HED HMD	
Quasi-Static Field $\rho \ll \lambda_0$	A. Surface/Surface (i) General $ \gamma_0 \rho \ll 1$	VED VMD HED HMD	
	(ii)	VED VMD HED HMD VED	
	(iii) γ ₀ ρ ≪1; γ ₁ ρ ≪1	VMD HED HMD	
	B. Free Space/Sub-Surf. (i) $ \gamma_0 R^{\dagger} \ll 1$ (ii) $ \gamma_1 R^{\dagger} \gg 1$ (iii) $ R^{\dagger} \gg z $	VED VMD HED HMD	
	C. Sub-Surf./Free Space (i) $ \gamma_0 R \ll 1$ (ii) $ \gamma_1 R \gg 1$ (iii) $R \gg h $	VED VMD HED HMD	
	D. Sub-Surf./Sub-Surf.	VED VMD HED HMD	

 λ_{o} = wave length in free space

 ρ = horizontal distance

z = depth of the field point

h = depth of the dipole source

 γ_0 = propagation constant in free space

 $\gamma_1=$ propagation constant in a homogeneous conducting half space $R=\sqrt{\rho^2+z^2}$ $R'=\sqrt{\rho^2+h^2}$

The lower boundary can be separated into two parts: the oceans and the emerged land. In both cases man has mobility and various interests, including communications and geological prospecting. The theory of wave propagation in layered media has been treated by many authors [Ref. 17, 29, 39 and 31], and from the preceding considerations it is intuitive to conceive the earth's crust as a system of layers with different electrical conductivities. The oceans represent a very interesting scenario with respect to both operative ranges and propagation conditions. In fact, the electrical conductivity (o) distribution in the oceans at operative man-size ranges is far more uniform than in equal volumes of solid earth crust and, mainly for this reason, long distance ELF communications can be assessed with satisfactory reliability. Figure 8 shows the most important parameters in sea water: wave length, skin depth and attenuation [Ref. 3]. The operational implications of such parameters are evident.

4.2.1 ELF Underwater Links

After an appropriate choice of the theoretical implications related to the scenarios in which the link is to be established [Table 2], the following practical considerations must be taken into account.

- (i) Far-field propagation conditions are very seldom actuated and can only be used for long-distance communications [Ref. 32].
- (ii) Short-distance communications can be effected in the near field or in quasi-static propagation conditions. Therefore, communication system design must take into account the particular formulation of the various electromagnetic field components.
- (iii) At operational man-size ranges it is impossible to localize the direction of an ELF source.
- (iv) Provided the geometrics and physics of the essential parameters are known, the propagation conditions are practically independent from sea and meteorological states.
- (v) Due to the attenuation factor of sea water, far-off natural and manmade noise is not received in the zone of interest.
- (vi) The structure and the depth of the bottom, and the morphology and structure of the coast-line influence the values of electromagnetic field components. Consequently, the spatial distribution of the field must be known.

 The above considerations represent the basis for a reliable underwater radio link.

If considered as a current element, the electric dipole can be represented by a conductor of length dl, isolated in respect to the surrounding space, through which flows a current I fed by means of two electrodes that are the terminals of the conductor and which are both immersed in the medium — the sea water. If $\mathrm{d} l \ll \lambda$ where λ = wave length, the dipole can be considered as an elemental antenna and will produce

a Hertz potential as shown in the formula.

$$\overline{\pi} = \frac{\mathbf{I} d\mathbf{l}}{4 \pi (\sigma + \mathbf{j} \omega \dot{\epsilon})} = \frac{\epsilon^{-\gamma^{\Gamma}}}{\mathbf{r}}$$
(15)

where I = dipole current

d1 = dipole length

σ = medium conductivity mhos/m

r = distance from the dipole in spheric coordinates.

Y = propagation constant

w = angular velocity

 ϵ = dielectric constant.

Assuming the time variation to be harmonic

$$I = I_0 e^{+j\omega t} . (16)$$

The electric and magnetic field components, \overline{E} and \overline{H} in a point P of the space are deduced from \overline{H} by means of the following relations:

$$\vec{E} = \gamma^2 \vec{\pi} + \text{grad div } \vec{\pi}$$
 (17)

$$\bar{H} = (0 + j\varepsilon) \operatorname{rot} \bar{\pi}$$
 (18)

The development of Eqs. (17) and (18) leads to the determination of non-null components of the field in spherical coordinates:

$$E_{\theta} = \frac{I dl}{4\pi(\sigma + j^{\omega}\varepsilon)} \frac{\sin \theta}{r^{3}} (1 + \gamma^{\Gamma} + \gamma^{2} r^{2}) e^{-\gamma \Gamma}$$
(19a)

$$H_{\odot} = \frac{I dl}{4\pi} \frac{\sin \theta}{r^2} (1 + \gamma^{r}) e^{-\gamma^{r}}$$
(19b)

$$E_{\mathbf{r}} = \frac{I d1}{2\pi(\sigma + \mathbf{j} w \varepsilon)} \frac{\cos \theta}{r^3} (1 + \gamma^{\Gamma}) e^{-\gamma^{\Gamma}}$$
(19c)

where the propagation constant Y is given by

$$Y = (-\varepsilon_{\perp}\omega^{2} + \mathbf{j}\omega_{\perp}\sigma)^{\frac{1}{2}} . \tag{20}$$

In Eq. (20), for w=0 one has also $\gamma=0$, in which case \overline{E} and \overline{H} are defined for a d.c. operated dipole.

The energy propagation between a transmitter and a receiver, both immersed in sea water, is outlined for the following three cases:

- (i) Through a dispersive infinite space (only sea water; no interface).
- (ii) Through a semi-infinite space (sea water/air; one interface).
- (iii) Through a duct (sea bottom/sea water layer/air; two interfaces).

The schematic representation of the propagation phenomenology in Fig. 9 shows how the transmitted energy can reach the receiver by means of three contributions: through sea

water only, through the air, and through the bottom. Figure 10 demonstrates, for propagation in infinite space with $\sigma=4$ mhos/m, the "no interface" case (i) computed in function of frequency for a distance of 1000 m in all directions [line (a)], and the horizontal range (ρ) between the transmitter and the receiver for the same distance of 1000 m and the total sea water path (z+h) = 100 m [line (b)].

Assuming the transmitted quantity of information to be equal to the number of binary impulses/s, which is twice the bandwidth of the transmission channel, the horizontal range has been computed in function of the quantity of information bits/s for a power of 1 Watt, a frequency of 2 Hz, and for sea paths (h+z) 0, 10, 100, and 500 m [see Fig. 11]. Figure 12 shows the behaviour of the attenuation relative to a 10% increase of bits/s for a power of 1 kW.

The above mentioned computations have been carried out on the basis of theories developed by various authors (Banos, Wesley, von Aulok [Refs. 6, 7 and 33]) applying the following relations:

$$E_{\rho} = \frac{I1}{2\pi^{0}} \frac{e^{-\gamma(z+h)}}{\rho^{3}} \cos \varphi \qquad (21a)$$

$$E_{\phi} = \frac{I1}{2\pi^{\circ}} \frac{2e^{-\gamma(z+h)}}{\rho^{\circ}} \sin \phi \tag{21b}$$

where:

 $(z+h) \ll \rho$

E = horizontal electric field component at the receiver [Fig. 9] in a position (x, y, z) with the transmitter in the point (0,0,h) of the system.

I = current in the transmitting dipole

1 = dipole length

 $\rho = (x^3 + y^2)^{\frac{1}{2}}$, horizontal range

z = receiver depth

h = transmitter depth

 $\gamma = 4.0 \times 10^{-3} \sqrt{f}$, propagation constant

σ = 4 mhos/m, conductivity of sea water

 $\varphi = \arctan y/x$

Figure 13(a) shows the geometry of a system based on the assumption of using an activated electric dipole of unitary length as a transmitter towed by a ship passing over a receiving dipole placed on the bottom in relatively shallow water; Fig. 13(b) shows the top view. Implications for modifications on an ELF signal are summarized in Fig. 14.

The transmitted signal (possibly a square wave) is subject to attenuation and deformation that are due partly to the propagation conditions in the sea (electrical conductivity and the presence of boundaries), and partly to geometry and the relative

motion of the transmitter in respect to the receiver. Calculations on perpendicular and parallel courses are shown in Fig. 15 and the corresponding experimental qualitative results in Fig. 16 [Ref. 34].

4.2.2 Influences of Boundaries

In these theoretical and experimental examples the influence of other pertinent local conditions, such as natural and man-made background noise, bottom profile, and coast-line presence, has been neglected. However, for the design of a reliable operational transmitting/receiving system, particular care must be devoted to such parameters. Since it is practically impossible for these conditions to be theoretically computed, it is first necessary for appropriate experimental measurements to be made in the zone in order to obtain the needed data for system design.

Figures 17 and 18 give some experimental results supported by theoretical considerations based on the following two factors:

- (i) ELF background noise detected by two electric dipoles near the coast line, one parallel and the other perpendicular [Fig. 17].
 - (ii) Influence of the bottom on ELF signal propagation [Fig. 18].

A method for the theoretical calculation of ELF electromagnetic propagation in shallow water has been developed. The formulae of Van Aulock [Ref. 7], in connection with propagation in a semi-infinite medium, suggested a simple physical interpretation of the contributions to the field strength at a point and, consequently, a simple method for describing shallow water propagation taking into account both boundaries by the method of images, with the addition of a contribution from changes induced at the air/sea interface by the incident field from the source [Ref. 35].

Banos and Wesley [Ref. 33] derived single expressions for the electric field strength in both media in the geometrical conditions $\rho >> \delta$, $|z+h| \ll \rho$, and Wait [Ref. 4] in the case of z=h=0. The following relations are valid in the conducting medium:

Banos and Wesley

 $\delta \ll \rho \ll \lambda_0$, $z + h \ll \rho$

$$E_{\rho_1} = \frac{Id1}{2\pi\sigma} \cdot \frac{e^{-\gamma_1(z+h)}}{\rho^3} \cos \varphi \qquad (22a)$$

$$E_{\varphi_1} = \frac{IdI}{2\pi^{\circ}} \frac{e^{-\gamma_1 (z+h)}}{\rho^{\circ}} 2 \sin \varphi \qquad (22b)$$

$$E_{Z_1} \cong 0$$
 (22c)

water only, through the air, and through the bottom. Figure 10 demonstrates, for propagation in infinite space with $\sigma=4$ mhos/m, the "no interface" case (i) computed in function of frequency for a distance of 1000 m in all directions [line (a)], and the horizontal range (ρ) between the transmitter and the receiver for the same distance of 1000 m and the total sea water path (z+h) = 100 m [line (b)].

Assuming the transmitted quantity of information to be equal to the number of binary impulses/s, which is twice the bandwidth of the transmission channel, the horizontal range has been computed in function of the quantity of information bits/s for a power of 1 Watt, a frequency of 2 Hz, and for sea paths (h+z) 0, 10, 100, and 500 m [see Fig. 11]. Figure 12 shows the behaviour of the attenuation relative to a 10% increase of bits/s for a power of 1 kW.

The above mentioned computations have been carried out on the basis of theories developed by various authors (Banos, Wesley, von Aulok [Refs. 6, 7 and 33]) applying the following relations:

$$E_{\rho} = \frac{I1}{2\pi^{\circ}} \frac{e^{-\gamma(z+h)}}{\rho^{3}} \cos \varphi \qquad (21a)$$

$$E_{\varphi} = \frac{I1}{2\pi^{Q}} \frac{2e^{-\gamma(z+h)}}{\rho^{3}} \sin \varphi \qquad (21b)$$

where:

 $(z+h) \ll \rho$

E = horizontal electric field component at the receiver [Fig. 9] in a position (x, y, z) with the transmitter in the point (0,0,h) of the system.

I = current in the transmitting dipole

1 = dipole length

 $\rho = (x^3 + y^2)^{\frac{1}{2}}$, horizontal range

z = receiver depth

h = transmitter depth

 $\gamma = 4.0 \times 10^{-3} \sqrt{f}$, propagation constant

 $\sigma = 4 \text{ mhos/m, conductivity of sea water}$

 $\varphi = \arctan y/x$

Figure 13(a) shows the geometry of a system based on the assumption of using an activated electric dipole of unitary length as a transmitter towed by a ship passing over a receiving dipole placed on the bottom in relatively shallow water; Fig. 13(b) shows the top view. Implications for modifications on an ELF signal are summarized in Fig. 14.

The transmitted signal (possibly a square wave) is subject to attenuation and deformation that are due partly to the propagation conditions in the sea (electrical conductivity and the presence of boundaries), and partly to geometry and the relative

motion of the transmitter in respect to the receiver. Calculations on perpendicular and parallel courses are shown in Fig. 15 and the corresponding experimental qualitative results in Fig. 16 [Ref. 34].

4.2.2 Influences of Boundaries

In these theoretical and experimental examples the influence of other pertinent local conditions, such as natural and man-made background noise, bottom profile, and coast-line presence, has been neglected. However, for the design of a reliable operational transmitting/receiving system, particular care must be devoted to such parameters. Since it is practically impossible for these conditions to be theoretically computed, it is first necessary for appropriate experimental measurements to be made in the zone in order to obtain the needed data for system design.

Figures 17 and 18 give some experimental results supported by theoretical considerations based on the following two factors:

- (i) ELF background noise detected by two electric dipoles near the coast line, one parallel and the other perpendicular [Fig. 17].
 - (ii) Influence of the bottom on ELF signal propagation [Fig. 18].

A method for the theoretical calculation of ELF electromagnetic propagation in shallow water has been developed. The formulae of Van Aulock [Ref. 7], in connection with propagation in a semi-infinite medium, suggested a simple physical interpretation of the contributions to the field strength at a point and, consequently, a simple method for describing shallow water propagation taking into account both boundaries by the method of images, with the addition of a contribution from changes induced at the air/sea interface by the incident field from the source [Ref. 35].

Banos and Wesley [Ref. 33] derived single expressions for the electric field strength in both media in the geometrical conditions $\rho >> \delta$, $|z+h| \ll \rho$, and Wait [Ref. 4] in the case of z=h=0. The following relations are valid in the conducting medium:

Banos and Wesley

 $\delta \ll \rho \ll \lambda_o$, $z + h \ll \rho$

$$E_{\rho_1} = \frac{Id1}{2\pi\sigma} \cdot \frac{e^{-Y_1(z+h)}}{\rho^3} \cos \varphi \qquad (22a)$$

$$E_{\varphi_1} = \frac{Id1}{2\pi^{\circ}} \frac{e^{-\gamma_1(z+h)}}{\rho^{\circ}} 2 \sin \varphi \qquad (22b)$$

$$E_{Z_1} \cong 0$$
 (22c)

Wait

$$z = h = 0, \quad \rho \ll \lambda_0$$

$$E_{\rho_1} = \frac{Idl}{2\pi^0} \frac{1 + (1 + \gamma_1 \rho)e^{-\gamma_1 \rho}}{\rho^3} \cos \phi$$
 (23a)

$$E_{\varphi_{\lambda}} = \frac{IdI}{2\pi^{\circ}} \frac{2 - (1 + \gamma_{\lambda} \rho)e^{-\gamma_{\lambda} \rho}}{\rho^{3}} \sin \varphi \qquad (23b)$$

$$\mathbf{E}_{\mathbf{Z}_{1}} \cong 0 \tag{23c}$$

In the remaining area, the formulae of Van Aulock are used:

$$E_{\rho_{1}} = \frac{\operatorname{Id1}}{4\pi\sigma} \left\{ \left[\frac{a^{2}}{\delta_{\rho}^{2}} - \gamma_{1}^{2} \right] \left[\frac{e^{-\gamma_{1}}\sqrt{\rho^{2} + (z - h)^{2}}}{\sqrt{\rho^{2} + (z - h)^{2}}} + \frac{e^{-\gamma_{1}}\sqrt{\rho^{2} + (z + h)^{2}}}{\sqrt{\rho^{2} + (z + h)^{2}}} \right] - \frac{2}{\rho} \frac{\partial}{\partial_{\rho}} \left[\mathscr{A}\left(\rho_{1}\left(z + h\right) - \frac{e^{-\gamma_{1}}\sqrt{\rho^{2} + (z + h)^{2}}}{\sqrt{\rho^{2} + (z + h)^{2}}} \right] \right\} \cos \varphi$$

$$(24a)$$

$$E_{\varphi_{1}} = -\frac{\mathbf{Idl}}{4\pi\sigma} \left\{ \left[\frac{1}{\rho} \frac{\partial}{\partial \rho} - \gamma_{1}^{2} \right] \left[\frac{e^{-\gamma_{1}} \sqrt{\rho^{2} + (z - h)^{2}}}{\sqrt{\rho^{2} + (z - h)^{2}}} + \frac{e^{-\gamma_{1}} \sqrt{\rho^{2} + (z + h)^{2}}}{\sqrt{\rho^{2} + (z + h)^{2}}} \right] - \frac{2 \frac{\partial^{2}}{\partial \rho^{2}} \left[\mathscr{A}(\rho_{1}(z + h) - \frac{e^{-\gamma_{1}} \sqrt{\rho^{2} + (z + h)^{2}}}{\sqrt{\rho^{2} + (z + h)^{2}}} \right] \right\} \sin \varphi$$

$$(24b)$$

$$E_{Z_{1}} = \frac{Id1}{4\pi\sigma} \left\{ \frac{\partial^{2}}{\partial_{z}\partial_{\rho}} \left[\frac{e^{-Y_{1}\sqrt{\rho^{2} + (z-h)^{2}}}}{\sqrt{\rho^{2} + (z-h)^{2}}} + \frac{e^{-Y_{1}\sqrt{\rho^{2} + (z+h)^{2}}}}{\sqrt{\rho^{2} (z+h)^{2}}} \right] \right\} \cos \varphi$$
 (24c)

where
$$\mathcal{J}[\rho_1(z+h)] = \frac{\gamma}{2} \left\{ I_0 \left[\frac{\gamma_1}{2} \left(\int \rho^2 + (z+h)^2 - (z+h) \right) \right] K_1 \left[\frac{\gamma_1}{2} \left(\int \rho^2 (z+h)^2 + (z+h) \right) \right] \cdot \left[\frac{z+h}{\sqrt{\rho^2 + (z+h)^2}} + 1 \right] - \left[I_1 \frac{\gamma_1}{2} \left(\int \rho^2 + (z+h)^2 - (z+h) \right) \right] K_0 \cdot \left[\frac{\gamma_1}{2} \left(\int \rho^2 + (z+h)^2 + (z+h) \right) \right] \left[\frac{z+h}{\rho^2 + (z+h)^2} - 1 \right] \right\}$$

 ${f I}_o$ and ${f I}_1$ are the modified Bessel functions of the first kind, and ${f K}_o$ and ${f K}_1$ are the modified Bessel functions of the second kind.

The total field strength at the receiver in a shallow-water sea

$$\left| E_{\rho} \right| = (1 + q) \left| E_{O} \right| \left[G(\frac{d}{\delta}, \frac{Z_{B}}{Z_{W}}) \right]^{2}$$

where:

|E₀| is the total field strength at receiver in shallow-water sea

|E₀| is the total field strength at receiver in semi-infinite sea

- q is the ratio of the contribution of the field strength through the bottom to that through the air, and ranges from unity for a perfect di-electric bottom, to zero for highly conductive bottom that strongly attenuates the wave.
- G is a function that depends on the ratios d/δ and $Z_{\mbox{\footnotesize B}}/Z_{\mbox{\footnotesize W}}$ and indicates by its numerical value the improvement of propagation in shallow water compared with that in deep water.
- d is the water depth (m).
- δ is the skin depth (m).

 Z_{R} is the electromagnetic impedance of the bottom.

 $\mathbf{Z}_{\mathbf{W}}$ is the electromagnetic impedance of the sea water.

The approximate relation

$$\frac{Z_{B}}{Z_{W}} = \sqrt{\frac{\sigma_{W}}{\sigma_{B}}} \tag{26}$$

is known to hold, where σ_W and σ_B are respectively the conductivity of the sea water and the bottom, measured in mhos/m.

By the transmission line theory, we also have

$$G = \left| \frac{Z_{S}}{Z_{W}} \right| = \left| \frac{\tanh \left[\frac{d}{\delta} (1+i) + \frac{Z_{B}}{Z_{W}} \right]}{1 + \frac{Z_{B}}{Z_{W}} \tanh \left[\frac{d}{\delta} (1+i) \right]} \right|$$
(27)

where \mathbf{Z}_{S} is the characteristic impedance of the medium regarded as transmission line. Using the following procedure:

- (i) Calculate G for a given geographic zone;
- (ii) measure | E | in the same zone;
- (iii) calculate $\left| \mathbf{E}_{\mathbf{o}} \right|$ assuming $\mathbf{q} \approx 1$

it is possible to deduce the ratio ${\rm Z_B/Z_W}$ from Eq. (27) and show that the resulting value of σ_B is consistent with the assumption that ${\rm q}\approx 1$.

The solid-line curves of Fig. 18 represent the electric field strength in cylindrical coordinates $\left| \mathbf{E}_{\mu} \right|$ of the radial component at the receiver, and refer to propagation in a semi-infinite sea with the receiver at the same depth as the upper shallow-water curves, but with the bottom denth as infinite. The unitary-strength source is at the surface. The dashed-line curves represent the most optimistic shallow-water propagation conditions, that is assuming the bottom impedance as infinite (impossible condition). The dotted-line curves represent experimental measurements for a real scenario in shallow water; it is notable how these lie between the theoretical most-optimistic and most-pessimistic curves.

5. DETECTION

ELF detection can be made by means of acoustic and/or electromagnetic principles. Although the physical mechanisms are quite different, the final signal processing is essentially much the same. The electromagnetic ELF passive detection takes advantage of all the concepts relevant to a receiving system — natural and man-made background noise, signals (information), unwanted man-made noise (electromagnetic ELF ship self-noise). A consequential heuristic consideration is that the word "detection" will be used more in the sense of characterization or identification of a source, and the investigation of the generation mechanism of the related perturbations by means of analysis of the signature. The above mentioned receiving concepts must, of course, be reviewed for operational purposes.

Any metallic ship will produce a varying electromagnetic field in the sea, not merely because of its actual physical presence but, primarily, because of its rotating on-board machinery. Due to the strong attenuation of sea water, the high frequency perturbations — as seen in the theory — are not irradiated very far from the ship, whereas the low frequency components become more significant with the relatively longer detection ranges. The main phenomena generating ELF perturbation from aboard ship are the galvanic currents caused by the iron of the hull and the brass of the propellers, both of which, when immersed in sea water, represent an electrolytic cell producing d.c. current. Corrosion currents of this type are well known to ship builders and designers. From detection experiments made with a ship passing over a submerged dipole, it was noted that the fundamental signature frequencies were strictly related to the number of revolutions and the number of blades of the propeller. This determination implies a modulation of the d.c. galvanic current. Although various investigations on the varying electromagnetic field around a ship have been carried out, the mechanisms of such modulation are not yet completely known.

Experiments have been made in order to evaluate the intensity of the electrolytic current produced by the "propeller-hull galvanic cell" by using a current transformer [Fig. 19]. The propeller shaft represented the primary, consisting of a single-turn coil. A Hall-effect cell gaussmeter was placed in a perpendicular slot on the transformer core in order to measure the magnetic field produced by the current flowing through the shaft; calibration and residual magnetization of the magnetic core were taken into account. A current of the order of maximum 10 amps was measured whilst floading a dry-dock with sea water. It is suspected that this current modulation is generated by a sort of "short circuit" that occurs somewhere between the propeller shaft and the hull (maybe in the passage of the shaft through the hull). The repetition rate of such "short circuits" is strictly correlated with the r.p.m. of the propeller shaft.

Figure 20 shows a typical power spectrum of noise produced by a ship and detected by a submerged dipole. The experiment was repeated at different r.p.m. conditions that proved the relationship to the fundalmental frequency. Figure 21(a) shows simultaneous recordings of the signal detected by the propeller-shaft transformer mentioned above, and that detected by a receiving dipole towed by the ship; the correlation of the two signals is quite evident. Figure 21(b) shows an enlargement of the propeller-shaft transformer signature and Fig. 22 an example of the ship signature. The sinusoidal signature is due to the self-magnetization of that section of the shaft where the transformer was located, and the spike must be due to the modulating "short circuit" phenomenon. Although qualitatively these results proved repetitive for about 90% of the experiments made (the failing 10% were probably due to imperfect performance of equipment), it was impossible to draw any quantitative conclusions. Figure 23 shows the signature of a ship passing over a submerged dipole on a perpendicular course.

From the point of view of propagation, detection of nearby man-made noise is an operation that is typical of the near-field or quasi-static conditions [see Table 2]. The passive detection of the ship electromagnetic noise and its analysis does not differ very much from the detection and analysis of the natural background noise. In order to increase the signal-to-noise ratio, namely

signature of the ship natural background noise

a set of at least two sensors appropriately spaced and aligned should be used.

One parameter that can characterize the ELF signature of a ship is the bandwidth. Assuming a rigorously constant revolution rate (r.p.m.), the bandwidth of the signal detected by a dipole can be derived from terms that contribute to the enlargement of the bandwidth, namely the total variation in frequency can be expressed as follows:

$$\Delta f_{tot} = \Delta f_D + \Delta f + \Delta f_A + \Delta f_N$$
 (28)

where Δf_D is the frequency spread due to the amplitude variation (damping) and propagation conditions.

is the frequency spread due to the non-uniformity of the revolution rate of the shaft.

 ${}^{\triangle}f_{\theta}$ is the frequency spread corresponding to the phase modulation introduced by the movement of the modulating point of the shaft system.

 Δf_N is the noise.

On analysing the signal detected by the internal sensor we may neglect from Eq. (28) the term Δf_D , which is due to propagation conditions in the medium, the formula then becomes

$$\Delta \mathbf{f}_{int} = \Delta \mathbf{f} + \Delta \mathbf{f}_{\theta} \tag{29}$$

and if we assume the shaft revolution rate to be constant we have

$$\Delta \mathbf{f_{int}} = \Delta \mathbf{f_{\theta}} \tag{30}$$

In Fig. 22 we can observe a basic sinosoidal signal with a frequency of $2f_0$ and a spiky signal superimposed at the sinosid with a frequency f_0 which is the shaft revolution per second. The sinosoidal signal is a result of the imperfect geometry of the toroidal transformer, combined with the local magnetic non-uniformity.

Recalling the formulae of the frequency and phase modulation for a sinosoidal signal:

Frequency mod.

$$a = A \sin[2\pi f_0 t + \varphi_0 - \frac{\delta}{f_m} \cos 2\pi f_m t]$$
 (31)

Phase mod.

$$a = A \sin[2\pi f_0 t + \varphi_0 + \gamma \sin 2\pi f_m t]$$
 (32)

where δ = frequency deviation

f_m = modulating frequency

f = carrier frequency

 $\varphi_0 = phase$

 γ = phase angle deviation

we may say that

$$\frac{\delta}{f_m} = (\gamma) \text{ radians}$$
 (33)

As an example, assuming γ = 0.1 radians and f_{m} = f_{o} = 3 Hz

$$\delta = f_m \cdot \gamma = 3.01 = 0.3 \text{ Hz}$$
 (34)

The bandwidth is then 0.6 Hz

$$\Delta f_{int} = \Delta_{\theta} = 0.6 \text{ Hz} . \tag{35}$$

6. ARRAYS OF ELF DETECTION DIPOLES

Taking into account the theroetical approach and the experience gained using a single-dipole sensor, an array of four dipoles (\mathbf{D}_1 , \mathbf{D}_2 , \mathbf{D}_3 , \mathbf{D}_4) was built and placed in shallow sea water [Fig. 24]. In this experiment the dipoles were combined to obtain far-off noise cancellation by means differences, i.e. $|\mathbf{D}_1 - \mathbf{D}_2|$ and $|\mathbf{D}_3 - \mathbf{D}_4|$ Other combinations could obviously be obtained. Cancellation of background noise at a sensor site implies a statistical knowledge of ELF background noise [Ref. 40], in other words, the spatial distribution of noise in the area of interest.

Figure 25(a) shows the signals simultaneously received and recorded at the array, including the differences for the parallel course. Figure 25(b) shows the computed background-noise, space correlation behaviour in function of frequency for dipoles D_3 D_4 and $\left|D_3-D_4\right|$.

6.1 Analysis

The analysis of signals must be made by means of the digital technique, using such methods as the power spectral analysis, Fast Fourier Transform (FFT), or the more recent Maximum Entropy Method (MEM) [Ref. 39 and 40]. In this example the power spectral analysis was used. After appropriate time-compression and sampling, the narrowest bandwidth obtained was found to be of the order $\Delta f = 0.051$ Hz. With the sample length of T = 16 s, the number of degrees of freedom resulted:

$$N = 2 \cdot \Delta f \cdot T = 2 \tag{36}$$

The program gave the facility of varying Δf in order to increase N; two values of Δf have been used:

$$\Delta f = 0.061$$
 and $\Delta f = 0.610$

After having selected ten independent samples, the relative power spectra were computed for each, and the energy level, relevant to a single bandwidth, was averaged over the ten power spectra (16 s samples). Thus, a new mean power spectrum was obtained. This means that N has to be multiplied by a factor of 100 to reach the value of the number of degrees of freedom 200.

As said before, the system can be used to evaluate the spatial distribution of the background noise. The power spectra of two simultaneous samples and that of their differences were computed, and a cancellation effect of ≈ 12 dB was established. If man-made noise sources are far-off in relation to the dipole-spacing and, if the dipoles are accurately parallel to each other, the cancellation effect can be improved still further.

Narrow bandwidth analysis could also be used in estimating ship signal bandwidth. The bandwidth of the received signal is related with the velocity of the source, namely the level increase (or decrease) at the receiver. In order to formulate some expected features of the filter output during a passage of a ship over the array, the problem has been divided into two parts:

- (i) Signal Filter Output
- (ii) Background Noise Filter Output

For part (i) it is assumed that the propagation follows the inverse cube law. For part (ii) it is known [Ref. 41] that if the noise has a normal distribution, the r.m.s. value of the filter output level is proportional to the square root of the filter bandwidth, as follows:

$$\Psi = \int \overline{BG}_{X}$$
 (37)

where G_{χ} is the power spectral density and B is the noise bandwidth. The fluctuation of the noise level in the filter will have a unitary time bandwidth product:

$$\mathbf{B} \cdot \mathbf{T} = \mathbf{1} \tag{38}$$

In fact, the normalized standard error expression of the amplitude output is

$$E = \frac{s.d. \left[\mathbb{Y}_{\eta} \right]}{\mathbb{Y}_{\eta}} \simeq \frac{1}{2\sqrt{BT}}$$
 (39)

which, in other words, represents the fluctuations of the noise in the filter that has a number of degrees of freedom

$$n = 2 B \cdot T = 2 \qquad . \tag{40}$$

On the basis of such a fluctuation it is possible to define the threshold level in accordance with the false-alarm rate required. If a very narrow-band filter fails to attenuate the signal more than it reduces the noise, and considering that the number of degrees of freedom of the filter output cannot be N < 2, the fluctuation of the noise is limited. In addition, in a very narrow filter there is no delay of the signal but simply an attenuation of no more than the noise reduction. As a result it has been argued that the filter output should not be investigated more often than each $1/\Delta f$ s. This argument is probably not strictly correct since the output signal can cross the threshold level at any instant within the time interval of $1/\Delta f$ s and, consequently, it would be worthless to wait minutes for detection. If the above speculations are true the very narrow filter technique could be useful but, of course, the needed number of filters increases with the decreasing bandwidth.

Bearing in mind the preceding considerations, a particular analysis of background noise was made. The character of the noise detected did not appear stationary, it fluctuated more than would be expected for normally distributed noise [Ref. 22].

A "spiky" sample was clipped in the computer [Fig. 26] and the relative clipped and unclipped power spectra compared [Fig. 27]. This represents an outline for approaching the technique of clipping levels of high-amplitude, atmospheric noise spikes, and notch-filtering man-made interferring signals, with the purpose of improving the signal-to-noise ratio at ELF ranges. Recently W.B. Meyers and J.R. Davis [Refs. 30 and 31] developed an hybrid analogue-digital signal processing method to investigate the potential of employing non-linear noise processing. Figure 28 shows the mean energy values in function of bandwidth, with steps of 0.6 Hz, for a clipped atmospheric background noise at ELF range.

6.2 Conclusive Considerations on Analysis

If the fluctuations are higher than expected, the actual fluctuation must be common throughout the total frequency band, and consequently, a correlation between the power amplitudes in the different bands should exist. If this correlation is uniform in all the different frequency bands, the presence of an extraneous signal in the noise should be perceptible as a decrease in the correlation factor between the signal frequency band and the other bands. Figure 29 shows the background noise fluctuations in time for three contiguous frequency bands of 0.6 Hz width. Figure 30 shows the correlation factor computed between the power in the 0.6 Hz bandwidths in the contiguous bands. Figure 31 illustrates the correlation between the different bandwidths and that denominated A (12.6 Hz - 13.2 Hz). The correlation coefficient fluctuates with a mean value of 0.5.

In order to obtain reliable operational indications on the criteria for detecting "signal in noise" at such ranges, the above outlined process needs an extensively elaborate statistical basis.

7. CONCLUDING REMARKS

The technology of sensors is continuously improving. Many types of magnetometers have been built for detecting different types of electromagnetic ELF and lower-frequency signals [Ref. 43]. In particular, the SQUID (Superconducting Quantum Interference Device) has proved extremely useful in detecting man-made signals in the deep sea where the atmospheric background noise is strongly attenuated [Ref. 44]. Arrays towed by submarines for ELF detection have been studied and developed [Ref. 45].

Many problems outlined in this review and others not mentioned here, such as the complex dielectric constant of various types of water [Ref. 46], are still open to advanced research, mainly in the signal processing and data reduction fields; communication and detection problems both overlap into signal processing. Two of the most important parameters for characterizing a transmission channel are the temporal and spatial statistical characteristics of the medium (operational scenario) and, consequently, the definition of the scattering function of the relevant transmission channel, and finally the optimal strategy.

ACKNOWLEDGEMENTS

The author is grateful to Mr S. Falck, Director of SACLANT ASW Research Centre La Spezia, for his support and permission to use results achieved by the author and his colleagues during his term as scientist at SACLANTCEN; also to the Italian Navy (MMI) and the Italian National Research Council (CNR), without whose support the development of the measurements and analysis referred to herein would not have been possible.

REFERENCES

- N. Tesla, "The transmission of electric energy without wires", The Elec. World and Eng, March 1904; reprinted in Lectures, Patents and Articles, Nikola Tesla Museum, Belgrade, 1956.
- W.O. Schumann, "On the propagation along the earth surface of very long electric waves and the lightening discharge", Phys. Abs. 6155/1953, Z. angew. Phys, Germany, 1952.
- M.B. Kraichman, "Handbook of electromagnetic propagation in conducting media", Hdq. Naval Material Command, NAVMAT P-2302, 1970.
- J.R. Wait, "Electromagnetic waves in stratified media", Pergamon Press, 1970.
- J. Galejs, "Terrestrial extremely low frequency propagation", NATO ASI, Bad Homburg, Germany, July 1963.
- A. Banos, "Dipole radiation in the presence of a conducting half-space", Pergamon Press, 1966.
- W. Von Aulock, "Low frequency EM dipole fields in a semi-infinite conductor", USN Bureau of Ships Technical Report No. 104, Washington, 1952.
- 8. A. Wasiljeff, "The influence of time and space variant random filters on signal processing", NATO ASI on Signal Processing with Emphasis on Underwater Acoustics, Portovenere, La Spezia, Italy, 1976.
- R. Laval, "Time-frequency-space generalized coherence and scattering functions", NATO ASI on Signal Processing with Emphasis on Underwater Acoustics, Portovenere, La Spezia, Italy, 1976.
- 10. K.A. Søstrand, "Mathematics of the time-varying channel", NATO ASI on Signal Processing with Emphasis on Underwater Acoustics, Portovenere, La Spezia, Italy, 1976.
- G. Tacconi, "On some parallelisms between radar and sonar transmission channels", NATO ASI on Radar Target Identification and Imaging, Goslar/ Harz, Germany, 1975.
- 12. L.M. Brekhovskikh, "Waves in layered media", Academic Press, 1960.
- 13. J.R. Wait, "Mode theory and the propagation of ELF radio waves", J. Res., NBS, Vol. 64D, 1961, pp 387-404.
- 14. A. Egeland, Ø. Holtet and A. Omholt, "Cosmical geophysics", Universitetsforlaget, Oslo, Norway, 1973.
- 15. S. Bernstein, et al. "Long range communications at extremely low frequencies", IEEE Proc. Vol. 62, March 1974.
- 16. V.I. Tatarskii, "The effects of the turbulent atmosphere on wave propagation", Israel Prog. for Scient. Trans., 1971.
- 17. J.R. Davis and W.D. Meyers, "Observations of ELF signal and noise variability of northern latitude paths", NRL Report 7923, Naval Research Laboratory, Washington D.C., Nov. 1975.
- D.F. Bleil (Ed), "Natural electromagnetic phenomena below 30 KC/s", NATO ASI, Bad Homburg, Germany, 1963; Publ. Plenum Press, New York, 1964.

- P.H. Nelson, "Ionospheric perturbations and Schumann resonance data", Project No. 371-401, Geophysics Lab., Mass. Inst. of Techn., Cambridge, U.S.A.
- 20. A. Balser, C.A. Wagner, "Diurnal power variation of the earth ionosphere cavity modes and their relationship to worldwide thunderstorm activity", J. Geophys. Res., Feb. 1962.
- 21. G. Tacconi, et al., "High sensitivity equipment for measuring the horizontal electric field component in the frequency interval of 1-32 Hz on the sea bottom in shallow water", SACLANTCEN Technical Memorandum No. 141, SACLANT ASW Research Centre, La Spezia, Italy, May 1968.
- 22. G. Tacconi, "The measurement of the ELF horizontal electric field component of the background noise in the sea", NATO ASI, Spatind, Norway, April 1974.
- 23. L. Brock-Nannestad, "EM phenomena in the ELF range: natural background noise and instrumentation for its measurement", SACLANTCEN Technical Report No. 37, SACLANT ASW Research Centre, La Spezia, Italy, June 1965.
- J.R. Wait, "Propagation of ELF electromagnetic waves and project SANGUINE/SEAFARER", IEEE J. of Ocean. Engin., April 1977, pp 161-172.
- 25. B.E. Keiser, "Early development of the project SANGUINE Radiating system", IEEE Trans. on Communications, Vol. COM-22, No. 4, April 1974, pp 364-371.
- J.R. Wait (Ed), "IEEE Transactions on Communications", Vol. COM-22, No. 4, April 1974.
- 27. M.L. Burrow and C.W. Niessen, "ELF communication system design" Ocean-72, IEEE Intern.Conf. on Eng. in the Ocean Environ., N.Y. 1972.
- 28. F.J. Kelly, D.J. Baker and G.A. Chayt, "Spreading of waves launched by ELF/VLF satellite", NRL Report 7814, Naval Research Laboratory, Washington D.C., Dec. 1974.
- 29. J.R. Davis and W.D. Meyers, "Solar-geophysical effects on northern and mid-latitude ELF propagation", NRL Report 7771, Naval Research Laboratory, Washington D.C., July 1974.
- 30. W.D. Meyers and J.R. Davis, "ELF nonlinear noise processing experimental measurements: Part 1 - preliminary results for July and October 1975", NRL Memorandum Report 3226, Naval Research Laboratory, Washington D.C., March 1976.
- J.R. Davis and W.D. Meyers, "ELF nonlinear noise processing experimental measurements: Part 2 synoptic sample of diurnal and seasonal noise variation in Norway", NRL Report 8039, Naval Research Laboratory, Washington D.C., Oct. 1976.
- 32. P.R. Bannister, "Far-field extremely low frequency (ELF) propagation measurements, 1970-1972", IEEE Trans., Vol. COM-22, No. 4, April 1974, pp 468-474.
- 33. A. Banos and J. Wesley, "The horizontal dipole in a conducting half-space", Scripps Institute of Oceanography, Rep. 53-33, 1953.
- 34. G. Tacconi, "On the evaluation of man-made electromagnetic noise interferring with communications in the ELF range", AGARD Meeting on Electromagnetic Noise, Interference and Compatability, Paris, October 1974.
- 35. T. Strarup, G. Tacconi, J.E. Lokken, "ELF passive detection of submarines in shallow water", SACLANTCEN Technical Report No. 134, SACLANT ASW Resea Research Centre, La Spezia, Italy, 1969.
- 36. A.W. Ellinthorpe, "The Azores Range", USNUSC, New London, U.S.A., 1973.
- 37. G. Tacconi, "Sulle possibilità di comunicazione attraverso il mare mediante onde el ttromagnetiche nelle gamma delle basse frequenze", XX Convegno Internazionale delle Communicazioni, Genova, Italy 8-18 Oct. 1972.
- 38. G. Tacconi, "A reliable underwater telecommand", IFAC Symposium on Automation of Off-shore Operations, Bergen, Norway, June 1976.
- 39. R.T. Lacoss, "Autoregressive and maximum likelihood spectral analysis" NATO ASI on Signal Processing with Emphasis on Underwater Acoustics, Portovenere, La Spezia, Italy 1976.

- 40. A.B. Baggeroer, "Confidence intervals for maximum entropy spectral estimates", NATO ASI on Signal Processing with Emphasis on Underwater Acoustics, Portovenere, La Spezia, Italy, 1976.
- 41. J.S. Bendat and A.G. Piersol, "Measurement and analysis of random data", Wiley-Interscience, New York, 1966.
- J.A. Holtet (Ed), "ELF-VLF radio wave propagation", NATO ASI, Spatind, Norway, April, 1974.
- 43. J.E. Lokken, "Instrumentation for receiving electromagnetic noise below 3,000 cps", NATO ASI, Bad Homburg, Germany, 22 July 2 August, 1963.
- 44. S.A. Wolf, M. Nisenoff and J.R. Davis, "Superconducting ELF magnetic field sensors for submarine communications", NRL Report 7720, Naval Research Laboratory, Washington D.C., May, 1974.
- 45. C.T. Fessenden and D.S. Cheng, "Development of a trailing-wire E-field submarine antenna for extremely low frequency (ELF) reception", IEEE Transactions on Communications, Vol. COM-22, No. 4, April 1974, pp 428-437.
- 46. V. V. Akindinov, V.I. Naryshkin and A.M. Ryazantsev, "Electromagnetic waves in sea water (Review)", 1975.

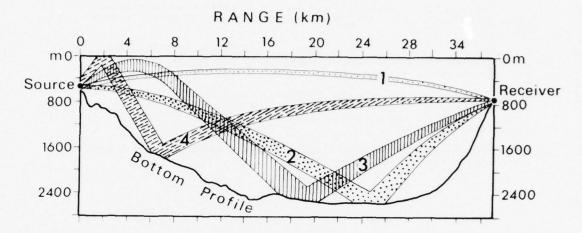


Fig. 1(a) Ray-tracing of a bounded underwater transmission channel.

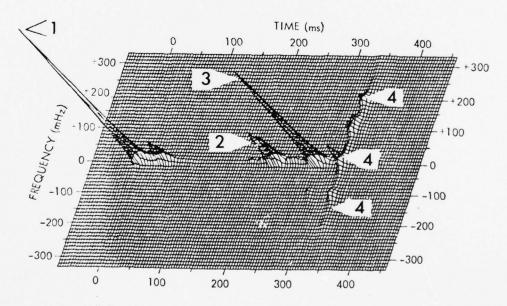


Fig. 1(b) Scattering function of the communication channel [from Ellinthorpe, Ref. 36].

Fig. 2 General system for ELF propagation.

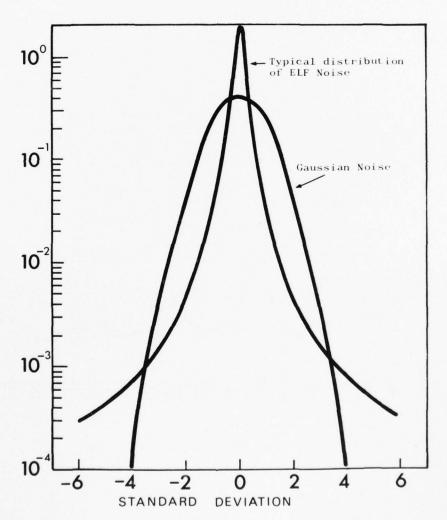


Fig. 3 Natural ELF background noise distribution [from Bernstein et al, Ref. 15].

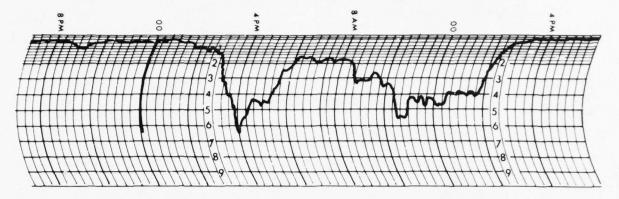


Fig. 4 Long-range communication (signal received from about 5,000 km at 75 Hz).

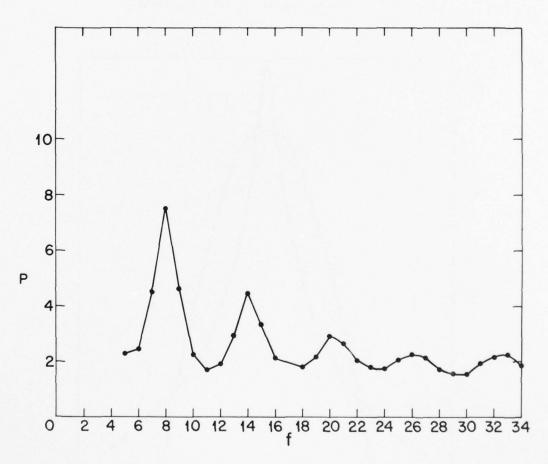


Fig. 5 Schumann modes [from Balser, Wagner, Ref. 20].

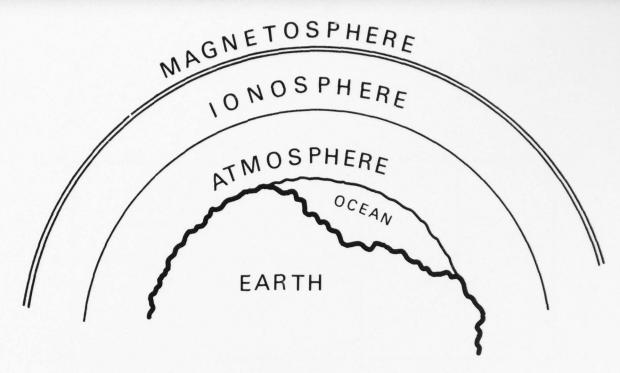


Fig. 6 Principle of ELF transmission in the earth/ionosphere gap.

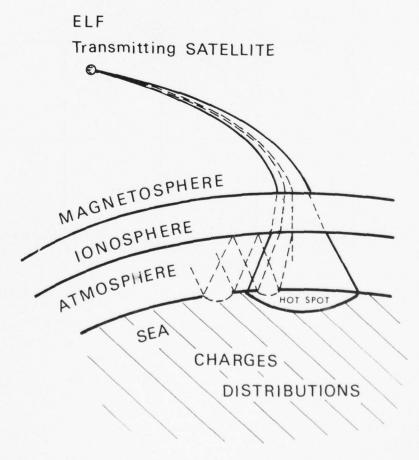
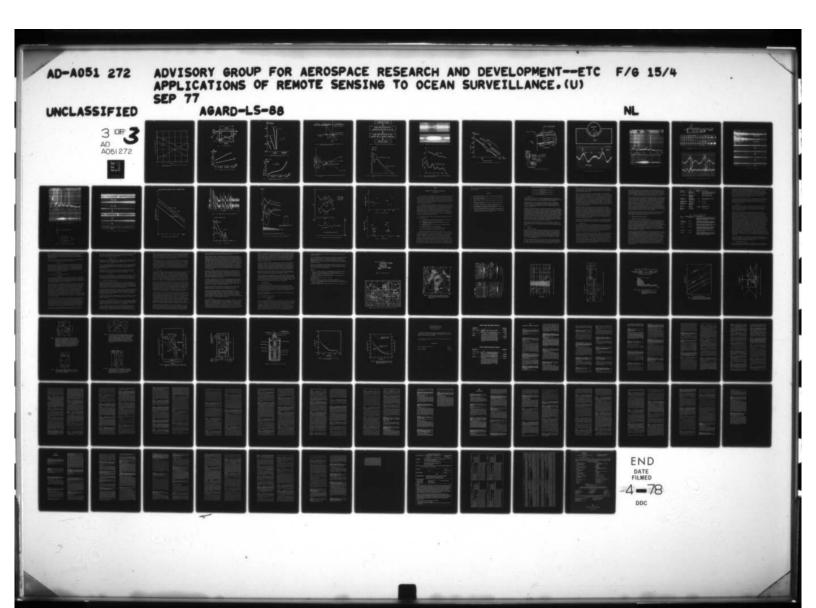
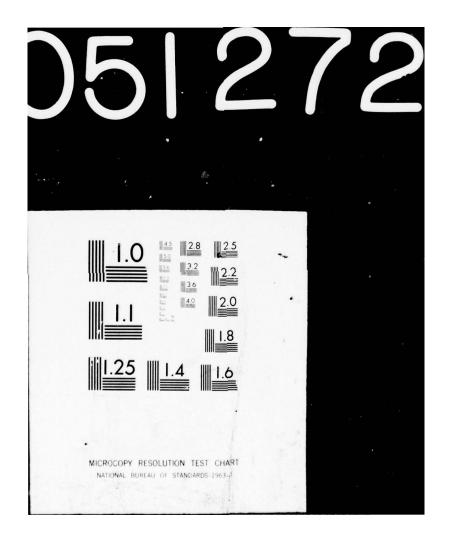


Fig. 7 Satellite/earth ELF communication [from Kelly et al, Ref. 28].





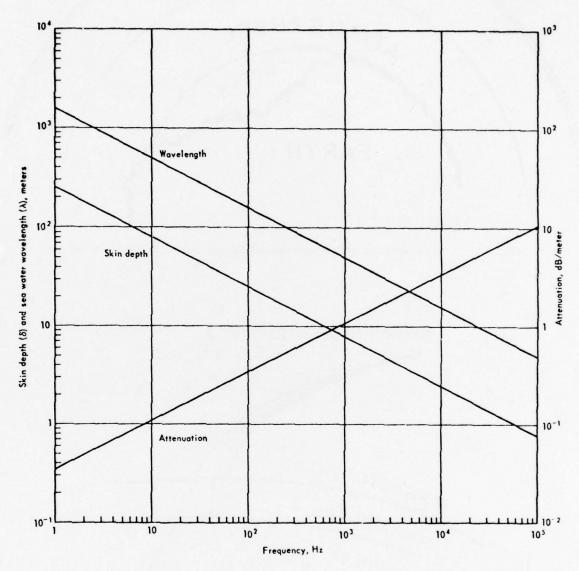


Fig. 8 Sea water charteristics (skin depth, wave length, attentuation) [from Kraichman, Ref. 3].

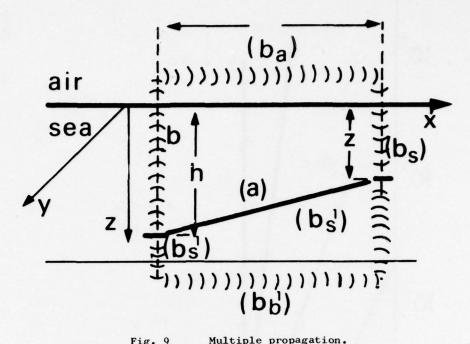


Fig. 9 Multiple propagation.

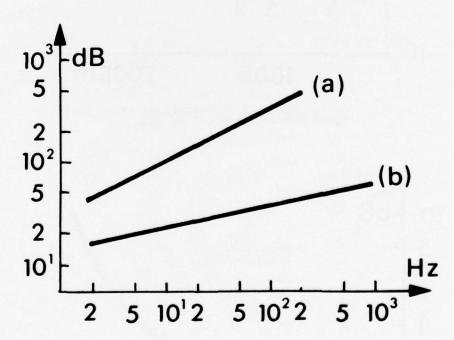


Fig. 10 Attentuation in function of frequency.

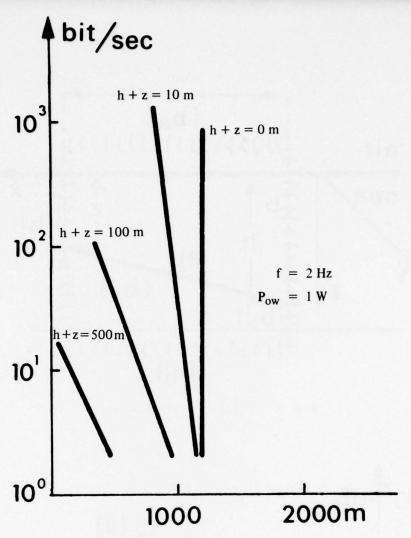


Fig. 11 Horizontal range in function of number of bit/s [from Tacconi, Refs. 37 and 38]

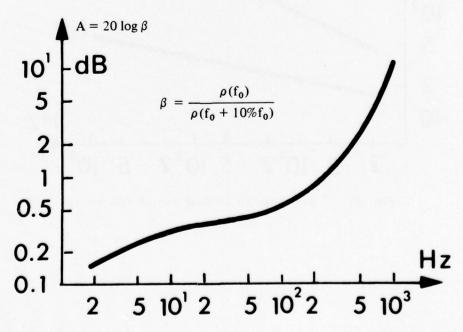


Fig. 12 Attentuation in function of 10% increase in bit/s rate [from Tacconi, Refs. 37 and 38]

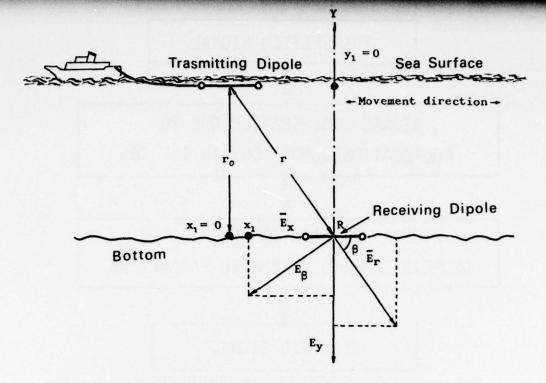


Fig. 13(a) Elemental ELF short-range underwater transmission system [from Tacconi, Refs. 37 and 38]

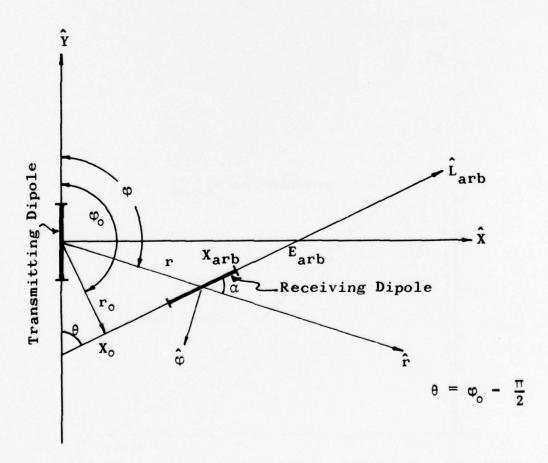


Fig. 13(b) Top view geometry of an underwater ELF short-range transmission system.

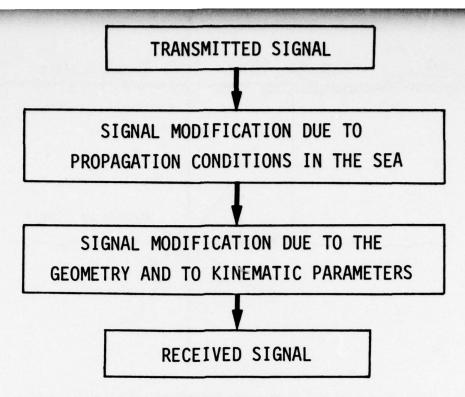


Fig. 14 Implications for short-range signal modification.

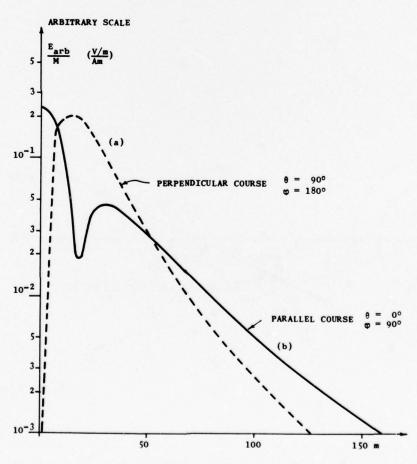
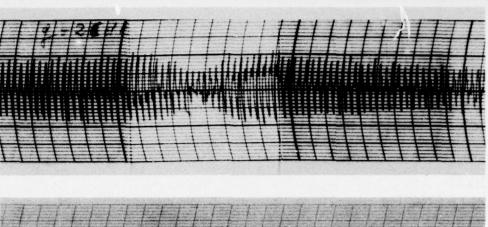


Fig. 15 Field intensity theoretical level for parallel and perpendicular courses.



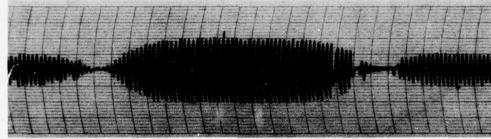


Fig. 16 Experimental results of parallel and perpendicular courses.

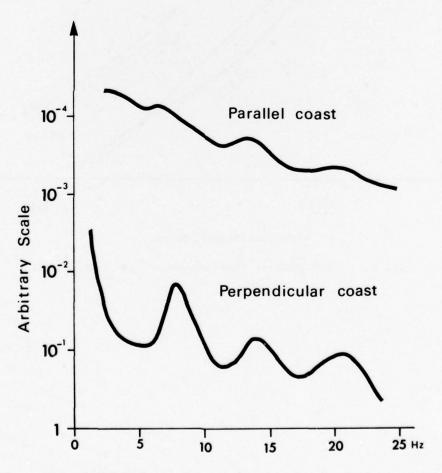


Fig. 17 Natural ELF background noise detected by two dipoles perpendicular and parallel to the coast line.

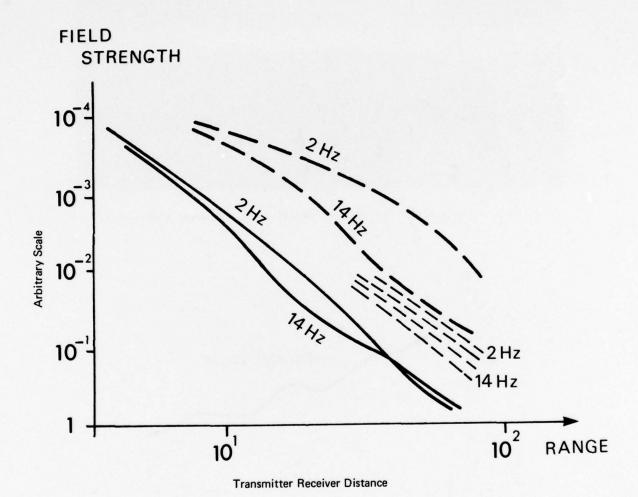


Fig. 18 ELF electric field components in shallow water.

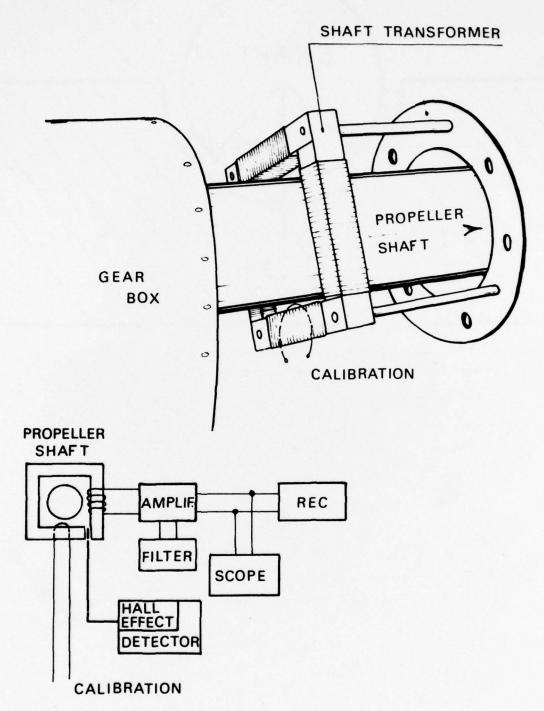
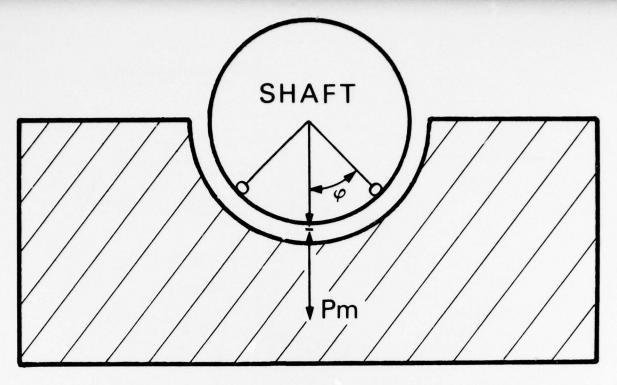


Fig. 19(a) Shaft transformer set-up.



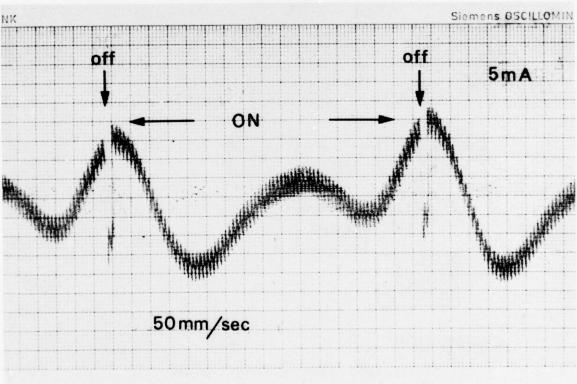


Fig. 19(b) Shaft/hull and dummy shaft signature

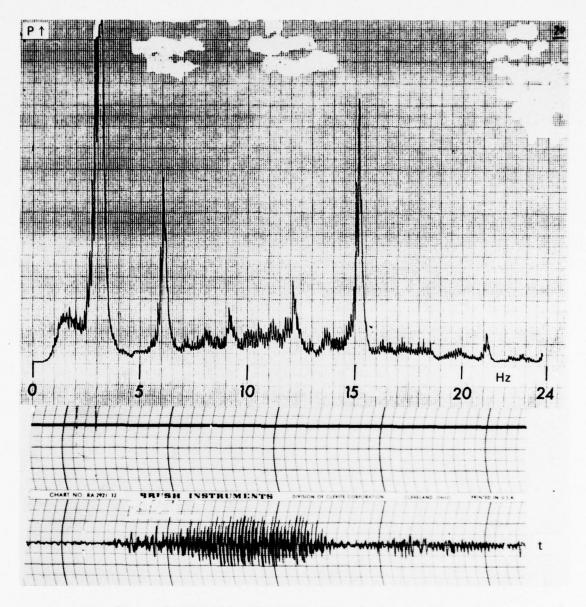


Fig. 20 Typical ship signature with relative power spectrum.

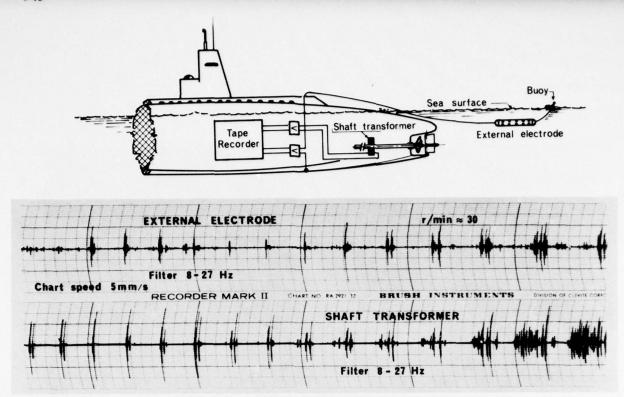


Fig. 21(a) Simultaneous recording of internal shaft signature and relative ELF signal.



Fig. 21(b) Shaft transformer signature at low r.p.m. rate.

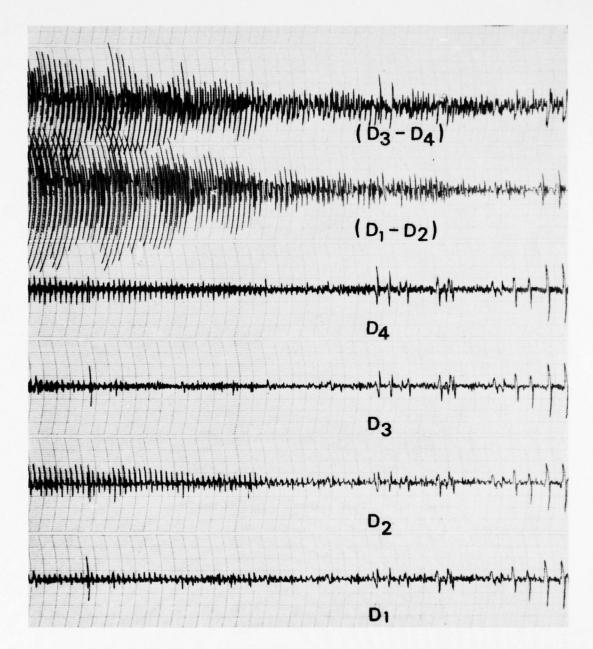


Fig. 22 Example of ship ELF signature.

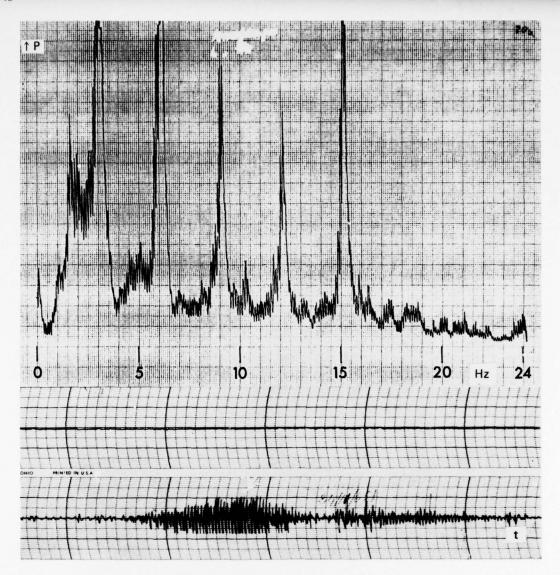


Fig. 23 Ship signature (perpendicular).

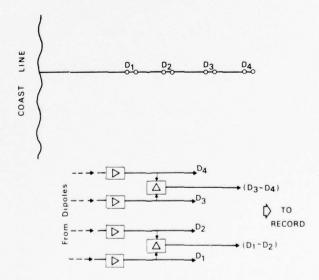


Fig. 24 Four-dipole ELF receiving system.

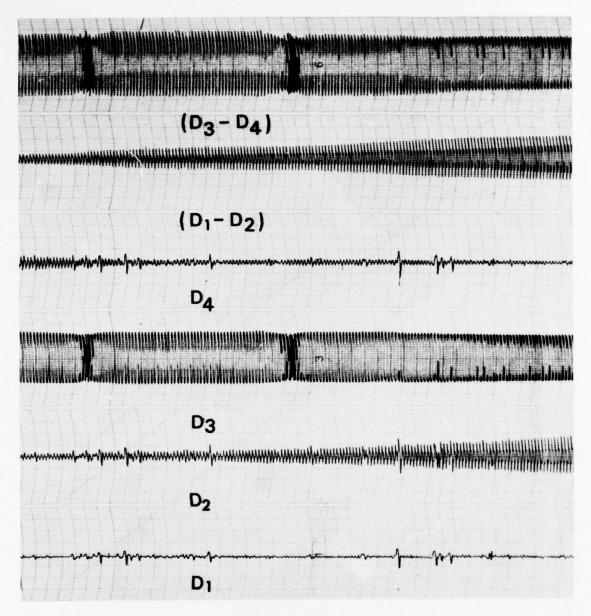


Fig. 25(a) Signals received by the four dipoles.

BACK GROUND NOISE SPACE CORRELATION

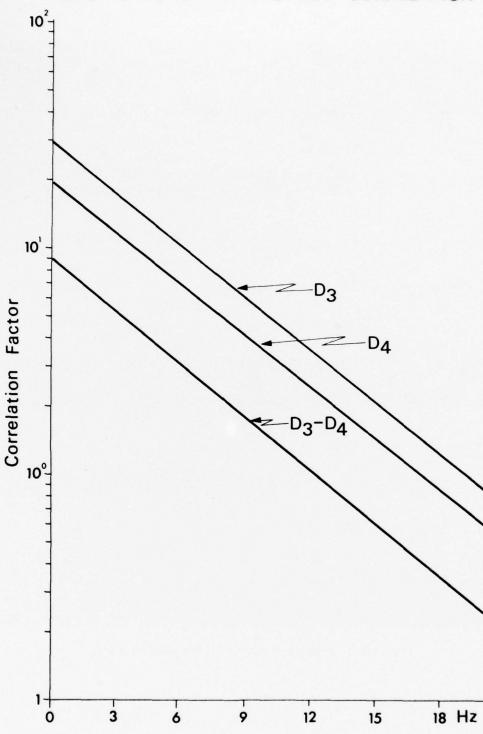


Fig. 25(b) Space correlation function.

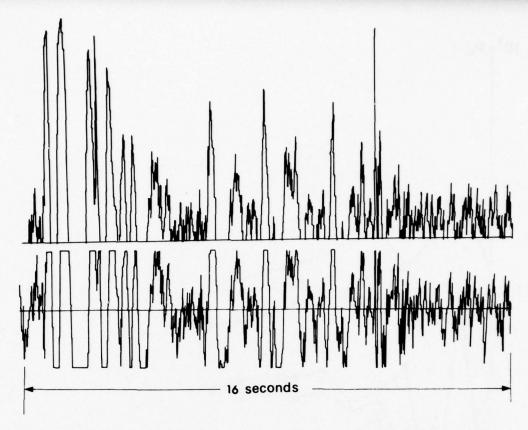


Fig. 26 ELF background noise - spiky and clipped sample.

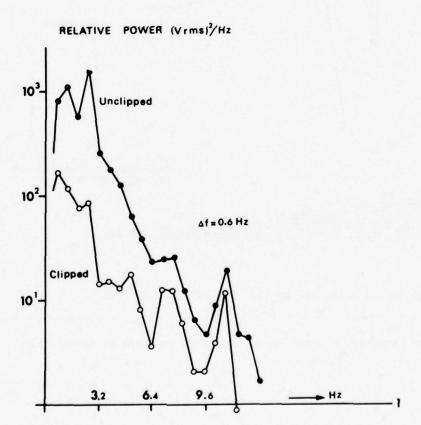


Fig. 27 Power Spectra.

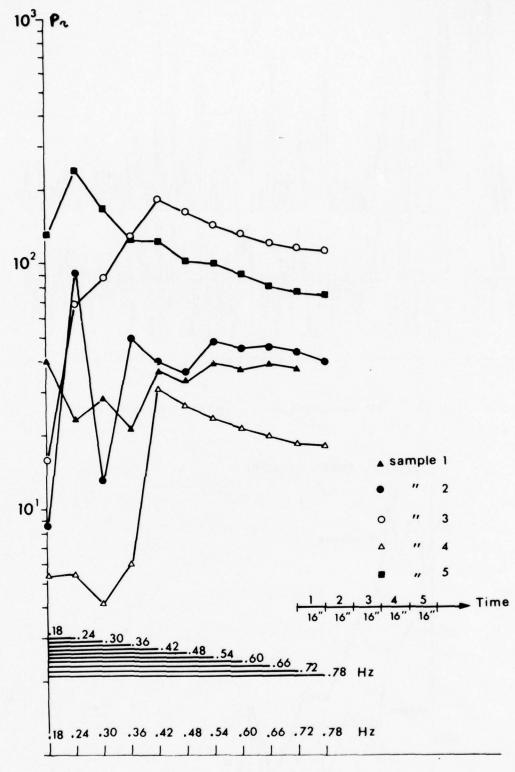


Fig. 28 Mean energy values in function of bandwidth.

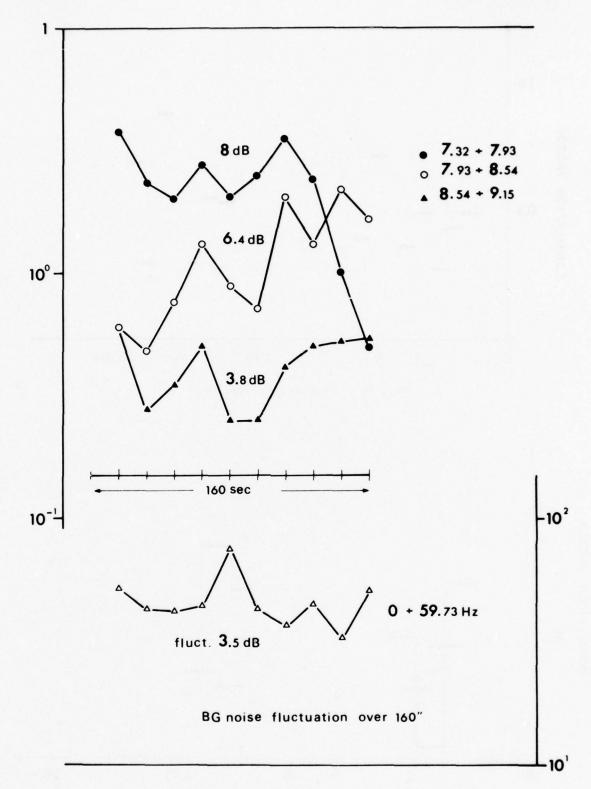


Fig. 29 Fluctuations of ELF noise in contiguous bands.

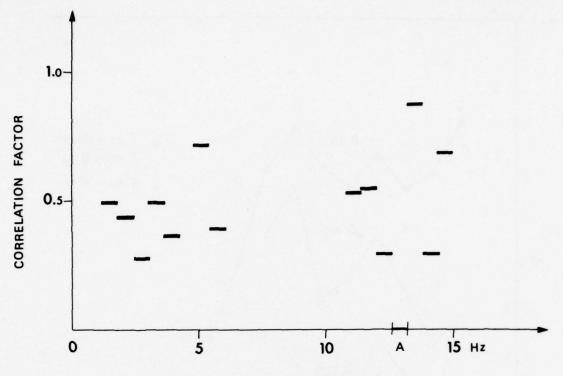


Fig. 30 Correlation factors.

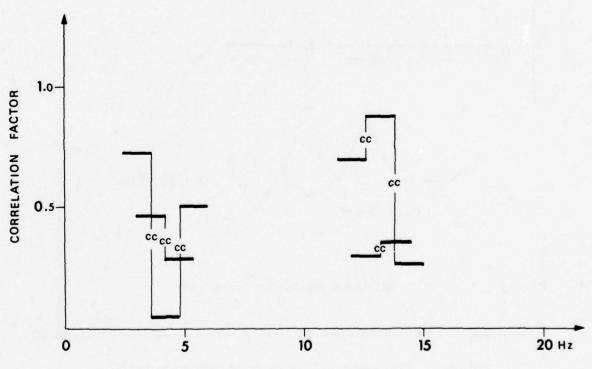


Fig. 31 Correlation factor.

FUNDAMENTALS OF ELF COMMUNICATION AND DETECTION

Giorgio Tacconi

In the main text it was emphasized that any type of physical measurement could be considered a sort of non- or quasi-semantic communication and, in effect, a number of applications on ELF perturbation propagation relative to electromagnetic and acoustic or elastic phenomena are already under study. These applications, which were not treated in the main text, should at least be mentioned in order to give a wider view of ELF phenomena relevant to communications.

ELF methodology as used in electromagnetic prospecting systems could be similarly applied to lithospheric communications [Ref. A.1]. Elastic phenomena in the ULF frequency range (<1 Hz) are used by geophysicists in investigating the earth's crust, and for prospecting purposes at infrasonic and sonic frequencies from 1 Hz to 100 Hz. Communications through a very general multistructured medium as, for instance, the system ocean = coastline = land, could be effected by means of ELF acoustic-refracted arrivals, e.g. compressional and shear waves [Ref. A.2 and A.3], or interface waves, e.g Stoneley, Scholte, Rayleigh waves [Ref. A.4].

Other subjects that are also open to consideration (probably some are already under investigation), are:

- (i) Non-linear conductivity effects in earth, rocks, water and interfaces.
- (ii) Ions generation and flow at earth/sea interfaces.
- (iii) Electromagnetic fields associated with rock stresses and releases (earthquakes, volcanos).
- (iv) Generation of LF acoustic and electromagnetic perturbations by high altitude aircraft.
- (v) Telluric electric fields Tsumani effects.
- (vi) Electrochemical noise for electrodes, chemical migrations.
- (vii) Influence of man-made noise contributing to the total.

All types of communication involving spatial parameters require an estimate of the statistical characteristics in time and in space [Ref. A.5]. Although, at present, the Gaussian assumptions are conveniently useful, day-by-day they are proving more inadequate. Mathematicians, physicists and scientists investigating communication theories and systems are engaged in advanced tentatives to operationally apply new algorithms to treat random non-Gaussian processes. Algorithms such as "non stationary and non-Gaussian signal/noise analysis" [Ref. A.6 and A.7], stochastic calculus and Martingales [Ref. A.6 and A.8], which may at present appear to resemble abstract mathematical exercises, in fact, represent two important features: to confirm and improve

the actual analysis systems and to open new and, may be, more reliable systems to signal processing.

REFERENCES

- A.1 F.S. Grant and F.G. West, "Interpretation theory in applied geophysics", McCraw-Hill, New York, 1965.
- A.2 W.M. Ewing, W.S. Jardetsky, F. Press, "Elastic waves in layered media", McCraw Hill, New York, 1957.
- A.3 L.M. Brekhovskikh, "Waves in layered media", Academic Press, New York, 1960.
- A.4 L. Cagniard, "Reflection and refraction of progressive seismic waves", McCraw-Hill, New York, 1962.
- A.5 C.P. Patil, S. Kotz, J.K. Ord, "Proceedings of NATO ASI on statistical distributions in scientific work", Calgary, Canada, August 1974.
- A.6 J.K. Skwirzynski, "Proceedings of NATO ASI on communication systems and random process theory", Darlington, U.K., Aug 1977.
- A.7 E. Wong, "A Martingale approach to random fields", NATO ASI on Communication Systems and Random Process Theory, Darlington, U.K., Aug. 1977.
- A. 8 A. Segall, "Stochastic processes in estimation theory", IEEE Transaction on Information Theory, Vol. 22, No.3, May 1976.

ELECTRIC AND MAGNETIC SENSING SYSTEMS: APPLICATIONS

Frank Chilton Science Applications, Inc., Palo Alto, California

Lowell Wood
Lawrence Livermore Laboratory, Livermore, California

Rod Buntzen Naval Ocean Systems Center, San Diego, California

0. INTRODUCTION

The objective of this lecture is to review the underlying principles of electric and magnetic sensing, to discuss some of the more recent advances in the associated technologies and to provide some insight into the use of such systems in ocean surveillance.

Primary applications of electric and magnetic sensors are found in the surveillance activities of the U.S. Navy. This application suite first became possible because of extensive pre-World War II development work by the Gulf Oil Company, in search of new oil fields. Magnetic detection became a Navy capability in 1941 as the result of this industrial development work.

Detection activity support remains the primary thrust of electric and magnetic technology development within the U.S. Navy today. Extremely sensitive devices such as superconducting quantum interference devices (SQUIDS) represent the single most important new basic physical principle involved. Such technology plus signal processing and systems engineering gains have expanded and refined the detection application parameter space. For example, magnetic gradient measurements of the saline (and therefore electrically conducting) flow associated with surface and internal ocean waves are being considered. Such measurements are important to development of technologies for both acoustic and non-acoustic ASW. In many system concepts, signal-to-noise ratios and false-alarm rates depend on both temporal and spatial distributions of the ocean natural wave background. If magnetic measurements of acceptable quality can be made by aircraft, high-sweep-rate mapping of the surface and internal wave spectra of an entire ocean basic could be seriously contemplated.

We will briefly discuss these applications below. We will not discuss the performance of specific systems or possible military tactics related to various sensing systems. It is intended that these topics will be developed as appropriate during the scheduled discussion periods.

1.0 BACKGROUND

1.1 Magnetic Field Sources

Although the source of the earth's magnetic field remains unproven, the more fashionable theories suggest that the main field originates from electric currents in the earth's liquid core, which are associated with slow convective movements. Large scale eddies in such convective motions apparently engender local variations in the field, which bear no apparent relation to crustal features. Mathematically represented, the earth's magnetic field originates from a dipole source (with a length $\sim 1/3$ its diameter) at the earth's center, skewed at approximately 15 degrees from the earth's rotational axis (as shown in Fig. 1), to a good approximation.

This dipole source establishes a field at the earth's surface with intensity between 0.25 to 0.7 Gauss (1 Gauss = 10^5 gamma), as indicated in Fig. 2. Changes occur continually in the spatial and temporal fine structure of this field distribution due to solar and lunar cycles, solar activity variations, magnetospheric and ionospheric activity, and ocean

storms. Any spatial variation from this dipole field is termed an anomaly. Anomalies are commonly caused by waves, ore deposits and ferromagnetic objects (including surface and subsurface ships). The incremental field levels associated with these anomalies can be quite large, as indicated in Fig. 3.

Figure 4 illustrates the basic effect of a local dipole source on the total magnetic field, in two dimensions. A stronger total magnetic intensity (+) will be measured where the magnetic lines of force happen to be aligned with those of the earth; the net intensity drops (-) where their vector quantities oppose. Thus the anomaly contributes positive and negative components to the total field. If the unperturbed ambient field is somehow measured and subtracted out, only that signal caused by the presence of the anomaly (e.g. a ship) remains. In or over a calm, deep sea, the ambient magnetic field is relatively constant, because of the relatively homogeneous magnetic character of sea water and the substantial separation from possible underlying crustal anomalies. In such circumstances, a steel ship interposes itself as a discernable magnetic anomaly. This is not surprising since there is a relatively large amount of energy associated with the magnetization of a multi-thousand ton steel vessel.

Measurement of magnetic field intensity and direction for the purpose of detecting anomalies requires a large scale description of the unperturbed field. The earth's total magnetic field can be represented as the vector sum of horizontal (surface tangent plane) and vertical components. The horizontal component may itself be represented as the sum of true north and east components in the local tangent plane. The magnetic dip (inclination) is defined as the angle formed by the horizontal and total field vectors. The declination is the angle made by the true north and local magnetic north vectors. A total field magnetometer measures the absolute value of the local field intensity, but without an associated direction. One method of measuring the field direction with a total field magnetometer is to use biasing coils in the planes of mean declination and inclination to generate reference angles.

Another property of the magnetic field is its gradient, or rate of change with distance for each directional component described. Measurement of the gradient associated with a magnetic anomaly has certain detection advantages, as will be discussed subsequently.

1.2 Target Strengths

The magnetic moments associated with a field anomaly comprise the target strength term when considering the range at which the anomaly may be detected. These moments are both static and non-static. The static moments are related to the constitutive equation(s) between B and H for the material(s) comprising the anomaly generator, and in the case of a ship, are influenced by such characteristics as structure, size, weight, heading and inclination. Non-static moments of such a source are those which are related to distributions of galvanic currents and rotating machinery.

As with the local terrestrial magnetic field, the total moment ($\rm M_T$) of an anomaly may be represented by a vector directed along some coordinate system axes. Permanent moments for ocean-going vessels are widely variable, because of the widely varying magnetic histories of the components of such vessels. Maximum values for the permanent moments of interest are of the order of 3 \times 10 6 gamma-m 3 . Real-world values can be less than this, and depend on the amount of effort expended to reduce such effects during vessel construction or by subsequent degaussing procedures. Induced moments are caused by the earth's field, and not as easily reduced. Although many different estimates of the magnitude of such moments exist, the maximum induced moments of present multi-thousand ton steel vessels may be of the order of 10 8 gamma-m 3 .

1.3 Noise

Since electric and magnetic surveillance applications will require consideration of the detection of static and non-static dipole moments and internal wave-associated water flow, the characterization of noise must extend from about 1 kHz down to nearly DC. Typically the noise competing with signal consists of contributions from the sources described in Table 1. The frequency and amplitude of these sources is shown in Fig. 5. Lower frequency noise (<1 Hz) associated with ocean internal wave spectra is discussed in Section 4.

Noise is treated by a number of approaches including instrument design, signal processing and operational procedures. Many previously limiting thermal noise and stability problems are being overcome with cryogenically cooled or superconducting systems. Sensor rotation and servo noise effects are highly dependent on magnetometer type; noise levels of the order of 10^{-2} gamma ($\gamma = 10^{-5}$ G) represent the state-of-the-art of currently used systems. Outboard (probe) and towed-bird systems are used to isolate sensitive magnetometers from platform power-related and structure noise. Operationally, sensor altitude can be adjusted to reduce wave/swell MHD noise contributions, and magnetic compensation systems are used to discriminate against maneuver noise. One of the most recent operational systems is the Canadian Aviation Electronics Company one with semi-automatic compensation, which uses servo motors to adjust compensator coils driven by error signals from aircraft maneuver amplitude and rate sensors. Newer systems will depend on processed analog signals from field measurement inputted to directly cancel the disturbance.

Geomagnetic anomaly and gradient noise is the most difficult to process against. Variable filters offer the largest single improvement, but at the sacrifice of some detection range. Matched filters that conform to the expected signal shape are also being investigated and are discussed in a later section.

2.0 MAGNETOMETER AND GRADIOMETER SYSTEMS

2.1 Magnetometer Concepts and Operating Principles

The total magnetic field may be measured by a number of component-measuring devices, or by one device which is sensitive to the magnitude of the total field, independent of its orientation. These devices typically operate via elementary interactions between nuclei (or atomic electrons) and the local magnetic field. Although many physical mechanisms have been considered for potential magnetometer design, only a few have enjoyed operational success in the US and European communities. Table 2 summarizes the more successful approaches, and indicates the sensitivities of the order of 10^{-3} gamma are possible. However, the real-world noise environment circumscribes the utility of such sensitivities. Gradiometer approaches are an attempt to use devices with greater inherent sensitivity, and are discussed in the next section.

To appreciate the basic physical principles of presently deployed magnetometers, consider nuclear protons and orbital electrons spinning about their relative axes. This motion gives rise to corresponding magnetic dipole moments. In an external magnetic field, the particles' axes will tend to loosely align with the field by precessing about the field vector. The frequency of precession is directly proportional to the external magnetic field intensity and hence provides a means to accurately monitor its value. In addition to spin, the orbital electron motion yields another magnetic dipole moment. The total magnetic moment of the atom is the vector sum of the magnetic moments of the nucleus and electrons. Thus, certain orientations of an atom's magnetic moment can be attained relative to the direction of an external magnetic field. Finally, the external field splits a particular electron energy level into several sub-levels (Zeeman effect). Populations in the various orientations (states) can be pumped and observed by a variety of means (Table 2).

Table 1 Magnetic Detection System Noise Sources

Noise Type	Examples	Coherent (C) Random (R)	Typical Approaches
Instrument Noise	Thermal Noise Gyroscopic Maneuver Noise	R C	Cryogenic technology (Josephsen sensors) Effect is inverse with Larmor frequency Utilize light gas such as Helium
Aircraft/Ship Noise	Vehicle Maneuvering Turbulence Electromagnetic Compatibility	C R	Aircraft compensation coils Removal of dc loops, shielding
Geomagnetic micropulsations	Pulsations of the Magnetosphere & and resulting E/M	C-time	Correlation with second magnetometer remove coherent noise
Geomagnetic Anomaly/ Gradient Noise	Earth crust anomalous noise	C-space	Most difficult
Magnetohydrodynamic Wave Noise	Wind wave noise Internal waves Ocean swells	c	Flying higher
High Frequency Noise	Lightning Contribution	R-but non-Gaussian	Suppression by clippers Narrow filters
Man-made Power-related Noise	50, 60, 400 Hz power sources	С	Phase lock techniques

Table 2 Summary of Major Magnetometer Designs

Type Theor	etical Sensitivity Limit	Operating Principle
Flux gate	0.001 gamma	AC excitation of a magnetically saturable core material. Harmonic of drive frequency distorted proportional to field along core axis. Bucking fields insure maximum sensitivity at low drive fields.
Pulse Proton Precession (NMR)	0.1 gamma	Prealigned spins in proton-rich material relaxed. Pre- cession occurs and the frequency of the corresponding voltage in pickup coils gives ambient magnetic field.
Overhouser	0.001 gamma .	Similar to above, except uses material doped with paramagnetic salts with higher moments and spin alignment by RF, instead of strong local magnetic field.
Cs, Rb Vapor	0.001 gamma	Optically pumped alkali vapor exhibits Zeeman effect; RF absorption by vapor causes resonant absorption of optical energy. RF frequency producing peak optical absorption gauges the ambient magnetic field.
Metastable He	0.001 gamma	Same as above, but temperature—independent and simple resonance line structure.
Josephson	10 ⁻⁷ gamma	Impedance of a superconducting circuit is a periodic function of the number of magnetic flux quanta threading it. Extreme sensitivity, as fractional flux quanta detection is attained by time averaging.

A good example of currently deployed magnetometer operation is based on the use of metastable He. The basic layout of this magnetometer is shown in Fig. 6. A helium lamp illuminates a helium cell where resonance absorption occurs and electrons are pumped to higher energy levels and then fluoresce to lower-lying, occasionally metastable ones. An RF field which is swept in frequency to attain resonance with a sub-level pair, thus redistributing population between these levels, is used to determine the ambient magnetic field strength. Energy state redistribution is monitored by a differential signal as seen by the IR detector.

A difficult systems problem encountered in field-qualifying metastable He magnetometers was attaining the required frequency stability of the RF generator over the frequency range required. Minor changes in the lamp's output intensity, coefficient of amplification, angular errors between the optical axis and magnetic field vector, etc. all affect the signal accuracy.

2.2 Gradiometers

The only practical means of detection of extraordinarily low magnetic field intensities of 10^{-9} Gauss (which is coincidentally the order of magnitude of magnetic field intensities generated at the surface of the skull by the living brain, or the field intensity perturbation of a compact car at the distance of roughly a kilometer or two) is via the Josephson effect.

The Josephson effect is an example of the interferometry that is possible from manipulation of macroscopic quantum phenomena which are responsible for superconductivity, superfluid helium, ferromagnetism, ferroelectricity, lasers and other large scale, coherent quantum manifestations. Fig. 7 shows a typical design for a superconducting SQUID (Superconducting Quantum Interference Device). The essential point is that a SQUID has a "weak" (in the superconducting sense) link which allows the penetration of magnetic field lines through a mostly superconducting volume from which it would otherwise be excluded due to the Meissner effect. Fig. 7 also shows the interferometric pattern that results from increasing the magnetic field intensity externally imposed on a SQUID, which then intrudes into the area between the two oxide junctions. The essential point is that each oscillation in the macroscopic current flowing through the electron interferometer defined by the two Josephson junctions connected in parallel represents the entry of another flux quantum (which is approximately equal to 2×10^{-7} Gauss-cm²) into the area enclosed by the two Josephson junctions. With time-averaging over a period of some seconds, the oscillatory current signal is sufficiently stable that it is possible to easily read the area integral of the magnetic field intensity to 0.1% of a flux quantum. If the background noise of all types is sufficiently reduced, it is presently possible to read the areal magnetic field intensity integral to 10^{-5} of a flux quantum, with an averaging time of about 1 second. Since the magnetic loop or pickup coil can be on the order of 1 cm^2 (or larger) in area, being able to stably define the imposed magnetic field intensity to 10^{-3} % of a flux quantum leads to absolute sensitivities of the order of 10^{-12} gauss, such sensitivities have indeed been demonstrated in laboratory environments.

Naturally, the possibility of such sensitivity in field magnetic measurements has revolutionized low magnetic field, or equivalently low current, or low voltage measurement techniques. Josephson was recently awarded the Nobel Prize for his theoretical and conceptual work on electron tunneling in superconductors.

3.0 SYSTEMS PERFORMANCE ESTIMATES

Some basic comparisons between magnetometers and gradiometers illustrate their relative advantages and disadvantages for magnetic (or electric) detection. Such comparisons

will not consider specific signal processing techniques and do not reflect any particular sensor system performance. Much of the real-world data of target moments, noise compensation capability, inherent system noise, filter design, etc. is beyond the unclassified nature of this lecture, but must be considered to make actual performance estimates meaningful.

Instead, the general trends of system performance are discussed. The total-field signal level H at any point from a dipole of strength M may be written as

$$H = \frac{M}{R_0^3} \sum A_i \phi_i(\theta^i), \qquad (1)$$

where R_0 is the closest point of detector approach to the anomaly source, and A_i and ϕ_i are Anderson function coefficients and the functions, respectively; ϕ_i are generally expressed in terms of a dimensionless parameter, θ , describing the detector's range along the track from the closest point of approach (CPA). Taking the Anderson function multipliers as unity for the purpose of illustration, a magnetometer maximum detection range R_0 for a dipole of strength M in the absence of noise as a function of its sensitivity field intensity H can be expressed as

$$R_0 \stackrel{\sim}{\sim} \left(\frac{M}{H}\right)^{1/3}$$
 (2)

A similar expression for a gradiometer performance is

$$R_0 \sqrt[7]{\left(\frac{3M}{\text{grad H}}\right)^{1/4}}$$
 (3)

Figure 8 brackets the possible parameter space of interest for magnetic anomaly detection. Notice that gradiometer minimum sensitivities should be less than about 10^{-5} gamma to be competitive with magnetometer systems that achieve sensitivities within a factor of 10 of their theoretical maximum (see Table 2). Real systems must contend with noise, however, and some form of signal processing is generally required.

Although various forms of signal processing are being studied in order to upgrade present magnetometer performance, only matched filter processing is discussed here. Such signal processing techniques are applicable to signals from both magnetometer and gradiometer sensors. In such cases, a detection circuit mixes the signal, S(t), with the combined noise components, (N(t)), discussed earlier, which are assumed to be white Gaussian random in nature. This signal-plus-noise forms the input to a matched filter which in turn inputs to a voltage threshold detection circuit. High quality knowledge of the signal shape expected allows the necessary filter to be constructed to maximize the instantaneous signal power output in the presence of any level of noise. This specification is easy to make but somewhat more difficult to put into effect, though less so as high performance digital microprocessors continue to develop. Of course the anomaly field strength is a function of its aspect angle at the detector, if the anomaly is other than magnetically isotropic.

Operation of the matched filter in the presence of white Gaussian random noise leading to a detection event is illustrated in Fig. 9. The horizontal axis represents the filter output voltage, while the vertical axis represents the differential probability of observing that particular voltage. The noise-only and noise-plus-signal distribution generally overlap, so that some signals are missed and some noise triggers the detector circuit by being higher than threshold (thus generating a finite false alarm rate). A desired probability of detection P(D) and corresponding false alarm rate are chosen to meet operational requirements, as constrained by the detector-plus-filter quality.

The quantity of interest is the detection range which corresponds to a given $P_{\overline{D}}$ and false alarm rate, and is determined by the detectivity (or ratio of signal energy to

noise energy, N) in the band of interest. The signal energy is obtained by squaring the signal level and time-integrating it over the period of observation. For example, detectability may be written for a magnetometer as

$$d_{M} = \frac{M^{2}}{R_{0}^{5}N} C (A_{i}; v,k)$$
 (4)

where $C(A_i; v, k)$ is a constant dependent on the Anderson function coefficients, detector platform speed, and units conversion factors. The probability of detection relates to the detectability for the case of white Gaussian random noise as

$$P_{D} = 1 - e^{-\alpha d_{M}}$$
 (5)

where α is a constant, approximately 0.282. A similar equation for a gradiometer would use a corresponding detectability with a R_0^{-7} dependence. These relationships suggest how insensitive magnetic anomaly detection range is to the particular parameters (and technologies) involved.

As mentioned earlier, corrosion currents give ships a static electric DC moment. If a typical source of sacrificial zinc and a bronze screw is represented as a horizontal electric dipole, its signal strength at a distance \mathbf{R}_0 can be given as

$$S(r) \alpha \frac{P}{R_0^3}$$
 (6)

where P is the electric moment (Amp-ft). DC electric field detection ranges are shorter than magnetic detection ranges because the electric moments are so much smaller. AC fields associated with variable resistance in the DC current path given rise to alternating electric fields which, however, are rapidly attenuated by propagation through sea water.

4.0 SURFACE AND INTERNAL WAVE SENSING

Detection of such extraordinarily small magnetic fields (10^{-12} G) as described in the foregoing has led to the prospect of remotely measuring ocean internal wave spectra. If presently explored approaches to such measurements proves successful, an airborne magnetic gradiometer could be employed to make high sweep-rate surveys of internal wave backgrounds over large ocean areas. Such estimates of ocean surface and internal wave spectra might play an important role in ocean surveillance, as suggested earlier.

The basis for generation of magnetic fields by internal waves is simply the Faraday effect. The Faraday effect for conductors moving in a magnetic field has been known for about 150 years and is the basis for such diverse applications as homopolar generators and motors, V×B velocity meters (used for ship speed and for determining currents in oceanography), measurement of blood flow rates; etc.

To appreciate the basic nature of Faraday induction in the case of ocean waves, we consider the Maxwell equations for a magnetized, conducting medium moving with a velocity small compared to that of light:

$$\nabla \times \mathbf{B} = \mu_0 \quad \sigma \mathbf{y} \times \mathbf{B}, \quad \nabla \cdot \mathbf{B} = 0 \tag{7}$$

The Fourier transform applied to these equations yields a negative exponential dependence on height above the surface for each spectral component, as noted by Podney, some of whose normalized results are indicated in Figs. 10 to 13. In these Figures, K denotes wave number of a progressive wave, D the ocean depth, and λ the wavelength.

From these results, it is apparent that the order of magnitude of the magnetic field gradients generated above the ocean surface by both surface waves (which would act as a "projection screen" for detecting internal waves) and for internal waves are of the order of 10^{-8} Gauss/m, unless there are unusually high surface wave speeds. Such small

magnetic fields would be detectable with superconducting magnetic gradiometers; however, actually making the measurement is non-trivial. In fact, it is extremely difficult, because the Earth's magnetic field gradient is of order of 10^{-7} Gauss/M, so that the measurement can be made meaningful only if one measures a gradient of the component of the anomaly field along the direction of the Earth's field.

Measurements have been made of the internal wave amplitude, direction and phase speed, by Physical Dynamics Inc., at a station off San Diego, California, in a water depth of 17 m. The temporal power spectral densities (PSD) are shown in Fig. 14. Considerable variability in the PSD level is shown, which also represents variations in the gradient signals expected. Adequate signal-to-noise ratio requires a resolution of 10^{-3} γ/m in the internal wave frequency band. To observe surface waves requires about the same resolution at frequencies up to ~ 0.1 Hz. Such resolution over a frequency range of $5\times 10^{-4}-10^{-1}$ Hz is difficult to achieve with present day gradiometers, especially at the low frequency end.

4.1 System Design

In order to attain system sensitivity comparable to the sensitivity of which superconducting instrumentation is capable, a number of design features unique to superconducting instrumentation are required. First, the SQUID is usually used as a detector in the $10^{-1\pm0.3}$ Hz regime, because that is a low noise portion of the ambient electromagnetic spectrum. Physically, the "pumping" of the SQUID means that a flux quantum is moved in and out of the Josephson junction pair at rates as high as 10 gigahertz. The SQUID is either a thin film on a glass substrate (which has been etched or scribed to have a weak link) or a toroidal point contact structure (where a screw or wire makes mechanical contact with the other part of the superconducting toroid to provide the weak link).

The parts of the superconducting gradiometer circuit, which will be employed by Physical Dynamics Inc., are illustrated in Fig. 15, which indicates the tank circuit employed for the purpose of resonantly pumping the SQUID. On the far side, the two pickup loops that are characteristic of a superconducting gradiometer are shown. (A magnetometer would have only one pickup loop.) In such a superconducting gradiometer, the pickup loops are counterwound and thus provide an intrinsic gradiometer, rather than a gradiometer from magnetometer subtraction: the two loops are counterwound in order to provide a net cancellation of the homogeneous portion of the magnetic field separated by a distance, so that the gradient is measured directly. This technique reduces noise enormously.

Further consideration of Fig. 15 indicates some of the design innovations that have been recently introduced. In order to obtain low noise performance from the pickup coils, the leads proceed through a superconducting shield which keeps the basic detection circuit entirely shielded from stray magnetic fields of local origin, as well as those produced in the instrumentation by vibration or temperature fluctuation. A transformer is introduced between the pickup loops and the SQUID in order to attenuate radio frequency interference. This radio frequency interference attenuation is particularly important for low frequency detection situations, such as the fields associated with internal waves (for which there is little interest above about 0.1 Hertz, in any event). The radio frequency interference originating from radio and radar antennae in the vicinity is frequently quite capable of swamping such sensitive instrumentation without such a shield.

A particular superconducting gradiometer system is shown in cutaway in Fig. 16. The superconducting circuit (indicated in Fig. 15) is shown at the bottom of the system. Because this is a cryogenic system, it must be operated at liquid helium temperatures, at 4°K. A number of design features are relatively unique to the system's cryogenics. For example, there is an interior vessel, an outer vessel and an intervening vacuum

layer. The insulation is not shown; superinsulation (thin aluminum mylar sheets) is wrapped around the inner vessel, space-filling the vacuum layer.

Because vibrating metal parts or paramagnetic impurities would swamp the very weak magnetic signals of interest, the inner and outer vessels are made of epoxy-fiberglass. The liquid helium 'hold time' of such systems can be as long as 30 days, which indicates the phenomenal thermal performance of the superinsulation and the fiberglass vessels. A socket made of Kevlar (which also has good nonparamagnetic and thermal properties, as well as remarkable strength at low temperatures) is provided for the superconducting circuitry, and a long neck tube comes up from the inner vessel in order to provide a long thermal path. The long rise also permits the boiled-off liquid helium gas to cool the long tubes of the probe structure. This is effective because at lower temperatures the thermal conductivity of the probe structure is greatly decreased, so that the cooling decreases the heat leak into the interior vessel by two independent mechanisms: direct cooling of the heat leaking along the probe structure, and also reducing the thermal conductivity of the probe structure.

The support tubes labeled "probe structure" are designed to be long and have circular bands which provide thermal contact between the support rods, at a given height, in order to prevent any bending due to slightly different temperatures along the support rods, as well as acting as stiffening rings. A socket spacer is put over the probe socket in order to prevent the probe socket from vibrating inside the interior cryogenic vessel and generating sources of system noise. Since this is a cryogenic system, the top plate of the probe has liquid He fill ports.

The required sensitivity level of the internal ocean wave experiment mentioned earlier is so low that practically all sources of system and background noise must be examined. System noise includes the intrinsic noise limit of the SQUID itself, noise from the detector electronics, temperature fluctuations in the detector metal structure and helium bath, mechanical vibration of metal parts, trapped flux, paramagnetic impurities, and vibrations about any component misalignment or imbalance.

Examples of background noise include the field from the surface waves, motion of the ferromagnetic parts of any support structure, and fluctuations in the ambient total magnetic field gradient, of both terrestrial and extraterrestrial origins.

Diagnostic measurements characterizing the background against which internal—wave associated fields are studied typically include direct measurements on the internal waves to determine the depth, amplitude, phase velocity, and direction, using thermistors in vertical arrays through the thermocline. Other desirable diagnostic measurements include the sub-surface current, wind speed and direction, wave height, tide height, barometric pressure, sea surface temperature, salinity profile, and time lapse photographs every few seconds of the sea surface during daylight hours.

4.2 System Noise

Different types of SQUIDs have been examined for the purpose of finding those with lowest system noise. The interesting feature of a typical SQUID noise spectrum (Fig. 17) is the white noise region above approximately 1 Hz and the approximately \mathbf{f}^{-1} noise below that frequency. (The low frequency noise is not exactly \mathbf{f}^{-1} noise, but it has approximately that empirical value for the exponent.) Of course, the SQUID noise is not really the most important source of noise, nor was it expected to be. It happens though, to be the noise source which may be most readily measured, and because it is intrinsic to the system, it constitutes the design limit which one would like the rest of the system to meet.

A recent low noise experiment at the La Posta Astrophysical Observatory (about 70 miles east of San Diego) serves to demonstrate the effects of the local environment on ultrahigh sensitivity SQUIDs. In this experiment, effects of fluctuating ambient temperature and pressure and terrestrial magnetic field fluctuation-induced magnetization currents in the paramagnetic materials and eddy currents in superinsulation and metal parts were examined. In the frequency region below 0.1 Hz, SQUID noise appeared to dominate the system, as shown in Fig. 18. Also investigated were the effects of radio frequency interference at the transformer.

The effect of temperature changes is primarily important in the way that the temperature fluctuations or drift can affect the paramagnetic susceptibility of the fiberglass in the cryogenic enclosure. Estimates show that a temperature change of the order of 0.1° K is equivalent to a 10^{-7} Gauss/m change in gradiometer output. The temperature/pressure relationship in liquid helium means that pressure fluctuations can cause temperature fluctuations which can then change the paramagnetic susceptability. Estimates show that these are about an order of magnitude lower than the direct temperature fluctuations.

Similarly, any fluctuations in the earth's magnetic field would affect the paramagnetic susceptability of the cryogenic enclosure; estimates indicate that these were more than an order of magnitude less than the effect of the temperature fluctuation.

Induced eddy currents in the conducting materials of the gradiometer were also estimated from the fluctuation values expected for the earth's magnetic field. The most important conducting material is the 50 layers of aluminized mylar used as superinsulation. Changes of the order of 10% of the earth's field could cause gradient changes of the order of 10^{-7} Gauss/m in the frequency band of interest below 1.0 Hz. Care in geometric layout of the metal on the mylar film can significantly alleviate this noise problem.

5.0 ISSUES AND COMMENTS

5.1 Total Field MAD in Practice

Total field MAD gear was developed originally to reduce the sensitivity to maneuver noise, which engendered false alarms. In practice, it is often operated at a $S/N \geq 3$ to further reduce false alarms. This results in a short range for detection, in exchange for the benefit of positive identification. One then knows that the magnetic anomaly is nearby, but the one data point of a total field anomaly tells little about where it is, even with signal processing.

Further, since detector-deploying platforms are easily detected, self-propelled anomaly generators will maneuver away.

5.2 The Ideal Magnetic Anomaly Detector

The signal is a magnetic dipole field,

$$B = \frac{RM \cdot R}{R^5} - \frac{R}{R^3}$$

where M is the magnetic moment vector, and R is the range vector. What one would really like to do is measure enough data points, either instantaneously or over time, to determine R and M. Clearly, taking six independent data points at different points of space would be a minimum. Obtaining such a data set implies either taking measurements with several magnetometers and gradiometers in one system, or making six or more total field magnetometer measurements at different times and places, and using signal processing to extrapolate back to different points at the same time. (One total field magnetometer with points in a straight line does not work well because the rotational symmetry yields an ambiguity in the solution, leading to the use of at least two parallel MAD systems in

geophysical prospecting (and, when important to be timely and efficient, two or more aircraft have been used).

It is clearly preferable to use combinations of superconducting magnetometer-gradiometer systems to sample the local field at many more than the minimal six data points, and then to do signal processing (e.g. using a least squares fit) on the resulting overdetermined data set, so as to effectively reduce measurement error to as great an extent as desired, while determining the direction, range and lower order magnetic polar moments of the anomaly.

The sensitivity of superconducting instrumentation promises a bright future for the making of field measurements with sensitivities not hitherto attainable on real-world systems such as surface waves, internal waves, and other low strength ELF signals, as well as on marine magnetic anomalies directly.

REFERENCES

- R. Ziemer, G. Gillespie, "Planning for the ARPA/OWEX Internal Wave Magnetic Sensing Experiment (U)," Physical Dynamics, Inc. PD-SM-76-112, March 1976.
- W. Podney, "Electromagnetic Fields Generated by Ocean Waves," Journal of Geophysical Research, Vol. 80, No. 21, July 20, 1975, p. 2977.
- M.B. Kraichman, "Handbook of Electromagnetic Propagation in Conducting Media (U)," NAVMAT P-2302, 1970.

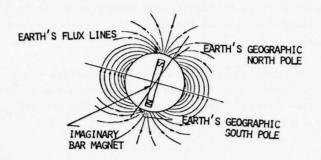
"World Magnetic Survey," (1957-1969), A.J. Zmuda, ed.

IAGA Bulletin No. 28

IUGG Publication Office, 39 Ter, Rue Gay - Lussac, Paris, France, 1971.

- F. Chilton, "Alternating Magnetic Fields from Ocean Internal Waves," January 1977.
- F. Chilton, et al, "Superconducting Devices," NASA Technology Utilization Report, Stanford Research Institute, 1970.

John Clarke, "Josephson Junction Detectors," Science 21 June 1974, Vol. 184, No. 4143.



 $\underline{\text{FIGURE 1}}$ - The Earth as a Magnet

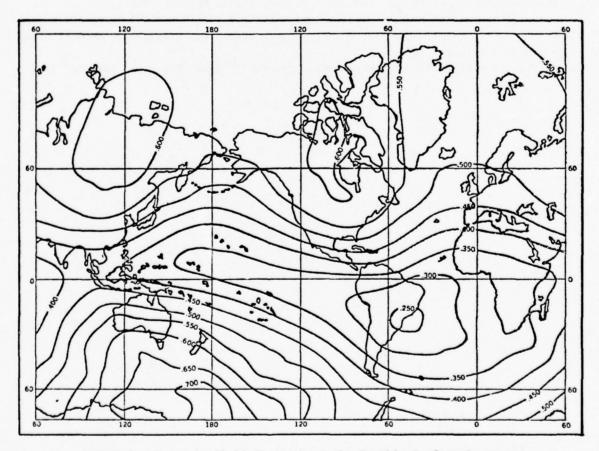


FIGURE 2 - Magnetic Field Strength on the Earth's Surface in gauss

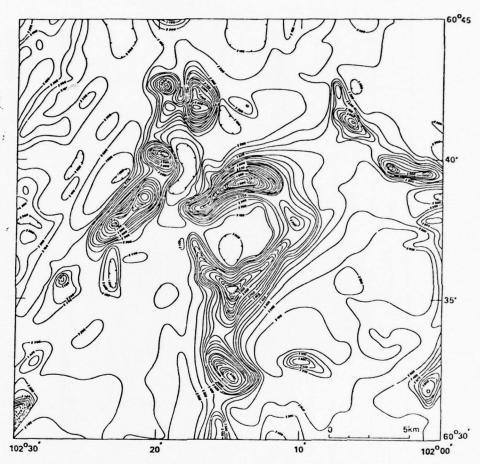


FIGURE 3 - Anomalies in Gammas of Outcropping Metamorphic and Igneous Rocks -- Canadian Shield, Northwestern Canada. After Geological Survey of Canada, Aeromagnetic Series, Sheet 65 D/9. Contours every 100 gammas.

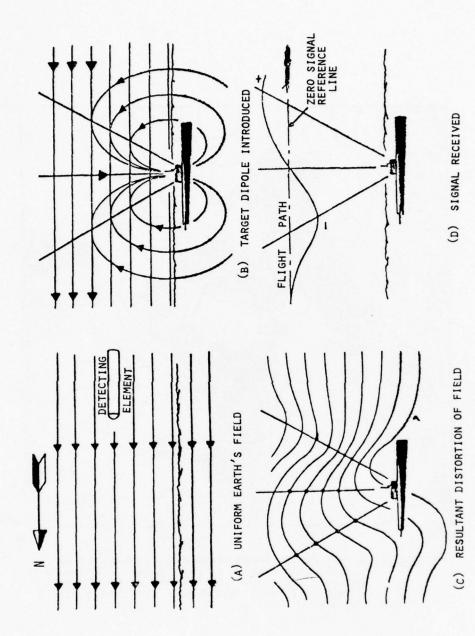


FIGURE 4 - Anomalies Produced by a Naval Magnetic Anomaly



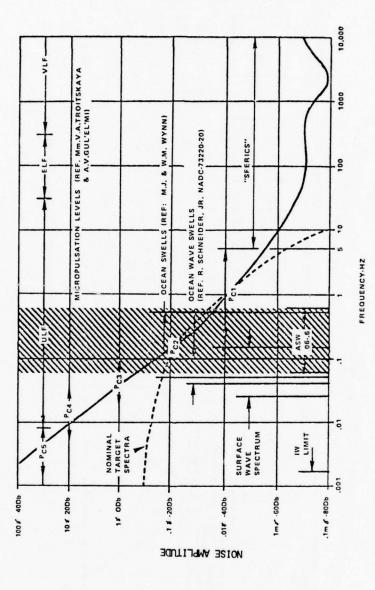


FIGURE 5 - Frequency and Amplitude Characteristic of Magnetic Noise

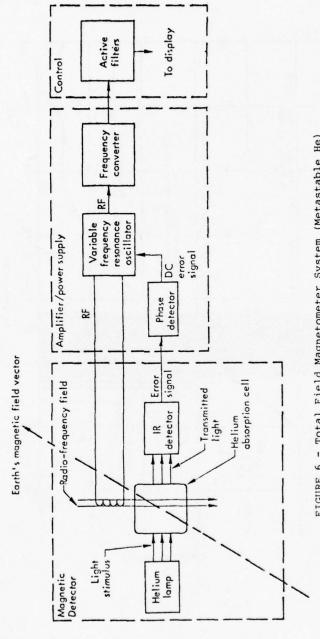
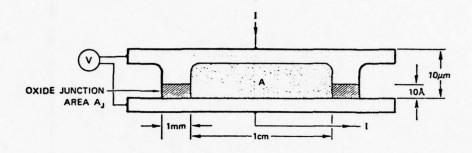


FIGURE 6 - Total Field Magnetometer System (Metastable He)



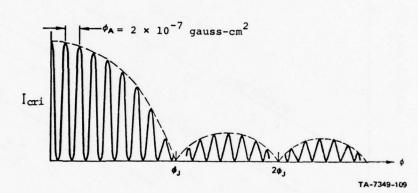
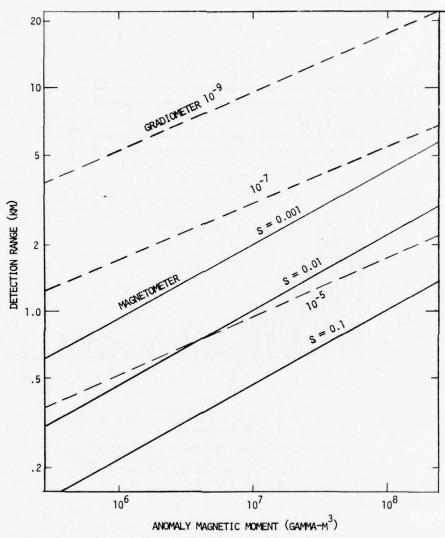


FIGURE 7 - Upper: Schematic Diagram of Double Josephson Junction Magnetometer

Lower: Predicted Variation of Total Current through Double Josephson Junction Magnetometer as a Function of Applied

Magnetic Flux, .



 $\frac{\text{FIGURE 8}}{\text{and Gradiometers without Noise Considerations.}} - \frac{\text{Detection Range Relationships for Magnetometers}}{\text{sensitivities are given in gammas (= }10^{-5} \text{ Gauss).}}$

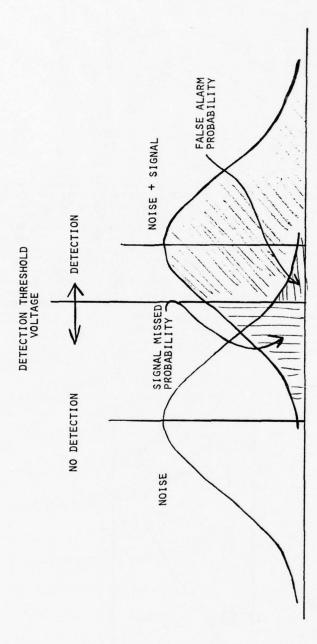


FIGURE 9 - Matched Filter Operation (White Gaussian Random Noise)

FILTER OUTPUT (VOLTS)

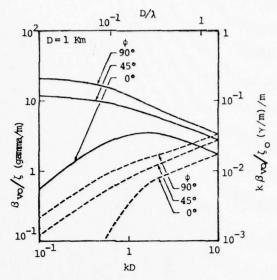


FIGURE 10 - Magnitudes of magnetic fields and horizontal gradients in the direction of wave propagation generated at the surface of a 1-km deep ocean by a 1-m high surface wave propagating in polar regions ($\phi=90^\circ$) and along magnetic meridians at intermediate and equatorial latitudes ($\phi-45^\circ$ and 0°) shown as functions of kD ($k=2\pi/\lambda$) along the lower abscissa and as functions of D/ λ along the upper abscissa. Solid curves delineate magnetic field strengths per unit wave height and correspond to the left-hand coordinate scale marked in units of γ/m . Dashed curves delineate magnitudes of horizontal gradients along the direction of wave propagation per unit wave height and correspond to the right-hand coordinate scale marked in units of $(\gamma/m)/m$.

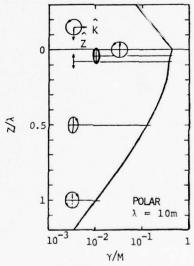


FIGURE 11 - Profiles of polarization and magnitude of the magnetic field generated in a deep ocean (kD >> 1) by a 1-m high surface wave having a wavelength of 10 m and propagating in polar regions. Altitude and depth are measured in units of an ocean wavelength.

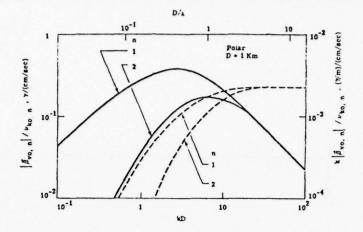


FIGURE 12 - Magnitudes of magnetic fields and corresponding horizontal in the direction of wave propagation generated at the surface of a 1-km deep ocean in polar regions by internal wave modes 1 and 2, each having surface speeds of 1 cm/s, shown as function os kD along the lower abscissa and as function of D/λ along the upper abscissa. Solid curves delineate magnetic field strengths per unit surface speed and correspond to the left-hand coordinate scale marked in units of γ/(cm/s). Dashed curves delineate magnitudes of horizontal gradients in the direction of wave propagation and correspond to the right-hand coordinate scale marked in units of (γ/m)/(cm/s).

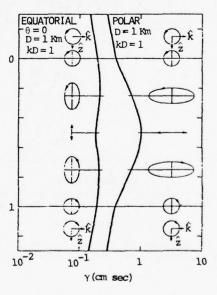


FIGURE 13 - Profiles of polarization and magnitude of the magnetic field generated in a 1-km deep ocean by a fundamental mode internal wave (n = 1) propagating in polar regions and along magnetic meridians in equatorial regions and having a surface speed of 1 cm/s and a wavelength corresponding to kD = 1. Altitude and depth are measured in units of an ocean depth.

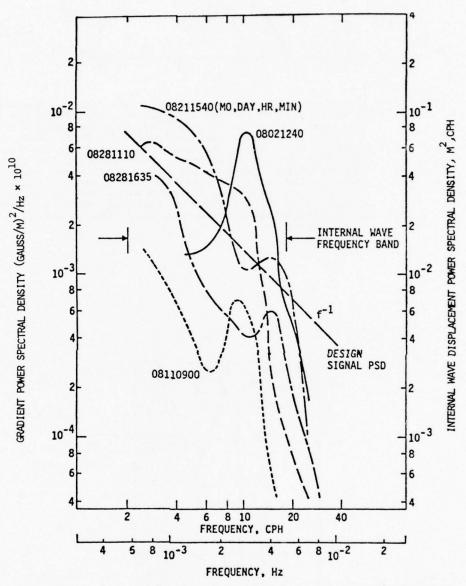


FIGURE 14 - Power spectra of measured internal wave displacement and predicted corresponding magnetic gradient signal levels.



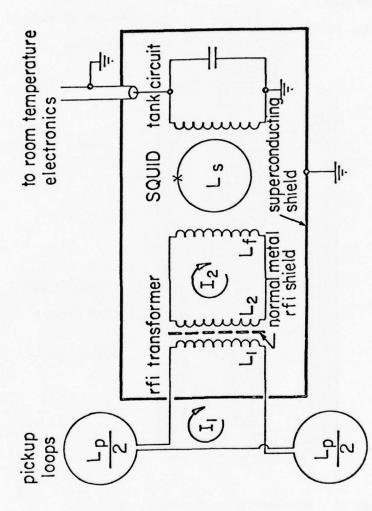


FIGURE 15 - Superconducting Gradiometer Circuit Layout

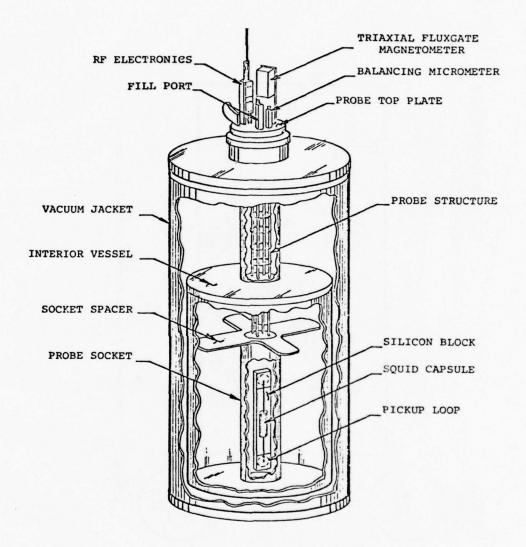
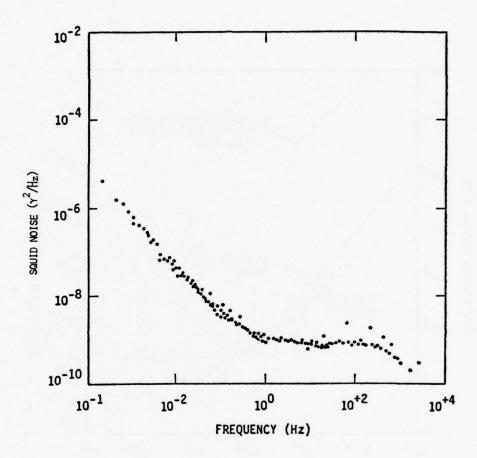


FIGURE 16 - Superconducting Gradiometer Schematic



 $\frac{ \mbox{FIGURE 17}}{\mbox{Point Contact SQUID.}} \mbox{- Noise Power Spectrum for ScT Toroidal}$

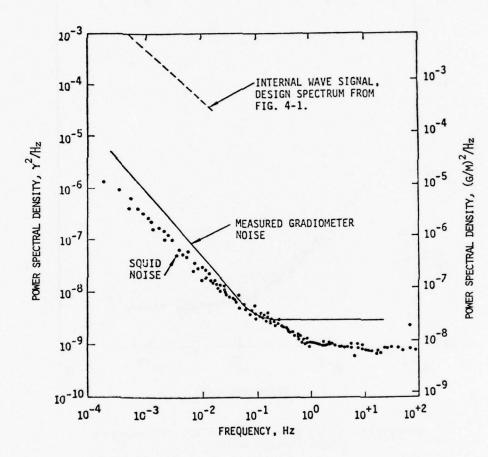


FIGURE 18 - Spectra of toroidal point contact SQUID, measured gradiometer noise in a quiet environment, and predicted internal wave gradient signal level.

AGARD Lecture Series No. 88

Applications of Remote Sensing to Ocean Surveillance

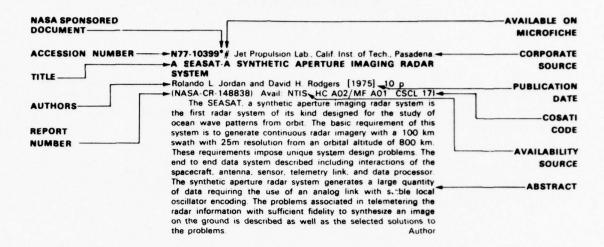
This Bibliography with abstracts has been prepared to support AGARD Lecture Series No. 88 by the Scientific and Technical Information Office of the US National Aeronautics and Space Administration, Washington, D. C., in consultation with Dr. Roger Keeler, the Lecture Series Director and Director of Naval Technology, NAVMAT.

It is hoped that this material will be of value to scientists and engineers and in particular to those who are new in the field.

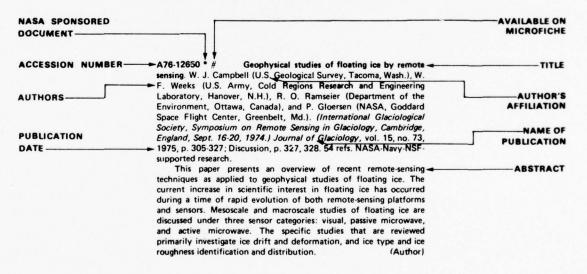
BIBLIOGRAPHY

Section 1.	Sensors, Instruments, Research	Page	B-1
Section 2.	Applications	Page	B-14
Section 3.	Background	Page	B-20

TYPICAL CITATION AND ABSTRACT FROM STAR



TYPICAL CITATION AND ABSTRACT FROM IAA



01

SENSORS, INSTRUMENTS, RESEARCH

N74-21979*# City Coll of the City of New York Univ Inst of Oceanography

A JOINT METEOROLOGICAL, OCEANOGRAPHIC AND SENSOR EVALUATION PROGRAM FOR EXPERIMENT S193 ON SKYLAB Monthly Plans and Progress Report, period ending 18 Apr. 1974

Willard J. Pierson, R. K. Moore, and E. P. McClain, Principal Investigators 18 Apr 1974 2 p EREP (Contract NAS9-13642)

(E74-10454, NASA-CR-137443) Avail NTIS HC \$4.00 CSCL

N74-25888*# National Aeronautics and Space Administration.

Goddard Space Flight Center, Greenbelt, Md.
ESTIMATION OF SEA SURFACE TEMPERATURE FROM REMOTE SENSING IN THE 11-13 MICRON WINDOW REGION

C. Prabhakara, G. Dalu, and V. G. Kunde Feb. 1974 30 p.

refs Submitted for publication (NASA-TM-X-70649: X-911-74-60) Avail: NTIS HC \$4.50

The Nimbus 3 and 4 IRIS spectral data in the 11-13 micron water vapor window region are analyzed to determine the sea surface temperature (SST). The high spectral resolution data of IRIS are averaged over approximately 1 micron wide intervals to simulate channels of a radiometer to measure the SST. Three channels are utilized to measure SST over cloud-free oceans. However, two of these channels are sufficient in routine SST determination. The differential absorption properties of water vapor in the two channels enable one to determine the water vapor absorption correction without detailed knowledge of the vertical profiles of temperature and water vapor. The feasibility of determining the SST is demonstrated globally with Nimbus 3 data where cloud-free areas can be selected with the help of albedo data from the MFIR experiment on board the same satellite

N74-26869* # Ohio State Univ. Research Foundation, Columbus

Dept. of Geodetic Science.
BASIC RESEARCH AND DATA ANALYSIS FOR THE NATIONAL GEODETIC SATELLITE PROGRAM AND FOR THE EARTH AND OCEAN PHYSICS APPLICATION PROGRAM Semiannual Status Report, Jul. - Dec. 1973 Jan. 1974 117 p refs

Grants NGL-36-008-093; NGL-36-008-204; OSURF Proj.

2514; OSURF Proj. 3820-A1) (NASA-CR-138671; SASR-13) Avail: NTIS HC \$9.00 CSCL 05B

Accomplishments in the continuing programs are reported. The data were obtained in support of the following broad objectives: (1) to provide a precise and accurate geometric description of the earth's surface: (2) to provide a precise and accurate mathematical description of the earth's gravitational field; and (3) to determine time variations of the geometry of the ocean surface, the solid earth, the gravity field, and other geophysical parameters.

N74-32789*# Applied Science Associates, Inc., Apex, N.C. ENGINEERING STUDIES RELATED TO THE SKYLAB PROGRAM. TASK H: MICROWAVE/OPTICAL/INFRARED IMAGE PROCESSING FOR OCEAN CURRENT RECOGNI-TION Final Report
A. G. Smith Jul. 1974 49 p refs

(Contract NAS6-2307) (NASA-CR-137468) Avail: NTIS HC \$5.50 CSCL 08C

Images from the Skylab S-193 radar altimeter were selected from data obtained on appropriate passes made by Skylabs 2, 3, and 4 missions for the following three objectives (1) to serve as a precursor to an investigation for the planned GEOS-C mission, in which radar altimeter data will be analyzed to reveal ocean current related to surface topography. (2) to determine the value of satellite infrared and visual radiometer data as potential sources of ground truth data, the results of which be incorporated in the planning of the SEASAT program; and (3) to determine whether optimal data reduction techniques are useful for revealing clues on Gulf Stream topographic signature characteristics. The results obtained which apply to the stated objectives are discussed.

N75-14214 *# ECON, Inc., Princeton, N.J.

THE ECONOMIC VALUE OF REMOTE SENSING OF EARTH RESOURCES FROM SPACE: AN ERTS OVERVIEW AND THE VALUE OF CONTINUITY OF SERVICE. VOLUME 9: OCEANS

Keith R. Lietzke 20 Dec. 1974 134 p

(Contract NASw-2580)

(NASA-CR-141270; Rept-74-2002-10-Vol-9) Avail: NTIS HC \$5.75 CSCL 05C

The impact of remote sensing upon marine activities and oceanography is presented. The present capabilities of the current Earth Resources Technology Satellite (ERTS-1), as demonstrated by the principal investigators are discussed. Cost savings benefits are quantified in the area of nautical and hygrographic mapping and charting. Benefits are found in aiding coastal zone management and in the fields of weather (marine) prediction, fishery harvesting and management, and potential uses for ocean vegetation. Difficulties in quantification are explained, the primary factor being that remotely sensed information will be of greater benefit as input to forecasting models which have not yet been constructed.

N75-17052# National Environmental Satellite Service, Washing-

POTENTIAL VALUE OF EARTH SATELLITE MEASURE-MENTS TO OCEANOGRAPHIC RESEARCH IN THE SOUTHERN OCEAN

E. Paul McClain Jan. 1975 23 p refs (NOAA-TM-NESS-61) Avail: NTIS HC \$3.25

Methods to improve the mapping and monitoring of icepack concentration, character, and condition from satellite observations in the visible, near infrared, and thermal infrared parts of the spectrum are reviewed along with techniques developed to map sea surface temperatures and temperature gradients on regional and hemispheric scales from space. Examples of NOAA and ERTS measurements, higher in spectral and spatial resolution than those previously available, and of measurements from the passive microwave imager aboard Nimbus 5 and their applications are presented. A brief discussion of future sensor systems expected to be of interest to Southern Ocean researchers is Author

N75-25494# Naval Research Lab., Washington, D.C. WIND WAVE STUDIES. PA PART 2: THE PARABOLIC

Tyrone R. Larson and John W. Wright 31 Dec. 1974 24 p

(NRL Proj. R07-17; WR02101002)

(AD-A006554; NRL-7850) Avail: NTIS CSCL 08/3

Coherent microwave backscatter is the basis of a probe technique useful for studying surface water waves in a laboratory tank. A parabolic antenna is focussed to give a plane wave at short range, typically 1.2 m, and an illuminated area of controllable size. The technique strongly discriminates against all water waves except those which have a particular Bragg resonant wavelength ranging between 0.25 cm and 10 cm and propagate parallel to the plane of incidence. The resulting doppler spectra provide a

powerful tool for wind wave, breaking, and spray studies. unique method for directly measuring the water wavenumber resolution is described, together with a technique for absolute calibration of the backscattered power in terms of wave height.

N75-27449 Joint Publications Research Service, Arlington, Va OBSERVATIONS USING FRENCH ELECTRONIC EQUIP MENT AND THE EOLE SATELLITE

I V Farengolts *In its* Soviet Antarctic Inform Bull. (JPRS-64980) 11 Jun. 1975 p 23-27 refs Transl into ENGLISH from Inform Byull. Sov. Antarkt Eksped. (Leningrad), no. 90, 1975

On August 16, 1971 a meteorological satellite was launched from Wallops Island to study the atmosphere over the Southern Hemisphere, to collect information on pressure and temperature, and to observe glaciology, geodesy, oceanography, and interaction between the atmosphere and ocean. Through cooperation with Argentina, Great Britain, U.S.S.R., U.S., France, Australia, and Japan, the satellite tracking of iceberg drift was accomplished using electronic buoys. Continuous information on the Antarctic circumpolar current was obtained for use in polar expeditions.

N75-29717# International Business and Research, Inc., Coral Gables, Fla Aero Oceanics Div.

PROJECT STORMWATER: THE COLLECTION OF BATHYTHERMOGRAPHIC DATA AND AIRBORNE RADIATION
SEA SURFACE TEMPERATURE MEASUREMENTS IN THE
WAKE OF HURRICANE IRAH Final Report, 14 May - 14 Nov. 1973

Mark Goldstein 27 Aug. 1974 53 p (Contract NOAA-03-3-022-100: NR Proj. 083-293) (AD-A005909; RIF20233) Avail: NTIS CSCL 08/10

Sea surface temperatures collected in the wake of Hurricane Irah indicated that no cold water upwelling was observed at the surface. This absence of upwelling indicates that the effects of the speed and intensity of a storm on the thermocline depth are not clearly understood and need further study. The failure of the telemetry systems between the AXBT and the receiver in the aircraft resulted in a considerable loss of data. New developments in these systems have been made which have corrected these deficiencies. Further developments offer a wide range of depth capabilities from 1,500 ft. to 6,000 ft. Also the calibration for the new probes is quite stable eliminating the necessity for individual calibrations.

N75-29979*# Scientific Translation Service, Santa Barbara, Calif TRANSFORMATION IN THE ATMOSPHERE OF SOLAR RADIATION REFLECTED FROM THE OCEAN

M. S. Malkevich, L. G. Istomina, and V. Nordberg. Washington NASA: Jul. 1975 33 p. refs. Transl. into ENGLISH from an unpublished Russian report

(Contract NASw-2791)

(NASA-TT-F-16487) Avail: NTIS HC \$3.75 CSCL 03B

Data from measurements of the spectra of reflected solar radiation over the Atlantic Ocean during the tropical experiment TROPEKS-72 are analyzed. The contribution of the atmosphere to the total brightness of the ocean-atmosphere system is evaluated Author

N76-10652 World Meteorological Organization, Geneva

REVIEW OF OBSERVATIONAL SYSTEMS

In its A 4-Dimensional Assimilation of Meteorol. Observations Jan. 1975 p 3-16 refs

The observational requirements for the first GARP Global Experiment are reviewed and the accuracy and error characteristics of the different data sources are summarized.

N76-11494* National Center for Atmospheric Research, Boulder

SATELLITE OBSERVATIONS OF WEATHER AND CLI-MATE

William W. Kellogg In NASA, Washington Seasat-A Sci. Contrib. Jul. 1974 p 74-78 refs CSCL 04B

The SEASAT-A program is viewed as a new way to obtain atmospheric observations for weather and climatic studies in the framework of the Global Atmospheric Research Program (GARP). Total information derived from SEASAT-A sensor package provides a synoptic picture of the upper parts of the world's oceans as a prerequisite to the development of dynamic ocean models and combined ocean/atmospheric models for weather forecasting requirements

N76-11496* Naval Research Lab., Washington, D.C. EXPLOITATION OF SEASAT-A OCEANOGRAPHIC MEAS-UREMENTS FOR NAVY R AND D APPLICATIONS

V. Noble In NASA, Washington Seasat-A Sci. Contrib. Jul. 1974 p 85-88 CSCL 08J

Basic research, exploratory development and operational demonstration potentials for exploitation of SEASAT-A data are discussed. Some of the interactions and tradeoffs in sensor design and measurement technology, and advanced development of environmental analysis and prediction products for operational fleet support are outlined.

N76-11499* Coast Guard, Washington, D.C. Oceanography

ADVANTAGES OF AN OCEANOGRAPHIC SATELLITE IN THE STUDY OF OCEAN CURRENT SYSTEMS
R. O. Robe In NASA, Washington Seasat-A Sci. Contrib. Jul.

1974 p 99-100 CSCL 08C

SEASAT-A instruments for the study of oceanic currents are: a scanning radiometer with a temperature resolution of about + or - 1 C for locating ocean fronts by thermal difference, and a precision altimeter for monitoring sea surface slopes that drive

N76-11501* Florida Univ., Gainesville. Coastal and Oceanographic Engineering Lab.

ON THE REMOTE SENSING OF DIRECTIONAL WAVE SPECTRA AND SURFACE WINDS
O. H. Shemdin In NASA, Washington Seasat-A Sci. Contrib

Jul. 1974 p 103-108 refs

The potential benefits of remote SEASAT-A satellite sensing of wind directional wave spectra by active microwave systems are elaborated. It is shown that a combined effort which uses supplemental satellite information in numerical forecasting and hindcasting schemes upgrades the accuracy of existing forecasting methods of an order of magnitude GG

N76-11505* Florida State Univ. Tallahassee.
PHYSICAL OCEANOGRAPHY FROM SATELLITES: CUR-RENTS AND THE SLOPE OF THE SEA SURFACE

W. Sturges In NASA, Washington Seasat-A Sci. Contrib. Jul. 1974 p 128 refs

CSCL 08J

A global scheme using satellite altimetry in conjunction with thermometry techniques provides for more accurate determinations

of first order leveling networks by overcoming discrepancies between ocean leveling and land leveling methods. The high noise content in altimetry signals requires filtering or correction for tides, etc., as well as carefully planned sampling schemes.

N76-11507* Army Cold Regions Research and Engineering Lab., Hanover, N.H.

SEASAT AND FLOATING ICE

W. F. Weeks In NASA, Washington Seasat-A Sci. Contrib. Jul. 1974 p 134-135 CSCL 08L

Data collected by SEASAT would be useful in developing predictive physical models for the drift and deformation of sea ice, for estimating the heat budget of the polar seas, for the optimum routing of shipping through pack ice areas, for the design of both offshore structures and shipping capable of surviving in heavy pack ice, and for the tracking of large icebergs and ice islands. The instrument package for SEASAT-A is particularly useful for studying sea ice in that the Coherent Imaging Radar (CIR), the Scanning Multifrequency Microwave Radiometer (SMMR) and the Compressed Pulse Radar Altimeter (CPRA) are not limited by the presence of clouds

N76-19776# Informatics, Inc., Rockville, Md.
BIBLIOGRAPHY OF SOVIET MATERIAL ON INTERNAL WAVES, NUMBER 5, JUNE - OCTOBER 1975 Stuart G. Hibben, L. H. Boylan, and M. Ness 10 Nov 1975

34 p (Contract MDA903-76-C-0099: DARPA Order 3097)

(AD-A017553) Avail NTIS CSCL 08/3

The report is the fifth bibliography of Soviet open-source publications relating to internal wave studies. It covers material received from June through October 1975. The main selection criteria are studies of small-scale variation in ocean parameters and of airborne techniques for deducing internal wave conditions

N76-20619# National Oceanic and Atmospheric Administration. Environmental Research Labs.

AN EVALUATION OF THE USE OF THE EARTH RESOURCES TECHNOLOGY SATELLITE FOR OBSERVING OCEAN CURRENT BOUNDARIES IN THE GULF STREAM SYSTEM George A Maul Jan 1975 130 p

PB-246932/8: NOAA-TR-ERL-335. AOML-18.

NOAA-75101402) Avail NTIS HC \$6.00 CSCL 08C

Remote sensing of ocean color to locate current boundaries was tested in the eastern Gulf of Mexico. A 1-year time history of the Gulf Loop Current was made by a ship in synchronization with the Earth Resources Technology Satellite (ERTS). Surface chlorophyll-a, temperature, and scattering observations show that color signature of the current is present when thermal indications are absent, and thus this flow can potentially be monitored by a combination of visible and infrared techniques.

N76-20794# Informatics, Inc., Rockville, Md. BIBLIOGRAPHY OF SOVIET MATERIAL ON INTERNAL WAVES, NUMBER 4, JANUARY - MAY 1975 Stuart G. Hibben, L. H. Boylan, and M. Ness. 6 Jun. 1975

22 p refs

are studies of small-scale variation in ocean parameters and of

airborne techniques for deducing internal wave conditions. An

(Contract N00600-75-C-0018, DARPA Order 2790) (AD-A010858) Avail NTIS CSCL 08/3

index of serial source abbreviations is appended

This is the fourth bibliography of Soviet open-source publications relating to internal wave studies. It covers material received from January through May 1975. Main selection criteria

N76-21859# Scripps Institution of Oceanography, San Diego, AN INSTRUMENT FOR THE MEASUREMENT OF SPECTRAL

Visibility Lab

ATTENUATION COEFFICIENT AND NARROW ANGLE VOLUME SCATTERING FUNCTION OF OCEAN WATERS

Final Report, Mar. 1973 - Jun. 1975

R. W. Austin and T. J. Petzold Sep. 1975 13 p. Presented at the Ocean Optics Seminar of the Soc. of Photo-Optical Instrumentation Eng. Ann. Tech. Symp., 19 Aug. 1975

(Contract N66857-73-C-0146, ARPA Order 2431)

(AD-A017878; SIO-Ref-75-25) Avail NTIS CSCL 08/10

A new instrument has been developed for the study of those optical properties of ocean water that affect the transmission of image-forming light. The instrument performs simultaneous measurements of the volume attenuation coefficient and the volume scattering function at three angles. Any of ten wavelengths covering the spectral range from 400 to 670 nanometers may be used. A depth capability of 500 meters permits the examination of water below the euphotic zone and the bottom waters on the continental shelf. The considerations leading to the design of the instrument, its capabilities and the unique features it incorporates are discussed. Some examples of the data obtained with the instrument are presented

N76-24758# Bochum Observatory (West Germany) Inst fuer Weltraumforschung

REMOTE SENSING OF SEA CURRENTS, THEIR AREAL DISTRIBUTION AS WELL AS THEIR ECOLOGICAL IMPOR-TANCE FOR THE ITALIAN ADRIATIQUE COAST, BASED UPON INFRARED SATELLITE DATES (NOAA-VHRR)
Heinz Kaminski 1975 19 p refs In GERMAN, ENGLISH

summary Presented at the Symp of the Foederation Europaeischer Gewaesserschutz, Venice, 22 24 Oct. 1975 Avail NTIS HC \$3.50

A zone with a distinct temperature gradient in the area of the Italian Adriatic coast was found from the data of the environmental earth research satellites NOAA 2, 3 and 4. This coastal zone obviously depends on the submarine topography. difference in density of the water masses, constant wind streams, influence of the tides, and inflows from the Alps and the Apennines. The zone can be monitored permanently the whole year long and it shows a distinct maximum in the winter half-year Therefore the mixing with the free Adriatic water is obviously very much limited, so that load factors resulting from industrial sites and urbanizations are to be taken into consideration concerning their quantity for this small constant transport zone in the coastal area in immediate front of the Italian Adriatic The results of environmental earth research satellites make it possible to carry out large area plannings and large area supervisions. The present result is part of a voluminous study describing the supervision of the European waters and the atmosphere. The overlapping study is in the hands of the European Council Author (ESA)

N76-24871# Naval Research Lab., Washington, D.C. Advanced Space Sensors Applications Branch

AN INVESTIGATION OF THE REMOTE DETERMINATION OF SEA SURFACE TEMPERATURE USING MICROWAVE RADIOMETRY Interim Report

James P. Hollinger, Robert M. Lerner, and MacMillan M. Wisler Nov. 1975 56 p. refs (NRL Proj. G01-10: WF52551702) (AD-A018771: NRL-MR-3159) Avail NTIS CSCL 08/3

This is an interim report on an ongoing program to develop a passive microwave system for the remote all-weather measurement of sea surface temperature from a satellite platform. It presents the results of a theoretical investigation of the interdependence of the relevant environmental and instrumental parameters and their effect on the measured microwave brightness temperature and the sea surface temperature derived from it. The parameters considered are sea surface temperature. sea salinity, ocean roughness (wind speed), atmospheric water vapor, clouds, and the observational frequency. Detailed descriptions of the calculations of the emission and reflection of the sea surface, the emission and absorption of the atmosphere, the translation and rotation of the antenna properties

N76-24872# Naval Postgraduate School, Monterey, Calif. A COMPARISON OF SATELLITE IMAGES CAPABLE OF DETECTING OCEAN SURFACE FEATURES M.S. Thesis Bruce William Platz, Jr. Sep. 1975 91 p refs. (AD-A019380) Avail. NTIS CSCL 08/3

This study compares the capabilities of the images obtained from the archives for the satellites of National Oceanic and Atmospheric Administration (NOAA). Defense Meteorological Satellite Program (DMSP), and Earth Resources Technology Satellite (ERTS) systems-for-displaying information about oceanic currents and circulation features.

N77-10399*# Jet Propulsion Lab., Calif Inst. of Tech., Pasadena.
A SEASAT-A SYNTHETIC APERTURE IMAGING RADAR SYSTEM

Rolando L Jordan and David H Rodgers [1975] 10 p (NASA-CR-148838) Avail: NTIS HC A02/MF A01 CSCL 17I

The SEASAT, a synthetic aperture imaging radar system is the first radar system of its kind designed for the study of ocean wave patterns from orbit. The basic requirement of this system is to generate continuous radar imagery with a 100 km swath with 25m resolution from an orbital altitude of 800 km. These requirements impose unique system design problems. The end to end data system described including interactions of the spacecraft, antenna, sensor, telemetry link, and data processor. The synthetic aperture radar system generates a large quantity of data requiring the use of an analog link with stable local oscillator encoding. The problems associated in telemetering the radar information with sufficient fidelity to synthesize an image on the ground is described as well as the selected solutions to the problems.

A74-19032 * An iterative scheme for determining sea surface temperatures, temperature profiles, and humidity profiles from satellite-measured infrared data. M.-D. Chow (New York University; NASA, Goddard Institute for Space Studies, New York, N.Y.). *Journal of Geophysical Research*, vol. 79, Jan. 20, 1974, p. 430-434. 12 refs, Contract No, N00014-67-A-0467-0022.

A74-24257 # Observational studies of mesoscale cellular convection. E. M. Agee and K. E. Dowell (Purdue University, West Lafayette, Ind.). *Journal of Applied Meteorology*, vol. 13, Feb. 1974, p. 46-53, 12 refs. NSF Grant No. GA-24136A2.

An observational study of mesoscale cellular convection oc curring over vast regions of the North Atlantic and North Pacific has been done for the period from Jan. 1, 1969, through June 30, 1970. Satellite cloud photography from the ESSA 7, ESSA 9, and ATS 3 satellites and conventional rawinsonde data have been analyzed for a total of 38 cases, consisting of 25 open and 13 closed convective patterns. Computations have shown that: (1) the average diameter is 30 km for open cells and 32 km for closed cells; (2) the average convective depth for open cells is 2.3 km, greater than the 1.3 km average for closed cells; (3) the average aspect (diameter-to-depth) ratio for open cells, 15:1, is less than that for closed cells, 28:1; (4) the aspect ratio is inversely proportional to increasing convective depth; (5) sea surface temperature exceeds the air temperature on the average by 2.1C in open cells but is 0.4 C less in closed cells; and (6) directional and magnitude shear (in the vertical) of the horizontal wind is small, less than 7 deg per km and 2 m per sec per km, respectively, but indicative of backing cold air advection in open cells and veering or warm air advection in closed cells. (Author)

A74-27305 * An S-band radiometer design with high absolute precision. W. N. Hardy (British Columbia, University, Vancouver, Canada), K. W. Gray (Royal Radar Establishment, Malvern, Worcs, England), and A. W. Love (Rockwell International Corp., Space Div., Downey, Calif.). IEEE Transactions on Microwave Theory and Techniques, vol. MTT-22, Apr. 1974, p. 382-390. 12 refs. Contracts No. NAS1-10106; No. NAS1-10691.

A radiometer for the remote measurement of sea surface temperature is described. The development of an instrument capable not only of high relative accuracy (i.e., resolution) but also of high absolute precision is considered. The concepts underlying the design of an instrument capable of an absolute accuracy of a few tenths degrees Kelvin in the measurement of brightness temperature at S band are described. The role of the antenna is discussed, and the importance of high ohmic and beam efficiencies is stressed. The hardware itself is fully described, along with an outline concerning the design of a unique cryogenically cooled termination used to calibrate the whole radiometer, including antenna. Finally, some test results are presented that show that the design goals for the instrument have been closely approached. (Author)

A74-37295 Target image frequency spectrum in Doppler radars. S. A. Hovanessian (Hughes Aircraft Co., Canoga Park, Calif.). *IEEE Transactions on Aerospace and Electronic Systems*, vol. AES-10, July 1974, p. 497-503. 5 refs.

A mathematical model to study target image return frequency spectrums in Doppler radars is described. The model includes the effects of eclipsing, sea surface slope distribution, and surface reflectivity characteristics. The procedure of calculations has been computerized and the analytical results are compared to flight-test values obtained from flight over the ocean. The calculated values of amplitude-frequency spectrums of target image returns correspond reasonably well with the respective recorded flight-test data. (Author)

A74-41016 Observations from Skylab of mesoscale turbulence in ocean currents. R. E. Stevenson (U.S. Navy, Scripps Institution of Oceanography, La Jolla, Calif.). *Nature*, vol. 250, Aug. 23, 1974, p. 638-640. 7 refs.

Evidence of mesoscale turbulence in warm-water currents flowing poleward from equatorial oceans was obtained by astronauts aboard Skylab. A study of photographs taken aboard Skylab 2 over the northwest Caribbean Sea shows that the vortices varied in diameter from 3 to 20 nautical miles. The associated atmospheric manifestations indicated cool surface water temperatures in the eddies and down-current boundaries with waters warmer than those of the open current. It was found that turbulent vortices were constantly embedded within the main stream of warm ocean currents.

G.R.

A74-46261* Satellite instrumentation for ocean surface measurements. J. Eckerman (NASA, Goddard Space Flight Center, Greenbelt, Md.). In: Institute of Electrical and Electronics Engineers, International Convention and Exposition, New York, N.Y., March 26-29, 1974, Technical Papers. New York, Institute of Electrical and Electronics Engineers, Inc., 1974, p. 34/2 1-34/2 8. 32 refs.

Sea surface observables for ocean dynamics applications are related to topography, physical structure, and the chemothermodynamic state. Radar sensors are required for the topography and physical structure groups of observations. The characteristics of narrow band radar are considered, taking into account long pulse radar to measure wind speed and a long pulse radar-interferometer mode for wave sensing. Time domain radar techniques offer the alternative to determination of the sea surface structure by measuring the magnitude of the scattering cross-section. Multifrequency radiometric observations in the microwave visible and infrared spectral regions are required for ocean chemothermodynamic state measurements.

A74-46262 * Precision satellite altimetry. J. T. McGoogan (NASA, Wallops Station, Wallops Island, Va.). In: Institute of Electrical and Electronics Engineers, International Convention and Exposition, New York, N.Y., March 26-29, 1974, Technical Papers.

New York, Institute of Electrical and Electronics Engineers, Inc., 1974, p. 34/3 1-34/3 7. 9 refs.

This paper is intended to provide a general background on the concept of precision altimetry, including geometry, measurement techniques and calibration. The altimeter project activities associated with the NASA Earth and Ocean Physics Program are presented. The present capabilities of various altimetry techniques will be discussed and supporting data presented. (Author)

A74-46263 * Satellite radar scatterometry. C. T. Swift and W. L. Jones, Jr. (NASA, Langley Research Center, Hampton, Va.). In: Institute of Electrical and Electronics Engineers, International Convention and Exposition, New York, N.Y., March 26-29, 1974, Technical Papers. New York, Institute of Electrical and Electronics Engineers, Inc., 1974, p. 34/4 1-34/4 6. 11

Questions of air-sea interaction are considered along with the theoretical results of an analysis of radar backscatter from the ocean and experimental measurements of radar backscatter. Scatterometer design specifications have been established based on user requirements of accuracy, swath width, resolution cell-size, and a 100 km grid spacing of the measurements. The instrument errors associated with the fan beam mode of operation are shown in a graph.

G.R.

A75-16096 * Skylab radar altimeter - Short-wavelength perturbations detected in ocean surface profiles. C. D. Leitao and J. T. McGoogan (NASA, Wallops Flight Center, Wallops Island, Va.). Science, vol. 186, Dec. 27, 1974, p. 1208, 1209. 7 refs.

Short-wavelength anomalies in sea surface topography, caused by the gravitational effects of major ocean bottom topographic features, have been detected by the radar altimeter aboard Skylab. Some features, such as deep ocean trenches, seamounts, and escarpments, displace the ocean surface by as much as 15 meters over 100-kilometer wavelengths. This experiment demonstrates the potential of satellite altimetry for determining the ocean geoid and for mapping major features of the ocean bottom. (Author)

A75-17203 # Measurement of sea surface currents using airborne Doppler radar and inertial navigation systems. J. F. R. Gower (Environment Canada, Marine Sciences Directorate, Victoria, British Columbia, Canada). In: International Symposium on Remote Sensing of Environment, 9th, Ann Arbor, Mich., April 15-19, 1974, Proceedings. Volume 3. Ann Arbor, Mich., Environmental Research Institute of Michigan, 1974, p. 1657-1667.

A75-19749 The effect of pulse width on radar measurement of ocean wave height. T. Y. Young (Miami, University, Coral Gables, Fla.). *International Journal of Electronics, First Series*, vol. 37, Dec. 1974, p. 833-848. 15 refs.

This paper examines various factors that affect the accuracy of radar measurement of ocean wave height from space, with particular emphasis on the effect of pulse width. It is shown that at a given signal-to-noise ratio, large or small, there is a pulse width that yields an optimal estimation accuracy. Both optimal and suboptimal estimation schemes are considered, and performance curves are presented. (Author)

A75-23756

Airborne radiometric measurement of land and sea surface temperatures. T. A. Hariharan (Indian Space Research Organization, Space Applications Centre, Ahmedabad, India). In: Remote sensing of earth resources. Volume 3 - Proceedings of the Third Conference on Earth Resources Observation and Information Analysis System, Tullahoma, Tenn., March 25-27, 1974.

Tullahoma, University of Tennessee, 1974, p. 161-172.

Some preliminary results of airborne radiometric measurement of temperature over land and sea surfaces obtained with an infrared line scanner are described. Over sea, areas with features of anomalous

temperature distribution were noticeable. Measurements made from four different altitudes over the same area indicate the atmospheric effects in the 10-12 micron window region. Predawn measurements over land seems to indicate anomalous temperature distributions in areas suspected to have weak geothermal manifestations. (Author)

A75-24088 Remote sensing of the sea surface from satellites (Fernerkundung der Meeresoberfläche von Satelliten aus). W. Alpers, K. Hasselmann, and M. Schieler (Hamburg, Universität, Hamburg, West Germany). Raumfahrtforschung, vol. 19, Jan.-Feb. 1975, p. 1-7. 21 refs. In German.

Remote sensing techniques for satellite-borne measurements of the sea surface are reviewed briefly. Three methods for determining significant parameters of ocean wave spectra using microwaves are discussed in detail: the nanosecond-pulse radar altimeter, the two-frequency radar interferometer for rms wave height measurement, and the off-nadir looking two frequency radar. The last technique seems to be very promising for measuring the complete two-dimensional ocean wave spectrum from satellites.

(Author

A75-25419 # Interpretation of radiation measurements on board Meteor satellites and verification of the transition from the albedo of the ocean atmosphere system to shortwave radiation on the ocean surface (Interpretatsiia radiatsionnykh izmerenii na sputnikakh 'Meteor' i obosnovanie perekhoda ot al'bedo sistemy okeanatmosfera k korotkovolnovoi radiatsii na poverkhnosti okeanov). N. A. Timofeev (Akademiia Nauk Ukrainskoi SSR, Morskoi Gidrofizicheskii Institut, Moscow, USSR). Akademiia Nauk SSSR, Izvestiia, Fizika Atmosfery i Okeana, vol. 11, Jan. 1975, p. 15-26. 20 refs. In Russian.

A75-27115 Determination of oceanic geoid from short arc reduction of satellite altimetry. D. C. Brown (DBA Systems, Inc., Melbourne, Fla.). In: The use of artificial satellites for geodesy and geodynamics; Proceedings of the International Symposium, Athens, Greece, May 14-21, 1973. Athens, National Technical University of Athens, 1974, p. 509-522. Contract No. F19628-72-C-0085.

An investigation was made to determine whether extremely high orbital accuracies are inherently essential to the effective utilization of satellite altimetry for geoidal improvement. A short-arc approach is described in which weakly constrained orbital state vectors defining as many as several thousand short arcs (1/6 to 1/8 revolution in length) are recovered simultaneously with the parameters necessary to defining the geoidal surface. Computer simulations demonstrate the feasibility and accuracy of the short-arc method. An oceanic geoid having an rms accuracy of 1-2 m can be produced from the reduction of data from observations of the Geos C satellite. The short-arc approach does not depend on establishing a highly accurate reference orbit and, thus, places only minimal requirements on satellite tracking by external systems.

A.T.S.

A75-30451 * The development of an L-band radiometer dual-mode horn. M. C. Bailey (NASA, Langley Research Center, Hampton, Va.). *IEEE Transactions on Antennas and Propagation*, vol. AP-23, May 1975, p. 439-441.

An antenna was developed for the remote microwave measurement of ocean surface temperature during a flight test in a C54 aircraft. The basic antenna is a conical dual-mode horn similar to the dual-mode horn described by Potter (1963). The pertinent internal dimensions of the horn are given. The measured E and H plane patterns for the linearly polarized horn for a range of frequencies are shown in a graph.

G.R.

A75-30500 Environmental earth satellites for oceanographic-meteorological studies of the Bering Sea. E. P. McClain (NOAA, Washington, D.C.). In: Oceanography of the Bering Sea: With emphasis on renewable resources. Fairbanks, University of Alaska Press, 1974, p. 579-593. 17 refs.

Present day operational earth satellites already provide much information useful to the oceanographer and meteorologist in the

Bering Sea area. Near-future operational and development satellites will make available more types of data and higher-resolution coverage. Because the Bering Sea is a relatively remote and inaccessible part of the world, subject moreover to incursions of polar ice, comprehensive and repetitive survey by surface vessels or aircraft would be costly, time-consuming, very difficult and to some extent hazardous. The polar-orbiting environmental earth satellite is thus in many ways an ideal sensor platform for areas such as the Bering Sea. Remote sensing does entail certain limitations, however, and it is in such areas of weakness that the data collection and relay capabilities of sun-synchronous polar satellites and earth-synchronous equatorial satellites are important. (Author)

A75-33856 # Preliminary analysis of Skylab radscat results over the ocean. R. K. Moore, J. P. Claassen, J. D. Young (University of Kansas Center for Research, Inc., Lawrence, Kan.), W. J. Pierson, Jr., and V. J. Cardone (New York, City University, New York, N.Y.). In: Specialist Meeting on Microwave Scattering and Emission from the Earth, Berne, Switzerland, September 23-26, 1974, Proceedings. Berne, Universität Bern, 1974, p. 47-53.

Preliminary observations at 13.9 GHz of the radar backscatter and microwave emission from the sea have been analyzed using data obtained by the radiometer-scatterometer on Skylab. Results indicate approximately a square-law relationship between differential scattering coefficient and windspeed at angles of 40 deg to 50 deg, after correction for directional effects, over a range from about 4 up to about 25 meter/sec. The brightness temperature response was also observed, and considerable success was achieved in correcting it for atmospheric attenuation and emission. (Author)

A75-33924 Trend-surface analysis of ocean outfall plumes. N. P. Psuty (Rutgers University, New Brunswick, N.J.) and J. R. Allen (Northeastern University, Boston, Mass.). *Photogrammetric Engineering and Remote Sensing*, vol. 41, June 1975, p. 721-730. 9 refs.

Measures of water quality associated with ocean outfall effluent plumes are approached through the use of standard photographs which are transformed into numerical data sets and handled by the statistical technique of trend-surface analysis. The solutions for the rend surfaces are presented and the residuals are analyzed to discern their covariation with water-quality variables. A high correlation is indicated for the measures of dissolved oxygen and the values derived from the photographic images. (Author)

A75-35454 # Remote sensing of oceans using microwave sensors. K. Krishen (Lockheed Electronics Co., Inc., Houston, Tex.). In: Remote sensing applied to energy-related problems; Proceedings of the Symposium-Course, Miami, Fla., December 2-4, 1974. Coral Gables, Fla., University of Miami, 1974, p. \$2-25 to \$2-57.57 refs.

This paper presents a review of the results of a study of the ocean surface phenomena. The use of active and passive microwave sensors to detect ocean surface waves, temperature, salinity, storm cells, and oil slicks is demonstrated. The aircraft- and spacecraft-acquired microwave data are presented. The radar back-scattering cross section data shows strong correlation between ocean surface winds/waves, storm regions, and oil slicks. A strong dependence upon these parameters has been shown in the Ku-band at a radar frequency of 13.9 GHz. The relationship between radiometric brightness temperature and ocean surface temperature, salinity, and sea state are set forth. Evidence of the suitability of microwave sensors in providing data independent of sunlight under almost all weather conditions is provided. (Author)

A75-35905 # Large area assessment of water temperature, chlorophyll concentration and transparency. F. C. Polcyn and C. T. Wezernak (Michigan, Environmental Research Institute, Ann Arbor, Mich.). American Institute of Aeronautics and Astronautics, Thermophysics Conference, 10th, Denver, Colo., May 27-29, 1975, Paper 75-686. 4 p. NOAA-supported research.

The era of a multispectral scanner aboard satellites and aircraft

offers the promise of measurement of large scale water movements and the simultaneous quantitative assessment of several important water quality parameters. Recent data collection and analysis of multispectral aircraft data for two points of the tidal cycle (outgoing and incoming tides) has been completed for the New York Bight. Eight lines at 10,000 ft altitude each covering 3 miles by 24 miles were flown on 7 April 1973. Fifteen channels of multispectral data were collected. Surface Temperature maps ranging from 6 C to 13 C were produced which show the pattern of out flow and return over the area. Ocean fronts, upwellings, and eddies and general surface circulation was delineated. Simultaneous spectral data in the visible region were also collected. Techniques for delineating surface chlorophyll concentrations and Secchi disk transparency were demonstrated and regional maps produced. The use of remote sensing in providing information vital to studies of the highly complex and dynamic estuarine and coastal environment, as represented by the New York Bight, is demonstrated.

A75-36464 * Microwave scattering from the ocean surface.
W. L. Jones, W. L. Grantham, L. C. Schroeder, J. W. Johnson, and C.
T. Swift (NASA, Langley Research Center, Hampton, Va.). In:
Microwaves in service to man; International Microwave Symposium,
Palo Alto, Calif., May 12-14, 1975, Digest of Technical Papers.
New York, Institute of Electrical and Electronics
Engineers, Inc., 1975, p. 26-28. 18 refs.

This paper is a review of current aircraft and satellite microwave remote sensing programs concerned with the measurement of ocean wave and surface wind conditions. These particular measurements have been identified by the user community as offering significant economic and technological benefits. Active microwave remote sensing techniques for these applications have been described theoretically and verified experimentally. The results of recent aircraft and satellite experimental programs are presented herein along with plans for the SeaSat-A Satellite Scatterometer. (Author)

A75-36835 A new technique for observing mid-latitude ocean currents from space. G. A. Maul and S. R. Baig (NOAA, Miami, Fla.). In: American Society of Photogrammetry, Annual Meeting, 41st, Washington, D.C., March 9-14, 1975, Proceedings.

Falls Church, Va., American Society of Photogrammetry, 1975, p. 713-716.

Infrared observations from the Synchronous Meteorological Satellite are used to locate the cyclonic edge of the Gulf Stream in the offing of the Middle Atlantic Bight. Film loops are made from the high resolution infrared scanner using observations every 30 minutes. For periods of one to three days, the stream's meanders can be considered quasi-stationary. The high velocity of clouds makes identification of the current possible because of the relative motion difference and is analogus to land identification. The technique requires only one channel of carefully gridded data and is free of atmospheric radiative transfer corrections necessary in other multichannel compositing schemes. (Author)

A75-38497 Spectral characteristics of remote sensors (Prostranstvenno-spektral nye kharakteristiki distantsionnykh datchikov). S. V. Dotsenko, A. N. Nedovesov, M. G. Poplavskaia, and V. A. Ryzhenko. Akademia Nauk Ukrainskoi SSR, Morskie Gidrofizicheskie Issledovania, no. 2, 1974, p. 162-173. 5 refs. In Russian.

The analytical expression of spectral characteristics of remote sensors designed for measurements of physical fields of the ocean surface from aircrafts and artificial earth satellites is obtained. These characteristics are received for the uniformly averaged sensor and also for the sensors of radiometers installed in artificial satellites 'Kosmos 149' and 'Tiros II'. Their comparative analysis is given.

Author

A75-40608 * Ocean color measurement from high altitude. W. A. Hovis, Jr. (NASA, Goddard Space Flight Center, Earth Observation Systems Div., Greenbelt, Md.). In: Technology today for tomorrow; Proceedings of the Twelfth Space Congress, Cocoa Beach, Fla., April 9-11, 1975. Cocoa Beach, Fla., Canaveral Council of Technical Societies, 1975, p. 3-9 to 3-14, 5 refs.

Investigations into the feasibility of sensing ocean color from high altitude for determination of chlorophyll and sediment distributions have been carried out using sensors on NASA aircraft, coordinated with surface measurements carried out by oceanographic vessels. Spectrometer measurements in 1971 and 1972 led to development of an imaging sensor now flying on a NASA U-2 and the Coastal Zone Color Scanner to fly on Nimbus G in 1978. Results of the U-2 effort have shown the imaging sensor to also be of great value in sensing pollutants in the ocean. (Author)

A75-45848 * Earth and ocean dynamics satellites and systems. F. O. Vonbun (NASA, Goddard Space Flight Center, Greenbelt, Md.). International Astronautical Federation, International Astronautical Congress, 26th, Lisbon, Portugal, Sept. 21 27, 1975, Paper 75-121, 38 p. 37 refs.

An overview is presented of the present state of satellite and ground systems which are used for studies concerning the dynamics of the solid earth and the oceans. It is pointed out that very good progress has been made in the area of earth and ocean dynamics since the described program was initiated in 1969. Construction of the mathematical models needed for data interpretation and analyses for earth dynamics phenomena and for ocean dynamics are in progress.

A75-46673 On the use of the earth resources technology satellite /LANDSAT-1/ in optical oceanography. G. A. Maul (NOAA, Physical Oceanography Laboratory, Miami, Fla.) and H. R. Gordon (Miami, University, Coral Gables, Fla.). Remote Sensing of Environment, vol. 4, no. 2, 1975, p. 95-128. 41 refs. NASA Order S-70246-AG.

Observations of the Gulf Stream System in the Gulf of Mexico were obtained in synchronization with LANDSAT-1. Computer enhanced images, which are necessary to extract useful oceanic information, show that the current can be observed by color (diffuse radiance) or sea state (specular radiance) effects associated with the cyclonic boundary even in the absence of a surface thermal signature. The color effect relates to the spectral variations in the optical properties of the water and its suspended particles, and is studied by radiative transfer theory. Significant oceanic parameters identified are: the probability of forward scattering, and the ratio of scattering to total attenuation. Several spectra of upwelling diffuse light are computed as a function of the concentration of particles and yellow substance. (Author)

A75-47051 * Antenna pattern corrections to microwave radiometer temperature calculations. F. B. Beck (NASA, Langley Research Center, Hampton, Va.). *Radio Science*, vol. 10, Oct. 1975, p. 839-845. 9 refs.

In making microwave radiometer calculations of sea surface temperature, it is necessary to consider the errors resulting from the antenna radiation pattern. This is especially true for antennas with high sidelobes that are scanned in viewing angle and for antennas with high cross-polarized components. It is concluded that the plane wave brightness temperature is not by itself sufficient to describe the true radiometer temperature of the sea surface. This discrepancy can be attributed to one or more of the following: failure to use the total radiation pattern, error in determining the sea surface dielectric constant, error in sky model profile, or radiation pattern spillover onto water surroundings.

A76-11807 # Some results measuring ocean surface parameters from aerial photographs (Nekoturye rezul'taty izmereniia parametrov morskoi poverkhnosti po aerofotosnimkam). E. K. Korchagin and R. N. Semenov (Moskovskii Institut Inzhenerov Geodezii, Aerofotos'emki i Kartografii, Moscow, USSR). Geodeziia i Aerofotos'emka, no. 6, 1974, p. 67-71. 7 refs. In Russian.

Results of measurements of the mean height of ocean waves from stereophotographs processed by the straight line method are examined. It is shown that in the case where one of the two profiling directions coincides with the direction of the crests of ripple waves in the presence of wind waves, the measurements exhibit anisotropy.

The factors responsible for the anisotropy are identified. The mean wave heights determined from stereophotographs are compared with the mean heights of wind waves calculated on the basis of the wind factors responsible for wave formation.

V.P.

A76-12003 # Study of the condition of continental covers and water areas by microwave-radiometric methods (Issledovanie sostoianiia materikovykh pokrovov i akvatorii metodami SVCh radiometrii). A. E. Basharinov, L. F. Borodin, A. S. Gurvich, M. S. Malkevich, and A. M. Shutko. *Uspekhi Fizicheskikh Nauk*, vol. 116, Aug. 1975, p. 743-746. 13 refs. In Russian.

Factors that determine the intensity and polarization of thermal radio emission from terrestrial land and ocean surfaces are briefly outlined. Some results of measurements of this emission by satellites and aircraft are presented. It is shown that: (1) the intensity and polarization of emission from land surfaces depend on the effective temperature and degree of blackness of the emitting object, (2) emission from water areas originates in a thin surface layer, (3) the intensity and polarization of emission from water surfaces depends on temperature, the salt content of the water, the intensity of sea swells, white caps and oil slicks on the surface, and the presence of ice fields.

F.G.M.

A76-12650 * # Geophysical studies of floating ice by remote sensing. W. J. Campbell (U.S. Geological Survey, Tacoma, Wash.), W. F. Weeks (U.S. Army, Cold Regions Research and Engineering Laboratory, Hanover, N.H.), R. O. Ramseier (Department of the Environment, Ottawa, Canada), and P. Gloersen (NASA, Goddard Space Flight Center, Greenbelt, Md.). (International Glaciological Society, Symposium on Remote Sensing in Glaciology, Cambridge, England, Sept. 16-20, 1974.) Journal of Glaciology, vol. 15, no. 73, 1975, p. 305-327; Discussion, p. 327, 328. 54 refs. NASA-Navy-NSF-supported research.

This paper presents an overview of recent remote-sensing techniques as applied to geophysical studies of floating ice. The current increase in scientific interest in floating ice has occurred during a time of rapid evolution of both remote-sensing platforms and sensors. Mesoscale and macroscale studies of floating ice are discussed under three sensor categories: visual, passive microwave, and active microwave. The specific studies that are reviewed primarily investigate ice drift and deformation, and ice type and ice roughness identification and distribution. (Author)

A76-14445 Airborne laser profiling of swell in an open ice field. P. Wadhams (Cambridge University, Cambridge, England). Journal of Geophysical Research, vol. 80, Nov. 20, 1975, p. 4520-4528, 26 refs.

Airborne laser profiles of swell entering the drift ice off the east coast of Newfoundland were made using a Geodolite profiler mounted in a DC 4 ice patrol aircraft. Concurrent infrared imagery along the track enabled the floe size distribution to be recorded. A linear decay of wave energy with 'effective penetration' (distance penetrated multiplied by fractional ice cover) was found, the decay rate increasing with wave frequency. A simple theoretical model based on progressive reflection from rows of floes gave good agreement with the observations.

(Author)

A76-15772 Complementary roles of spacecraft and aircraft in remote sensing of earth's resources. A. J. Moffat (Litton Systems/Canada/, Ltd.,Rexdale, Ontario, Canada) and W. F. Kohler. Canadian Journal of Remote Sensing, vol. 1, Nov. 1975, p. M-16 to M-18.7 refs.

The relative roles of the remote sensing techniques and data collecting capabilities of aircraft and satellite borne remote sensing systems in the observation and/or measurement of various parameters of earth resources are considered. Satellite systems are best suited to synoptic mapping of surface features of large areal extent and the imaging of data involving slow changes in the observed resource. Aircraft lend themselves to the study of rapidly changing phenomena and for the high-resolution study of smaller geographical areas. Aircraft systems can be used to verify and complement certain types of satellite data.

C.K.D.

A76-15884 * Application of Fourier transforms for microwave radiometric inversions. J. J. Holmes, C. A. Balanis, and W. M. Truman (West Virginia University, Morgantown, W. Va.). *IEEE Transactions on Antennas and Propagation*, vol. AP-23, Nov. 1975, p. 797-806. 14 refs. Grant No. NGR 49-001-056.

Existing microwave radiometer technology now provides a suitable method for remote determination of the ocean surface's absolute brightness temperature. To extract the brightness temperature of the water from the antenna temperature, an unstable Fredholm integral equation of the first kind is solved. Fourier transform techniques are used to invert the integral after it is placed into a cross correlation form. Application and verification of the methods to a two-dimensional modeling of a laboratory wave tank system are included. The instability of the ill-posed Fredholm equation is examined and a restoration procedure is included which smooths the resulting oscillations. With the recent availability and advances of fast Fourier transform (FFT) techniques, the method presented becomes very attractive in the evaluation of large quantities of data. (Author)

A76-19081 Interpretation of radiation measurements on 'meteor' satellites, and the basis for conversion from the albedo of the ocean-atmosphere system to the shortwave radiation at the ocean surface. N. A. Timofeev (Akademiia Nauk Ukrainskoi SSR, Morskoi Gidrofizicheskii Institut, Moscow, USSR). (Akademiia Nauk SSSR, Izvestiia, Fizika Atmosfery i Okeana, vol. 11, Jan. 1975, p. 15-26.) Academy of Sciences, USSR, Izvestiya, Atmospheric and Oceanic Physics, vol. 11, Aug. 1975, p. 8-14. 20 refs. Translation.

A76-24053 Measurement of the sea wave spectrum by aerial photography (Mesure du spectre de la houle par photographie aérienne). B. de Lagarde (Société Bertin et Cie., Plaisir, Yvelines, France) and E. de Bazelaire (Toulon, Centre Universitaire, France). (Association Technique Maritime et Aéronautique, Session, 75th, Paris, France, May 12-16, 1975.) Association Technique Maritime et Aéronautique, Bulletin, no. 75, 1975, p. 239-255; Discussion, p. 256-260. In French.

It is shown that one aerial photograph of the sea surface contains potentially all the information needed to determine the directional energy spectrum of the sea. This information is optically processed in coherent light, making it possible to obtain the Fourier transform of the function in two variables z equals f(x,y) which is representative of the sea surface. In the Fourier plane, each component of the sea waves appears in the form of a luminous spot. The azimuth of the spot indicates the direction of propagation; the distance of the spot from the center is proportional to the spatial frequency; the intensity of the spot is a function of the energy of the component.

A76-24536 # Survey of investigations of oceanographic fields by remote sounding from spacecraft (Obzor issledovanii okeanograficheskikh polei metodom distantsionnogo zondirovaniia s kosmicheskikh letatel'nykh apparatov). V. V. Polovinko. *Geodeziia i Aerofotos'emka*, no. 3, 1975, p. 171-177. 9 refs. In Russian.

A76-24747 # Radiation balance of the ocean-atmosphere system and its components from calculated data and satellite measurements (Radiatsionnyi balans sistemy okean-atmosfera i ego sostavliaiushchie po dannym raschetov i sputnikovykh izmerenii). N. A. Timofeev (Akademiia Nauk Ukrainskoi SSR, Morskoi Gidrogizicheskii Institut, Moscow, USSR). Akademiia Nauk SSSR, Izvestiia, Fizika Atmosfery i Okeana, vol. 11, Dec. 1975, p. 1330-1333. 7 refs. In Russian.

A76-26707 Subsurface water parameters - Optimization approach to their determination from remotely sensed water color data. S. C. Jain and J. R. Miller (York University, Downsview, Ontario, Canada). Applied Optics, vol. 15, Apr. 1976, p. 886-890. 18 refs.

A method using an optimization scheme has been developed for the interpretation of spectral albedo (or spectral reflectance) curves obtained from remotely sensed water-color data. This method uses a two-flow model of the radiation flow and solves for the albedo. Optimization fitting of predicted to observed reflectance data is performed by a quadratic interpolation method for the chlorophyll concentration and scattering coefficient. The technique is applied to airborne water-color data obtained from Kawartha Lakes, the Sargasso Sea, and the Nova Scotia coast. The modeled spectral albedo curves are compared with those obtained experimentally, and the computed optimum water parameters are compared with ground-truth values. It is shown that the backscattered spectral signal contains information that can be interpreted to give quantitative estimates of the chlorophyll concentration and turbidity in the waters studied. (Author)

A76-29267 Aircraft measurements of the earth's albedo over India. A. Mani (Indian Meteorological Department, New Delhi, India), O. Chacko, V. Desikan, and G. Vijayan (Indian Meteorological Department, Poona, India). (Symposium on Earth's Near Space Environment, New Delhi, India, Feb. 18-21, 1975.) Indian Journal of Radio and Space Physics, vol. 4, Dec. 1975, p. 304-309.

Satellite observations of the earth albedo consistently indicate that the earth is a warmer and darker planet than was previously believed and that more solar energy is absorbed by the atmosphere than hitherto accepted. In order to verify these observations, direct measurements of the albedo of various surfaces were made on the ground at a number of stations in India and from aircraft over extensive land and sea areas. Two thermoelectric pyranometers were used to measure the global and reflected solar radiation, the data being continuously recorded in flight. These data were supplemented by observations over the Arabian sea from an oceanographic ship during 1974. The measurements show that the albedo over land varies from 0.10-0.25, depending on the nature of the surface and that over the sea from 0.04-0.13 depending on the state of the sea The albedo of clouds varies from 0.40-0.60 for active cumulus to 0.25-0.35 for altostratus. (Author)

A76-30747 A note on SAR imagery of the ocean. T. R. Larson (Ball Brothers Research Corp., Boulder, Colo.), L. I. Moskowitz, and J. W. Wright (U.S. Navy, Naval Research Laboratory, Washing:on, D.C.). *IEEE Transactions on Antennas and Propagation*, vol. AP-24, May 1976, p. 393, 394, 5 refs.

An example of SAR imagery of the ocean surface including the Gulf Stream Boundary reported by Moskowitz (1973) is used to discuss potential mechanisms of SAR image formation of the ocean. It is pointed out that images in addition to those due to modulation of surface scatterer strength may result from organized scatterer motions such as those due to currents or wave orbital velocities. The modulation of scattering cross section by large waves is expected to depend on the magnitude and direction of the wind, making the relationship between image strengths and wave amplitudes rather complicated. It is suggested that the effect of wave orbital accelerations upon azimuthal focus might provide a more direct measure of wave amplitude. (Author)

A76-31444 # Microwave sensing of the sea state (Ferner-kundung des Seegangs mit Mikrowellen). W. Alpers (Hamburg, Universität, Hamburg, West Germany). In: Symposium on Earth Survey, Porz-Wahn, West Germany, April 7-11, 1975, Reports.

Cologne, Deutsche Forschungs- und Versuchsanstalt für Luft- und Raumfahrt, 1975, p. 281-289. 13 refs. In German.

The application of two active microwave systems - the synthetic-aperture side-looking radar and the two-frequency scatterometer - to the remote sensing of ocean waves is discussed. A brief description of the application characteristics of other microwave systems, such as the nanosecond radar altimeter, the two-frequency radar interferometer, and the microwave radiometer is given also. The economic usefulness of sea state forecasts is pointed out.

V.P.

A76-31480 World-wide satellite surveillance of surface wind impact of a test case. V. J. Cardone and W. J. Pierson (New York, City University, New York, N.Y.). In: Technology for the new

horizon; Proceedings of the Thirteenth Space Congress, Cocoa Beach, Fla., April 7-9, 1976. Cocoa Beach, Fla., Canaveral Council of Technical Societies, 1976, p. 3-7 to 3-20. 19 refs.

On Skylab, a combination microwave radar-radiometer (S193) made measurements from which the winds near the sea surface could be inferred. The analysis of the measurements showed that the wind speed could be computed from the radar measurements with at least the accuracy of the wind speed that would have been reported by a weather ship at the time and location of the radar measurement. The impact of this remote sensing capability will be realized in 1978 with the launch of SEASAT-A, which will carry operational versions of active and passive microwave sensors that will be able to measure both wind speed and direction. Global over ocean routine vector wind measurements should significantly improve the specification of the surface wind and indirectly the surface pressure over the oceans, determine the intensity and structure of tropical cyclones and contribute to improved accuracy of numerical weather forecasting models applied to both the tropics and extratropical atmosphere.

(Author)

A76-32988 * # Skylab earth resources experiment package /EREP/ - Sea surface topography experiment. F. O. Vonbun, J. G. Marsh (NASA, Goddard Space Flight Center, Greenbelt, Md.), J. T. McGoogan, C. D. Leitao (NASA, Wallops Flight Center, Wallops Island, Va.), S. Vincent (Phoenix Corp., McClean, Va.), and W. T. Wells (Wolf Research and Development Corp., Riverdale, Md.). Journal of Spacecraft and Rockets, vol. 13, Apr. 1976, p. 248-250. 9 refs.

The S-193 Skylab radar altimeter was operated in a round-the-world pass on Jan. 31, 1974. The main purpose of this experiment was to test and 'measure' the variation of the sea surface topography using the Goddard Space Flight Center (GSFC) geoid model as a reference. This model is based upon 430,000 satellite and 25,000 ground gravity observations. Variations of the sea surface on the order of -40 to +60 m were observed along this pass. The 'computed' and 'measured' sea surfaces have an rms agreement on the order of 7 m. This is quite satisfactory, considering that this was the first time the sea surface has been observed directly over a distance of nearly 35,000 km and compared to a computed model. The Skylab orbit for this global pass was computed using the Goddard Earth Model (GEM 6) and S-band radar tracking data, resulting in an orbital height uncertainty of better than 5 m over one orbital period.

(Author)

A76-33355 * Radar imaging of ocean surface patterns. W. E. Brown, Jr., C. Elachi, and T. W. Thompson (California Institute of Technology, Jet Propulsion Laboratory, Space Sciences Div., Pasadena, Calif.). Journal of Geophysical Research, vol. 81, May 20, 1976, p. 2657-2667, 23 refs. Contract No. NAS7-100.

The paper presents some examples of imaging radar ooceano-graphic observations and discusses physical phenomena on the surface that may cause the radar image. The different ocean scattering theories are briefly discussed, including the tangent plane model, the Bragg-Rice model, and the Rayleigh scattering model. All but one of the images presented were obtained with an L-band HH-polarized radar; they include deep-ocean swells, coastal swells, wave refractions, internal waves, ship wakes, abrupt transitions in open-ocean surface roughness, surface slicks, island wind shadowing, and currents. Analyses are shown to suggest that the primary source of the L-band imagery of ocean surface patterns is the variation of small-scale surface roughness and local tilt angle. It is also noted that surface irregularities behave as isotropic scatterers for a radar wavelength of 25 cm.

F.G.M.

A76-34935 Circulation observations in the Louisiana Bight using LANDSAT imagery. L. J. Rouse and J. M. Coleman (Louisiana State University, Baton Rouge, La.). Remote Sensing of Environment, vol. 5, no. 1, 1976, p. 55-66. Contract No. N00014-75-C-0192. NR Project 388-002.

A method for quantifying the turbidity of offshore water masses using LANDSAT imagery is discussed and the results of a laboratory

experiment correlating radiance with concentrations of suspended Mississippi River sediment are presented. The results of the experiment are used to plot suspended sediment contours on eight LANDSAT images of the Louisiana Bight. These contours are observed to depend on the speed and direction of the wind as well as the amount of fresh water discharged by the Mississippi River. The presence of a clockwise circulation in the bight is also indicated by the contours. (Author)

A76-35021 # Radar observations of controlled oilspills. J. van Kuilenburg (Netherlands Interdepartmental Working Community for the Application of Remote Sensing Techniques, Delft, Netherlands). In: International Symposium on Remote Sensing of Environment, 10th, Ann Arbor, Mich. October 6-10, 1975, Proceedings. Volume 1. Ann Arbor, Mich., Environmental Research Institute of Michigan, 1975, p. 243-250. 11 refs.

A report is given of studies and experiments concerning the radar detection of oilslicks at the seasurface. From scatterometer observations of oilslicks in a wavetank it is concluded that oil is always detectable, but also that oil-type and thickness are of little influence on the radarecho. The radar observation of the damping of water waves which travel into the polluted area is proposed as an indicator of the physical oil properties. A radar operating in the VV-polarization mode is shown to be optimal because of the strength of the radarecho, the observed contrast and the low noise. However, experiments using a SLAR operating in the HH-mode, showed this polarization combination to perform well enough for the purpose of oil detection. In general the conclusion is drawn that the SLAR performs well for detection and mapping of oilspills but that other sensors are needed for classification and quantification of oilspills.

(Author)

A76-35064 # Detection and measurement of the oceanic thermal front east of Korea with the Defense Meteorological Satellite System. O. K. Huh (U.S. Naval Oceanographic Office, Washington, D.C.). In: International Symposium on Remote Sensing of Environment, 10th, Ann Arbor, Mich., October 6-10, 1975, Proceedings. Volume 1. Ann Arbor, Mich., Environmental Research Institute of Michigan, 1975, p. 653-659. 6 refs. Navysponsored research.

The scanning sensors of the Defense Meteorological Satellite System have provided excellent thermal infrared (8-13 micrometer) and visual range (0.4-1.1 micrometer) imagery of the oceanic regions near the Korean Peninsula. These data were acquired by direct readout from the two polar orbiting satellites which passed over the region near dawn, noon, early evening and midnight, local sun time. Sea surface temperature gradient features including oceanic fronts, eddies, frontal waves, convergences and divergences are clearly depicted on the electro-optically contoured film display at 1.6 K contour intervals. This near real-time thermal infrared data (at 3.7 km spatial resolution) provided relative temperatures, some 2-10 K colder than the actual surface measurements. Thermal gradients were faithfully reproduced, however, and could be estimated from the imagery to less than 1 K. The technical effectiveness of combining real-time high quality, high repetition rate satellite data with ship or aircraft operations has again been demonstrated as measurement traverses were deployed based on satellite data. (Author)

A76-35625 Experimental results of the remote sensing of sea-surface salinity at 21-cm wavelength. G. C. Thomann (Wichita State University, Wichita, Kan.). *IEEE Transactions on Geoscience Electronics*, vol. GE-14, July 1976, p. 198-214. 12 refs.

The complex dielectric constant of sea water is a function of salinity at 21-cm wavelength, and sea-water salinity can be determined by measuring radiometric temperature at 21 cm and thermodynamic temperature. Three aircraft and two helicopter experiments using two different 21-cm radiometers were conducted under different salinity and temperature conditions. Ground-truth measurements were used to calibrate the data in each experiment. RMS deviations of between 2 and 3% were found between remote and ground-truth boat measurements. Part of this deviation is attributed to position mislocation between the aircraft and boats. Accuracies of

1 to 2% are possible with a single surface calibration point necessary only every two hours if the following conditions are met - water temperatures about 20 C, salinities above 10%, level aircraft flight, and extreme care near land masses. (Author)

A76-36675 * # Seasat-A - An ocean observation satellite. F. L. Williams and S. W. McCandless, Jr. (NASA, Special Programs Office of Applications, Washington, D.C.). COSPAR, Plenary Meeting, 19th, Philadelphia, Pa., June 8-19, 1976, Paper. 10 p.

Mission details, onboard equipment, and measurements to be taken are described for the Seasat-A global ocean monitoring satellite. The satellite is designed for mapping the global ocean geoid, charting ice fields and leads, precision measurement of sea surface topography, global monitoring of wave height and wave directional spectra, surface winds and wind direction, current patterns, and ocean temperature. Data handling subsystems, a compressed pulse radar altimeter, coherent synthetic aperture imaging radar, microwave wind scatterometer, scanning wisible/IR radiometer, scanning multispectral (5 freq) microwave radiometer mounted on the satellite are described briefly.

R.D.V.

A76-39035 * Tests and comparisons of satellite-derived geoids with Skylab altimeter data. J. G. Marsh (NASA, Goddard Space Flight Center, Greenbelt, Md.), B. C. Douglas (NOAA, National Ocean Survey, Rockville, Md.), S. Vincent, and D. M. Walls (Wolf Research and Development Corp., Riverdale, Md.). Journal of Geophysical Research, vol. 81, July 10, 1976, p. 3594-3598. 10 refs.

During the Skylab 4 mission, the S-193 radar altimeter was operated nearly continuously for a revolution around the world on Jan. 31, 1974. This direct measurement to the sea surface has provided an independent basis for the evaluation of the precision of global geoids computed from satellite-derived earth gravity models. This paper presents comparisons between the Skylab data and several recent gravity models published by Goddard Space Flight Center, the Smithsonian Astrophysical Observatory, and the National Oceanic and Atmospheric Administration. The differences between the altimeter geoid and the satellite geoids were as large as 20 m, rms values ranging from 8 to 10 m. These differences also indicated a systematic long-wavelength variation (about 100 deg) not related to error in the Skylab orbits. Truncation of the models to degree and order 8 did not eliminate the long-wavelength variation, but in every case the rms agreement between the satellite geoids and the altimeter geoid was slightly improved. Orbits computed with the truncated models were found to be inferior to those computed with the complete models. (Author)

A76-39765 Radiative transfer - A technique for simulating the ocean in satellite remote sensing calculations. H. R. Gordon (Miami, University, Coral Gables; NOAA, Physical Oceanography Laboratory, Miami, Fla.). Applied Optics, vol. 15, Aug. 1976, p. 1974-1979. 18 refs.

A method is presented for computing the radiative transfer in the ocean-atmosphere system which does not require detailed knowledge of the optical properties of the ocean. The calculation scheme is based on the observation that the upwelling radiance just beneath the sea surface is approximately uniform, which implies that the effect of the ocean can be simulated by a lambertian reflector just beneath the sea surface. It is further shown that for aerosol concentrations up to ten times the normal concentration, the radiative transfer in homogeneous and vertically stratified atmospheres (of the same optical thickness) is nearly identical. Examples indicating the applicability of these results to the remote sensing of ocean color from space are discussed in detail. (Author)

A76-40995 An investigation of a cold eddy on the eastern side of the Gulf Stream using NOAA 2 and NOAA 3 satellite data and ship data. F. M. Vukovich (Research Triangle Institute, Research Triangle Park, N.C.). Journal of Physical Oceanography, vol. 6, July 1976, p. 605-612. Contract No. NOAA-3-35402.

A study of a cold eddy on the eastern side of the Gulf Stream was performed combining data from the NOAA 2 and NOAA3 satellites and from the Cape Fear Technical Institute's R/V Advance

II. The satellite data were used initially to identify and locate the eddy in real time. The location data obtained from the satellite imagery was used to plan an oceanic field program using the Advance II to collect temperature and salinity data in the perturbation. The analysis of satellite data indicated that the cold eddy was elliptic in shape with the major axis varying from 180 to 120 km and a minor axis varying from 120 to 100 km. The analysis also suggested that the circulation of the eddy was entraining warm Gulf Stream water, strengthening the warm ring around the eddy. The subsurface analysis indicated that the cold eddy was characterized by a very pronounced dome of relatively cold, less saline water below 200 m, the temperature and salinity were uniform, both vertically and horizontally. (Author)

A76-43453 Temperature deviation of the ocean surface as measured by satellites. T. Takashima. COSPAR, Plenary Meeting, 19th, Philadelphia, Pa., June 8-19, 1976, Paper. 7 p. 9 refs.

The deviation of the ocean surface from an effective blackbody temperature is investigated in the window region by the adding method. The model atmosphere contains only aerosols in accordance with the Junge power-law size distribution and the refractive index of liquid water. It was observed that the temperature deviation is small at the vertical direction and increases rapidly with an increase in the nadir angle of observations. The deviation is smaller for a hazy atmosphere than for a clear atmosphere except for the subarctic winter, unlike that of the underlying surface of a perfect blackbody.

(Author)

A76-45962 # Aerial thermal surveys for mapping the fresh water springs flowing into the sea. G. M. Lechi and A. M. Tonelli (CNR, Istituto per la Geofisica della Litosfera, Milan, Italy). In: International Scientific-Technological Conference on Space, 16th, Rome, Italy, March 18-20, 1976, Proceedings. Rome, Rassegna Internazionale Elettronica Nucleare ed Aerospaziale, 1976, p. 139-141.

A76-46169 # Study of the Seasat project for a proposal of a French participation. J.-J. Chevalier and M. Piau (ONERA, Groupe de Recherches de Géodésie Spatiale, Toulouse, France). International Astronautical Federation, International Astronautical Congress, 27th, Anaheim, Calif., Oct. 10-16, 1976, Paper ST-76-02. 6 p.

The three-axis stabilized U.S. oceanographic and meteorological satellite Seasat A is scheduled for launch at the end of 1978. The paper analyzes the scientific objectives of the Seasat mission, the main scientific instrumentation onboard the satellite, and atmospheric influence on remote sensing. Information is given on the French participation in the Seasat mission. The satellite will carry out investigations in oceanography (surface winds, generation of waves, sea state, tsunamis, storm surges, upwellings, global model of tides, and cartography of currents), in meteorology and climatology (climatic fronts, wind speeds, clouds, heat exchange, polar studies), in glaciology (iceberg detection and movement, ice cartography), and in geodesy (undulations of the geoid and gravity anomalies). Technical characteristics of the onboard sensors, including visible infrared and microwave scanning radiometers, side looking radar with synthetic aperture, K-band altimeter, and radiometer, and their application in the Seasat mission are discussed.

A77-10112 Gulf Stream kinematics inferred from a satellite-tracked drifter. A. D. Kirwan, Jr. (Texas A & M University, College Station, Tex.), G. McNally, and J. Coehlo (California, University, La Jolla, Calif.). Journal of Physical Oceanography, vol. 6, Sept. 1976, p. 750-755. 11 refs. Contract No. N00014-75 C-0537.

A drifter was deployed in the Gulf Stream and tracked for five months by the Nimbus 6 satellite. From this experiment, assessments are made of the technical capability of the satellite fixing system for measuring ocean currents, the drifter trajectory as it relates to the Gulf Stream position as determined by other independent means, and the kinematics and accelerations following the Stream axis. It is shown that the trajectory agrees quite well with the other data on the location of the Gulf Stream. The velocities, accelerations, and kinetic energies derived from the trajectory are compared with

previous studies. The kinetic energy of the Gulf Stream as inferred from the drifter is compared with some recent calculations made from ship drift.

(Author)

A77-10894 # Multiband space imagery - A contribution to the study of oceanic dynamics. V. I. Kravtsova (Moskovskii Gosudarstvennyi Universitet, Moscow, USSR). International Astronautical Federation, International Astronautical Congress, 27th, Anaheim, Calif., Oct. 10-16, 1976, Paper 76-060. 15 p. 7 refs.

Effective application of multiband photography to the study of water areas is based on the use of the differences in the spectral brightness of various coasts, surfaces, and submerged objects and on the use of differences in the depth of penetration (into water) of light rays of various spectral bands. The use of a 'special signature' is essential in the interpretation of submerged objects, such as the contours of water vegetation. The effectiveness of multiband photography is demonstrated by images obtained in the visible and near infrared bands. Some difficulties involved in the interpretation of photographs of shallows are discussed.

V.P.

A77-10896 # The rules of classification of water surface conditions in remote sounding from space. Iu. E. Sidorov and S. V. Solonin (Leningradskii Gidrometeorologicheskii Institut, Leningrad, USSR). International Astronautical Federation, International Astronautical Congress, 27th, Anaheim, Calif., Oct. 10-16, 1976, Paper 76-062. 9 p.

The paper deals with the problem of statistical synthesis of the rules for classifying ocean surface conditions in the case of incomplete a priori information on the parameter distributions in remote sounding measurements, at different frequencies, of the outgoing microwave radiation of the ocean/atmosphere system. A solution is obtained by formulating the classification problem as a problem of estimating the parameters of a linear equation that relates the radio brightness temperatures at various wavelengths for various conditions at the ocean surface.

V.P.

A77-11085 * # A Seasat-A Synthetic Aperture Imaging Radar System. R. L. Jordan and D. H. Rodgers (California Institute of Technology, Jet Propulsion Laboratory, Pasadena, Calif.). American Institute of Aeronautics and Astronautics, Systems Design Driven by Sensors, Pasadena, Calif., Oct. 18-20, 1976, Paper 76-966. 10 p.

The Seasat-A Synthetic Aperture Imaging Radar System is the first radar system of its kind designed for the study of ocean wave patterns from orbit. The basic requirement of this system is to generate continuous radar imagery with a 100-km swath with 25 m resolution from an orbital altitude of 800 km. These requirements impose unique system design problems and their solutions will be stated. The end to end data system will be described including interactions of the spacecraft, antenna, sensor, telemetry link, and data processor. The synthetic aperture radar system generates a large quantity of data (110 megabits per second) requiring the use of a dedicated data link. The data link selected for use with the synthetic aperture radar is an analog link with stable local oscillator encoding. The problems associated in telemetering the radar information with sufficient fidelity to synthesize an image on the ground will be described as well as the selected solutions to the problems. (Author)

A77-11235 * Detailed gravimetric geoid confirmation of sea surface topography detected by the Skylab S-193 altimeter in the Atlantic Ocean. J. G. Marsh (NASA, Goddard Space Flight Center, Earth Survey Applications Div., Greenbelt, Md.) and E. S. Chang (EG & G/Washington Analytical Services Center, Inc., Riverdale, Md.). Bulletin Géodésique, vol. 50, no. 3, 1976, p. 291-299. 13 refs. SSSR, Izvestiia, Fizika Atmosfery i Okeana, vol. 11, Dec. 1975, p. 1330-1333.) Academy of Sciences, USSR, Izvestiya, Atmospheric and Oceanic Physics, vol. 11, July 1976, p. 830-832. 7 refs. Translation.

A77-11592 Detection of oceanic thermal fronts off Korea with the Defense Meteorological Satellites. O. K. Huh (Louisiana State University, Baton Rouge, La.). Remote Sensing of Environment, vol. 5, no. 3, 1976, p. 191-213. 18 refs. Navy-supported research.

Satellites of the Defense Meteorological Satellite Program used scanning infrared radiometers (8-13 microns) to provide serial images four times daily of sea-surface temperature gradients over the Sea of Japan, the Yellow Sea, and adjacent portions of the East China Sea. The electro-optically contoured infrared radiation temperatures faithfully reproduced the mesoscale structure of the surface temperature field. The radiometry provided near real-time, synoptic thermal charts of the surface waters for oceanographic observations, and for deployment of ship and aircraft sampling missions. The principal advantages of the satellite system are the high repetition rate of satellite overpasses, the flexible near real time display capabilities, the electro-optical data contouring capabilities, the geographic gridding system, and the high resolution and quality of the digital data stream.

A77-14519 The radiation budget of the ocean-atmosphere system and its components according to calculations and satellite measurements. N. A. Timofeev (Akademiia Nauk Ukrainskoi SSR, Morskoi Gidrofizicheskii Institut, Moscow, USSR). (Akademiia Nauk SSSR, Izvestiia, Fizika Atmosfery i Okeana, vol. 11, Dec. 1975, p. 1330-1333.) Academy of Sciences, USSR, Izvestiya, Atmospheric and Oceanic Physics, vol. 11, July 1976, p. 830-832. 7 refs. Translation.

A77-14732 # Some results of a study of sea-surface state using a highly sensitive radiometer (Nekotorye rezul'taty issledovaniia sostoianiia morskoi poverkhnosti pri pomoshchi vysokochuvstvitel'nogo radiometra). V. I. Andrianov, A. A. Glotov, S. V. Dotsenko, S. O. Lomadze, D. T. Matveev, V. G. Mirovskii, V. V. Nikitin, N. Ia. Nikolaev, M. D. Raev, and I. A. Troitskii (Akademiia Nauk SSSR, Institut Kosmicheskikh Issledovanii and Institut Fiziki Atmosfery; Akademiia Nauk Ukrainskoi SSR, Morskoi Gidrofizicheskii Institut, Moscow, USSR). Akademiia Nauk SSSR, Izvestiia, Fizika Atmosfery i Okeana, vol. 12, Aug. 1976, p. 868-874. 7 refs. In Russian.

Results are reported for a study of statistical sea-surface properties which employed a radiometer operating at a wavelength of 2.08 cm with a fluctuation sensitivity of 0.03 deg and a response time of one second. The radiometer was installed on a cliff about 50 m from the shore line at a height of about 8 m above mean sea level; its parabolic reflector was directed toward the open sea. Spectral methods of studying fluctuations in thermal radio emission are evaluated as a means of determining the statistical properties of a choppy sea surface. The results presented show that a radiometer of such high sensitivity may be used as a remote-sensing device for measuring temporal statistical sea-surface properties from distances of several tens or hundreds of meters.

F.G.M.

A77-15024 Singular behavior of the stress field at the wedge-shaped corners of branching cracks. V. K. Varatharajulu (Cornell University, Ithaca, N.Y.). *Journal of Engineering Mathematics*, vol. 10, Apr. 1976, p. 163-172. 13 refs. ARPA-NSF-sponsored research.

A77-15777* Internal wave observations made with an airborne synthetic aperture imaging radar. C. Elachi (California Institute of Technology, Jet Propulsion Laboratory, Pasadena, Calif.) and J. R. Apel (NOAA, Pacific Marine Environmental Laboratory, Seattle, Wash.). Geophysical Research Letters, vol. 3, Nov. 1976, p. 647-650. 10 refs. NOAA-DARPA-supported research; Contract No. NAS7-100.

Synthetic aperture L-band radar flown aboard the NASA CV-990 has observed periodic striations on the ocean surface off the coast of Alaska which have been interpreted as tidally excited oceanic internal waves of less than 500 m length. These radar images are compared to photographic imagery of similar waves taken from Landsat 1. Both the radar and Landsat images reveal variations in reflectivity across each wave in a packet that range from low to high to normal. The variations point to the simultaneous existence of two

mechanisms for the surface signatures of internal waves: roughening due to wave-current interactions, and smoothing due to slick formation.

A77-16225 Use of enhanced infrared satellite imagery for sea ice and oceanographic studies. K. O. L. F. Jayaweera (Alaska, University, Fairbanks, Alaska), (International Conference on Port and Ocean Engineering Under Arctic Conditions, 3rd, University of Alaska, Fairbanks, Alaska, Aug. 1975.) Ocean Engineering, vol. 3, Oct. 1976, p. 293-298. Grants No. NOAA-5-35190; No. NOAA-04-6-158-44039.

Infrared (IR) imagery from the NOAA 2, 3 and 4 satellites could be used to measure accurately the absolute temperature of the sea surface and sea water. Comparison with measured temperatures indicate that the satellite observed values are within 2 C of those measured. Contouring temperatures and observing temperature fluc tuations within 0.5 C is also possible by enhancing the infrared image. This is done by confining the 16 steps of gray of the image to a desired small temperature scale. The existence of open water areas within the pack ice and the positions of the ice edges could be readily distinguishable by generating special imagery in such a way that the gray scale covers two temperature ranges with a gray tone jump at the freezing point of sea water. In this way ice-water boundary appears as a line of demarcation between two different gray tones. Because the IR imagery is available all year round these techniques are readily applicable at all times especially during the winter months when the low sun angles make visible imagery not useful. (Author)

Island wind shadows observed by satellite and radar. J. W. Deardorff (National Center for Atmospheric Research, Boulder, Colo.). American Meteorological Society, Bulletin, vol. 57, Oct. 1976, p. 1241, 1242. 13 refs.

It is proposed that the mechanism responsible for maintaining an island wind shadow is the stable thermal stratification induced when the air first passes over the heated island and then over the sea. The enhanced atmospheric stability to the lee of the island is associated mainly with anomalously warm air rather than with an anomalously cool ocean surface. The air is heated when traversing the land or island in the daytime, and it emerges downstream of the island generally warmer than neighboring air that did not traverse land. After the warm air passes out over the cooler water surface, stable atmospheric stratification gradually develops from the surface upward (a stable internal boundary layer).

Models of radar imaging of the ocean surface waves. C. Elachi and W. E. Brown, Jr. (California Institute of Technology, Jet Propulsion Laboratory, Space Sciences Div., Pasadena, Calif.). IEEE Transactions on Antennas and Propagation, vol. AP-25, Jan. 1977, p. 84-95. 30 refs. Contract No. NAS7-100.

A number of models which would explain ocean wave imagery taken with a synthetic aperture imaging radar are analyzed analytically and numerically. Actual radar imagery is used to support some conclusions. The models considered correspond to three sources of radar backscatter cross section modulation: tilt modulation, roughness variation, and the wave orbital velocity. The effect of the temporal changes of the surface structure, parametric interactions, and the resulting distortions are discussed.

Microwave radiometric determination of wind speed at the surface of the ocean during BESEX. T. T. Wilheit, Jr. (NASA, Goddard Space Flight Center, Greenbelt, Md.) and M. G. Fowler (Environmental Research and Technology, Inc., Lexington, Mass.). IEEE Transactions on Antennas and Propagation, vol. AP-25, Jan. 1977, p. 111-120, 14 refs.

Microwave radiometric measurements were made at wavelengths ranging from 0.8 to 2.8 cm at altitudes from 0.16 to 11 km under well documented meteorological conditions over the Bering Sea. It is shown that determinations of wind speed at the ocean surface and liquid water content of the clouds may be made from such data. Determinations were made from two simultaneous but independent sets of radiometric measurements. The wind speeds and liquid water contents made from these two sets showed remarkable agreement.

Independent estimates of these parameters made from in situ measurements showed reasonable agreement as well. (Author)

A77-20767 * Radiometric observations of sea temperature at 2.65 GHz over the Chesapeake Bay. H.-J. C. Blume (NASA, Langley Research Center, Hampton, Va.), A. W. Love, M. J. Van Melle (Rockwell International Corp., Downey, Calif.), and W. W. Ho (Rockwell International Science Center, Thousand Oaks, Calif.). IEEE Transactions on Antennas and Propagation, vol. AP-25, Jan. 1977, p. 121-128. 18 refs.

A77-20771 An experimental study of a pulse compression scatterometer system. D. L. Schuler (U.S. Navy, Naval Research Laboratory, Washington, D.C.). IEEE Transactions on Antennas and Propagation, vol. AP-25, Jan. 1977, p. 140-145. 9 refs.

The ideal scatterometer, operating from either an aircraft or a satellite platform, should be capable of making rapid, accurate estimates of the sea backscatter cross section over as wide a range of grazing angles as possible. A hybrid estimation procedure has been developed for pulse compression radars which uses both frequency and spatially decorrelated samples of sea backscatter cross section to provide an unbiased estimate of sea backscatter cross section having minimum variance over the entire range of grazing angles for which radar reception is not noise-limited. (Author)

A77-20773 * Effects of random phase changes on the formation of synthetic aperture radar imagery. C. Elachi and D. D. Evans (California Institute of Technology, Jet Propulsion Laboratory, Pasadena, Calif.). IEEE Transactions on Antennas and Propaga tion, vol. AP-25, Jan, 1977, p. 149-153. 9 refs. Contract No. NAS7-100.

The effects of Gaussian random fluctuation and linear change of the echo phase on the response of the azimuth matched processor of a synthetic aperture radar (airborne or spaceborne for ocean-surface sensing) is analyzed numerically. It is found that the random fluctuation would not alter appreciably the processor response if its standard deviation is less than pi, while its normalized correlation time is larger than 1. If these two bounding conditions are not satisfied, then the sidelobe level becomes relatively large and overshadows the central peak. In the case of linear displacement it is found that the main effect is the spatial displacement of the point scatterer in the image plane.

N76-70869# Texas A&M Univ College Remote Sensing Center REMOTE SENSING CENTER GRANT PROGRAM SUMMARY Progress Report, Feb. Aug. Original contains color Aug. illustrations. (Grant NGL-44-001-001) (NASA-CR-146017; RSC-09) Avail: NTIS

Changes that have occurred in the program relative to the Demonstration Projects and the preparations being made for the new activities to be initiated are discussed. Emphasis is placed on the demonstration of remote sensing techniques in close cooperation with the user community

N76-76625# Environmental Research Inst. of Michigan, Ann Arbor. Infrared and Optics Div INTERPRETATION MANUAL FOR THE AIRBORNE REMOTE

SENSOR SYSTEM Robert Horvath Jan. 1974 100 p refs (Contract DOT-CG-33568-A)

(AD-A019460; USCG-250-44) Avail: NTIS

Technical guidelines are presented for personnel charged with operating and interpreting the output from the airborne remote sensor system (ARSS). Emphasis is placed on what a particular image feature indicates about the target observed. Observed effects of petroleum products are qualitatively analyzed in the 0.3 to 0.4 micrometer ultraviolet region, and the 8 to 14 micrometer thermal infrared region. The effects of false targets such as fish oils, ship wakes, effluents, and seaweed are included

along with imagery from a series of tests involving discharges of various types of oils. Instructions are given for operating equipment to optimize results.

Author

N77-71511# Draper (Charles Stark) Lab., Inc., Cambridge, Mass. INTERPRETATION OF FORCE VECTOR RECORDER DATA DESCRIBING BUOY SYSTEM DYNAMICS M.S. Thesis - MIT

Prafulla K. Padhi Feb. 1976 77 p refs (Contracts N00014-74-C-0163; N00014-75-C-1065; NR Proj. 083-318; NR Proj. 294-042)

(AD-A023418; T-623) Avail: NTIS

The force vector recorder is a self-contained recording instrument which measures three components of specific force. (force-balance accelerometer sensors), two components of earth's magnetic field (flux gate magnetometer sensors), and water pressure (strain gage diaphram sensor). This instrument was mounted above the drogue in an ocean test of a drogued drifting buoy system. The theoretical background and procedures for determining drogue dynamics and Euler attitude angles from the sea test data tape are described.

Author

77-01001 # Naval Undersea Center, San Diego, Calif.
ELECTROMAGNETIC FIELDS IN THE OCEAN AND ELECTRORECEPTIVE FISH Research Report, Jul. 1975 - Jul.
1976

E. H. Satorius Feb. 1976 36 p

(Proj. SF34-371)

(AD-A028927; NUC-TP-504) Avail: NTIS

The possibility of the detection of dipole fields by electrosensing fish was studied. In particular, a skate (Raja Clavata) which is sensitive to threshold electric fields of 1 microvolt/meter was examined. The results indicate that skates detect electric dipole fields at short distances (approximately 100 M at f=0, 1, or 10 hz and for dipole source current moments on the order of 60 a-m). A comparison between the electric dipole sensing capabilities of skates and artificial system is made. In general, it appears that the optimum single-element manmade sensing system is superior to the skate for purposes of long-range detection of narrowband, extremely low frequency signals.

77-01002 # Texas A&M Univ., College Station. Dept. of Oceanography.

GULF STREAM KINEMATICS INFERRED FROM A SATEL-LITE-TRACKED DRIFTER

A. D. Kirwan, Jr., G. McNally, and J. Coehlo Feb. 1976 7 p Publ. in J. of Phys. Oceanog., v. 6, no. 5, Sep. 1976 p 750-755

(Contract N00014-75-C-0537)

(AD-A032606; Contrib-652) Avail: NTIS

The technical capability of the Nimbus 6 satellite fixing system for measuring ocean currents and the trajectory, kinematics, and accelerations of a drifter following the Gulf Stream axis was assessed. The trajectory obtained during a five-month tracking period agrees with other data on the location of the Gulf Stream. The velocities, accelerations, and kinetic energy derived from the trajectory are compared with previous studies. The kinetic energy of the Gulf Stream as inferred from the drifter is compared with recent calculations made from ship drift.

Author

77-01003 # Naval Intelligence Support Center, Washington, D. C. Transl. Div.

SPECTRAL CHARACTERISTICS OF CYLINDRICAL SEN-SORS OF HYDROPHYSICAL INSTRUMENTS

S. V. Dotsenko, V. N. Kuleshova, and A. N. Nedovesov Oct. 1976 8 p Transl. into ENGLISH from Morsk. Gidrofizicheskiy Inst. (USSR), v. 51, no. 1, 1972 p 88-95 (AD-AO33047; NISC-Trans-3869) Avail: NTIS

The article discusses the transformation of the spectrum of the measured field into the spectrum of the output signal by a cylindrical sensor during its uniform linear motion and for the two types of orientation. The calculations presented make it possible to construct sensors with specified spectral characteristics.

Author

77-01004 # Louisiana State Univ., Baton Rouge. Coastal Studies Inst.

DETECTION OF OCEANIC THERMAL FRONTS OFF KOREA WITH THE DEFENSE METEOROLOGICAL SATELLITES Technical Report

Oscar Karl Huh Jun. 1976 26 p Publ. in Remote Sensing of Environ., v. 5, 1976 p 191-213 (Contract N00014-75-C-0192)

(AD-A033745; TR-226) Avail: NTIS

Scanning radiometers of the Defense Meteorological Satellite Program provided useful thermal infrared (8-13 micron) imagery of the oceanic regions near the Korean Peninsula. The near real time thermal infrared data (at 3.7 km. spatial resolution) provided temperatures some 2-10 C cooler than the actual surface measurements. The thermal gradients were faithfully reproduced, however, and relative temperature differences were successfully estimated to less than 0.1 C. A combination of methods was used to avoid possible confusion with atmospheric temperature and humidity gradients. The oceanic thermal front between the Tsushima Current and the Korean coastal waters was routinely detected. Thermal patterns of a one-sided divergence and a cyclonic eddy were also detected in the coastal waters at the flow separation where the western edge of the Tsushima Current curves away from the coast into the Sea of Japan.

Author

02

APPLICATIONS

N75-28664# Informatics, Inc., Rockville, Md.
BIBLIOGRAPHY OF SOVIET MATERIAL ON INTERNAL
WAVES, APRIL - DECEMBER 1974

Stuart G. Hibben and Lee H. Boylan 27 Jan 1975 30 p

(Contract N00600-75-C-0018; DARPA Order 2790) (AD-A005565) Avail: NTIS CSCL 08/3

The report is the third bibliography of Soviet open-source publications relating to internal wave studies. It covers material received from May through December 1974. Main selection criteria are studies of small-scale variation in ocean parameters and of airborne techniques for deducing internal wave conditions. index of serial source abbreviations is appended.

N76-10674* Wayal Research Lab., Washington, D.C. ANALYSIS OF SKYLAB 2 S193 SCATTEROMETER DATA Final Report

Arthur K. Jordan, Charles G. Purves, and James F. Diggs 2 May

1975 20 p refs (NASA Order L-7913-A; NRL Proj. RO2-37) (NASA-CR-145536; AD-A010517; NRL-7877) Avail: NTIS

CSCL 04/2

SKYLAB II S193 Scatterometer data for the passes of June 5, 1973, over the Gulf of Mexico and June 6, 1973, over Pacific Hurricane AVA were analyzed. The S193 scatterometer measured the radar cross section of the ocean at 13.9 GHz (Ku-band) as a function of incidence angle. The fields-of-view of the scatterometer were known. In the absence of a large body of Ku-band ocean radar data, the results of the NRL experiments at X-band (8.9 GHz) were used for comparison. The S193 data of June 5, 1973, when a practically uniform wind field was present, show reasonable agreement with the NRL empirical and theoretical models.

N76-11683# National Environmental Satellite Service, Washing-

A SUMMARY OF THE RADIOMETRIC TECHNOLOGY MODEL OF THE OCEAN SURFACE IN THE MICROWAVE REGION

John C. Alishouse Mar. 1975 31 p refs

(COM-75-10849-8; NOAA-TM-NESS-66; NOAA-75052201) Avail: NTIS HC \$4.00 CSCL 08J Between November 1970 and March 1974, studies were pursued to determine sea-surface temperature and roughness from a satellite-borne microwave radiometer, Such factors as salinity, foam, wave spectra, polarization, and atmospheric attenuation were investigated to determine optimum frequencies and accuracy limitations. The resultant model developed is a two-dimensional two-scale model that incorporates upwind and crosswind wave spectra and considers waves that are both large and small in comparison with the radiometer's wavelength.

GRA

N76-13710# Earth Satellite Corp., Washington, D.C.
APPLICATIONS OF THE NIMBUS 5 ESMR TO RAINFALL DETECTION OVER THE OCEANS AND TO SEA-ICE **DETECTION** Final Report

Romeo R. Sabatini, Dennis L. Hlavka, and Ronald Arcese Apr. 1975 81 p refs (Contract N66314-73-C-1572)

(AD-A013245; EPRF-TR-6-75(ESC)) Avail NTIS CSCL 04/2 The report explores the applicability of the Nimbus 5 Electrically Scanning Microwave Radiometer (ESMR) to rainfall

detection over the oceans and to sea ice detection. Two different but complementary approaches are taken - a theoretical approach which involved the theoretical calculations of brightness temperature (t sub b) in a prepared scenario of model atmospheres and surface conditions, and an empirical approach which made use of simultaneous measurements of our parameters of interest from other sensors: WSR-57 radar for precipitation, and images from other satellites (NOAA and LANDSAT) for sea-ice.

N76-14579*# National Aeronautics and Space Administration. Langley Research Center, Langley Station, Va.

NATIONAL AERONAUTICS AND SPACE ADMINISTRATION OPERATIONS: REMOTE SENSING EXPERIMENTS IN THE J. W. Usry and J. B. Hall, Jr. Nov. 1975 62 p. refs

(NASA-TM-X-72802) Avail: NTIS HC \$4.50 CSCL 08B

Results are given of remote sensing experiments conducted in the New York Bight between April 7-17, 1975, to evaluate the role of remote sensing technology to aid in monitoring ocean dumping. Remote sensors were flown on the C-54, U-2, and C-130 aircraft while the National Oceanic and Atmospheric Administration obtained concurrent in situ sea truth data using helicopters and surface platforms. The test site, aircraft platforms, experiments, and supporting sensors are described. The operation of each aircraft are discussed and aircraft flight lines, flight parameters, and data identification parameters are presented in figures and tables. Author

N76-15762# Delaware Univ., Newark. Coll of Marine

INTERPRETATION OF STRUCTURES OVER OCEANIC REGIONS IN DMSP DATA

Karl-Heinz Szekielda May 1975 42 p refs

(Contract N66314-74-C-1294)

(AD-A014320; CMS-C-1-75; EPRF-TR-5-75(UD)) Avail: NTIS CSCL 08/10

Images obtained by the Defense Meteorological Satellite Program (DMSP) over the Gulf of Mexico were interpreted. In differentiating the optical characteristics of various targets. hydrography, and the frequency of occurrence of features, it was concluded that structures recognized in the offshore region were not caused by chlorophyll concentration, current boundaries (temperature gradients), sea state, or sediments. It is suggested that the atmosphere might be the significant cause for the structures recognized over cloud-free regions by the DMSP. This conclusion will be limited strictly to the case studies presented.

N76-16607# Environmental Research Inst. of Michigan, Ann Infrared and Optics Div

REMOTE SENSING STUDIES IN THE NEW YORK BIGHT Final Report

T. Wezernak, D. R. Lyzenga, and F. C. Polcyn. Jul. 1975

(COM 75 11358/9. ERIM-109300-5-F; NOAA-75082104) Avail NTIS HC \$4 50 CSCL 08J

The results are described of a remote sensing program of data collection and analysis undertaken in the New York Bight Aircraft multispectral missions were carried out on 7 April 1973 The morning mission on that date coincided with the ERTS-1 satellite pass over the area. The principal objectives of the program were to provide data, which when combined with shipboard measurements, would describe the surface waters of the area and their general circulation. Specifically the remote sensing program was designed to provide the following information: (1) sea surface temperature distribution. (2) surface chlorophyll concentrations. (3) secchi disc transparency. (4) document ocean dumping practices, and (5) movement of water masses as evidenced by dye tracer materials

N76-21860# Naval Research Lab., Washington, D.C.
OCEAN SCIENCES DIVISION: RECENT DEVELOPMENTS IN INSTRUMENTATION AND TECHNIQUES Final Report Richard Nekritz Nov. 1975 26 p (AD-A018133; NRL-MR-3150) Avail NTIS CSCL 08/3

Since 1966, when the Ocean Sciences Division originated its scientists have developed a variety of instruments and techniques to apply to their studies of marine chemistry, air-sea interactions, air-mass trajectories, fog generation, pollution, and ocean turbulence. This report describes several of these developments, some of which may be applicable to the scientific or technical problems of other investigators. Author (GRA)

N77-17554# Environmental Research Inst. of Michigan, Ann

BASIC REMOTE SENSING INVESTIGATION FOR BEACH RECONNAISSANCE Interim Report, 1 Jun. - 31 Dec. 1975 F. Thompson, R. Shuchman, C. Wezernak, D. Lyzenga, and D. Leu Jul 1976 127 p refs

(Contract N00014-74-C-0273)

(AD-A029041; ERIM-108900-5-P) HC A07/MF A01 CSCL 15/4

Progress is reported on three tasks designed to develop remote sensing beach reconnaissance techniques applicable to the benthic, beach intertidal, and beach upland zones is designed to develop remote sensing indicators of important beach composition and physical parameters which will ultimately prove useful in models to predict beach conditions. Task 2 is designed to develop remote sensing techniques for survey of bottom features in the benthic zone. Task 3 is designed to develop radar processing techniques to delineate important beach intertidal and upland parameters and to better understand the potential of radar-derived information when used with optical sensor data

A74-26007 # Heat and moisture budget analyses using BOMEX data. T. Nitta and S. Esbensen (California, University, Los Angeles, Calif.). Monthly Weather Review, vol. 102, Jan. 1974, p. 17-28. 21 refs. NSF Grant No. GA-31694.

Large-scale heat and moisture budgets over the tropical Atlantic Ocean are examined during Phase 3 (June 22 to 30, 1969) of the Barbados Oceanographic and Meteorological Experiment. From the satellite cloud photographs of ATS-3, the analyzed period is subdivided into an undisturbed part and a disturbed part. During the undisturbed period, downward motion predominates from the surface to about 500 mb and a large apparent heat sink and apparent moisture source are found near the top of the trade inversion layer. The upward heat flux due to cumulus clouds is confined below the 700-mb level. On the other hand, during the relatively disturbed period, upward motion takes place at low levels and the heat flux due to cumulus convection extends to at least 500 mb. Values of the total heat flux estimated by large-scale budgets agree well with those obtained independently by bulk aerodynamic computations.

(Author)

NTIS

A74-33750 The cell structure of certain marine fogs and the cellular vortices created in the atmosphere by radiative cooling (La structure cellulaire de certains brouillards marins et les tourbillons cellulaires crées dans l'atmosphère par refroidissement rayonnant). P. Schreschewsky. Académie des Sciences (Paris), Comptes Rendus, Série B - Sciences Physiques, vol. 278, no. 20, May 13, 1974, p. 905-907. 5 refs. In French.

Analysis of the cell structure observed in two instances of coastal fog occurring over the Pacific Ocean north of San Francisco and along the peninsula of Lower California, respectively. It is found that in both of these examples the cell structure is such as to confirm the two conditions posed by Liddy (1968) for the formation of marine fogs - namely, radiative cooling for the upper surface of the cloud layer, with the air superimposed on this layer being stable and not mixing with it. This is in contrast to the mechanism employed by Bénard which involved uniform heating from below. Nevertheless, it is recommended that the cells observed in these two cases be called Bénard cells A.B.K.

A74-39278 Use of remote sensing in the study of Antarctic marine resources, S. Z. El-Sayed and K. A. Green (Texas A & M University, College Station, Tex.). In: Approaches to earth survey problems through use of space techniques; Proceedings of the Symposium, Konstanz, West Germany, May 23-25, 1973.

Berlin, East Germany, Akademie-Verlag GmbH, 1974, p. 47-63. 22 refs. NSF Grant No. GV-36215X.

The krill is a valuable Antarctic marine resource which will some day be commercially exploited as a food source. The physical, chemical, and biological milieu of the Antarctic seas in which the krill is found is described generally in terms of pack ice distribution, light variations, cloud cover, physical oceanography, the distribution of nutrient salts, and phytoplankton and zooplankton population. The distribution of krill is discussed, and the extent, color, location and other features of krill swarms which may render them susceptible to remote sensing are indicated. Technique for the remote sensing of chlorophyll and sea temperature are available, but a technique for detecting krill swarms is not yet developed, though studies are in progress.

A74-44646 # Use of artificial earth satellites to measure the swell of the sea (Ispol'zovanie iskusstvennykh sputnikov zemli dlia izmereniia volneniia). A. A. Zagorodnikov. Akademiia Nauk SSSR, Izvestiia, Fizika Atmosfery i Okeana, vol. 10, July 1974, p. 791-798. 20 refs. In Russian

A74-45067 Measurement of water vapor content over the oceans by SHF radiometers aboard Cosmos-243. L. M. Mitnik. In: Advances in satellite meteorology, 2. New York, Halsted Press; Jerusalem, Israel Program for Scientific Translations, 1974, p. 65-73, 14 refs. Translation.

Maps are given of atmospheric water vapor content over the tropical and subtropical latitudes of the Pacific, Atlantic, and Indian oceans, constructed on the basis of the earth's thermal emission measured aboard Cosmos-243. Isolines of water vapor content are drawn at 0.5 g/sq cm intervals. The main features of the moisture field are discussed (time variations in water vapor content during various synoptic situations, comparison with water vapor values derived from radiosonde data). The maps of water vapor content show that the distribution indicates stable seasonal features of the atmospheric circulation. The continents strongly affect the atmospheric distribution of water vapor. For example, in the Southern Hemisphere the boundary between dry and moist air is displaced markedly northward with decreasing distance to Australia and, particularly, South America.

A75-10644 * # The detection by ERTS-1 of wind-induced ocean surface features in the lee of the Antilles Islands. R. Cram and K. Hanson (Miami, University, Coral Gables, Fla.). Journal of Physical Oceanography, vol. 4, Oct. 1974, p. 594-600. 8 refs. Contract No. NOAA-04-30-2212. NASA Order S-70246-AG-1.

Photographic data received from the ERTS-1 satellite over the Lesser Antilles Islands show distinct ocean features on the leeward side of each island. Attempts to relate these features to ocean eddy formations with the aid of ground truth data proved unsuccessful. However, surface and upper air wind data indicate a good correlation with the size, shape, and downwind extent of the ocean features. Studies to date indicate strongly that these features result from horizontal differences in a sea surface roughness due to the wind-shadow effect of the islands. The results suggest that horizontal variations in the reflectance of the sea surface will make remote sensing of the ocean mixed layer more difficult than previously anticipated. The surface reflection seems to be large enough to mask the smaller variations in backscattered energy from the mixed layer Efforts to limit the effect of surface reflectance by photographic differencing of two multi-spectral scanner bands were unsuccessful. (Author)

A75-10645 # A satellite-aircraft thermal study of the upwelled waters off Spanish Sahara. P. E. La Violette (U.S. Department of Defense, Naval Oceanographic Office, Washington, D.C.). Journal of Physical Oceanography, vol. 4, Oct. 1974, p. 676-684. 10 refs. DOD-Navy-sponsored research.

Review of the upwelling along the coast of Spanish Sahara and of several associated thermal features observed in a satellite-aircraft oceanographic survey conducted during the period from the 18th through the 26th of August 1973. Analyses of the aircraft and satellite radiation data show that these features consisted of variable cool and warm eddies which extended more than 100 km northwest from the coastal upwelling zone. These features may represent a periodic occurrence.

M.V.E.

A75-11255 * Satellite photography of eddies in the gulf loop current. G. A. Maul (NOAA, Physical Oceanography Laboratory, Miami, Fla.), D. R. Norris (NASA, Johnson Space Center, Earth Observations Div., Houston, Tex.), and W. R. Johnson (Lockheed Electronics Co., Inc., Houston, Tex.). Geophysical Research Letters, vol. 1, Oct. 1974, p. 256-258. 9 refs.

Cyclonic ocean eddies, approximately 12 to 32 kilometers in diameter, have been photographed in the eastern Gulf of Mexico by SKYLAB. Apparently caused by horizon velocity shear, these features are associated with the Gulf Loop Current, whose position was known a fortnight before and after the observation. The eddies were discovered in sunlight-enhanced patterns of streamlines on the surface, and appear to be embedded in the flow. (Author)

A75-12028 # Certain problems in carrying out nautical electrical prospecting with alternating current (Deiaki pitannia stvorennia mors'koi elektrorozvidki zminnim strumom). M. I. Kalashnikov. Akademiia Nauk Ukrains'koi RSR, Visnik, vol. 38, Sept. 1974, p. 75-84. 24 refs. In Ukrainian.

Consideration of the possibility of developing effective methods of nautical electrical prospecting based on schemes which are similar to electrical prospecting from an aircraft and involve the use of field sources and receivers which allow inflight operation of dataprocessing equipment. The techniques of carrying out aeroelectrical prospecting work are reviewed, dwelling especially on prospecting by the induction method, using harmonic and anharmonic fields, and the long-cable method, both of which generally involve the use of a towed gondola to house the receiver. The types of field sources that can be employed in aeroelectrical prospecting with alternating current under open-sea conditions are discussed, the requirements on field receivers mounted on moving gondolas are noted, and certain drawbacks of nautical electrical prospecting are cited. The possibility of realizing a nautical electrical prospecting scheme using the long-cable method is evaluated. ARK

A75-12034 * # Skylab and ERTS-1 investigations of coastal land-use and water properties in Delaware Bay. V. Klemas, D. Bartlett (Delaware, University, Newark, Del.), and R. Rogers (Bendix Corp., Aerospace Systems Div., Ann Arbor, Mich.). American Institute of Aeronautics and Astronautics and American Geophysical Union, Conference on Scientific Experiments of Skylab, Huntsville, Ala., Oct. 30-Nov. 1, 1974, AIAA Paper 74-1220. 10 p. 10 refs. Contracts No. NAS5-21837; No. NAS1-12304; No. N00014-69.4.0407

Study of coastal land use and water properties of Delaware Bay using digital and visual analysis of enhanced imagery from NASA's Earth Resources Technology Satellite (ERTS) and from the Skylab Earth Resources Experimental Package (EREP). ERTS is shown to have the advantage of repetitive coverage of the test site which facilitates change detection experiments by gathering data under a variety of tidal, seasonal, and atmospheric conditions. Skylab-EREP data, on the other hand, are superior in both spatial and spectral resolution.

A75-12984 # Determination of earth and ocean tides from the analysis of satellite orbits. K. Lambeck (Paris VI, Université, Paris; Groupe de Recherches de Géodésie Spatiale, Brétigny-sur-Orge, Essonne, Prances)...In: Symposium on Earth's Gravitational Field and Secular Variations in Position, Sydney, Australia, November 26-30, 1973, Proceedings. Kensington, Australia, University of New South Wales, 1974, p. 522-528. 28 refs.

Some general information concerning solid earth tides, ocean tides, and their interaction is discussed, and the principal concepts

and analytical approaches applied to tidal studies by satellite are briefly described. The tidal potential at a satellite causes an additional force function that has to be accounted for when the satellite's equations of motion are integrated. This potential introduces perturbations in the motion of close earth satellites. Studies have shown that there is an important interaction between earth and ocean tides as observed from orbit analyses. Neglect of ocean tides can introduce errors in k2 of as much as 15 per cent and of several degrees in phase. The ocean tide models, even the comparatively well known M2 tide, are inadequate for making the precise ocean corrections, particularly for the important diurnal tides. P.T.H.

A75-14803 * Estimation of sea surface temperature from remote sensing in the 11- to 13-micron window region. C. Prabhakara, V. G. Kunde (NASA, Goddard Space Flight Center, Greenbelt, Md.), and G. Dalu (CNR, Istituto di Fisica dell'Atmosfera, Rome, Italy). Journal of Geophysical Research, vol. 79, Nov. 20, 1974, p. 5039-5044, 26 refs.

The Nimbus 3 and 4 Iris spectral data in the 11- to 13-micron water vapor window region are analyzed to determine the sea surface temperature (SST). The high spectral resolution data of Iris are averaged over approximately 1-micron-wide intervals to simulate channels of a radiometer to measure the SST. In the present exploratory study, three such channels in the 775- to 960-per cm (12.9-10.5 micron) region are utilized to measure the SST over cloud-free oceans. However, two of these channels are sufficient in routine SST determination. The differential absorption properties of water vapor in the two channels make it possible to determine the water vapor absorption correction without detailed knowledge of the vertical profiles of temperature and water vapor. The feasibility of determining the SST is demonstrated globally with Nimbus 3 data, where cloud-free areas can be selected with the help of albedo data from the medium-resolution infrared radiometer experiment on board the same satellite. The SST derived from this technique agrees with the measurements made by ships to about 1 C. (Author)

A75-23340 Geoid definitions for the study of sea surface topography from satellite altimetry. R. S. Mather (New South Wales, University, Sydney, Australia). In: International Symposium on Applications of Marine Geodesy, Columbus, Ohio, June 3-5, 1974, Proceedings. Washington, D.C., Marine Technology Society, 1974, p. 279-289. 20 refs.

This paper concentrates on the development of techniques for obtaining geoid definitions from mixed data sets consisting of oceanic 'geoid heights' deduced from the altimetry, and gravity anomalies largely in continental areas, from solutions of the geodetic boundary value problem. It discusses how data subject to significant systematic errors with substantial wavelengths can be successfully used in the quadratures evaluation of such solutions. Arguments are outlined for the incorporation of gravity field models with errors at the 5% level in the disturbing potential, in the system of geodetic reference. The adoption of such a procedure would permit a common model to be used both in the solution of the boundary value problem, as well as in orbit determination, on reinforcement with the appropriate resonant terms. The advantage of quadratures methods in high-precision determinations lies in the elimination of prohibitive matrix inversion problems, provided conditions for convergence can be established by appropriate modification of the data acquisition procedures.

A75-23343 Geoid determination from satellite altimetry using sample functions. R. D. Brown (Computer Sciences Corp., Los Angeles, Calif.). In: International Symposium on Applications of Marine Geodesy, Columbus, Ohio, June 3-5, 1974, Proceedings. Washington, D.C., Marine Technology Society, 1974, p. 315-329. 10 refs.

For implementation of the sample function geopotential model, Lundquist and Giacaglia (1969) proposed an algorithm, involving the assumption of a diagonal normal matrix. Another, simpler, algorithm was proposed by Giacaglia and Lundquist (1972) in order to reduce the amount of computational work required in using the first

algorithm. The procedure to be used in numerical simulations of these two algorithms as applied to the altimeter problem is discussed along with the results of numerical simulation tests using both algorithms.

A75-23346 * Detailed gravimetric geoid for the GEOS-C altimeter calibration area. J. G. Marsh (NASA, Goddard Space Flight Center, Greenbelt, Md.) and S. Vincent (Computer Sciences Corp., Silver Spring, Md.). In: International Symposium on Applications of Marine Geodesy, Columbus, Ohio, June 3-5, 1974, Proceedings. Washington, D.C., Marine Technology Society, 1974, p. 371-379. 6 refs.

The GEOS-C spacecraft scheduled for launch in late 1974 will carry a radar altimeter for the purpose of measuring sea surface topography. In order to calibrate and evaluate the performance of the altimeter system, ground truth data are required. In this respect a detailed gravimetric geoid has been computed for the GEOS-C altimeter calibration area in the Atlantic Ocean off the East Coast of the U.S. This geoid is based upon a combination of mean free air surface gravity anomalies and the Goddard Space Flight Center GEM-6 satellite-derived spherical harmonic coefficients. Surface gravity anomalies have been used to provide information on the short wave length undulations of the geoid while the satellite-derived coefficients have provided information on the long wave length components. As part of these analyses, GSFC, SAO and OSU satellite-derived gravity models were used in the computations. Although geoid heights based upon the various satellite models differed by as much as 30 meters in the Southern Hemisphere, the differences in this Atlantic Ocean area were less than 4 meters.

(Author)

A75-27343 # Oceanographic studies of the northern Gulf of California. L. K. Lepley, J. P. Hendrickson, C. Flanagan (Arizona, University, Tucson, Ariz.), and G. Calderon (Secretariat de Marina, Mexico). In: Annual Conference on Remote Sensing in Arid Lands, 4th, Tucson, Ariz., November 14-16, 1973, Proceedings.

Tucson, University of Arizona, 1974, p. 227-258. 12

Analysis of ERTS imagery of the northern Gulf of California with the aid of surface truth sampling of physical oceanographic parameters is described. Oceanographic and meteorological data obtained by surface observations are discussed, and a seasonal circulation model is constructed for the Gulf waters. ERTS imagery in all four MSS bands is used to evaluate the circulation model, and is analyzed to predict the depth of turbidity patterns, to obtain spectral models of mixed water bodies and glitter patterns, and to observe gyres, upwelling plumes, internal waves, the tidal current velocity, tidal phases, fresh water runoff, and other phenomena. The circulation model is revised on the basis of the satellite imagery data. Suggestions for further studies are made, and charts and ERTS photographs are appended.

Evolution of Gulf Stream eddies as seen in satellite infrared imagery. H. G. Stumpf and P. K. Rao (NOAA, National Environmental Satellite Service, Suitland, Md.). Journal of Physical Oceanography, vol. 5, Apr. 1975, p. 388-393. 9 refs.

Pronounced eddies along the western edge of the Gulf Stream were again observed by the Very High Resolution Radiometer aboard the NOAA-2 satellite. A rare sequence of infrared images obtained over a period of seven days shows for the first time the complete evolution of meanders through the eddy stage.

The use of artificial earth satellites to measure ocean waves. A. A. Zagorodnikov. (Akademiia Nauk SSSR, Izvestiia, Fizika Atmosfery i Okeana, vol. 10, July 1974, p. 791-798.) Academy of Sciences, USSR, Izvestiya, Atmospheric and Oceanic Physics, vol. 10, July 1974, p. 487-491. 20 refs. Translation.

A75-34927 * Study of a water quality imager for coastal zone missions. W. F. Staylor, E. F. Harrison (NASA, Langley

Research Center, Mission Analysis Section, Hampton, Va.), and V W. Wessel (LTV Aerospace Corp., Hampton, Va.). In: Institute of Environmental Sciences, Annual Technical Meeting, 21st. Anaheim, Calif., April 14-16, 1975, Proceedings. Volume 1.

Mount Prospect, III., Institute of Environmental Sciences, 1975, p. 64-72. 7 refs.

The present work surveys water quality user requirements and then determines the general characteristics of an orbiting imager (the Applications Explorer, or AE) dedicated to the measurement of water quality, which could be used as a low-cost means of testing advanced imager concepts and assessing the ability of imager techniques to meet the goals of a comprehensive water quality monitoring program. The proposed imager has four spectral bands, a spatial resolution of 25 meters, and swath width of 36 km with a pointing capability of 330 km. Silicon photodetector arrays, pointing systems, and several optical features are included. A nominal orbit of 500 km altitude at an inclination of 50 deg is recommended. P.T.H.

A75-36826 Recent advances in the application of data from NOAA operational environmental satellites to oceanography. E. P. McClain and A. E. Strong (NOAA, National Environmental Satellite Service, Washington, D.C.). In: American Society of Photogrammetry, Annual Meeting, 41st, Washington, D.C., March 9-14, 1975, Proceedings. Falls Church, Va., American Society of Photogrammetry, 1975, p. 577-587. 20 refs.

Data from the NOAA series of polar-orbiting satellites, particularly those from its Very High Resolution Radiometer (VHRR), are receiving rapidly increasing and more quantitative use both in oceanographic research and, recently, for operational marine purposes. The thermal infrared observations are being used to detect, map, measure, and monitor ocean and Great Lakes' thermal contrasts associated with currents, upwelling, and river outflow. The visibleband data have found their greatest use in the monitoring of sea ice features, motions and conditions. Visible-band data are also valuable for filtering clouds from infrared scenes and in some studies of ocean roughness.

A75-40607 * The U.S. SEASAT program. S. W. McCandless (NASA, Washington, D.C.) and T. W. Thompson (California Institute of Technology, Jet Propulsion Laboratory, Pasadena, Calif.). In: Technology today for tomorrow; Proceedings of the Twelfth Space Congress, Cocoa Beach, Fla., April 9-11, 1975. Cocoa Beach, Fla., Canaveral Council of Technical Societies, 1975, p.

3-1 to 3-8.

The SEASAT program is a space-based operational oceanographic measurement system, which will be capable of providing continuous, all-weather, world-wide, timely data on global ocean dynamics and other physical properties of practical importance to a wide community of governmental and private sector users. This paper describes user requirements, case studies of projected applications, the sensor systems employed, and testing programs. (Author)

A75-45776 * Satellite altimetry applied to marine geoid determination. C. D. Leitao and J. T. McGoogan (NASA, Wallops Flight Center, Wallops Island, Va.). International Astronautical Federation, International Astronautical Congress, 26th, Lisbon, Portugal, Sept. 21-27, 1975, Paper 75-122. 12 p. 8 refs.

The pioneering satellite radar altimeter aboard Skylab has provided a wealth of information about ocean surface topography for both the oceanographic and geodetic communities. This report describes typical satellite altimetry concepts and discusses the parameters measured, geometry utilized, and techniques employed to generate ocean geoid estimates. The standard deviation of the noise on the altitude measurements is shown to range from one to three meters when the altimeter antenna is nadir aligned. The altimeter is shown to sense short wavelength ocean surface features which are not included in present conventional global geoids. An estimate of a local geoid in the Atlantic, using only altimeter data, is presented. Finally, results demonstrate that the Skylab radar altimeter system capability is less than 10 meters RMS. (Author)

A76-10826 Application of synchronous meteorological satellite data to the study of time dependent sea surface temperature changes along the boundary of the Gulf Stream. R. Legeckis (NOAA, National Environmental Satellite Service, Washington, D.C.). Geophysical Research Letters, vol. 2, Oct. 1975, p. 435-438. 21 refs.

A76-15457 * Remote sensing applied to numerical modelling. S. Sengupta, S. S. Lee, T. N. Veziroglu (Miami, University, Coral Gables, Fla.), and R. Bland (NASA, Kennedy Space Center, Earth Resources Branch, Cape Canaveral, Fla.). In: Remote sensing: Energy-related studies; Proceedings of the Symposium, Miami, Fla., December 2-4, 1974. Washington, D.C., Hemisphere Publishing Corp.; New York, Halsted Press, 1975, p. 335-364-35 refs.

Progress and remaining difficulties in the construction of predictive mathematical models of large bodies of water as ecosystems are reviewed. Surface temperature is at present the only variable than can be measured accurately and reliably by remote sensing techniques, but satellite infrared data are of sufficient resolution for macro-scale modeling of oceans and large lakes, and airborne radiometers are useful in meso-scale analysis (of lakes, bays, and thermal plumes). Finite-element and finite-difference techniques applied to the solution of relevant coupled time-dependent nonlinear partial differential equations are compared, and the specific problem of the Biscayne Bay and environs ecosystem is tackled in a finite-differences treatment using the rigid-lid model and a rigid-line grid system.

A76-21797 Remote sensing of the dynamics of sea ice and water temperatures with the aid of satellites (Fernerkundung von Meereisdynamik und Wassertemperaturen mit Satelliten). H. Kaminski (Bochum, Sternwarte, Bochum, West Germany). Naturwissenschaften, vol. 62, 1975, p. 211-213. 20 refs. In German.

Studies of the area distribution of sea water temperatures and the dynamics of sea ice are important in connection with investigations of the global energy balance and the determination of climatic fluctuations. Such studies can also contribute to the safety of navigation and the efficiency of fishing operations. The conduction of such studies is discussed, taking into account the results of the study and the employed technique.

G.R.

A76-31479 Application of radar and microwave scattering to ocean wave research. J. W. Wright (U.S. Navy, Naval Research Laboratory, Washington, D.C.). In: Technology for the new horizon; Proceedings of the Thirteenth Space Congress, Cocoa Beach, Fla., April 7-9, 1976. Cocoa Beach, Fla., Canaveral Council of Technical Societies, 1976, p. 3-1 to 3-5. 13 refs.

The use of the Bragg and two-scale scattering of radar to measure the structure and properties of ocean waves is discussed. In the case of first-order Bragg scattering, the scattered electromagnetic field is proportional to the surface displacement. Thus the influence of all waves outside a narrow window at the Bragg resonance is strongly filtered out. This makes possible the measurement of such wave properties as temporal growth and approach in wind-wave tanks and spectral energy transfer in wave tanks or at sea. Moreover, the Doppler shift is the frequency of the Bragg wave in first order scattering, which means that phase velocities may be used to measure surface currents and to probe the profile of the mean flow on both sides of the air-water interface. In the case of two-scale scattering, the smaller scale scatterers are advected about by the orbital motions of the large wave, distinct Doppler splittings are obliterated and the width of the Doppler spectrum is about the rms orbital speed of the wave system. B.J.

A76-34934 * The nature of multiple solutions for surface wind speed over the oceans from scatterometer measurements. J. C. Price (NASA, Goddard Space Flight Center, Atmospheric and Hydrospheric Applications Div., Greenbelt, Md.). Remote Sensing of Environment, vol. 5, no. 1, 1976, p. 47-54.

The satellite SEASAT-A will carry a radar scatterometer in order to measure microwave backscatter from the sea surface. From pairs

of radar measurements at angles separated by 90 deg in azimuth the surface wind speed and direction may be inferred, though not uniquely. In this paper the character of the solutions for wind speed and direction is displayed, as well as the nature of the ambiguities of these solutions. An economical procedure for handling such data is described, plus a criterion for the need for conventional (surface) data in order to resolve the ambiguities of solutions. (Author)

A76-36209 # The relation between the thermal radio-frequency radiation of the sea surface and ice conditions according to data from Kosmos-384 (O sviazi teplovogo radioizlucheniia poverkhnosti okeana s ledovymi usloviiami po dannym ISZ 'Kosmos-384'). K. P. Vasil'ev and D. T. Matveev. In: Sea hydrological forecasts and information (Morskie gidrologicheskie prognozy i informatsii). Leningrad, Gidrometeoizdat (Gidrometeorologicheskii Nauchno-Issledovatel'skii Tsentr, Trudy, No. 119), 1975, p. 28-39. 17 refs. In Russian.

The radiation characteristics of sea ice, and the effect of snow cover on these characteristics, are discussed. Radiometric data in the sea surface in the Antarctic region, taken by Kosmos-384, are analyzed in conjunction with observations of the ice conditions in the area. It is shown that reliable information on ice conditions in polar regions can be obtained under virtually all weather conditions from satellite measurements of brightness temperature. Good agreement between the ice conditions determined from Kosmos-384 radiometric data and those revealed by television photographs taken by Meteor-10 was found in areas with no cloud cover. C.K.D.

A77-20363 California Current eddy formation - Ship, air, and satellite results. R. L. Bernstein (California, University, La Jolla, Calif.), L. Breaker (NOAA, National Environmental Satellite Service, Redwood City, Calif.), and R. Whritner (U.S. Naval Weather Service, North Island Naval Air Station, San Diego, Calif.). Science, vol. 195, Jan. 28, 1977, p. 353-359. 9 refs. NSF Grant No. OCE-75-23361; Contract No. N00014-75-C-0260.

A review of historical background on the mean flow and mesoscale variations in the California Current indicates that until recently quantitative measurements of the circulation of the California Current were limited to hydrographic determinations of temperature and salinity. The advent of satellite-borne infrared scanners of sufficient sensitivity has made it possible to obtain high-quality imagery of sea-surface temperature gradients for evaluation of meanders and eddies embedded in the California Current. Satellite scanner systems can locate major ocean frontal boundaries if they are associated with even quite weak horizontal sea-surface temperature gradients. It is shown that the California Current is an unstable flow, continuously developing meanders with wavelengths of several hundred kilometers, which can intensify over several months and go to cutoff, creating isolated eddies. Numerous topograhic maps and survey photographs supplement the text. S.D.

N75-72339# Naval Ship Research and Development Center, Annapolis, Md

DISPERSION OF SANITARY WASTEWATER DISCHARGES FROM NAVY SHIPS

Craig S. Alig Aug. 1974 153 p refs (Contract SF53554706)

(AD-785227; NSRDC-4194) Avail: NTIS

Assessing the impact of Navy Shipboard Sanitary Waste Discharges within the contiguous zone of the United States requires generation of data on the dispersion and fate of pollutants from shipboard sources. To generate data applicable for the 3 to 12-mile coastal zone, studies were conducted in the Norfolk. Va. area, and San Clemente Island, California. Controlled releases were made of sanitary waste water and tracer dye mixtures.

Author

N77-75886# Informatics, Inc., Rockville, Md.
BIBLIOGRAPHY OF SOVIET MATERIAL ON INTERNAL
WAVES Technical Report, May - Aug. 1976
Stuart G. Hibben, L. H. Boylan, and M. Ness 1 Sep. 1976

(Contracts MDA903-76-C-0254; MDA903-76-C-0099; DARPA Order 3097).

(AD-A029787; Rept-7) Avail: NTIS

This is the seventh bibliography of Soviet open-source publications related to internal wave studies. It covers material received from May 1976 through August 1976. Main selection criteria are studies of small-scale variation in ocean parameters and of airborne techniques for deducing internal wave conditions. An index of serial source abreviations is appended.

77-02001 # Environmental Research Inst. of Michigan, Ann Arbor.

PROCEEDINGS OF THE 9TH INTERNATIONAL SYMPOS-IUM ON REMOTE SENSING Final Report, 15-19 Apr. 1974

Jerald J. Cook Apr. 1974 566 p Symp. held at Michigan, 15-19 Apr., 1974 Vol. 3

(Contract AF-AFOSR-7222-74; AF Proj. 9751)

(AD-A008469, AFOSR-75-0515TR-Vol-3) Avail: NTIS

A partial listing of topic areas includes: microwave hologram techniques for application to earth resources; the usefulness of imaging passive microwave systems for rural and urban terrain analysis, single flight stereo radar capabilities; electrically scanning microwave radiometers; measurement of sea surface currents using airborne Doppler radar and inertial navigation systems; a practical oil sensor; multispectral remote fluorimeter for detection of oil films; passive microwave sensing of oil slicks; oil slick detection by X band synthetic aperture radar; airborne oil pollution surveillance system; the remote Raman spectrometer as a viable instrument for remote sensing; optical data processing analysis of stream patterns exhibited on ERTS 1 imagery; remote sensing of rock type in the visible and near infrared; remote sensing to detect the toxic effects of metals on vegetation for mineral exploration; the use of space photos for detecting oil and gas fields; a summary of ERTS data applications in Alaska. Author

77-02002 # Delaware Univ., Newark.
RESEARCH IN THE COASTAL AND OCEANIC ENVIRONMENT Final Report, 1 Sep. 1969 - 31 Aug. 1975
William S. Gaither and C. Y. Yang Jan. 1977 19 p
(Contracts N00014-69-A-0407; N00014-75-C-0876)
(AD-A035824) Avail: NTIS

(AD-A035824) Avail: NTIS

An interdisciplinary investigation under the program Research in the Coastal and Oceanic Environment for the period September 1969 to August 1975 is considered. A wide spectrum of topics including studies of energy exchange, sedimentary processes, vegetative growth, properties of marine soils and sediments, wave energy concentration, dissipation of waves in shore areas, wave breaking characteristics, wave defense devices, methods of predicting wave height and direction, tides, winds and storm surges, dynamic geological models, remote sensing techniques for wave reconnaissance mechanics of sediment movement, and biogeochemistry of marsh gases are discussed. The research program was reoriented, beginning in 1972, toward developing predictive tools tailored to the Navy's needs.

Author

03 BACKGROUND

N74-15038*# City Coll. of the City of New York Univ. Inst. of Oceanography.

A JOINT METEOROLOGICAL, OCEANOGRAPHIC AND SENSOR EVALUATION PROGRAM FOR EXPERIMENT S193 ON SKYLAB Monthly Plans and Progress Report, period ending 14 Jan. 1974

Willard J. Pierson, R. K. Moore, and E. P. McClain, Principal Investigators 14 Jan 1974 3 p. EREP (Contract NAS9-13642)

(E74-10233; NASA-CR-136496) Avail. NTIS HC \$3.00 CSCL 14B

N74-30663*# Kansas Univ. Center for Research, Inc., Lawrence Remote Sensing Lab.

PRELIMINARY S-193 RADSCAT OCEANOGRAPHIC DATA FOR SKYLAB 2

Willard J. Pierson, Jr., Richard K. Moore, Principal Investigators, Arun Sobti, and James Young Feb. 1974 31 p. refs. EREP (Contract NAS9-13642)

(E74-10525; NASA-CR-138274; CRES-TM-254-3) Avail NTIS HC \$4.75 CSCL 08C

N74-34772*# Virginia Inst. of Marine Science, Gloucester Point APPLICATION OF REMOTE SENSING TO STUDY NEAR-SHORE CIRCULATION Annual Report for Year 2

John Zeigler, Robert Lobecker, Donald Stauble, Christopher Welch Larry Haas, and C. S. Fang. Sep. 1974. 96 p. refs. (Grant NGL-47-022-005)

(NASA-CR-140189) Avail NTIS HC \$8.00 CSCL 80C

The research to use remote sensing techniques for studying the continental shelf is reported. The studies reported include (1) nearshore circulation in the vincinity of a natural tidal inlet; (2) identification of indicators of biological activity; (3) remote navigation system for tracking free drifting buoys; (4) experimental design of an estuaring tidal circulation; and (5) Skylab support work.

N74-34854# Environmental Research Inst. of Michigan, Ann Arbor

BASIC INVESTIGATIONS FOR REMOTE SENSING OF COASTAL AREAS Quarterly Report, 15 Apr. - 15 Jul. 1974

Robert K. Vincent 26 Jul. 1974 6 p

(Contract N00014-74-C-2073, NR Proj. 389-166) (AD-783710, ERIM-108900-1-L) Avail NTIS CSCL 08/6

task 2 has just begun, with nothing reportable as yet.

The purpose of this contract is to investigate remote sensing methods for monitoring coastal areas. The effort is divided into three tasks, involving research on. Compositional mapping of beaches and river systems, multispectral radar imaging for coastal mapping, and enhancement of ocean bottom features with passive multispectral scanners. During the first quarter, significant progress was made on tasks 1 and 3, but work on

N75-12172*# National Aeronautics and Space Administration. Langley Research Center, Langley Station, Va.

A SIMULATION OF SYNTHETIC APERTURE RADAR IMAGING OF OCEAN WAVES Calvin T. Swift 29 Oct. 1974 14 p Presented at the 1974

Calvin T. Swift 29 Oct. 1974 14 p Presented at the 1974 USNC/URSI Meeting, Boulder, Colorado, 14-17 Oct. 1974 (NASA-TM-X-72629) Avail: NTIS HC \$3.25 CSCL 17I

A simulation of radar imaging of ocean waves with synthetic aperture techniques is presented. The modelling is simplistic from the oceanographic and electromagnetic viewpoint in order to minimize the computational problems, yet reveal some of the physical problems associated with the imaging of moving ocean waves. The model assumes: (1) The radar illuminates a one-dimensional, one harmonic ocean wave. (2) The scattering is assumed to be governed by geometrical optics. (3) The radar is assumed to be down-looking, with Doppler processing (range processing is suppressed due to the one-dimensional nature of the problem). (4) The beamwidth of the antenna (or integration time) is assumed to be sufficiently narrow to restrict the specular points of the peaks and troughs of the wave. The results show that conventional processing of the image gives familiar results if the ocean waves are stationary. When the ocean wave dispersion relationship is satisfied, the image is smeared due to the motion of the specular points over the integration time. In effect, the image of the ocean is transferred to the near field of the synthetic aperture.

N75-12396*# National Oceanic and Atmospheric Administration.

AN ASSESSMENT OF THE POTENTIAL CONTRIBUTIONS TO OCEANOGRAPHY FROM SKYLAB VISUAL OBSERVATIONS AND HAND-HELD PHOTOGRAPHY Monthly Progress Report. Aug. 1974

Report, Aug. 1974 George A. Maul, Principal Investigator and Michael McCaslin Aug. 1974 18 p EREP

(NASA Order T-4713-B)

(E75-10017; NASA-CR-140731) Avail: NTIS HC \$3.25 CSCL 08.J

N75-13371*# National Aeronautics and Space Administration Lyndon B. Johnson Space Center, Houston, Tex.

THE ERTS-1 INVESTIGATION (ER-600). VOLUME 2: ERTS-1 COASTAL/ESTUARINE ANALYSIS Report for period Jul. 1972 - Jun. 1973

R. Bryan Erb Jul. 1974 286 p refs Original contains color illustrations

(NASA-TM-X-58118; JSC-08457) Avail NTIS HC \$8.75 CSCL 08J

The Coastal Analysis Team of the Johnson Space Center conducted a 1-year investigation of ERTS-1 MSS data to determine its usefulness in coastal zone management Galveston Bay, Texas, was the study area for evaluating both conventional image interpretation and computer-aided techniques. There was limited success in detecting, identifying and measuring areal extent of water bodies, turbidity zones, phytoplankton blooms, salt marshes, grasslands, swamps, and low wetlands using image interpretation techniques. Computer-aided techniques were generally successful in identifying these features. Aerial measurement of salt marshes accuracies ranged from 89 to 99 percent Overall classification accuracy of all study sites was 89 percent for Level 1 and 75 percent for Level 2.

N76-10586# Aerojet Electrosystems Co., Azusa, Calif.
DEVELOPMENT OF A PROTOTYPE AIRBORNE OIL
SURVEILLANCE SYSTEM Final Report

A. T. Edgerton, J. J. Bommarito, R. S. Scwantje, and D. C. Meeks May 1975 325 p. refs (Contract DOT-CT-22170-A)

(AD-A011275, AESC-1812FR-1, USCG-D-90-75) Avail: NTIS CSCL 13/2

A prototype airborne oil surveillance system was developed for the U.S. Coast Guard by Aerojet ElectroSystems Company. The multisensor system permits real-time day/night, all-weather detection, mapping and documentation of oil spills at sea. The system was installed aboard a Coast Guard HU-16 Albatross and flight tested off the California Coast. Surveillance data were

obtained from natural seeps, a series of controlled oil spills. routine shipping and targets of opportunity. The airborne system consists of a sidelooking radar, a passive microwave imager, a multispectral low light level TV, a multichannel line scanner, a position reference system, and a real-time processor/display console. The system reliably detected and mapped oil spills and seeps for conditions ranging from dense undercast to clear, wind speeds from 0 to 26 knots and daytime to total darkness. Test results demonstrate that airborne oil surveillance is practical and the system can be invaluable to other Coast Guard missions Color illustrations reproduced in black and white.

N76-11506* Coastal Engineering Research Center, Fort Belvoir,

EXPECTED SCIENTIFIC YIELD OF SEASAT-A AND ITS APPLICATION TO CORPS OF ENGINEERS PROGRAMS

P. G. Teleki In NASA, Washington Seasat-A Sci. Contrib. Jul. 1974 p 129-133 CSCL 05B

The Corps of Engineers interest in SEASAT-A is a natural outgrowth of its mission to protect and manage the Nation's shorelines. In regard to the expected payload on SEASAT-A the following general study areas can be identified: gravity waves, wind waves, wind-wave interaction, storms and hurricanes, ice, coastal currents, tsunamis, and to a very small extent geoid modelling as it applies to determination of sea level and tides.

N76-11514 Joint Publications Research Service, Arlington, Va FUTURE POSSIBILITY OF INVESTIGATING THE OCEAN

USING ARTIFICIAL SATELLITES
K. N. Fedorov and V. Ye. Sklyarov In its Exploration of Earth Resources by Space Methods (JPRS-65858) 6 Oct. 1975 p 36-48 refs Transl. into ENGLISH from Issled. Zemnykh Resursov Kosmich. Sredstvami (Moscow), no. 2, 1975 13 p

The temperature field and level changes of the ocean surface were measured by remote sensors onboard artificial satellites. Radars and lasers were found promising for measuring waves. Ice cover, coastal zones, ocean bottom, and buoys are also being studied by satellite sensors.

N76-11817* National Aeronautics and Space Administration. Lyndon B. Johnson Space Center, Houston, Tex.
ACTIVE MICROWAVE REMOTE SENSING OF OCEANS,

CHAPTER 3

In its Active Microwave Workshop Report 1975 p 157-162

CSCL 08.1

A rationale is developed for the use of active microwave sensing in future aerospace applications programs for the remote sensing of the world's oceans, lakes, and polar regions. Summaries pertaining to applications, local phenomena, and large-scale phenomena are given along with a discussion of orbital errors.

Author

Author

N76-11818* National Aeronautics and Space Administration. Lyndon B. Johnson Space Center, Houston, Tex

TECHNICAL BACKGROUND, CHAPTER 3, PART B In its Active Microwave Workshop Report 1975 p 162-181

A description is given of the physics of electromagnetic scattering from the sea and a guideline is presented to relate an observable (such as the radar cross section) to the hydrodynamics or physical properties of the sea. As specific examples of the interdisciplinary science of electromagnetics and geophysical oceanography, the physics is discussed in connection with data provided by three instruments: namely, the scatterometer, the altimeter, and the imaging radar. The data provided by each instrument are discussed in context with specular point and Bragq scattering theories. Finally, the degrading effect of extraneous sources of noise is discussed as a limiting mechanism of the accuracy of the ocean surface measurement. Author

N76-11820* National Aeronautics and Space Administration Lyndon B. Johnson Space Center, Houston, Tex

LARGE-SCALE PHENOMENA, CHAPTER 3, PART D

In its Active Microwave Workshop Report 1975 p 192-220

CSCL 08J

Oceanic phenomena with horizontal scales from approximately 100 km up to the widths of the oceans themselves are examined Data include: shape of geoid, quasi-stationary anomalies due to spatial variations in sea density and steady current systems, and the time dependent variations due to tidal and meteorological forces and to varying currents.

N76-13714# Army Engineer Waterways Experiment Station, Vicksburg, Miss. Hydraulics Lab.
CATALOG OF TIDAL INLET AERIAL PHOTOGRAPHY Final

Report

John H. Barwis Jun. 1975 180 p ref (AD-A012798; AEWES-GITI-75-2) Avail: NTIS CSCL 08/6

Data on approximately 6000 aerial photographic coverages of tidal inlets are presented in tabular form, along with information on how any given photograph may be obtained. The compilation covers inlets along the Atlantic, Gulf, and Pacific coasts of the contiguous U.S. coastline from 1938 to 1974, and includes the following information: (1) Inlet name: (2) Geographic coordinates: (3) National Ocean Survey navigation chart covering inlet; (4) Georef grid square; (5) Month and year of photography; (6) Federal, state, or commercial agency holding film; (7) Project number; (8) Pertinent exposure numbers; (9) Scale, and (10) Film type. Information is also given on sources of additional photography, and on obtaining photography of beach areas between any two inlets. An index, by Corps of Engineer District, Author (GRA) is given

N76-15321# Mar. Inc., Rockville, Md. A CONCEPTUAL STUDY OF THE FACTORS INVOLVED IN INSTALLATION, OPERATION, AND RECOVERY OF MOORS WITH ATTACHED BOTTOM-MOUNTED SENSORS Final

Shelton M. Gav. Jr. Jul. 1975 98 p refs (Contract N00014-74-C-0310; NR Proj. 294-032)

(AD-A013603; MAI-05-75-001) Avail: NTIS CSCL 13/10

A conceptual study is reported of potential failure mechanisms associated with installation, operation and recovery of deep-sea buoy moors with attached bottom-mounted sensors. The study is directed to the 'anchor-last' mode of installation. The effects considered include, among others, initial launch geometry, stability characteristics of the components (including torsional characteristics of the cables, both internally and externally generated), relation of the outlying instrument leads to the mooring riser, spin-stability of objects suspended by multiple lines and hydrodynamic effects such as strum and component rotation. The length of the instrument leads in relation to the depth is identified as an important parameter. The utility of modeling and the status of algorithms useful in the design of deep-sea mooring installations are discussed. A general installation procedure is suggested.

N76-21862# Draper (Charles Stark) Lab., Inc., Cambridge, Mass FINAL REPORT Final Report, 1 Sep. 1973 - 30 Sep. 1975 John M. Dahlen. Nov. 1975. 15 p. refs. (Contract N00014-74-C-0163; NR Proj. 083-318) (AD-A018076; C-4552). Avail. NTIS. CSCL 08/3

This letter report summarizes the work performed by CSDL and refers to technical reports, papers, and journal articles for detailed documentation. Instrumentation development for internal wave investigation and ocean deployments in direct engineering support of M.I.T. ocean science programs are described. This work entails active field programs with two advanced arrays making fundamental measurements of internal waves and microstructure in the open ocean -- the Microscale Sensing Array (MSA) and the Intermediate Internal Wave Array (IIWA). These systems were designed to complement earlier ONR-sponsored arrays. Bermuda Buoy (1970-71) and Ocean Telescope (1967-69). Theoretical and experimental investigation of techniques required for optimum interpretation of oceanographic measurements obtained from moored buoy systems are also described. This work has focused upon the basic dynamic measurement problems encountered in the above-mentioned M.I.T. program and in WHOI moored array experiments

MEASUREMENT OF WATER SURFACE INFRARED RADIA TION TEMPERATURE ALONG THE ITALIAN ADRIATIC COAST USING VHRR SATELLITE DATA MESSUNG DER INFRAROTSTRAHLUNGSTEMPERATUR DER SEROBERFLAECHE IM KUESTENVERLAUF DER ITALIE NISCHEN ADRIA MITTELS VHRR SATELLITENDATEN]
Heinz Kaminski Mar. 1975 16 p. refs. In GERMAN, ENGLISH

summary Presented at the 22nd Rass. Intern. Elettronica Nucl. ed Aerospaziale, Rome, Mar. 1975

Avail NTIS HC \$3 50

A zone with a distinct temperature gradient in the area of the Italian Adriatic coast was found from the data of the environmental earth research satellites NOAA 2, 3, and 4. This coastal zone obviously depends on the submarine topography difference in density of the water masses, constant wind streams influence of the tides, and inflows from the Alps and the Apennines. The zone can be monitored permanently the whole year long and it shows distinct maximum in the winter half-year. Therefore the mixing with the free Adriatic water is obviously very much limited, so that load factors resulting from industrial sites and urbanizations are to be taken into consideration concerning their quantity for this small constant transport zone in the coastal area in immediate front of the Italian Adriatic. The results of environmental earth research satellites make it possible to carry out large area plannings and large area supervisions. The present result is part of a voluminous study describing the supervision of the European waters and the atmosphere. The overlapping study is in the hands of the European Council

N76-28628*# National Aeronautics and Space Administration Goddard Space Flight Center, Greenbelt, Md

HYDROGRAPHIC CHARTING FROM LANDSAT SATELLITE A COMPARISON WITH AIRCRAFT IMAGERY

Elizabeth M. Middleton (Computer Sciences Corp., Silver Spring Md) and John L. Barker. May 1976. 10 p. refs. Proposed for Presentation at Ocean 76 Conf., Washington, D. C., 14-16 Sept.

(NASA-TM-X-71146 X-923-76-111) Avail NTIS HC \$3.50 CSCL 08H

The relative capabilities of two remote-sensing systems in measuring depth and, consequently, bottom contours in sandy-bottomed and sediment-laden coastal waters were determined quantitatively. The multispectral scanner (MSS), orbited on the LANDSAT-2 Satellite, and the ocean color scanner (OCS), flown on U-2 aircraft, were used. Analysis of imagery taken simultaneously indicates a potential for hydrographic charting of marine coastal and shallow shelf areas, even when water turbidity is a factor. Several of the eight optical channels examined on the OCS were found to be sensitive to depth or depth-related information. The greatest sensitivity was in OCS-4(0.544 \pm or

0.012 microns) from which contours corresponding to depths up to 12m were determined. The sharpness of these contours and their spatial stability through time suggests that upwelling radiance is a measure of bottom reflectance and not of water turbidity. The two visible channels on LANDSAT's MSS were less sensitive in the discrimination of contours, with depths up to 8m in the high-gain mode (3x) determined in MSS-4(0.5 to 0.6 microns) Author

N76-31879# Informatics, Inc., Rockville, Md.

SOVIET MATERIAL ON INTERNAL WAVE EFFECTS, NUMBER 5. MARCH 1976

Stuart G. Hibben, John Kourilo, B. L. Shresta, and M. Ness 15 Mar. 1976 100 p refs (Contract MDA903-76-C-0099; DARPA Order 3097)

(AD-A022472) Avail NTIS CSCL 08/3

This collection of abstracts on generation and detection of internal waves is based on items listed in the fifth Bibliography of Soviet Material on Internal Waves, published 10 Nov 1975 which covers material received June-Oct 1975. The abstracts are divided into internal effects and surface effects, comprising active and passive measurement of wave states. An author index is appended

N77-10630# Inter-American Tropical Tuna Commission, La Jolla.

COMPUTER PROCESSING OF LANDSAT-1 MSS DIGITAL IMAGERY FOR MARINE STUDIES

Robert G. Kirkham, Merritt R. Stevenson, and Forrest R. Miller Feb. 1976 77 p refs

(Grant NOAA-04-6-158-44043)

(PB-254655/4; NOAA-760 HC A05/MF A01 CSCL 08J NOAA 76042901)

A procedure in which a series of 15 computer programs was developed to process data from the 4 spectral bands of multispectral scanner systems aboard LANDSAT-1 for the central part of the Gulf of California are described. Methods to specifically produce digital auxiliary tapes of full scenes from the EROS Computer Compatible Tapes (CCT's) and from these tapes to construct digital images using a high speed line printer are discussed. Comparison of prominent surface features in the gulf with computer generated benchmarks showed the gridding program to be quite accurate in generating geographical benchmarks for the full scene imagery

N77-15604# National Environmental Satellite Service, Washing-

SATELLITE DERIVED SEA SURFACE TEMPERATURES FROM NOAA SPACECRAFT

Robert L Brower, Hilda S Gohrband, William G Pichel, T L Signore, and Charles C Walton Jun. 1976 84 p refs (PB-258026/4: NOAA-TM-NESS-78: NOAA-76062401) Avail NTIS HC A05/MF A01 CSCL 08J

Sea surface temperature values were derived from scanning radiometer infrared data from the NOAA series of polar orbiting satellites. The technique used to obtain these temperatures was the fully automated computer procedure, GOSSTCOMP (Global Operational Sea Surface Temperature Computation). Surface temperature retrievals were derived by statistical analysis and quality control techniques applied to instrument measurements covering roughly 100-km square areas. Retrieval temperatures were corrected for the effects of atmospheric attenuation by using time-coincident measurements derived from a vertical temperature profile radiometer. The basic product obtained was a daily set of 5,000 to 7,000 observations of sea surface temperature over the oceans of both hemispheres.

N77-23587# Environmental Research Inst. of Michigan, Ann.

BASIC INVESTIGATIONS FOR REMOTE SENSING OF COASTAL AREAS Quarterly Report, 16 Jul. - 15 Oct.

R. A. Shuchman, D. R. Lyzenga, and F. J. Thomson. 1976. 6 p refs

(Contract N00014-74-C-0273)

AD-A032447 ERIM-108900-8-L) Avail HC A01/MF A01 CSCL 17/8

During the quarterly period 16 July - 15 October 1976, three principle activities took place. The second year interim report was printed and distributed. Work was completed on obtaining critical optical properties of beach minerals to be used as inputs into the Beach and Environment Models. In the water modeling area, the water-atmosphere model was tested and used in a study for the Naval Coastal Systems Lab., and analysis of model results in the context of MRA development has begun In connection with this task, a letter was sent to the Editor of Applied Optics on the reflectance of a flat ocean in the limit of zero water depth

A74-37395 * Microwave radiometer measurements of the Cape Cod Canal. C. T. Swift (NASA, Langley Research Center, Hampton, Va.). Radio Science, vol. 9, July 1974, p. 641-653. 12 refs.

Microwave radiometer measurements were conducted from a railroad bridge which spans the Cape Cod Canal in Massachusetts. Data were collected as a function of viewing angle and polarization at frequencies of 1.4, 4.0, and 7.5 GHz. The results compare differences in the microwave emmissivity of a smooth vs rough water surface. Results are also given which show the effects of roughness on the bistatic scattering of sunlight.

A75-17208 # Multi-frequency radiometric measurements of foam and a mono-molecular slick. B. Au, J. Kenney, L. U. Martin (U.S. Navy, Naval Research Laboratory, Washington, D.C.), and D. Ross (NOAA, Miami, Fla.). In: International Symposium on Remote Sensing of Environment, 9th, Ann Arbor, Mich., April 15-19, 1974, Proceedings. Volume 3. Ann Arbor, Mich., Environmental Research Institute of Michigan, 1974, p. 1763-1773.

Microwave radiometric measurements have been made of both a surf-zone and an ocean region where small-scale roughness was suppressed by an artificial monomolecular slick. The foam measurements show near identical foam temperatures at 8.35 and 14.5 GHz, but large variations at 1.4 GHz. The resultant maximum foam emissivities at nadir range from 0.57 at 1.4 GHz to 0.84 at 14.5 GHz. The presence of the monomolecular slick on the ocean surface had the same effect as a decrease in surface roughness. For horizontal polarization, the emission decreased below that of the surrounding ocean for all viewing angles. At vertical polarization, the emission decreased below and increased above a viewing angle of approximately 60 deg. (Author)

A75-22724 Computer enhancement of ERTS-1 images for ocean radiances. G. A. Maul, R. L. Charnell, and R. H. Qualset (NOAA, Physical Oceanography Laboratory, Miami, Fla.). *Remote Sensing of Environment*, vol. 3, no. 4, 1974, p. 237-252. 12 refs. NOAA-supported research.

Subtle contrasts and low radiances observed by the ERTS multispectral scanner over the ocean require computer enhancement for adequate analysis. Experiments designed to evaluate contrast stretching, ratioing, differencing, smoothing, filtering, and false-color enhancing, indicate that the best information can be extracted by simple contrast stretching. Spectral analysis of the data shows that a low-pass, two-dimensional filter kernel, designed to be 6 db down at 10 scanspots, effectively eliminates the six-line banding caused by the multispectral scanner design. Automatic contouring techniques require careful scrutiny because data fields are created which can lead to false interpretations. Joint histograms of oceanic radiances did not prove to be useful due to the low range of energy in the several spectral intervals. Comparisons of satellite data with surface ship observations confirm theoretical predictions of the difficulty in interpreting scenes of the coastal zone. (Author)

A75-27129 Numerical testing of an altimeter reduction method. W. E. Strange (Computer Sciences Corp., Falls Church, Va.). In: The use of artificial satellites for geodesy and geodynamics, Proceedings of the International Symposium, Athens, Greece, May 14-21, 1973. Athens, National Technical University of Athens, 1974, p. 801-811. 6 refs.

Tests are reported for a method of recovering improved gravity anomaly information in a local area of the ocean using altimeter-derived geoid height information in the local area. The tests were conducted to investigate the accuracy with which the gravity field can be recovered with altimeter data of 1 to 2 meter accuracy, the level of accuracy of the GEOS-C altimeter. Computation of detailed geoid heights from satellite data is outlined, and tests made with the GEM 4 satellite are described. It is shown that recovery of a more detailed gravity field than that provided by satellite gravity data is possible with the proposed method.

F.G.M.

A76-20334 * Ocean color spectra measured off the Oregon coast - Characteristic vectors. J. L. Mueller (NASA, Goddard Space Flight Center, Hydrology and Oceanography Branch, Greenbelt, Md.). Applied Optics, vol. 15, Feb. 1976, p. 394-402. 20 refs. Contract No. N62306-70-C-0414.

The ocean color spectrum is defined as the ratio of the spectrum of light upwelled from the sea to the spectrum of light incident on the sea surface. Ocean color spectra, observed from an airplane flown over waters off Oregon, are analyzed. The original spectra are resolved into fifty-five wavelength bands, each 5 nm wide. The shapes of these spectra are parameterized by, and shown to be accurately recoverable from, their first four principal components. These components are the scalar projections of each spectrum on the first four characteristic vectors of the sample covariance matrix.

Regression equations are found with which phytoplankton pigment concentration and water transparency may be estimated as linear functions of the principal components. Pigment concentration estimates thus obtained are imprecise. The poor fit is at least partly due to the inappropriateness of the linear regression model and the neglect of other optically important substances typically present in sea water.

(Author)

A76-28079 * Application of remote sensing to thermal pollution analysis. H. W. Hiser, S. S. Lee, T. N. Veziroglu, and S. Sengupta (Miami, University, Coral Gables, Fla.). In: Remote sensing of earth resources. Volume 4 - Proceedings of the Fourth Annual Conference on Earth Resources, Tullahoma, Tenn., March 24-26, 1975.

Tullahoma, University of Tennessee, 1975, p. 481-497. 20 refs. Contract No. NAS10-8740.

A comprehensive numerical model development program for near-field thermal plume discharge and far field general circulation in coastal regions is being carried on at the University of Miami Clean Energy Research Institute. The objective of the program is to develop a generalized, three-dimensional, predictive model for thermal pollution studies. Two regions of specific application of the model are the power plants sites at the Biscayne Bay and Hutchinson Island area along the Florida coastline. Remote sensing from aircraft as well as satellites are used in parallel with in situ measurements to provide information needed for the development and verification of the mathematical model. This paper describes the efforts that have been made to identify problems and limitations of the presently available satellite data and to develop methods for enhancing and enlarging thermal infrared displays for mesoscale sea surface temperature measurements. (Author)

A76-28087 * Application of ERTS-1 and multiplexed SLAR imagery for the study of flooded shorelines. M. L. Bryan (Michigan, Environmental Research Institute, Ann Arbor, Mich.). In: Remote sensing of earth resources. Volume 4 - Proceedings of the Fourth Annual Conference on Earth Resources, Tullahoma, Tenn., March 24-26, 1975.
Tullahoma, University of Tennessee, 1975, p. 601-619. 7 refs. Contract No. NASS-21783. NASA Task 6.

The major purpose of this study is to determine the accuracy of visual interpretations of data from two different sensors (ERTS-1; ERIM's multiplexed SLAR) for the study of flooded shorelines. Uncomplicated and primarily visual interpretation techniques are employed. These methods are considered most readily available to officials of local and small regional organizations who may need rapid reconnaissance mapping and information for the organization of disaster relief. Assumptions concerning the timely receipt of such remotely sensed data by those directing the relief have been made. Generally, it is determined that ERTS-1 and SLAR data are complementary, especially with respect to the interpretation of urban or built-up areas which are flooded, and together they can provide the necessary information for guiding relief operations.

(Author)

A76-31482 The study of ocean circulation from space. G. A. Maul (NOAA, Atlantic Oceanographic and Meteorological Labora tories, Miami, Fla.). In: Technology for the new horizon. Proceedings of the Thirteenth Space Congress, Cocoa Beach, Fla., April 7-9.

Cocoa Beach, Fla., Canaveral Council of Technical Societies, 1976, p. 3-27 to 3-36. 21 refs.

Major ocean currents have surface manifestations that make them observable by spacecraft sensors. Under certain conditions, any one or a combination of the following may be used to identify the current's boundary: changes in sea surface temperature, salinity, color (diffuse), sea state (specular), sea surface topography, wave refraction patterns, and modifications to the lower atmosphere. Infrared sensors have been used most extensively to study ocean circulation; however, new instruments such as passive and active microwave sensors can sense temperature, salinity, sea state, and surface topography, and multispectral visible scanners and spectroradiometers are providing new information on ocean color and sea state. Man's role as an observer and photographer provides the highest spatial resolution to date for describing visible changes across boundaries as well as sea and swell patterns. (Author)

A76-32425 Extraction of oceanographic informations separately from atmospheric informations using space-multispectral imageries. K. Watanabe (Tokai University, Shimizu, Shizuoka, Japan). In: International Symposium on Space Technology and Science, 11th, Tokyo, Japan, June 30-July 4, 1975, Proceedings.

Tokyo, AGNE Publishing, Inc., 1975, p. 909-913.

An image-masking technique has been developed to separate areas of turbid water from cloud covers, smog layers, and sunglint in Landsat-1 multispectral imagery. Due to the attenuation of reflected light during transmission through a water layer, oceanographic information can be extracted by image subtraction of the pattern in the MSS-7 bandpass (0.8-1.1 microns) from the MSS-4 or MSS-5 (0.5-0.6 and 0.6-0.7 microns, respectively) patterns by an appropriate optical or digital process. Results obtained for Osaka Bay are discussed.

C.K.D.

A76-35002 # Utilization of remote sensing techniques for U.S. Coast Guard missions. G. F. Woolever, L. A. Kidd (U.S. Coast Guard, Washington, D.C.), J. P. Welsh, J. A. McIntosh, and L. D. Farmer (U.S. Coast Guard, Research and Development Center, Groton, Conn.). In: International Symposium on Remote Sensing of Environment, 10th, Ann Arbor, Mich., October 6-10, 1975, Proceedings. Volume 1. Ann Arbor, Mich., Environmental Research Institute of Michigan, 1975, p. 3-16. 8 refs.

The U.S. Coast Guard is implementing a variety of remote sensing techniques in the performance of several missions, such as for pollution surveillance, ice classification, iceberg detection and classification, vessel traffic system development, and search and rescue. Recent activities are briefly described, including examples of imagery and forecasts for future applications. (Author)

A76-35012 # Automated measurement of sea surface temperature from a geostationary environmental satellite. J. D. Tarpley and B. A. Raymond (NOAA, National Environmental Satellite Service, Suitland, Md.). In: International Symposium on Remote Sensing of Environment, 10th. Ann Arbor, Mich., October 6-10, 1975, Proceedings. Volume 1. Ann Arbor, Mich., Environmental Research Institute of Michigan, 1975, p. 139-148. 5 refs.

An automatic technique has been developed to measure sea surface temperature using 10 micron infrared data from a geostationary operational environmental satellite. Temperature derivatives are used to discriminate between cloudy and cloud free areas. Sea surface temperatures are retrieved at a resolution of 25 km and checked against a first guess field that is maintained and updated daily.

(Author)

A76-35017 # Addressing the remote sensing 'data-information gap' - Overhead monitoring in New York's St. Lawrence River-Eastern Lake Ontario coastal zone. T. M. Lillesand (New York, State University, Syracuse, N.Y.) and W. E. Tyson (St. Lawrence-Eastern Ontario Commission, Watertown, N.Y.). In: International Symposium on Remote Sensing of Environment, 10th, Ann Arbor, Mich., October 6-10, 1975, Proceedings. Volume 1.

Ann Arbor, Mich., Environmental Research Institute of Michigan, 1975, p. 189-201. 11 refs.

A76-35019 # Detection and analysis for water surface covered with oil film. M. Matsui, S. Tsutsumi (Kyoto Institute of Technology, Matsugasaki, Japan), and T. Takagi (Fukuyama University, Fukuyama, Hiroshima, Japan). In: International Symposium on Remote Sensing of Environment, 10th, Ann Arbor, Mich., October 6-10, 1975, Proceedings. Volume 1.

Ann Arbor, Mich., Environmental Research Institute of Michigan,

Ann Arbor, Mich., Environmental Research Institute of Michigan, 1975, p. 223-230.

The additive background radiation from all materials other than the targets to be detected presents a serious problem to the passive infrared sensors. This report describes both the scanning angle dependence of the spatial radiance distribution over the sea surface and the relationship of the sea surface radiance versus the thickness

of oil film by which the sea surface is covered uniformly, operating in the spectral region of 10 to 13 microns. (Author)

A76-35062 # Remote sensor for measurement of a tidal current velocity. S. Tsutsumi, Y. Itakura (Kyoto Institute of Technology, Matsugasaki, Japan), and T. Takagi (Fukuyama University, Fukuyama, Hiroshima, Japan). In: International Symposium on Remote Sensing of Environment, 10th, Ann Arbor, Mich., October 6-10, 1975, Proceedings. Volume 1.

Ann Arbor, Mich., Environmental Research Institute of Michigan, 1975, p. 637-646.

An amplitude-modulated reticle finds some applications to remote sensing of image-velocity. This type of sensor with a PbS detector was built to test the feasibility of measuring the temporal variation of a rapid tidal current velocity in the Inland Sea. Feasibility has been demonstrated and it should be possible to develop a system that could measure the instantaneous tidal current velocity. A modified system, which can make a simultaneous measurement of the magnitude and direction of the tidal current velocity, is proposed by the authors. (Author)

A76-35117 # Remote sensing as it applies to the International Ice Patrol. A. D. Super and S. R. Osmer (U.S. Coast Guard, Governors Island, N.Y.). In: International Symposium on Remote Sensing of Environment, 10th, Ann Arbor, Mich., October 6-10, 1975, Proceedings. Volume 2. Ann Arbor, Mich., Environmental Research Institute of Michigan, 1975, p. 1231-1234. 7 refs.

Poor success rates in detecting icebergs by surface radar lead to a continued need for effective monitoring of shipping corridors by the International Ice Patrol. Several remote sensing techniques have been investigated as possible means of improving the speed and accuracy of iceberg detection and tracking. A precision radiation thermometer is routinely used in airborne reconnaissance missions to map sea surface temperature for use in iceberg melt determinations and in detecting current patterns. ERTS-A imagery from Return Beam Vidicon bands in the 0.6 to 1.1 micrometers band was found to be minimally applicable to iceberg detection due to frequent fog cover, time delay in user receipt of data, insufficiently fine resolution, and insufficiently frequent coverage. A high degree of success in iceberg detection has been obtained using side-looking airborne radar data. Target discrimination is accomplished by analysis of basic clues, including size, shape, shadow, texture pattern, edge, wake, and tone.

A76-35124 Remote sensing techniques applied to the study of fresh water springs in coastal areas of Southern Italy. M. Guglielminetti, R. Boltri (IDROTECNECO S.p.A., Pesaro, Italy), and C. M. Marino (IDROTECNECO S.p.A., Pesaro; Milano, Università, Milan, Italy). In: International Symposium on Remote Sensing of Environment, 10th, Ann Arbor, Mich., October 6-10, 1975, Proceedings. Volume 2. Ann Arbor, Mich., Environmental Research Institute of Michigan, 1975, p. 1297-1309. 7 refs.

A76-38128 The application of Landsat-1 digital data to a study of coastal hydrography. R. P. Bukata, J. E. Bruton, J. H. Jerome, A. G. Bobba (Canada Centre for Inland Waters, Burlington, Ontario, Canada), and G. P. Harris (McMaster University, Hamilton, Ontario, Canada). In: Canadian Symposium on Remote Sensing, 3rd, Edmonton, Alberta, Canada, September 22-24, 1975, Proceedings. Ottawa, Canadian Aeronautics and Space Institute, 1976, p. 331-348. 6 refs.

Digital apparent-radiance data from the Landsat-1 spacecraft, collected along the coastline of Nottawasaga Bay in southern Georgian Bay, have been used to study the application of such data to coastal bathymetry. These data have been compared with existing hydrographic charts for areas which have been well-defined in terms of depth contours. The result is that the Band 4 (0.5-0.6 micron) MSS data clearly delineate the bottom contours in coastal regions for which the surface turbidity is substantially less than 1 FTU. Under such conditions of lake-water turbidity, the maximum optical

penetration defining the Band 4 response appears to be about 14 meters. The energy return from a relatively clear inland lake is discussed in terms of volumetric and bottom effects. Attempts are made at comparing the Landsat-1 digital data with 'in-situ' measurements of optical parameters. An iterative technique for estimating bottom reflectivity coefficients is also discussed.

Some uses of high resolution GOES imagery in the mesoscale forecasting of convection and its behavior. J. F. W. Purdom (NOAA, National Environmental Satellite Service, Washington, D.C.). In: Conference on Weather Forecasting and Analysis, 6th, Albany, N.Y., May 10-13, 1976, Preprints.

Boston, American Meteorological Society, 1976, p.

Phenomena of importance in the initiation of low level convergence which may eventuate in thunderstorms are scrutinized, with attention to features influencing the behavior of more mature thunderstorms, and utilizing GOES (Geostationary Operational Environmental Satellite) high-resolution imagery. Motion pictures constructed from GOES imagery are also utilized. Terrain-induced convective lines, convective cloud mergers, and convective line intersections are among the factors strongly influencing the initiation and sustenance of thunderstorms. Detailed discussion is presented of terrain effects due to land-water interfaces, convective area mergers and intersections, interactions of tornadic thunderstorms and other convective boundaries, and cloud mergers. Many mesoscale processes important in the initiation and maintenance of convection are readily evident in the satellite imagery without special enhancement. R.D.V.

The history of a holographic non-destructive test procedure. E. Archbold (Aeronautical Research Council, National Physical Laboratory, Teddington, Middx., England). In: The engineering uses of coherent optics; Proceedings of the Conference, Cambridge, Glasgow, Scotland, April 8-11, 1975. Cambridge University Press, 1976, p. 59-72.

Holographic interferometry is being used to non-destructively test light-weight laminated panels for areas of de-lamination. In cross-section the panels consist of two outer aluminum plates and a thinner middle plate separated by corrugated aluminium material, the layers being brazed together at the interfaces. The purpose of the test is to establish the completeness of the braze. The panels are stressed by increasing the internal pressure; a weak area due to a mis-braze bulges slightly and is revealed as a closed pattern of fringes on the holographic interferogram. From measurements of the diameter and maximum deflection of a bulge as revealed by the hologram, it is possible to deduce at which interface the mis-braze has occurred. The paper describes the development of the test procedure, through the feasibility studies to the establishment of equipment for testing a production series of panels.

N76-72184# Coastal Engineering Research Center, Fort Belvoir,

PHOTOGRAMMETRIC EXPERIMENTS ON NEARSHORE MIXING AND DIFFUSION

Paul G. Teleki and Dennis A. Prins Jul. 1974 18 p refs (AD-A014216; CERC-Reprint-9-74)

Aerial multispectral photography and fixed point metering were used to study coastal currents at two sites in California. The system combining current meters, low altitude photography and photodensitometric analysis of the suspended matter or tracer dyes is well suited to studying both advective and diffusive processes in the ocean. Experiments were carried out in the vicinity of marine structures to understand their influence on coastal circulation. Author

N77-71443# Coast Guard Research and Development Center,

DETERMINATION OF SMALL CRAFT LEEWAY Final

Report
G. L. Hufford and S. Broida Dec. 1974 41 p. refs (AD-A020977; CGR/DC-39/74) Avail: NTIS

Small craft leeway is determined as a function of the wind speed in the range of 5-20 knots to enable more precise forecasting of the leeway drift of a distressed surface vessel at sea. Leeway is calculated by measurement of the separation distance of the small craft from a dyed patch of surface water at sea, using time sequenced aerial photography. Leeway increases linearly with wind speed for small craft equipped with or without a sea anchor in the wide range studied. Leeway for small craft without sea anchor can be calculated mathematically. Results show that the small craft drifted off the downwind direction in about 80 percent of the experiments, and the drift angle is variable and difficult to predict.

N77-76160# Informatics, Inc., Rockville, Md.
SOVRAD: A DIGEST OF RECENT SOVIET R AND D
ARTICLES, VOLUME 2, NO. 6, 1976 Interim Report Stuart G. Hibben, Lee Boylan, and J. Kourilo Jun. 1976 19 p. refs (Contract MDA903-76-C-0254; DARPA Order 3097)

(AD A028838) Avail NTIS

This is a collection of brief abstracts on micellaneous topics from the current Soviet technical literature. The intent is to supply a quick look at items of possible interest, including topics not necessarily named in the DARPA interest profile, as a supplement to our reportage on specified topics. It is intented to publish this collection on a monthly basis, to continue to provide coverage of numerous aspects of Soviet R and D. Author

N77-77447# Informatics, Inc., Rockville, Md. SOVRaD: A DIGEST OF RECENT SOVIET R AND D SOVRaD: A DIGEST OF RECENT SOVIET R AND D ARTICLES, VOLUME 2, NO. 5, 1976
Stuart Hibben, Lee Boylan, and J. Kourilo May 1976 21 p

(Contract MDA903-76-C-0254; ARPA Order 3097) (AD-A027224) Avail: NTIS

This is a collection of brief abstracts on miscellaneous topics from the current technical literature. The intent is to supply a quick look at items of possible interest, including topics not necessarily named in the DARPA interest profile, as a supplement to our reportage on specified topics. Author

77-03001 # Louisiana State Univ., Baton Rouge. Coastal Studies Inst.

MEASUREMENT OF SWASH PROFILE AND ORBITAL MOTION ON THE BEACH Technical Report

Choule J. Sonu, Neal Pettigrew, and Rodney G. Fredericks 1974 21 p Publ. in Proc. of the Intern. Symp. on Ocean Wave Meas. and Anal., ASCE, New Orleans, 9-11 Sep. 1974 p 621-638 Prepared in cooperation with Tetra Tech, Inc., Pasadena, Calif (Contract N00014-69-A-0211-0003; NR Proj. 388-002) (AD-A002095; TR-175) Avail: NTIS

Capacitance wave wires and miniaturized ducted current meters were developed to measure swash profiles and internal velocities directly on the beach face. Both sensors exhibit linear response and are rugged enough to withstand field conditions Analysis of the data obtained from a linear array of these sensors along a very gentle beach profile is presented. Power spectrum variation in the upbeach direction reveals a low-pass filter effect of the beach along with an enhancement of power density in a infragravity frequency band. The difference between the swash cycle, i.e., the time a single wave takes to complete a return trip to the beach, and the incident wave period explains this latter effect, which may cause a higher wave run-up on a gentle beach than predicted from the incidence wave spectrum

77-03002 # Coastal Engineering Research Center, Fort Belvoir,

MEASUREMENT TECHNIQUES FOR COASTAL WAVES AND CURRENTS Miscellaneous Report P. G. Teleki, F. R. Musialowski, and D. A. Prins Nov. 1976

(AD-A033041: CERC-MR-76-11) Avail: NTIS

A towed oceanographic data acquisition system (TODAS) consisting of a towed platform (sea sled) with current meters and a wave gage was developed for collection of information on nearshore currents and waves. Data acquired by the sensors are telemetered to shore and digitally recorded. TODAS is used for real time evaluation of flow characteristics between shore and a depth of 9.14 meters (30 feet); this mobile battery operated system can be used at remote locations. The system was used principally in two experimental designs: monitoring the distribution of longshore currents in shore-normal profiles, and a combination of Eulerian-Lagranginan experiments where fixed point metering is supported by aerial photography of diffusing dye plumes and concentration measurements of the dye tracers.

	REPORT DOCU	JMENTATION PAG	GE	
1. Recipient's Reference	2. Originator's Reference	3. Further Reference		4. Security Classification of Document
	AGARD-LS-88 Final version	ISBN 92-835-0	202-7	UNCLASSIFIED
N	dvisory Group for Aero lorth Atlantic Treaty O rue Ancelle, 92200 Ne	rganization		ent
	PPLICATIONS OF RE		го	
	October 1977 in Oslo, N 12 October 1977 in Ro	• •	er in Den H	lelder, Netherlands
8. Author(s)				9. Date
	Various			September 1977
10. Author's Address				11.Pages
		Various		270
12. Distribution Statement	This document is dipolicies and regulat Outside Back Cover	ions, which are out	lined on the	
13. Keywords/Descriptors				
Ocean surveillance	Surface ship	detection	Oceanograp	phic intelligence
Remote sensing	Marine biolog			
Target acquisition	Surface temp	perature		
14. Abstract				

The sea covers more than three quarters of the earth and the concealment it provides to military forces will make it the area of major activities in the next decade. The defence of land and sea is vital to the NATO alliance. Land surveillance has been covered in several AGARD meetings while the oceans thus far have received little attention. Techniques for ocean surveillance from satellites and aircraft reached a high degree of sophistication as the result of the combined efforts in space and military programs. The limitations of these techniques come not so much from technology itself but rather from the propagation medium, air and sea. These techniques and the interpretation of results are totally different for land and sea.

This lecture series therefore presents the mathematical tools and their applications to the problems of resolving, recognizing and identifying targets and sources of activities in the ocean. This series should be of interest to physicists and engineers who want to learn the mathematical methods applicable to ocean surveillance, to military users who want to interpret results and infer tactical and strategic implications and to industries interested in developing future, generation hardware.

The lecture topics cover two broad categories of surveillance:

- Ocean targets, for instance ships (Imaging):
- Ocean phenomena indicative of military activities, for instance changes in biology or surface temperatures.

AGARD Lecture Series No.88 (Final version) Advisory Group for Aerospace Research and	AGARD-LS-88	AGARD Lecture Series No.88 (Final version) Advisory Group for Aerospace Research and	AGARD-LS-88
Development, NATO APPLICATIONS OF REMOTE SENSING TO OCEAN SURVEILLANCE Published September 1977 270 pages including Bibliography of 194 items	Ocean surveillance Remote sensing Target acquisition Surface ship detection	Development, NATO APPLICATIONS OF REMOTE SENSING TO OCEAN SURVEILLANCE Published September 1977 270 pages inleluding Bibliography of 194 items	Ocean surveillance Remote sensing Target acquisition Surface ship detection
The sea covers more than three quarters of the earth and the concealment it provides to military forces will make it the area of major activities in the next decade. The defence of land and sea is vital to the NATO alliance. Land surveillance has been covered in several AGARD meetings while the oceans thus far have received little attention. Techniques for ocean surveillance from satellites and aircraft reached a high degree of sophistication as the result of the combined efforts.	Marine biology Surface temperature Oceanographic intelligence	The sea covers more than three quarters of the earth and the concealment it provides to military forces will make it the area of major activities in the next decade. The defence of land and sea is vital to the NATO alliance. Land surveillance has been covered in several AGARD meetings while the oceans thus far have received little attention. Techniques for ocean surveil-lance from satellites and aircraft reached a high degree of sophistication as the result of the combined efforts	Marine biology Surface temperature Oceanographic intelligence
ecture Series No.88 (Final ver	AGARD-LS-88	o.88 (Final version)	AGARD-LS-88
Advisory Group for Aerospace Research and Development, NATO APPLICATIONS OF REMOTE SENSING TO OCEAN SURVEILLANCE Published September 1977 270 pages including Bibliography of 194 items	Ocean surveillance Remote sensing Target acquisition Surface ship detection	Advisory Group for Aerospace Research and Development, NATO APPLICATIONS OF REMOTE SENSING TO OCEAN SURVEILLANCE Published September 1977 270 pages including Bibliography of 194 items	Ocean surveillance Remote sensing Target acquisition Surface ship detection
The sea covers more than three quarters of the earth and the concealment it provides to military forces will make it the area of major activities in the next decade. The defence of land and sea is vital to the NATO alliance. Land surveillance has been covered in several AGARD meetings while the oceans thus far have received little attention. Techniques for ocean surveillance from satellites and aircraft reached a high degree of sophistication as the result of the combined efforts	Marine biology Surface temperature Oceanographic intelligence	The sea covers more than three quarters of the earth and the concealment it provides to military forces will make it the area of major activities in the next decade. The defence of land and sea is vital to the NATO alliance. Land surveillance has been covered in several AGARD meetings while the oceans thus far have received little attention. Techniques for ocean surveillance from satellites and aircraft reached a high degree of sophistication as the result of the combined efforts	Marine biology Surface temperature Oceanographic intelligence
P.T.O.		P.T.O.	

in space and military programs. The limitations of these techniques come not so much from technology itself but rather from the propagation medium, air and sea. These techniques and the interpretation of results are totally different for land and sea.

This lecture series therefore presents the mathematical tools and their applications to the problems of resolving, recognizing and identifying targets and sources of activities in the ocean. This series should be of interest to physicists and engineers who want to learn the mathematical methods applicable to ocean surveillance, to military users who want to interpret results and infer tactical and strategic implications and to industries interested in developing future generation hardware.

The lecture topics cover two broad categories of surveillance:

- Ocean targets, for instance ships (Imaging).
- Ocean phenomena indicative of military activities, for instance changes in biology or surface temperatures.

The material in this publication was assembled to support a Lecture Series under the sponsorship of the Electromagnetic Wave Propagation Panel and the Consultant and Exchange Programme of AGARD, presented on 3–4 October 1977 in Oslo, Norway, 6–7 October 1977 in Den Helder, Netherlands and 11–12 October 1977 in Rome, Italy.

ISBN 92-835-0202-7

in space and military programs. The limitations of these techniques come not so much from technology itself but rather from the propagation medium, air and sea. These techniques and the interpretation of results are totally different for land and sea.

This lecture series therefore presents the mathematical tools and their applications to the problems of resolving, recognizing and identifying targets and sources of activities in the ocean. This series should be of interest to physicists and engineers who want to learn the mathematical methods applicable to ocean surveillance, to military users who want to interpret results and infer tactical and strategic implications and to industries interested in developing future generation hardware.

The lecture topics cover two broad categories of surveillance:

- Ocean targets, for instance ships (Imaging).
- Ocean phenomena indicative of military activities, for instance changes in biology or surface temperatures.

The material in this publication was assembled to support a Lecture Series under the sponsorship of the Electromagnetic Wave Propagation Panel and the Consultant and Exchange Programme of AGARD, presented on 3-4 October 1977 in Oslo, Norway, 6-7 October 1977 in Den Helder, Netherlands and 11-12 October 1977 in Rome, Italy.

BN 92-835-0202-7

in space and military programs. The limitations of these techniques come not so much from technology itself but rather from the propagation medium, air and sea. These techniques and the interpretation of results are totally different for land and sea.

This lecture series therefore presents the mathematical tools and their applications to the problems of resolving, recognizing and identifying targets and sources of activities in the ocean. This series should be of interest to physicists and engineers who want to learn the mathematical methods applicable to ocean surveillance, to military users who want to interpret results and infer tactical and strategic implications and to industries interested in developing future generation hardware.

The lecture topics cover two broad categories of surveillance:

- Ocean targets, for instance ships (Imaging).
- Ocean phenomena indicative of military activities, for instance changes in biology or surface temperatures.

The material in this publication was assembled to support a Lecture Series under the sponsorship of the Electromagnetic Wave Propagation Panel and the Consultant and Exchange Programme of AGARD, presented on 3-4 October 1977 in Oslo. Norway 6-7 October 1977 in Den Helder, Netherlands and 11-12 October 1977 in Rome, Italy.

ISBN 92-835-0202-7

in space and military programs. The limitations of these techniques come not so much from technology itself but rather from the propagation medium, air and sea. These techniques and the interpretation of results are totally different for land and sea.

This lecture series therefore presents the mathematical tools and their applications to the problems of resolving, recognizing and identifying targets and sources of activities in the ocean. This series should be of interest to physicists and engineers who want to learn the mathematical methods applicable to ocean surveillance, to military users who want to interpret results and infer tactical and strategic implications and to industries interested in developing future generation hardware.

The lecture topics cover two broad categories of surveillance:

- Ocean targets, for instance ships (Imaging).
- Ocean phenomena indicative of military activities, for instance changes in biology or surface temperatures.

The material in this publication was assembled to support a Lecture Series under the sponsorship of the Electromagnetic Wave Propagation Panel and the Consultant and Exchange Programme of AGARD, presented on 3-4 October 1977 in Oslo, Norway, 6-7 October 1977 in Den Helder, Netherlands and 11-12 October 1977 in Rome, Italy.

ISBN 92-835-0202-7

- 4

AGARD

NATO A OTAN

7 RUE ANCELLE - 92200 NEUILLY-SUR-SEINE FRANCE

Telephone 745.08.10 · Telex 610176

DISTRIBUTION OF UNCLASSIFIED AGARD PUBLICATIONS

AGARD does NOT hold stocks of AGARD publications at the above address for general distribution. Initial distribution of AGARD publications is made to AGARD Member Nations through the following National Distribution Centres. Further copies are sometimes available from these Centres, but if not may be purchased in Microfiche or Photocopy form from the Purchase Agencies listed below.

NATIONAL DISTRIBUTION CENTRES

RELCHIM

Coordonnateur AGARD — VSL Etat-Major de la Force Aérienne Caserne Prince Baudouin Place Dailly, 1030 Bruxelles

CANADA

Defence Scientific Information Service Department of National Defence Ottawa, Ontario K1A OZ2

DENMARK

Danish Defence Research Board Østerbrogades Kaserne Copenhagen Ø

FRANCE

O.N.E.R.A. (Direction)
29 Avenue de la Division Leclerc
92 Châtillon sous Bagneux

GERMANY

Zentralstelle für Luft- und Raumfahrtdokumentation und -information Postfach 860880 D-8 München 86

GREECE

Hellenic Armed Forces Command D Branch, Athens

ICELAND

Director of Aviation c/o Flugrad Reykjavik ITALY

Aeronautica Militare
Ufficio del Delegato Nazionale all'AGARD
3, Piazzale Adenauer
Roma/EUR

LUXEMBOURG

· See Belgium

NETHERLANDS

Netherlands Delegation to AGARD National Aerospace Laboratory, NLR P.O. Box 126 Delft

NORWAY

Norwegian Defence Research Establishment Main Library P.O. Box 25 N-2007 Kjeller

PORTUGAL

Direccao do Servico de Material da Forca Aerea Rua de Escola Politecnica 42 Lisboa Attn: AGARD National Delegate

TURKEY

Department of Research and Development (ARGE)
Ministry of National Defence, Ankara

UNITED KINGDOM

Defence Research Information Centre Station Square House St. Mary Cray Orpington, Kent BR5 3RE

UNITED STATES

National Aeronautics and Space Administration (NASA), Langley Field, Virginia 23365 Attn: Report Distribution and Storage Unit

THE UNITED STATES NATIONAL DISTRIBUTION CENTRE (NASA) DOES NOT HOLD STOCKS OF AGARD PUBLICATIONS, AND APPLICATIONS FOR COPIES SHOULD BE MADE DIRECT TO THE NATIONAL TECHNICAL INFORMATION SERVICE (NTIS) AT THE ADDRESS BELOW.

PURCHASE AGENCIES

Microfiche or Photocopy

National Technical Information Service (NTIS) 5285 Port Royal Road Springfield Virginia 22151, USA Microfiche

Space Documentation Service European Space Agency 10, rue Mario Nikis 75015 Paris, France Microfiche

Technology Reports Centre (DTI) Station Square House St. Mary Cray Orpington, Kent BR5 3RF England

Requests for microfiche or photocopies of AGARD documents should include the AGARD serial number, title, author or editor, and publication date. Requests to NTIS should include the NASA accession report number. Full bibliographical references and abstracts of AGARD publications are given in the following journals:

Scientific and Technical Aerospace Reports (STAR), published by NASA Scientific and Technical Information Facility
Post Office Box 8757
Baltimore/Washington International Airport
Maryland 21240, USA

Government Reports Announcements (GRA), published by the National Technical Information Services, Springfield Virginia 22151, USA



Printed by Technical Editing and Reproduction Ltd Harford House, 7–9 Charlotte St, London W1P 1HD